Novel Pillar Formation In Evaporating Poly(Ethylene Oxide) Droplets

Kyle Anthony Baldwin

A thesis submitted in partial fulfillment for the degree of Doctor of Philosophy

Department of Physics and Mathematics

School of Science and Technology

Nottingham Trent University

September 2012

Abstract

Unlike the familiar "ring-stain" formed when spilt coffee drops are left to dry, liquids containing high molecular weight polymer molecules leave a range of other deposit patterns. In this thesis I observe that aqueous solutions of the polymer poly(ethylene oxide) (PEO) dries to form either the common coffee-ring stain, flat uniform "pancakes", or tall central "pillars".

To investigate this phenomenon, I varied experimental factors including: atmospheric temperature, humidity and pressure; polymer molecular weight and concentration; water-ethanol solvent ratios; droplet volume, contact angle and inclination. These factors indicate a region in parameter-space in which central pillars form, favouring fast drying, low temperature, high contact angle, high concentration, high or low (but not intermediate) water-ethanol ratio, and intermediate molecular weight.

I identify four stages in the pillar forming drying process, including a pseudo-dewetting liquid stage which appears to be driven by the formation of a contracting spherulite collar around the droplet's 3-phase contact line. If the liquid base radius recedes quickly enough compared with the height reducing effects of the evaporation, the growing solid deposit eventually lifts the droplet from the surface, resulting in the final central pillars. This is characterised by a minimum droplet volume when precipitation begins, above which the receding radius vanishes before the volume is lost to evaporation, resulting in tall central structures. Conversely, if the volume at the precipitation time is below this value, the height will reach zero during the pseudo-dewetting stage and the common coffee-ring stain is the result.

I show that the dimensionless Péclet number Pe, which compares the relative effects of evaporation and diffusion on the polymer motion, successfully predicts the precipitation time and thus the final deposit shape. To incorporate the effect of molecular weight into our understanding, a further parameter of liquid phase resistance to the contracting collar at high viscosities is introduced.

Declaration

The experiments described in this thesis were carried out by myself and, where indicated, in collaboration with colleagues. The data analysis and interpretation is my own work. This thesis has been written entirely by myself.

Kyle Anthony Baldwin

Acknowledgements

I would like to first acknowledge my professional collaborators/coworkers: Professor Khellil Sefiane for the opportunity to work with him at The University of Edinburgh; Professor Martin Shanahan, for his very useful calculations; Dr. Haida Liang for her expertise in OCT, and for her surprise every time I remembered her Astrophysics lectures; my second supervisor Professor Carl Brown; Dr. Richard Hill from The University of Nottingham for enabling me to perform exciting levitation experiments; Dr. David Willmer, for his knowledge, work, and general cynicism towards anything Microsoft; and Nicasio Geraldi for providing me with very nice PDMS substrates.

Thank you to the undergraduate students that I have supervised during my PhD for helping me with some of the more time consuming aspects of my research, particularly Manon Granjard, Samuel Roest and George Simpson. Without them all I would have had less time to think of ways to explain our findings.

Thank you to my mum for her relentless pursuit of all the details of my progress in life, and for impressing in me her love of all things Indian. Thank you to my dad for the Wednesday evening games of pool, and the constant reminder that "You only get out what you put in". Thank you to Suz for the much needed encouragement during those long months of writing and the belief that I could be the next Professor Brian Cox. Thank you to my old house mate and current best mate Adam, for introducing me to bouldering, squash and port, and generally making my PhD years a lot more fun.

Finally, a special thank you to Dr. David Fairhurst, who has not just been my supervisor, but has been my mentor and friend for the duration of my PhD and longer. Dave hasn't just taught me how to successfully change my title from Mr. to Dr., he has moulded me into the professional, inquisitive and clumsy physicist that I am today. It is safe to say that I owe Dave a pint.

Contents

Notation

The main variables used throughout this work are listed in this section. Many of these appear in the text with subscripts, the meaning of which should be made clear in the adjacent text.

A	Surface area
b	Kuhn length
B	Magnetic field strength
c	Concentration by mass
c_{sat}	Saturation concentration
D_{s}	Self diffusion coefficient
D_{c}	Cooperative diffusion coefficient
$\dot{e}$	Shear rate
E	Free energy
g	Acceleration due to gravity
G', G''	Storage and loss modulii
h	Droplet height
j	Local evaporative flux
k_B	Boltzmann constant
l	Monomer length
m	Mass
M_{W}	Molecular weight
M_{e}	Entanglement molecular weight
n	Number of steps in a random walk, number of monomers
N	Number of Kuhn steps
P	Atmospheric pressure
Pe	Péclet number

R	Droplet base radius
R_c	Radius of curvature
R_G	Radius of gyration
R_h	Hydrodynamic radius
RH	Relative humidity
RI	Refractive index
t_p	Precipitation time
T	Temperature
v	Excluded volume
V	Droplet volume
γ	Interfacial tension
ζ	Friction coefficient
η	Apparent viscosity
$[\eta]$	Intrinsic viscosity
η_s	Solvent viscosity
θ_c	Droplet contact angle
$\theta_\mathrm{R}, \theta_\mathrm{A}$	Receding and advancing contact angle
λ_c	Capillary length
ν	Flory exponent
ξ	Correlation length
ξ_T	Thermal blob size
ρ	Density
τ	Relaxation time
ϕ	Volume fraction
ϕ^*	Overlap concentration
ϕ^{**}	Concentrated solution threshold
ϕ_e	Entanglement concentration
χ	Magnetic susceptibility

Abbreviations

CCD	Charge-Coupled Device
DLS	Dynamic Light Scattering
DSC	Differential Scanning Calorimetry
LCST	Lower Critical Solution Temperature
OCT	Optical Coherence Tomography
PEG	Poly(ethylene glycol)
PEO	Poly(ethylene oxide)
PTFE	Polytetrafluoroethylene, Teflon
RHT	Relative-Humidity-Temperature
SANS	Small Angle Neutron Scattering
SEM	Scanning Electron Microscope

Somewhere, something incredible is waiting to be known.

CARL SAGAN

Chapter 1

Introduction

The goal of this research is to examine, report and explain the unusual behaviour of aqueous poly(ethylene oxide) (or PEO as it will be mostly referred to) droplets during evaporation, with particular emphasis on the different structures these drying droplets form as a product of the initial droplet dimensions, the atmospheric conditions and the properties of the solution.

As much as I would like to claim that I discovered the unusual behaviour of drying PEO droplets myself, it was in fact my PhD predecessor David Willmer who, whilst studying fairly unrelated rheological properties of shampoos, first noticed that this line of research could prove novel. What he saw was that under the right conditions, PEO tends to form tall central structures (or "pillars" as they would be later known), which were both similar and dissimilar to those of other drying polymer systems, a line of research which in itself has been barely touched upon in the literature. An example of a typical PEO "pillar is given below.

Initial Droplet   Dried Pillar

Figure 1.1: Example comparison between an initial PEO droplet and its fully dried "pillar" form.

However, due to the time constraints of his PhD, little progress could be made in the fundamental understanding of these observations. This is where I step in.

During the early days of my PhD the title of my research was undefined. Indeed projects including liquid crystals, particle suspensions, and drying droplet induced substrate buckling were considered as possible projects. Despite the variety of research possibilities, I was keen to revisit that which David Willmer had briefly touched upon. It was after all something entirely new and unexplained, and what could be more exciting to a scientist than a phenomenon not yet understood? From this point I devoted myself entirely to varying any and all possible droplet and atmospheric conditions in order to gather together a large wealth of PEO droplet drying observations, to then attempt to explain, once and for all, how a drying aqueous PEO droplets could grow into a tall structure up to twice the height of the initial droplet. Unfortunately (or amazingly, depending on your outlook), drying PEO droplets resisted simplicity.

Let's take a step back for a moment. Why, you may ask, is a drying droplet of importance to the scientific community? Indeed, my many friends in Chemistry marvel at the fact that I have managed to find such a line of research so interesting for so long! After all, I have devoted the last 3 years to watching things dry. The obvious metaphor for boredom seems to escape no one's notice. Despite the metaphor for the mundane, the scientific interest over the last decade in watching droplets dry (paint or otherwise) has been growing. The subtle interplay between the changes in surface forces and bulk behavior as a result of evaporation provides intellectual intrigue. Furthermore, the associated potential applications including (but not exclusive to) inkjet printing, printed electronics, cooling techniques, crop spray treatment etc. demand continued advancement in our understanding.

Detailed study of drying droplets is a field of research that only really began 15 years ago, with the seminal work of Deegan et. al. in which they explained the common occurrence of coffee ring stains [1], an example of which shown in Fig.1.2.
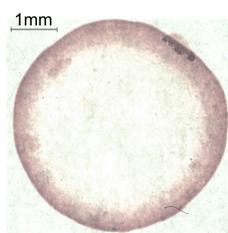
Figure 1.2: Example of the common coffee-ring stain.

It seems amazing to me that something as common as the rings that form after spillage of various drinks (a list which includes, but is not limited to, coffee, tea and wine) did not achieve scientific understanding until 1997. With the ring-stain explained, is drying droplet science finished? In short, the answer is an emphatic no. The final morphology of the dried solute is most certainly not always a ring but depends on many experimental factors including: the solvent evaporation rate (Marín et al. 2011 [2]); suspended particle shape (Yunker et al. 2011 [3]); self-assembly and organisation as mediated by solvent dewetting (Stannard 2011 [4]); interactions between solvent, vapour and substrate (Rowan et al. 2000 [5]; Li & Graf 2009 [6]); phase transitions within the droplet (Pauchard & Allain 2003 [7]; Parisse & Allain 1997 [8]); and the contribution of internal convection currents (Hu & Larson 2006 [9]).

In addition to suspensions, drying experiments have been performed on droplets of polymer solutions. Pauchard and Allain observed that during evaporation of Dextran (a branched polysaccharide), the concentration at the surface increases until a glassy skin forms [7]. They propose that the skin is water permeable yet incompressible so that upon further evaporative volume loss the constant-area skin is subjected to stress and buckles leading to various final shapes, including doughnut and sombrero-like deposits, which are predicted using geometric arguments from initial values of contact angle, humidity, temperature and concentration.

My first contribution to our understanding of PEO drying was to distinguish the processes that lead to the tall central pillars as separate from those discussed by the large volume of work published by Pauchard and Allain with regards to Dextran droplets. Proving that PEO drying follows a different process entirely led to our first publication. PEO, is a very common and widely used linear polymer - so widely used that at the time of writing this I have no less than 30 papers at hand whose sole purpose is to report the properties of PEO (sometimes referred to as poly(ethylene glycol), or PEG) in solution. The astonishing thing is not that we have discovered this unusual drying property, but that no one else has!

The main variables explored that will be detailed in this thesis can be summarised as follows:

- Droplet geometry. This includes varying initial contact angle (on substrates with varying degrees of hydrophobicity), droplet volume, substrate inclina-

tion and diamagnetic levitation.

- Solution properties. This includes varying initial concentration, polymer molecular weight, and solvent (water-ethanol) mixtures.

- Atmospheric conditions. This includes varying relative humidity (by introducing saturation salt solutions and silica gel beads), atmospheric pressure (with use of a vacuum pump) and temperature (wth use of either an oven or a hot plate).

The drying processes and final structures formed under these varying conditions will be observed through a variety of techniques including: CCD camera profile imaging, microscopy, optical coherence tomography (OCT), profilometry and confocal microscopy. Furthermore, an array of techniques will be used to characterize my samples including: rheology, differential scanning calorimetry (DSC) and densitometry.

With these observations at hand I will attempt to explain the effects these variable conditions have on the pillar formation process, which (and I hope the reader will agree) will prove to be more successful at explaining the effects of some variables (such as droplet geometry, concentration and atmospheric conditions), than others (such as ethanol content, substrate inclination and molecular weight).

With all this in mind, I will break down this thesis into the following sections:

- Background Information. This is further split into:

  - Chapter 2 ("Polymers"), which goes into some detail of the current understanding of the behaviour of polymers in solution, with particular emphasis on PEO.

  - Chapter 3 ("Droplets"), which provides an overview of the current understanding of liquids, sessile droplets and evaporation, and then focuses on many of the competing current lines of research into this field, which often do not agree.

- Methodology. Chapter 4 details the experimental protocol and methodology used throughout my research, and gives some information on the scientific background behind the techniques and devices used.

- Results and Discussion. This is split into three further sections:

  - Chapter 5 - PEO Droplet Pillaring. Here I report the initial observations of the structures that form with varying concentration, contact angle and volume, and describe a novel 4 stage drying process including pinned drying, pseudo-dewetting, boot-strap building and late stage contraction. This chapter will also propose several explanations for the appearance of the unusual growth stage, and describe a geometric argument to explain how high concentration/contact angle PEO droplets form tall central pillars, whereas low concentration/contact angle droplets form the well established coffee-type ring stains.

  - Chapter 6 - The Péclet Number. In this chapter I discuss the effects of varying atmospheric conditions and propose that the limiting factor behind pillar formation is a dimensionless number (Pe) which describes the competition between evaporation induced advective flow and diffusive back flow. I continue by exploring the effect of varying ratio water-ethanol-PEO ternary mixtures, and offer several explanations for the effect of the addition of a second, more volatile solvent.

  - Chapter 7 - The Role of Molecular Weight. This chapter reports some of the more puzzling observations found when varying the molecular weight of PEO, with various potential explanations offered to account for this behaviour, including viscoelasticity, diffusivity and contact line flow resistance.

- Conclusions. Lastly, we finish off with some brief final thoughts and conclusions in Chapter 8.

It is my sincere hope that the reader find the subject of this thesis as engaging as I have found it for the last 3 years, and perhaps, with any luck, shine a light on some of the gaps in my understanding. To me, the subject of this thesis, drying PEO droplets, is a puzzle that just keeps on giving.

A chain is no stronger than its weakest link,
and life is after all a chain.
WILLIAM JAMES

Chapter 2

Polymers

Polymers are everywhere. It is often forgotten that these long chain molecules, which are so common that it would be impossible to live a day without noticing their influence on our lives, were for a long time a mystery to science. They make up the fabrics of our clothing, the moulded plastic sheets we carry our groceries in, the thin strands of silk spiders weave their fly catchers with, and even the majority of the gunk that clogs our noses from time to time. One would think that these would therefore have been relatively simple to understand. However, by the time the first accurate description of the structure of a polymer was published by Staudinger in 1920 [10], we had already developed rapid fire gun warfare, invented the aeroplane and the pop-up toaster, and described the theory of general relativity!

Polymers not only serve technological uses, but also make up the fundamental building blocks of life - proteins. Our understanding of the unique properties of polymers in terms of both their chemistry and physical attributes still continues to advance today. While the many uses of polymers are far too all encompassing to satisfactorily list here, the reader should remember the next time he or she walks through a spiders web, or squeezes their squash ball, or takes a bite out of a juicy fillet steak, without polymers, the planet we live on would not be very interesting at all.

2.1 Polymer Configuration

2.1.1 What is a Polymer?

The word polymer comes from the greek words *poly* and *mer* meaning "many part", and refers to large molecules (or macromolecules) which consist of many repeating elementary units, called monomers. There are however several definitions of a monomer. If one was to examine a polymer chain with some kind of very high magnification microscope, it would seem logical to define the monomer as the smallest repeating chemical unit. Typically however, convention dictates that a monomer be defined as the original chemical compound that was used prior to polymerization (the process of covalently linking many monomers together into a single much larger molecule). There is a third definition, more commonly used by physicists, which is of a structural nature and is known as a Kuhn monomer, which will be discussed in detail in section 2.1.3. Depending on the context, the word monomer will be used interchangeably between these two definitions, and will be defined explicitly in the text.

The standard unit of measurement for the mass of a polymer chain is to multiply the mass of a single chemical monomer M_{mon} by the of the number of monomers N. For example, the simplest polymer is polyethylene, which consists of a purely repeating CH_2-CH_2 backbone. The mass of a single molecule is 0.028
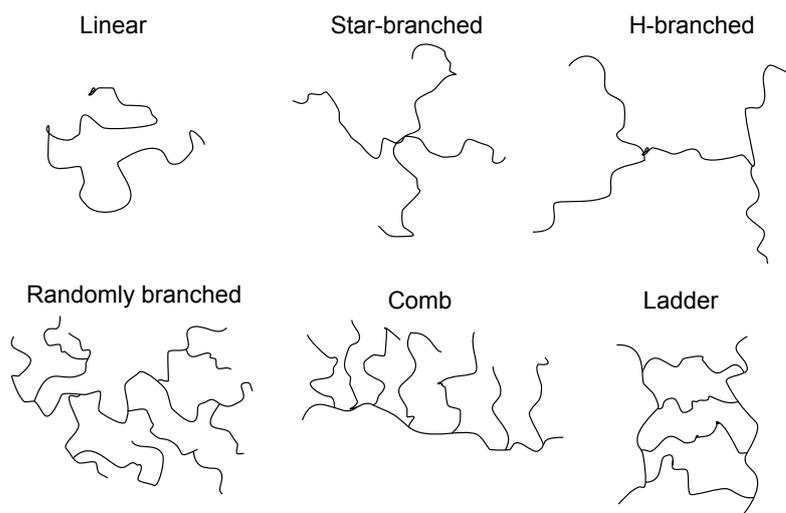
Figure 2.1: Diagram of several examples of polymer architecture including: linear, star-branched, H-branched, randomly branched, comb and ladder structures.

kg/mol. And so a chain made of 2000 units would have a molecular weight of 56 kg/mol. It should be immediately apparent that if one was to analyse the polyethylene make up, one could define the repeating unit as simply CH_2, and rename it polymethylene. However, traditionally this type of polymer is formed through the polymerization of ethylene, and so the polymer retains the name of this original molecule. This leads to alternative names for identically structured polymers purely for traditional reasons, for example poly(ethylene glycol) (PEG) and poly(ethylene oxide) (PEO), which are molecularly identical, but polymerized from different initial molecules.

Linearity also plays a crucial role. While molecular weight and monomer chemical make up are sufficient to define the total end-to-end length of the polymer if it is completely linear, this is not always the case, and depends largely on the process by which the polymer was synthesized. Several non-linear polymer architectures include: star-branched, H-branched, randomly branched, comb or ladder as shown in Fig.2.1. DNA for example is a type of double-helical ladder structure polymer. Because the research in this thesis focuses on the properties of PEO, a linear chain polymer, these unusual structures will be discussed no further.

Typically, polymers exist in several states:

- **Solution**. As with all compounds, polymer solubility is highly dependent on the solvent used, but also on the chemistry and structure of the polymer chain. Most polymers such as polyethylene, polystyrene or polyester, to name a few, will not readily dissolve in water as the carbon backbone is highly water repellent. This feature is preferable for many industrial applications. Clothing that dissolved when washed would not be very useful! However there are also many polymers that do dissolve in water such as: deoxyribonucleic acid, most commonly known as DNA; Dextran, a long chain sugar molecule [11]; and PEO*, a linear chain organic polymer, which will be the focus of much of this research.

- **Melt**. A melt is simply the 100% concentrated polymer heated above its melting temperature T_m [10]. Polymer melts are most often used to extrude the polymer into thin strands for the formation of fabrics for clothing or thin films for plastic sheets such as carrier bags. Polymer melts and solu-

---

*PEO solubility will be discussed in detail in section 2.4.1

tions typically differ from standard liquids by their distinctive viscoelastic properties, which will be discussed in section 2.3.2.

- **Glass**. Transitions to the glassy state are not true thermodynamic phase transitions, but important nonetheless. In a glassy state there is no molecular ordering, much like a liquid, but the relaxation time is essentially infinity. This means that while the molecules are not held in place in a regular lattice structure, they are still unable to flow, and can be pictured as being simply frozen in place. Given a slow enough cooling rate, all polymers display a glass transition, with the value at which the transition occurs dependent on the cooling rate. In the literature, values of T_g are given as the point at which this transition occurs as cooling rate approaches zero [10].

- **Rubbery**. If a polymer in the glassy state is heated it eventually will reach its glass transition temperature T_g. Above this temperature portions of the molecules can start to wiggle around, which then gives the polymer softness and flexibility. The polymers are now in their rubber state.

- **Semi-Crystalline**. Complete crystallinity is unlikely due to kinetic and steric effects: the polymers get in each other's way, but ordering into short scale lamellae is often preferable to forming a glassy state in some polymers. This state will be discussed in greater detail in section 2.4.3.

- **Liquid Crystalline**. Some polymers are rigid rod-like structures which have properties of both liquids and crystals (hence the name liquid crystals). While interesting, these will not be discussed any further.

2.1.2   Random Walks

In figure 2.1, it is clear that the end-to-end path a linear polymer takes seems to be fairly random. In fact randomness is one of the first key assumptions of the polymer arrangement that helps us to understand their unique behaviour. The path a polymer takes through space is assumed to be a freely-jointed chain. In this model, the chain is assumed to be made up of a series of monomers of fixed length l. The "freely-jointed" term comes in due to lack of limitations on the orientations and positions of monomers. Effectively, it is as if a long series of infinitely flat but completely rigid paper-clips were connected together. The rigidity of these clips

maintains both the length of the monomers and the end-to-end length of the chain. The infinitely thin aspect allows the chain to orient itself into any configuration (each with equal energy), even to the extent that two monomers can be in the same position in space. This is the first assumption of polymer configurations, and as we will see, it has both strengths and weaknesses. Fortunately, these weaknesses can be largely accounted for by some simple adjustments to the model. Let us first consider the configuration of one of these "paper-clip" polymers, a random walk.

A random walk is exactly how it sounds, it is a series of steps through space in which the direction of every step is independently and randomly chosen. Let us imagine a creature that lives in just one dimension, that is, it has freedom of movement forwards and backwards *only*. If it follows a continuous random walk, it will move one equal length step per time interval either forward or backward from each successive position, with each direction of motion being equally likely at all times. After n steps, we stop the creature's walk and record its final position as either a negative or positive value of x. Probability dictates that because forward and backward steps are equally likely at all times, if we were to repeat this random walk many times and take an average of the creature's final finishing position, the mean position would be at the origin, even though very few particular walks will finish at the origin.
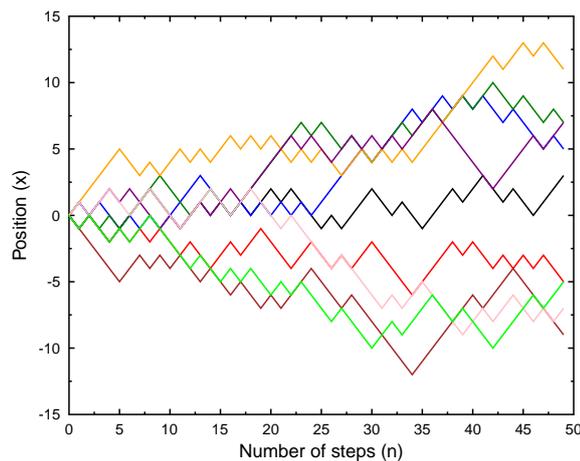
Figure 2.2: Plot of nine 1D random walks as position away from the origin against number of steps taken. Increasing variance in final position gives indication that rms distance increases with number of steps taken.

Fig.2.2 is a plot of nine 1D random walks with distance from origin against number of steps taken. Even with as small a sample as nine random walks, one should see that the mean distance away from the origin remains at around zero. However, if we disregard direction for a moment by squaring each final distance from the origin, and then taking the square root of the average result, we end up with what is known as the *root mean square* (or *rms*) distance. This result interestingly does not turn out to be zero, but increases linearly with the square root of the total number of steps taken:

$$\sqrt{\langle x^2 \rangle} \propto \sqrt{n} \tag{2.1}$$

In two dimensions, a random walk can be pictured by the *drunkard's walk* model, in which we imagine a drunk man walking away from the a bar on a two dimensional map which consists of a square grid of roads, each road the same length, each ending with the same intersection, as shown in Fig.2.3. Every time the drunk
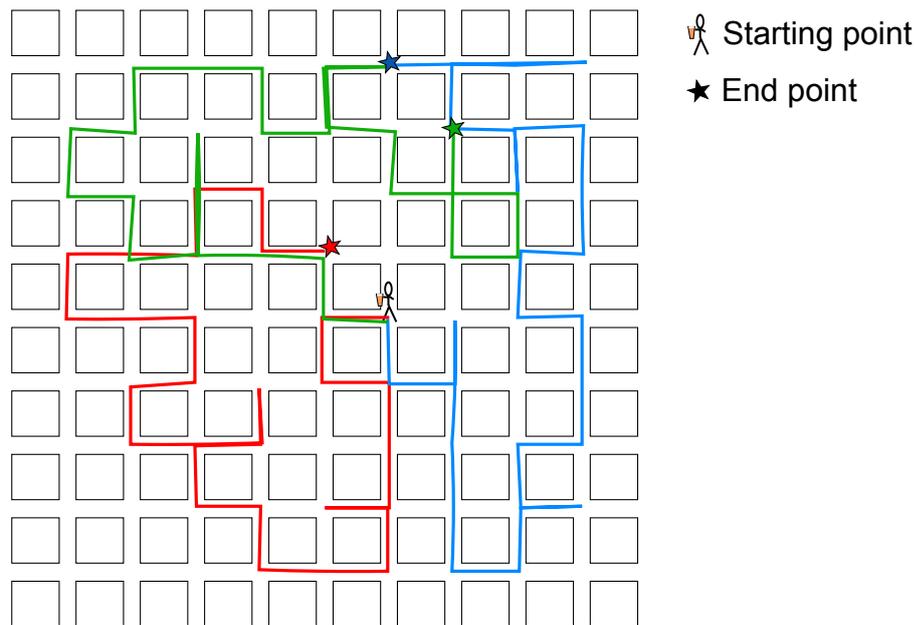
Figure 2.3: Drunkard's walk model of a 2D random walk. Different coloured lines represent different random walks taken. Stars represent their respective final positions after $n = 30$ steps.

man reaches an intersection he gets confused and picks a random direction from either forwards, backwards, left or right. Again, an average final position would find him back at the bar, but the rms position would increase proportionally with

the square root of the total number of roads he travelled down. And continu-
ing into 3D, we can imagine a bird flying randomly through the air. Fig.2.4 is
a plot of three 3D random walks, each with $n = 750$ steps, step length $l = 1$.
This diagram should serve as the starting point for picturing the random coil
arrangements used to understand polymer behaviour.
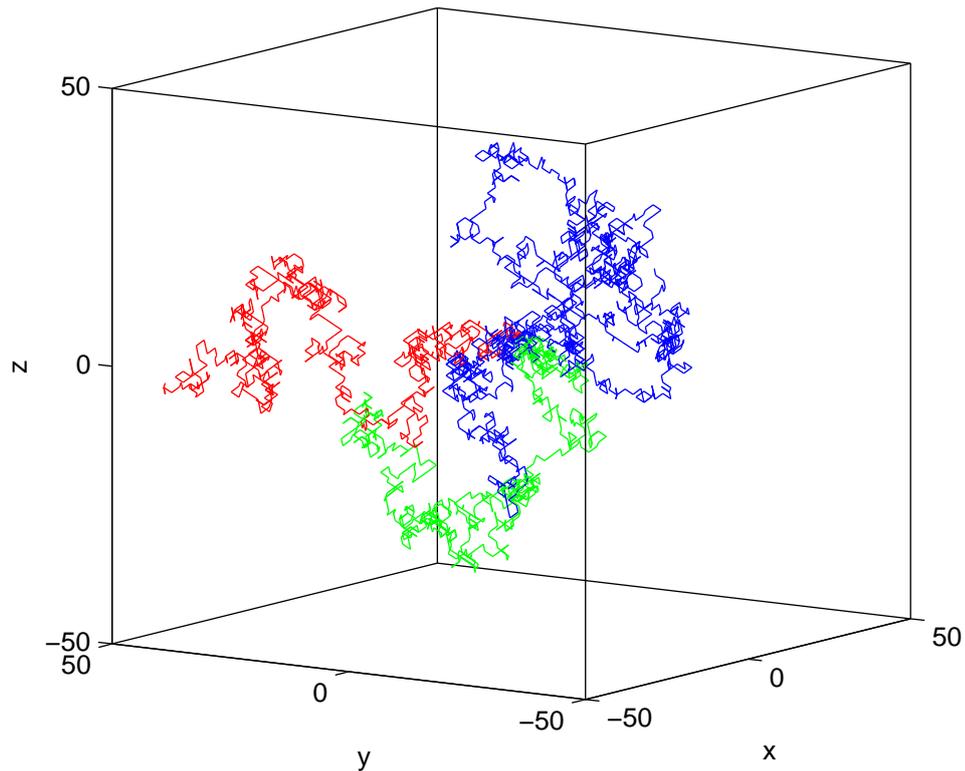
Figure 2.4: Plot of three different random walks of 750 steps (each step length equal
to one unit in space) in three dimensions.

Let us consider a polymer that consists of a fixed number n of random steps
through space, with $n + 1$ backbone atoms and the individual step length being
equal to the monomer length l. Let us assume that one end of the polymer is fixed
at the origin, and the other end is a distance r away. If we were to take an average
of every possible configuration of this polymer, the average value of r would be
zero. In the freely jointed chain model there is no correlation between the bond
angles, which is to say that every monomer can follow any direction regardless
of the position of the previous monomer. In this model, the rms distance is
simply the product of the length of each monomer and the square root of the

total number of monomers [10]:

$$\sqrt{\langle r^2 \rangle} = l\sqrt{n} \tag{2.2}$$

This assumption of a freely jointed chain is immediately troublesome as in reality a monomer certainly cannot overlap another monomer, and polymers do not follow a truly random walk at the monomer level as bond angles are fixed whereas there is no such restriction for a drunkard's walk. It turns out however that these random walk assumptions are still important, but to accommodate for the fixed bond angles of a real polymer, one only needs to introduce a new concept: the *Kuhn length*.

2.1.3 The Kuhn Length

While a bond angle between each monomer is fixed, it is free to rotate in 360° (provided other side groups do not get in the way). Fig.2.5 shows that due to this rotational freedom between each monomer, as the number of monomers increases so too does the number of possible configurations. The solid black line is a polymer chain made of just 4 units. The solid grey lines represent several other possible paths this chain could have taken due to the rotational freedom (dotted lines) between each monomer. This diagram obviously does not show all configurations, but gives an indication of the increasing freedom with each successive monomer.

At some value of monomer steps n there is a sufficient number of monomers, each with their cumulative degrees of rotational freedom, to lead to the end-to-end position being equally likely at any point in space (within a certain radius). i.e. it is equally likely to come back to the origin as it is to continue in the original direction. This type of chain would effectively be made of two steps in a three-dimensional random walk in space, each step with length b, the Kuhn length, named after the man who developed this concept, Werner Kuhn [12].

Now we can state that a real chain consisting of n monomers, each with length l and fixed bond angles, is also a series of larger Kuhn steps which are equally likely to be oriented in any direction, allowing us to once again consider a polymer to be a freely jointed chain. The chain can now be said to consist of N Kuhn steps, each of length b. Now we rewrite equation 2.2 for the rms polymer end-to-end
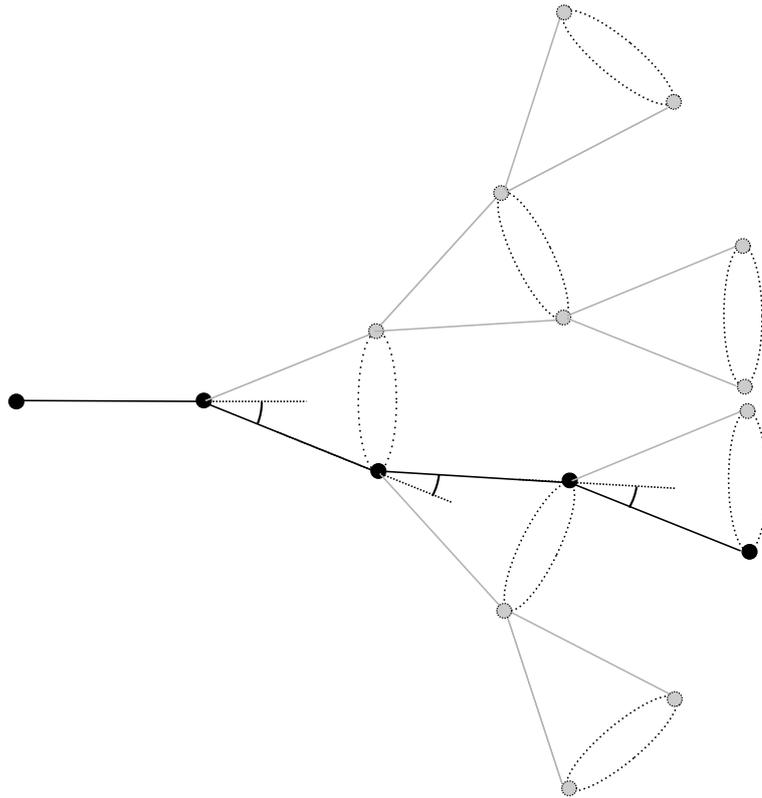
Figure 2.5: A diagram of the cumulative configurational freedom with each successive monomer. Solid black line represents a single path through space a series of 4 monomers could take, solid grey lines represent alternate equally likely paths due to the rotational freedom (represented by dotted lines) between each monomer.

distance:

$$\sqrt{\langle r^2 \rangle} = b\sqrt{N} \tag{2.3}$$

Up until now we have defined the size of a polymer by its rms end-to-end distance. However, a related, more useful term for polymer physicists is the *radius of gyration*, as this is a universal trait of polymers, including ones with branched or star-shaped configurations. This is defined as the rms distance of any point along the chain from the polymer's centre of gravity. For a linear polymer, the radius of gyration is given by:

$$R_{\mathrm{G}} = \sqrt{\frac{\langle r^2 \rangle}{6}} = \sqrt{\frac{b^2 N}{6}} \tag{2.4}$$

These ideal chain configurations however still assume zero interactions between monomers, and worse, we assume separate Kuhn segments can overlap. While we may have removed the problem of a fixed bond angle, overlapping chains still

seems rather unphysical. To continue to develop this polymer framework we must consider interactions between different segments of the polymer chain.

2.1.4   Real Chains

In an isolated polymer chain, the interactions between distant monomers are important. It is forbidden for two monomers to exist in the same volume of space at the same time. The volume of space that a monomer repels another monomer from entering is known as the excluded volume. In a good solvent we assume this volume to be approximately equal to the occupied volume of the monomer (assuming that monomers are roughly spherical in shape), $v \sim b^3$, and its effects on the random configuration of the polymer is to swell the otherwise preferable freely jointed chain into a more complicated *self avoiding* random walk, or *swollen coil*.

To understand a self avoiding random walk we must introduce two forces:

- E_{rep}, which is the free energy associated with the excluded volume interactions. The total free energy is a product of the number of segments N, the excluded volume (which we assume to be equal to b^3), the thermal energy $k_B T$ and the likelihood of an interaction between two segments, given by the concentration of segments in the total volume, $c \sim N/r^3$. Therefore[†]:

$$E_{\text{rep}} = \frac{k_B T}{2} \frac{b^3 N^2}{r^3} \qquad (2.5)$$

- E_{el}, which is an entropically driven increase to the free energy. When a polymer is stretched beyond its ideal random walk value, the number of different configurations it can take is lowered, resulting in a reduction in entropy. A reduction in entropy is unfavourable, and results in a spring-like restoring force proportional to the length of the extension. Using statistical mechanics (which is calculated in depth in the Appendix of Richard A.L. Jones's book "Soft Condensed Matter" [13]) to calculate the total number of possible configurations, this entropic increase to the free energy is given by:

$$E_{\text{el}} = k_B T \frac{r^2}{N b^2} \qquad (2.6)$$

[†]In like-like interactions, a factor of $1/2$ is introduced to avoid counting interactions twice.

These free energies are caused by opposing forces, therefore the polymer will be stable when the sum is at a minimum, given by differentiating the total free energy by r and setting equal to zero:

$$\frac{\partial E_{\text{Tot}}}{\partial r} = \frac{2k_B T r}{N b^2} + \frac{3k_B T}{2} \frac{b^3 N^2}{r^4} = 0 \tag{2.7}$$

Rearranging for r, and exchanging for the radius of gyration gives gives:

$$R_{\text{G}} \propto N^{3/5} \tag{2.8}$$

This is similar to the freely jointed chain model, but with N raised to 3/5 rather than 1/2. The power N is raised to is known as Flory's exponent (ν), and in dilute, good solvent conditions, is equal to 3/5, which is the common limiting case for a self-avoiding random walk, or swollen coil. Experimentally, the size of a dilute polymer in a good solvent follows this scaling law very closely[‡]. This is a remarkably fortuitous result. Since Flory first came up with this law, more careful analysis has shown that both the excluded volume repulsive energy and the entropic elastic energy have been overestimated by very similar amounts [10]. Flory did not take into account that as N increased, monomers from distant parts of the chain would be less and less likely to interact with each other. Flory's basic principles of a competition between excluded volume and entropy were correct, and the final result was close enough to the results found by more complicated theories[§] that experimental precision is not high enough to distinguish between the two exponents. His calculations however seem to reach this goal more by luck than by design.

We must also note that this argument can not work in concentration regimes where separate polymers are so highly packed together that they are limiting the number of possible configurations each other can take. Clearly if there is very little room for the polymer to position itself in, the number of possible configurations will be lowered. Therefore the entropic effects are diminished and the polymer follows an ideal chain scaling law with $R \propto N^{1/2}$ when the solution is concentrated. Essentially, neighbouring polymers are in every direction, which means that it no longer matters what configuration the polymer sits in. This

---

[‡]Size is measured through methods such as Dynamic Light Scattering (DLS), which is a technique that uses the scattering intensity of a sample to calculate its diffusivity, and thus its hydrodynamic radius.

[§]Renormalization group theory, exact numerations and computer simulations lead to an exponent of $\nu \approx 0.588$.

is not the whole picture however, as the transition from dilute to concentrated regimes has an intermediate concentration regime, known as *semi-dilute*, which has characteristics of both an ideal random walk and self avoiding random walk. This will be discussed in more detail in section 2.1.6.

One more important scaling law to introduce is the concept of a *thermal blob*. This a straightforward concept and requires little extra calculation. We have shown that a dilute polymer in good solvent follows a self-avoiding random walk. However, if we were to study the polymer more closely and observe the random walk behaviour on small length scales, we would see that this self-avoiding random walk is made of small ideal chain segments. Essentially, these segments are so small that the effects of the thermal energy $k_B T$ are greater than the effects of the excluded volume. As the length of the polymer is increased $k_B T$ remains constant while excluded volume effects play an ever increasing role on the polymer configurations. The self-avoiding "swollen coil" is now made up of a series of small ideal chain *thermal blobs*, with size ξ_{T}. The size of the thermal blob is given by:

$$\xi_{\mathrm{T}} \propto \frac{b^4}{|v|} \tag{2.9}$$

Where b is the Kuhn length and v is the excluded volume. The description previously made of the excluded volume is a simplistic one. In fact this "volume" can take on zero or negative values depending on the interaction between monomers and solvent. A positive value means that there is a volume of space in which neighbouring monomers are repelled from. However in theta solvents ($v = 0$) there is no repulsion between monomers, and in a poor solvent ($v < 0$), the interaction between monomers is attractive. These types of solvent interactions are discussed in the next section. In the argument above where we only considered a good solvent and assumed $v \sim l^3$, the thermal blob size would simply be equal to one Kuhn length, but this is not always the case.

2.1.5 Solvent Quality

Now we must consider the alteration in configuration caused by the interactions between separate polymer chains and solvents. First let us assume that the polymer solution is dilute (zero polymer overlap) and that the solvent and polymer are not chemically identical (which is actually sometimes the case, for example a long chain polystyrene molecule dissolved in its monomer unit, ethyl benzene).

We will define the interaction energies as ϵ_{pp}, ϵ_{ps} and ϵ_{ss} between two polymer molecules, a polymer and a solvent and two solvent molecules respectively. If we pick a point in space in the solution (this point could either be a solvent or a monomer), the probability of the nearest atom being one of the chain monomers is the polymer volume fraction ϕ, and the probability of it being a solvent molecule $1 - \phi$.¶ The total energy associated with polymer-polymer, polymer-solvent and solvent-solvent interactions are given by the product of the number of interactions and the energy per interaction [13]:

$$E_{pp} = \frac{zNv\phi}{2} \tag{2.10}$$

$$E_{ps} = zNv(1 - \phi) \tag{2.11}$$

where v is the occupied volume of the monomer, which is assumed to be equal to the volume of the solvent molecules, z is the number of neighbouring molecules per molecule and N is the total number of monomers. Because we assume all solvent molecules and monomers are equally sized and randomly positioned, we can calculate the number of solvent-solvent interactions as simply the difference between the number of solvent-solvent interactions before adding the polymer to the solution (N_{ss0}) and the total number of polymer-polymer and polymer-solvent interactions. Therefore the energy associated with all the solvent-solvent interactions is given by:

$$E_{ss} = \epsilon_{ss}(1 - \phi) + \epsilon_{ps}\phi \tag{2.12}$$

and the energy associated with all interactions:

$$E_{int} = \frac{1}{2}zNv\phi\epsilon_{pp} + zNv(1 - \phi)\epsilon_{ps} + N_{ss0}\epsilon_{ss} - \frac{1}{2}zNv\phi\epsilon_{ss} - zNv(1 - \phi)\epsilon_{ss} \tag{2.13}$$

This is the standard method picture for quantifying the interaction energies of a polymer-solvent mixture. At this point, we have a term for the total energy of interactions, but we also need to factor in the effect of the repulsive excluded volume interaction, given by equation 2.5. For simplicity, we now introduce a new parameter χ, which is a dimensionless number characterizing the relative strength of each interaction:

$$\chi = \frac{1}{2k_BT}z(2\epsilon_{ps} - \epsilon_{pp} - \epsilon_{ss}) \tag{2.14}$$

¶Note that this assumes that the size of a monomer molecule is identical to a solvent molecules, and that they are randomly distributed in the solution. Clearly at a point on the polymer chain the likelihood of a neighbouring volume of space being occupied by a monomer is higher than in the solvent.

We now write the sum of the energy contributions as:

$$E_{\text{rep}} + E_{\text{int}} = k_B T v (1 - 2\chi) \frac{N^2}{2r^3} + \text{constant} \qquad (2.15)$$

We know that the repulsive energy of excluded volume interactions is always positive. From this, we can make a few simple definitions based on the χ parameter:

- $\chi < 0.5$. The total contribution of energies remains positive, and the repulsive effects of the excluded volume are greater than the interactions between polymer and solvent, so the polymer remains a swollen chain, with $R_{\text{G}} \propto N^{3/5}$

- $\chi = 0.5$. The solvent interactions exactly cancel out with the repulsive effects of the excluded volume, and the polymer scales as an ideal chain, $R_{\text{G}} \propto N^{1/2}$. A solvent which causes this type of interaction is known as a *theta solvent.*

- $\chi > 0.5$. The polymer repulsion from the solvent outweighs the excluded volume repulsion, and the polymer collapses to form a compact *globule.* A globule is not considered to be truly dissolved, but rather a suspended particle which if concentration is increased is highly likely to aggregate with other globules and sediment than remain dispersed. The radius of the globule R_{gl} scales with $N^{1/3}$.

Fig.2.6 is a diagram of the differing configurations of a single dilute polymer depending on the polymer-solvent interactions.

As can also be seen from equations 2.14 and 2.15, the interaction energy is highly dependent on temperature. From this we can deduce that it is possible to produce a controllable coil-globule transition in a given polymer-solvent mixture through the careful control of temperature. In reality phase transition diagrams are not as simple as this, but this lays the groundwork for understanding how temperature can be a sensitive control of solubility.

2.1.6   Concentration Regimes

Until now we have assumed dilute solutions, which means that the volume encompassed by each polymer does not overlap another. In this thesis we will be
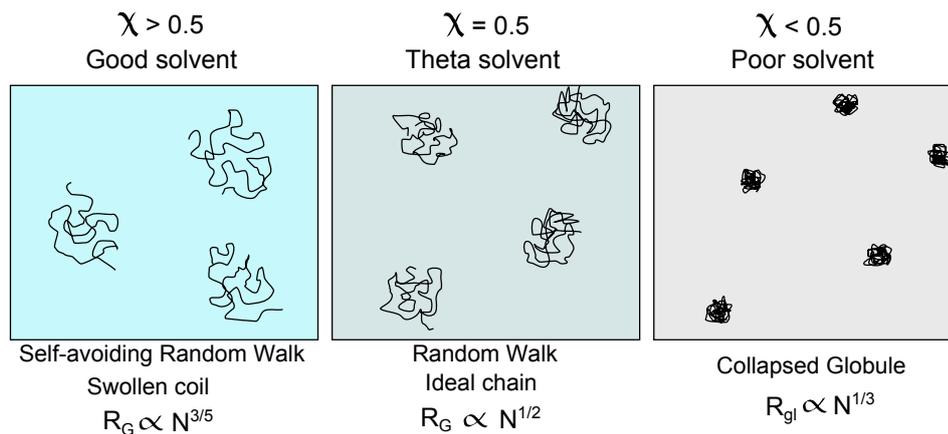
Figure 2.6: Diagram of the effect of solvent interactions on the size of the polymer coil. In a good solvent, excluded volume interactions dominate and the polymer behaves as a self-avoiding random walk, or swollen coil. In a theta solvent, interactions cancel each other out and the polymer follows an ideal random walk. In a poor solvent, solvent repulsion effectively cause monomer-monomer attractions, and the polymer size reduces into a tightly packed ball of thermal blobs, or a collapsed globule.

mostly dealing with good solvent conditions, therefore these will be discussed in greatest detail. As concentration in a good solvent is increased, we can imagine the spheres of radius R_{G} will approach each other. The point at which these spheres meet, as shown in Fig.2.7 is known as the overlap concentration ϕ^*.

The overlap concentration is also defined as the point where the global concentration of the solution is the same as the concentration within the polymer pervaded volume. Assuming each Kuhn segment has a volume $\frac{4}{3}\pi b^3$, the concentration within the sphere of this radius is given by:

$$\phi^* = \frac{Nb^3}{R_{\mathrm{G}}^3} \tag{2.16}$$

At the overlap concentration, we can also make another important statement: the solution is concentrated with dilute regions. This is shown best in Fig.2.8, in which we can see that in the circled regions, polymers are essentially surrounded entirely by solvent, and do not "notice" other polymers. Whereas if we would zoom out a little, we would see that there is zero space between these spheres, and we can consider the solution concentrated with these spheres. At this point we will introduce a new term known as the correlation length, ξ, which is the average distance between two polymer segments in solution. In the semi-dilute case, the correlation length is equal to the diameter of these spheres (although it
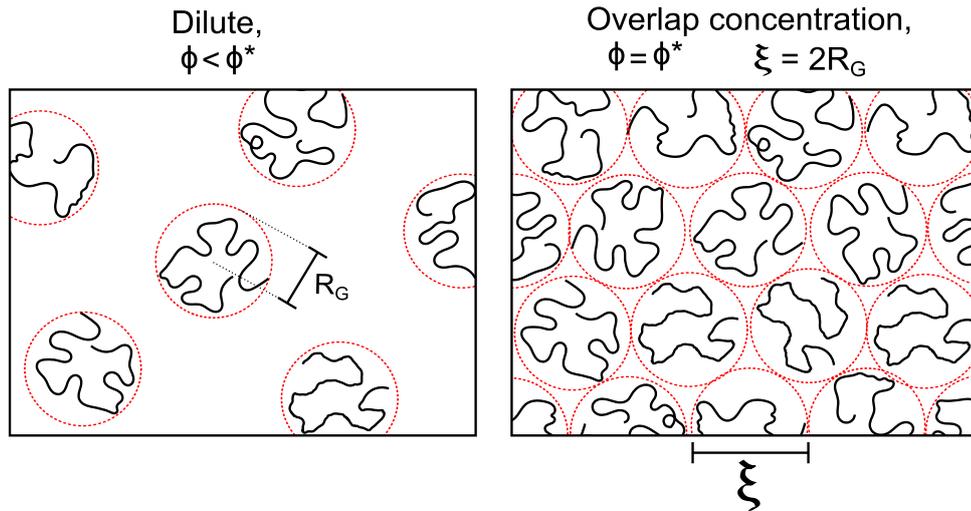
Figure 2.7: Diagram of the transition point between dilute and semi-dilute concentrations when the concentration within the pervaded volume of one polymer is equal to the concentration of the entire solution.

must be noted that in dilute solutions the correlation length is much larger than the small dilute region a polymer inhabits). The diameter of these spheres at the overlap concentration is simply twice the radius of gyration ($\xi(\phi = \phi^*) = 2R_\text{G}$). These spheres are known as *correlation blobs*. This may seem a trivial point as the overlap concentration is a very specific case. However, if we continue to increase the concentration, the solution remains concentrated with dilute regions, only the size of the correlation blobs decreases as shown in Fig.2.8, with the correlation length given by:

$$\xi = b \left(\frac{b^3}{v} \right)^{1/4} \phi^{3/4} \tag{2.17}$$

As we have already discussed, on a very small scale (below the size of the thermal blob, ξ_T), and in highly concentrated solutions, the scaling laws of the polymer follow an ideal chain. Now, we can describe a polymer in a semi-dilute solution has having 3 different scaling laws depending on the length scale at which it is observed. This is best shown in Fig.2.9, and summarised as follows:

- On length scales below ξ_T, the coil configuration behaves as an ideal chain due to thermal interactions.

- On length scales between ξ_T and ξ, the excluded volume interactions are strong enough to lead to a swollen chain configuration, with a self avoiding random walk of thermal blobs, shown by the chain of blue spheres in Fig.2.9.
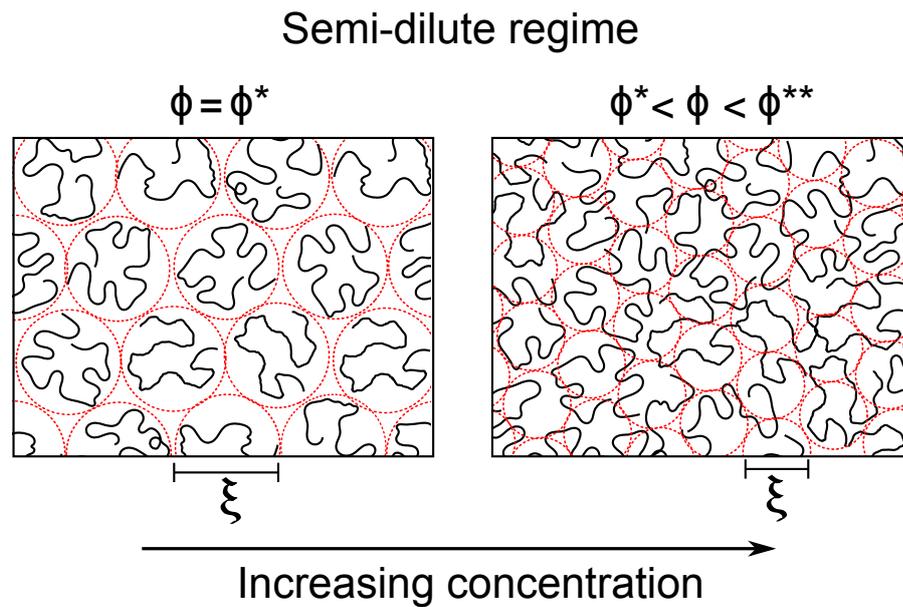
Semi-dilute regime

Figure 2.8: Diagram of the effect of increasing concentration (above ϕ^*) on the correlation length. Each correlation blob is a small dilute region, whereas the entire solution is concentrated with correlation blobs. This regime is known as semi-dilute and the size of these dilute correlation blobs decreases as concentration is increased.

- On length scales above ξ, the solution is effectively concentrated with correlation blobs (red circles). On this scale the solution is so highly concentrated that the polymer-polymer interactions are so frequent that the chain effectively does not care what position it rests in, and therefore the coil behaves as an ideal walk of correlation blobs.

The correlation length is predicted to be only dependent on concentration, and completely independent of chain length [14]. This is indeed supported by the extensive work of Brown and Nicolai concerning the behaviour of polystyrene in good solvents [15].

The correlation length ξ will increase with concentration, but the thermal blob ξ_{T} will maintain a fixed size (as this is only dependent on the thermal energy and the quality of the solvent). Therefore, at some critical concentration ($\phi = \phi^{**}$) the correlation length and thermal blob will be of equal size, and there will be no intermediate length scale in which the polymer follows a swollen coil configuration, and the chain follows an completely ideal random walk. This is known as a *concentrated* solution.
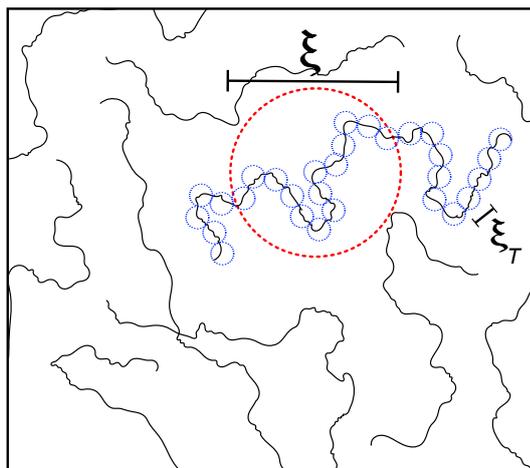
Figure 2.9: Diagram of the three important length scales in the semi-dilute regime. On the smallest length scale, within a single thermal blob, shown by the blue circles ($r < \xi_{\mathrm{T}}$), the thermal energy counters excluded volume effects and the chain is an ideal walk. Above this length scale, the chain is a self avoiding "swollen coil" of thermal blobs up until the correlation length (larger than the spheres given by the blue circles, but smaller than a sphere given by the red circle - $\xi_{\mathrm{T}} < r < \xi$). Above the correlation length (length scales larger than the red circle - $r > \xi$), concentration effects screen self-avoiding behaviour, and the coil scales as an ideal chain of correlation blobs.

2.2   Diffusion

So far we have pictured a polymer as simply a stationary object only interacting with the surrounding solvent molecules through attractive and repulsive effects. Clearly this is not realistic. The polymers will undergo Brownian motion due to the constantly bombarding solvent molecules bouncing around with their own random trajectories and velocities. Due to this bombardment, not only will a polymer display centre-of-mass displacement, but the individual monomers will "jiggle" causing the chain configuration to be in a state of constant flux. First let us consider the most commonly observed effect of Brownian motion - diffusion.

2.2.1   Self Diffusion

The random motion of a particle in a liquid due to Brownian motion is described by its mean square displacement from the origin. Similarly to the mean square

end to end distance in a polymer, which increases linearly with chain length due to the random walk configuration, the random motion of a suspended particle leads to a linear increase in mean squared displacement with time, with a constant of proportionality known as the diffusion coefficient D:

$$\langle r(t)^2 \rangle = 6Dt \tag{2.18}$$

The factor of 6 comes in to take into account diffusion in 3 dimensions. This type of diffusive motion depends on both the properties of the particle and the solvent. Let us imagine we apply a constant force f to the particle, leading to a constant velocity v in the direction of the applied force. Frictional forces between solvent and particle will create resistance to this flow, leading to a proportionality between force and velocity given by:

$$f = \zeta v \tag{2.19}$$

Where ζ is the friction coefficient [13]. Therefore, the random motion of a particle due to the constant bombardment of solvent molecules (each with its own directional force), is a function of both the thermal energy of the system (as the number of impacts and therefore total force will increase linearly with temperature) and the inverse of the friction coefficient ζ:

$$D = \frac{k_B T}{\zeta} \tag{2.20}$$

This is known as the *Einstein relation*. In 1880, Stokes also showed that the friction coefficient of a particle in a Newtonian liquid would be a simple product of the viscosity of the solvent η_{s}, and the size of the particle R_{p}:

$$\zeta = 6\pi \eta_{\mathrm{s}} R_{\mathrm{p}} \tag{2.21}$$

Which combined with equation 2.20 gives the Stokes-Einstein equation for the diffusion coefficient of a colloidal particle:

$$D = \frac{k_B T}{6\pi \eta_{\mathrm{s}} R_{\mathrm{p}}} \tag{2.22}$$

In a dilute solution, one may consider the motion of a single dissolved polymer to follow similar behaviour as a suspended colloidal particle. While we have already shown that a polymer follows a random-walk like configuration, and is therefore structurally very different to that of a hard sphere, we have also already given the polymer a characteristic radius of gyration R_{G}, so perhaps we can describe the motion of a polymer as a solid sphere with a similar radius.

Indeed, through light scattering techniques the diffusion coefficient of suspended polymers can be directly measured, which then gives a corresponding *hydrodynamic radius*, R_h:

$$D = \frac{k_B T}{6\pi\eta_s R_h} \tag{2.23}$$

The hydrodynamic radius radius is not so much a physical radius like the radius of gyration, but a quirk of the polymer's diffusive behaviour. By comparing the Stokes-Einstein relation to the Zimm model$^{\parallel}$, the hydrodynamic radius can be converted back into the radius of gyration through $R_G \sim 1.48 R_h$ [16]. This ratio is supported by experimental observations of DNA in solution which yielded a scaling factor in close agreement with predictions to within 3% error.

As concentration is increased above the overlap concentration, a modification to the equation must be made to account for frictional forces between polymers. Now the diffusion coefficient follows [17]:

$$D_s = D_0 \left(\frac{\phi}{\phi^*}\right)^{-1/2} \tag{2.24}$$

Where D_0 is the diffusion coefficient in a dilute solution. However, this is not the complete story in semi-dilute solutions. As concentration is increased above the overlap concentration ϕ^*, polymers no longer diffuse entirely as solo entities, rather collective behaviour must be taken into account. We now introduce a new diffusive term, the *cooperative diffusion coefficient*, D_c.

2.2.2 Cooperative and Gradient Diffusion

The cooperative diffusion coefficient D_c is similar to the self diffusion coefficient in that it describes diffusive motion with time, however the cooperative diffusion

---

$^{\parallel}$The Zimm model is a much more complicated polymer diffusive theory that expands on the simple Stokes-Einstein relation and models the polymer diffusion by making two vital assumptions:

- The polymer chain is made up of a series of ball and springs, each ball having a diffusion coefficient as that of a single colloidal particle in a solvent, but is connected to a spring which elastically resists large translations.

- Hydrodynamic interactions between monomers in the polymer chain lead to solvent molecules being trapped within the monomers excluded volume regions, which is presumably highly dependent on degree of polymer swelling.

coefficient describes the collective motion of more than one polymer through a density gradient [18], which would clearly only become important when the concentration is high enough that polymer chain interactions become likely ($\phi > \phi^*$).

Cooperative diffusion is best described, as is often the case with polymer physics, with a diagram. Fig.2.10 shows how the close proximity of polymers in one region can lead to collective motion with a preferred direction toward the region of lowest concentration. While each polymer is undergoing Brownian motion, the polymer
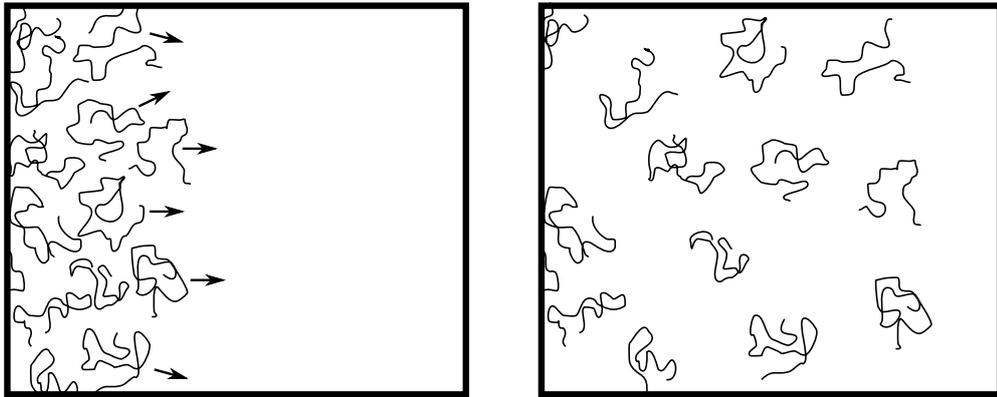
Figure 2.10: Diagram of the effect of cooperative diffusion. A concentration gradient leads to a greater degree of freedom in the direction of lowest concentration. Random motion leads to polymers cooperatively diffusing down a concentration gradient.

degrees of freedom become increasingly reduced as concentration is increased. If however instead of increasing the concentration globally we simply introduce a concentration gradient, diffusion will be limited in the direction of the region highest in concentration, and enhanced toward the region of lower concentration. Even though a single polymer is diffusing at the same rate (as Brownian motion is unaffected), a gradient in the concentration leads to very fast collective motion in the direction of the lowest concentration, homogenizing the solution. Now let us consider a solution of increased concentration. While self diffusion would become increasingly reduced by friction from neighbouring polymers, we can rewrite the Stokes-Einstein equation for the cooperative diffusion coefficient in terms of the distance between chains and the correlation length ξ:

$$D_{\mathrm{c}} = \frac{k_B T}{6\pi\eta_{\mathrm{s}}\xi} \qquad (2.25)$$

We have already shown that $\xi \propto \phi^{3/4}$, so it becomes clear that $D_{\mathrm{c}} \propto \phi^{-3/4}$ [15, 19,

20]. Similar to the arguments made in section 2.1.6, that the correlation length between two polymers in a semi-dilute solution is chain length independent, so is the collective behaviour. The reader should also note that at low concentrations (where polymer interactions are negligable), the cooperative and self diffusion coefficient are equivalent.

This description of cooperative diffusion is focused purely on the effect of closely packed unentangled polymers reducing each others respective degrees of freedom as concentration is increased. These arguments would work equally well with a concentration gradient of hard spheres. However, when collective diffusion, reptation [21] (which will be discussed in section 2.2.3) and network swelling [19] all play a role in the homogenization of the solution, the term that collectively describes these effects on the reduction of a concentration gradient is known as the *gradient diffusion coefficient*. This coefficient is not described easily by models as various factors must to be taken into account. However, this type of diffusion coefficient can be measured directly from the time required for two different concentration regions to homogenize [22].

Furthermore, the transition between dilute ($D_s = D_c \propto M_W^{-3/5}$) and semi-dilute ($D_s \propto M_W^{-2}, D_c \propto \phi^{3/5}$) behaviour at ϕ^*, is not sudden, but gradual, as shown in Fig.2.11 [18], possibly due to either polydispersity effects or the increasing likelihood of polymer interactions as the volume fraction approaches ϕ^*.

Up until now we have assumed that a polymer cannot impose a topological constraint on another, i.e. while polymers may be highly concentrated and bunched up together in the semi-dilute regime, if one was to attempt to pull a single polymer from the system, the remaining polymers would easily move themselves out of the way and rearrange themselves to fill the gap left behind, much like hard spheres. However, it is certainly true that two chains cannot pass through each other, and as the chain length is increased, entanglements become increasingly important to the polymer dynamics. Fig.2.12 is a diagram of a polymer entangled network. Think of the difference between a plate of spaghetti that has come straight from the pan, and spaghetti that has been cut up into smaller pieces before you eat. The same amount of spaghetti is on your plate in the same volume, but in the former case it is much harder to remove just one piece as they are inextricably twisted and tangled together. Clearly, both molecular weight and concentration play important roles in polymer entanglement, and entanglement
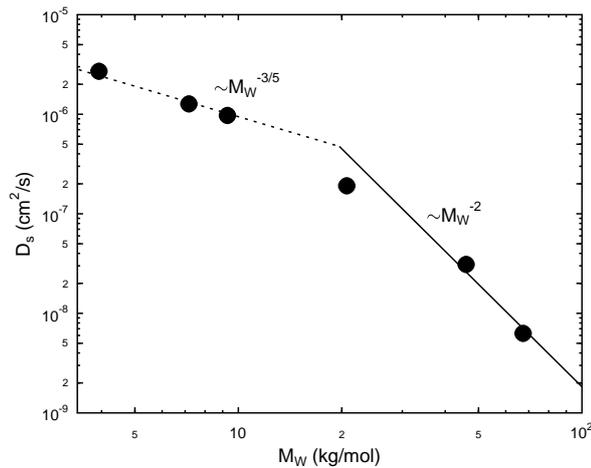
Figure 2.11: Plot of self diffusion coefficient as a function of molecular weight at constant concentration. Solid lines show predicted dilute and semi-dilute self diffusive behaviour. Data points agree with these predictions but show a gradual, rather than a sudden, transition between the two regimes. Data published by Zettl et. al. [18].

scaling laws will be discussed in more detail in section 2.3.1. In entangled solutions the diffusion becomes increasingly complex. The tube model, which will be discussed in the next section, is the best current approach to understanding polymer dynamics in a highly entangled polymer network. While it offers some success in predicting relaxation times, especially in recent years with the understanding of highly entangled branched polymers [23], it fails to account for the cooperative motions of more than one polymer, and cannot offer a prediction of the concentration at which this behaviour will become dominant. We will follow this model tentatively, with the hope to understand some of the effects polymer networks have on diffusion and large scale flow behaviour, while keeping in mind that our understanding of this regime is far from complete.

2.2.3   Reptation

The basic constraint that leads to entanglements is that no polymer can cross another's path. But what does that mean in terms of the diffusive motion of a single polymer in this network? Edwards proposed the tube model, which assumes that the presence of the many surrounding polymers effectively restricts a single polymer to a tube, as shown in Fig.2.13. Lateral motion within this tube is highly
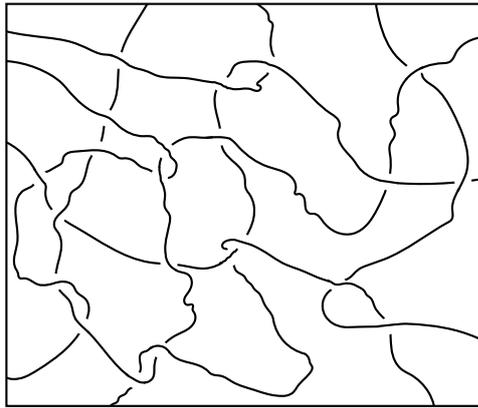
Figure 2.12: Diagram of an entangled polymer network.

Entangled network   Tube model
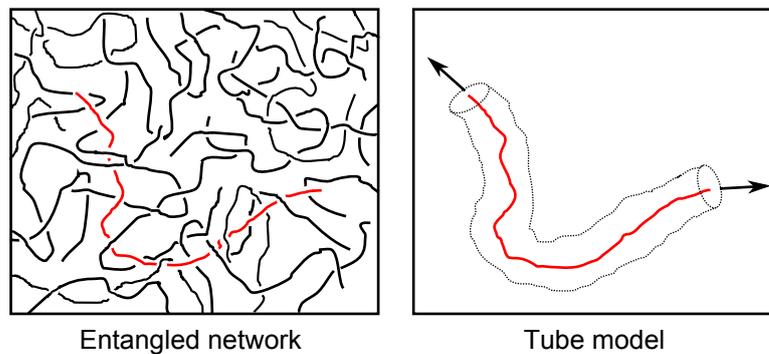
Figure 2.13: Diagram of the tube model for entangled polymer reptative diffusion.

restricted (the polymer cannot penetrate the tube walls), however motion along the contour length of the tube is relatively unhindered. The polymer can now move up and down along this tube (in a 1D random walk like motion), much like the slithering of a snake in grass. It is due to the analogy with snake-like (or reptile-like) motion that this form of diffusion is known as *reptation*.

Because the polymer is following a 1D random walk (and we assume that resistance in this direction is purely viscous drag from the solvent, which is proportional to the length of the polymer), the diffusivity of the polymer within a tube can be estimated using the total length of the tube and the time required for the polymer to travel this distance following a 1D random walk. Using the same arguments as in equation 2.18, we are left with the following equation for

polymer self diffusion:

$$D \propto \frac{L^2}{\tau_{\mathrm{T}}} \tag{2.26}$$

Where L is the length of the tube (which is proportional to the polymer molecular weight) and τ_{T} is the time required to escape the tube. Furthermore, by taking into account the mobility of each section of the tube, the number of sections and the thermal energy, the time required to escape is given as the total length of the tube cubed ($\tau_{\mathrm{T}} \propto M_{\mathrm{W}}^3$. Therefore, the diffusion coefficient can be simplified to:

$$D \propto M_{\mathrm{w}}^{-2} \tag{2.27}$$

This disagrees with experiments which yield the result $D \propto M_{\mathrm{W}}^{-2.3}$. This discrepancy has been tentatively explained with the incorporation of two adjustments to the theory. The first is that the tube in which the polymer is constrained is in a state of flux. Because the tube itself is made entirely of neighbouring polymers, which themselves are reptating, an additional tube lifetime must be taken into account. Secondly, the tube is not tightly wrapped around the polymer. The tube diameter is in fact a material parameter, which depends on chain flexibility, monomer bulkiness and concentration, but not the molecular weight [24]. Therefore, even in a melt, due to Brownian motion the polymer can retract into its tube for a certain time, allowing the tube (or rather the surrounding polymers) to rearrange itself (themselves), as shown in Fig.2.14. It is believed that these two effects can account for the discrepancies between the reptation model and observations.

The contour length fluctuation correction has been one of the major successes of the tube model as by taking this into account one can begin to understand the diffusive properties and relaxation times of highly branched polymers. If reptation of a fixed length polymer was the only possible method of movement, then clearly a star branched polymer would be fixed in place. However if we allow for contour length fluctuations, a branching arm could, through random Brownian motion, "wiggle" up one of its tubes. Consider a comb shaped polymer. Due to the many branches, being constrained laterally to their tubes, the backbone is fixed in place. However, if these branches are able to wiggle up their tubes and effectively bunch up together within the tube the backbone is placed in, the freedom of motion along the axis of the backbone will increase. This idea predicts that the relaxation time of the polymer is a function of the time required for a single branch to wiggle up the whole length of its confining tube, giving a relaxation time as
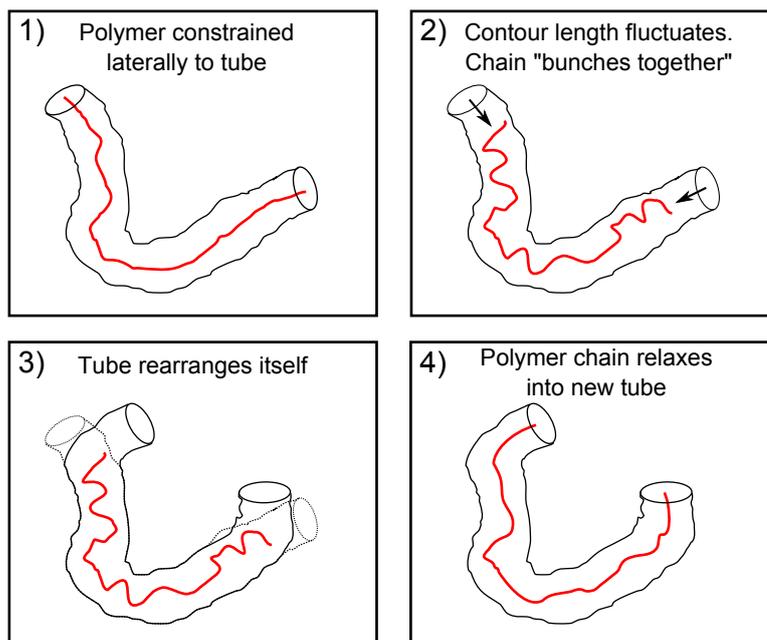
Figure 2.14: Diagram of the contour length fluctuations that lead to the discrepancies between predicted tube model and experimental values of viscosity.

an exponential function of the branched tube length. This idea is applicable for all manner of differently branched polymers, albeit difficult to predict in highly irregular branching. This rheological behaviour is the crucial difference between linear and branched polymer behaviour. While the chemistry of these molecules is almost identical, the configurations lead to very different flow behaviours.

2.3 Rheology

2.3.1 Entanglement Concentration and Molecular Weight

Until now, unlike ϕ^* and ϕ^{**} which have easily defined values, no simple description of the entanglement concentration ϕ_e has been given. That is because while it is easy to imagine an entangled network being a solution of interconnected chains, defining the point where entanglements begin is difficult. Clearly for entanglements to take place we need the chains to be overlapping, but at what point do we call the solution an entangled network? Several leaders in polymer physics have suggested the following relationship between the overlap concentration and

entanglement concentration [25–28]:

$$\phi_{\text{e}} = n^4 \phi^*$$ (2.28)

where n is a suggested universal entanglement constant, the number of cross-over points between chains required before a group of long molecules can begin to behave as a single network. It is predicted that this constant lies somewhere between 5 and 10 [27].

Experimentally, Dobrynin et. al. observed a distinct change in the viscosity behaviour of the sample at a particular concentration between ϕ^* and ϕ^{**}, which they concluded as being the elusive entanglement concentration. From the observations they found the following scaling laws between viscosity and concentration in two different semi-dilute regimes [26]:

- Semi-dilute unentangled, $\eta \propto \phi^{1/2}$.

- Semi-dilute entangled, $\eta \propto \phi^{3/2}$.

Approaching the problem in terms of molecular weight makes things easier. Lets start with a polymer melt, where $\phi = 1$. Again, the simple analogy is a plate of spaghetti. As a child we may all remember our parents diligently chopping the spaghetti into small pieces for us. This allowed easier removal of individual pieces, despite no change in concentration. If you had attempted to eat a plate of unchopped spaghetti, it is highly likely you would have ended up with an entangled mess of spaghetti on your fork much larger than your mouth! As with polymers, at some critical chain length they will be wrapped around each other to such an extent that it can would be very difficult to remove just one chain from the entangled network.

Richard Wool [29] approached the problem of predicting entanglement crossover point by assuming that that the number of crossing points p in any load bearing plane must exceed the number of chains n_{c} by at least $p > 3n_{\text{c}}$. Below this, chains can readily slip apart, whereas above this chains are sufficiently interpenetrated that entanglements play an important role in diffusion and flow behaviours. Wool continued this line of thinking by analysing the number of crossing points in terms of random coil parameters and found the following equation for the critical entanglement molecular weight M_{e} in the melt:

$$M_{\text{e}} \approx 30 C_\infty M_{\text{mon}}$$ (2.29)

where M_{mon} is the molecular weight of a single monomer and C_∞ is the characteristic ratio, which is the ratio between the real polymer size and the size predicted by the freely jointed chain model. This is an alternative approach to the Kuhn model described earlier, but because this is simply a number used to convert between reality and the model, with no real physical origin, it will not be discussed further. The values of M_{e} predicted by this equation were compared experimentally through measuring viscosity against M_{W}, and were found to be in good agreement [29]. PEO for example was predicted to have an entanglement molecular weight value of $M_{\mathrm{e}} = 5000$ g/mol, compared with viscosity measurements which gave the result $M_{\mathrm{e}} = 4400$ g/mol.

Wool then found an equation for M_{e} in terms of concentration (in a semi-dilute solution) by making the simple assumption that the number of crossing points per polymer is equal to the number of correlation blobs per polymer $N(c)$:

$$N(c) \propto c^{5/4} \tag{2.30}$$

giving the following concentration dependence on M_{e}:

$$M_{\mathrm{e}}(\phi) \approx 30.89 \frac{M_0 C_\infty}{\phi^{5/4}} \tag{2.31}$$

Furthermore, an increasingly entangled network will behave more and more like a single solid structure, and so the network's storage modulus must also be taken into account. With this in mind, we will move away from analysing predicted fluid behaviour from polymer models to predicting polymer chain parameters from the fluid rheology.

2.3.2   Viscosity and Elasticity

Condensed matter has various different responses to shear stress depending on whether it is a solid or a liquid. Here we will examine two of the most commonly observed responses to shear stress: viscosity and elasticity. Soft matter, which is a subcategory of condensed matter that encompasses many substances that blur the line between solid and liquid, often display components of both depending on the strength and duration of the applied shear. To begin to understand a polymeric fluids complex response to shear, first we must summarise both ideal cases: *Hookean solids* and *Newtonian fluids*.

First, we must define shear stress, σ. Fig.2.15 is a diagram of a plane of material which is fixed in position at the base, and dragged in one direction by an applied constant force per unit area ($\sigma = F/A$) at the top. The shear strain e is the
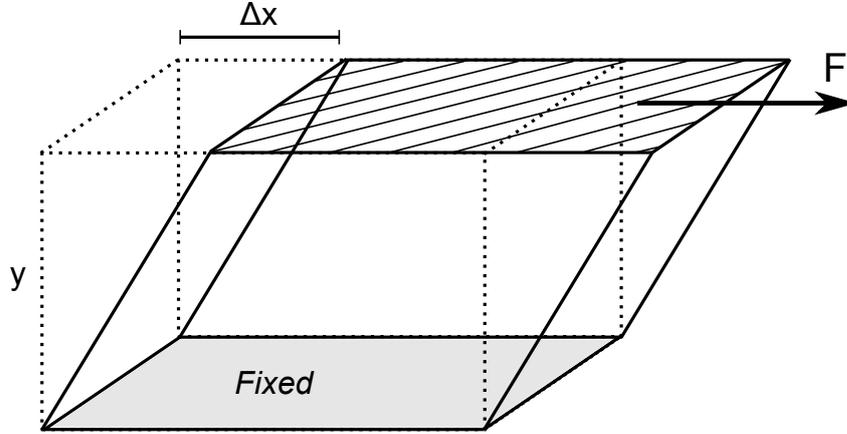
Figure 2.15: Diagram of the definition of shear deformation.

deformation in the direction of applied force with respect to the distance from the fixed bottom ($e = \Delta x/y$). If this material is a Hookean solid, a constant shear stress leads to a constant shear strain, with constant of proportionality being the shear modulus G:

$$\sigma = Ge \tag{2.32}$$

If this substance was a liquid however (and we imagine it is a sandwich of liquid trapped between two infinitely long plates), the molecules can rearrange themselves as the top plate moves with velocity v_{p}. Now the sandwiched fluid follows a linear velocity profile, with $v = 0$ at the bottom. The strain rate required to move the top plate of this liquid sandwich at a constant speed against the resistance of the fluid is proportional to the area of the plate and to the velocity gradient perpendicular to the plate:

$$\sigma = \eta \frac{\partial v(y)}{\partial y} \tag{2.33}$$

where η, the constant of proportionality is known as the viscosity. Since fluid velocity is the same as dx/dt, we can rewrite this in terms of the time derivative of the shear strain:

$$\sigma = \eta \dot{e} \tag{2.34}$$

This proportionality gives an easy method of measuring the viscosity of Newtonian fluids. However, some fluids, called non-Newtonian fluids, have a viscosity

which is a function of shear rate:

$$\sigma = \eta(\dot{e})\dot{e} \qquad (2.35)$$

If η increases with $\dot{e}$, it is known as shear thickening, whereas if it decreases it is known as shear thinning. A common example of a non-Newtonian fluid is a polymeric fluid, in which $\eta(\dot{e})$ is highly dependent on the degree of alignment and entanglement of the polymers prior to and during the applied shear. Usually with polymeric fluids (most often in linear chain unentangled solutions), the fluid will undergo shear thinning as increasing shear stress tends to align polymers in the direction of flow, which then has a lower resistance to shear, and a reduced viscosity.

Experiments by Dittmore et. al. [30] summarise the alignment of PEO chains in water under extensional flow very simply through single chain elasticity experiments. In these experiments one end of the polymer is fixed in place and an extensional force, F_{E}, is applied to the other end. They found that by measuring the extension of the chain as a function of F_{E}, they could predict whether the polymer follows a highly aligned ($5 < F_{\mathrm{E}} < 20$ pN), ideal chain ($0.7 < F_{\mathrm{E}} < 2$ pN) or swollen coil ($F_{\mathrm{E}} < 0.7$ pN) configuration due to their respective elasticities. While shear forces do not only pull on one end of the chain in this manner, this work gives an indication of the differential forces required to align a chains and lead to shear thinning of the fluid.

Substances which undergo shear thickening are typically highly concentrated colloid solutions. Custard is a prime example of a shear thickening fluid. Fig.2.16 is a schematic plot of shear stress against shear rate for Newtonian, shear thinning and shear thickening fluids.

2.3.3 Viscoelasticity

Real soft matter materials will often display a response to shear that combines both elastic and viscous behaviour, with an additional dependence on the timescale over which the shear is applied. This type of substance is known as viscoelastic. A simplistic picture of viscoelasticity is given by a creep test (which is a test most often used to measure the plasticity of solid materials, which will not be discussed further here), in which we apply a constant shear stress with
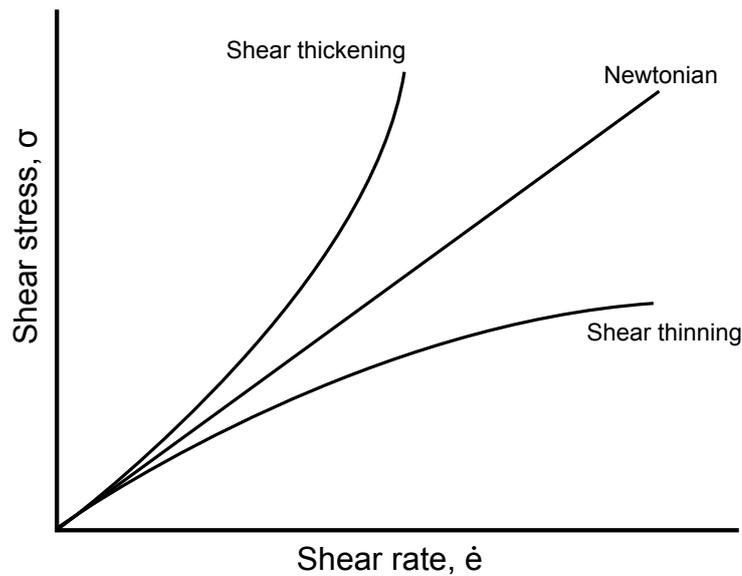
Figure 2.16: Plot of typical shear stress - shear rate curves for Newtonian, shear thinning and shear thickening fluids.

time. At very short times the molecules are unable to rearrange themselves quick enough to respond to the shear, giving a constant shear strain with time. But as time approaches the relaxation time of the fluid $(t \to \tau)$ the molecules begin to rearrange themselves and flow with a velocity profile given by a viscous fluid, as shown in Fig.2.17. This is a simple way of measuring the timescale (for a given shear stress) at which a substance transitions from elastic to viscous behaviour. In reality substances can be much more complicated than this and display more than one relaxation time, but we will not consider these types of substances in any greater detail. However, an additional drawback of analysing a substance via the creep test is that it gives no information about the relative effects of viscosity and elasticity as a function of the timescale. For example, is the transition between elastic and viscous behaviour sudden or gradual? If the answer is gradual, how do we identify the magnitude of both the elastic and viscous components as a function of the timescale over which the shear is applied? For this we use an oscillation test.

Oscillation is a non-destructive technique which "wobbles" the fluid through the sinusoidal application of shear stress. Experimentally this is achieved by applying shear to a fluid wedged between a truncated cone spindle and plate as shown in Fig.2.18, through rotation of the spindle in a repeating clockwise-anticlockwise motion, with a specific angular frequency of rotation. For a Hookean solid, shear
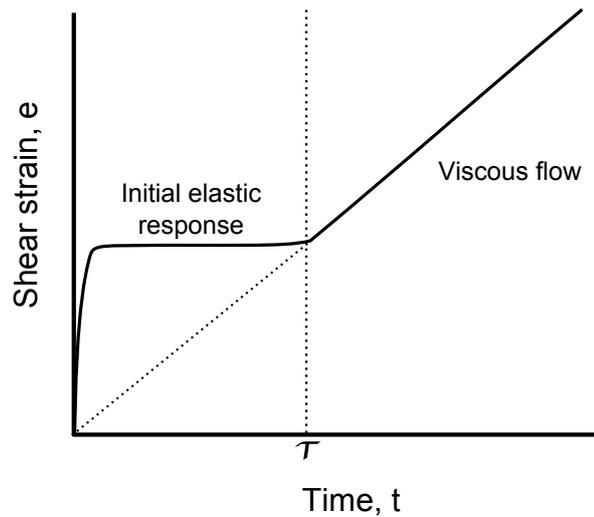
Figure 2.17: Schematic plot of the shear strain at a fixed shear stress as a function of time in a viscoelastic fluid.
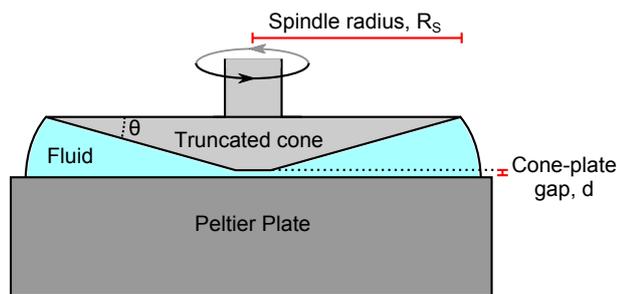
Figure 2.18: Truncated cone and plate geometry for rheology experiments

stress is directly proportional to strain, which means if the substance between the cone and plate is purely elastic the resulting strain rate wave produced in the material will be exactly in phase with the spindle motion. Conversely, in a Newtonian-fluid shear stress is directly proportional to the strain rate which leads to the motion of the fluid to be exactly 90° out of phase with the sinusoidal motion of the spindle.

Most fluids display some levels of viscoelasticity at high enough frequencies, being neither purely viscous Newtonian-fluids or elastic Hookean-solids, and will produce a sinusoidal stress wave which is out of phase with the oscillation of the spindle by between 0 and 90°. Even water, the standard archetype for a Newtonian fluid, will display some form of either shear thickening or elasticity if one were to apply forces on the liquid over timescales shorter than its relaxation time.

In this case the molecules will not have the time to flow around each other in the usual fluid-like fashion, and instead react as a rigid body of hard spheres. This timescale cutoff between solidity and fluidity is characterised by the Deborah number.

Fig.2.19 is a plot of the strain rate as a function of oscillating shear stress for a given angular frequency. The solid black line represents the shear stress applied
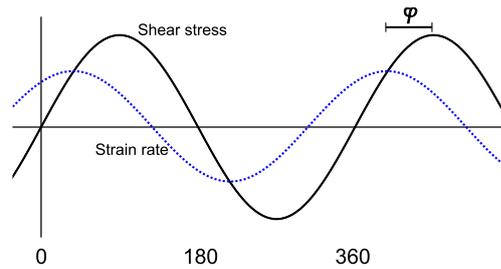
Figure 2.19: Plot of shear stress and shear rate against oscillation angle for a fixed angular frequency. The strain rate is out of phase with shear stress by angle φ.

to a viscoelastic fluid as a function of oscillation angle. The blue line represents strain rate, which may have a different amplitude to the shear stress, and be out of phase by angle φ. For an ideal Hookean solid $\varphi = 0°$, whereas for an ideal Newtonian liquid $\varphi = 90°$.

The strain rate now can be thought of as a sine curve in a purely elastic sample sample and a cosine curve in a viscous sample, so it follows that $\sin\varphi/\cos\varphi=\tan\varphi$ and

$$\tan\varphi = \frac{\text{elasticity}}{\text{viscosity}} \tag{2.36}$$

The elastic and viscous components are given by the storage modulus G' which is a measure of the elastic energy stored by the system that resists shear, and the loss modulus G'' which is the energy dissipated as heat due to viscous forces. Now we can rewrite the phase in terms of these moduli:

$$\tan\varphi = \frac{G'}{G''} \tag{2.37}$$

If we assume that the fluid is a perfect Maxwellian fluid, which describes the viscous and elastic responses as being analogous to the response given by an in series spring and dashpot as shown in Fig.2.20, where the spring represents the in phase elastic response of the fluid, and the dashpot the out of phase viscous
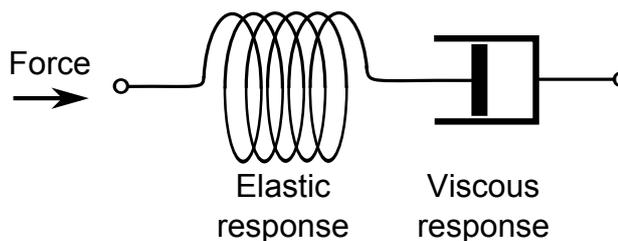
Figure 2.20: Diagram of the spring-dashpot model of the response to applied force in a Maxwellian fluid.

response, then the storage and loss modulus are given by:

$$G' = G_0 \frac{(\omega\tau)^2}{(1 + (\omega\tau)^2)} \tag{2.38}$$

$$G'' = G_0 \frac{\omega\tau}{(1 + (\omega\tau)^2)} \tag{2.39}$$

where τ is the relaxation time which describes the cross-over timescale between elastic and viscous behaviour[**], ω is the oscillation frequency and G_0 is the plateau modulus, which is the high frequency plateau value of G'.

Continuing with the Maxwellian spring-dashpot model, we would now expect oscillation experiments to yield curves G', G'' plotted against frequency as shown in Fig.2.21. Often the Maxwellian model does not fit well to real fluid behaviour. Yet, oscillation experiments still offer a robust method of measuring the relative elasticity and viscosity of fluids as a function of the timescale over which shear is applied, which can give information such as degree of entanglement or alignment of a polymeric fluid. Fig.2.22 is a typical example of the G' and G'' curves given by an oscillation experiment of a polymeric fluid.

Now we have gone over many of the broad-stroke aspects of polymeric liquids and solutions, let us consider a specific polymer, poly(ethylene oxide), or PEO as it will be more frequently referred to in this work.

2.4 Poly(ethylene oxide), PEO

PEO is a linear chain polymer, and is often the focus of experimental research due to both its simple structure and its high solubility in the most abundant solvent

---

[**]This model assumes only one relaxation time, which is often not the case.
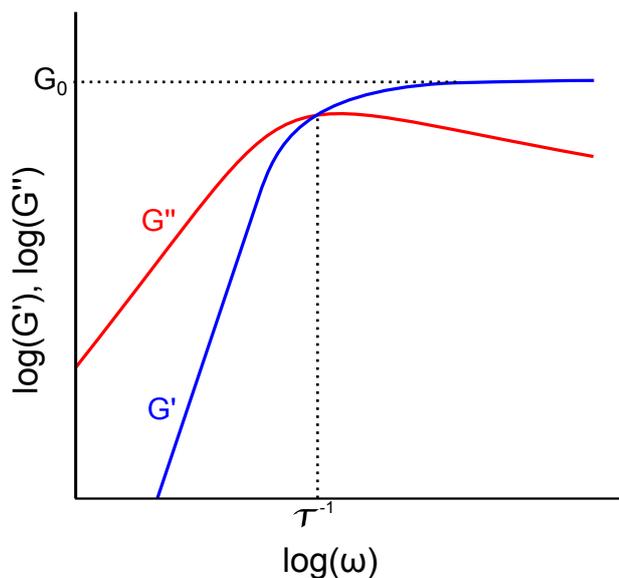
Figure 2.21: Representative plot of storage and loss modulus as a function of oscillation frequency for a Maxwellian viscoelastic fluid.

available - water. It is used for a wide range of industrial applications including: drag reduction in turbulent flows via the Toms effect [31–33]; contact lens coatings [34]; wood preserving agents [35]; food preservative [36]; green chemistry reaction medium [37]; pre bowel surgery medication [38]; and protein reaction catalysis [39]. This research focuses on the behaviour of drying PEO droplets, with much importance placed on the diffusivity, viscosity, surface tension, density and phase behaviours of these systems. With this in mind let us examine the properties specific to aqueous PEO solutions as described by the literature.

2.4.1 Solubility

Poly(ethylene oxide) (PEO)[††] is a linear chain polymer, and is often described as the "model water soluble polymer", due to both its simplistic chemical structure and its unusual high solubility in water at ambient conditions [40]. Table 2.1

[††]This polymer also goes by the name poly(ethylene glycol) (PEG) depending on which original molecule was used prior to polymerisation. Structurally these polymers are identical, however historically, the latter process yielded short length polymers (M_W < 100 kg/mol), whereas ethylene oxide yielded much larger chain lengths. Conventionally today both names are used depending on whether the molecular weight is below (PEG) or above (PEO) 100 kg/mol. To avoid confusion, I will use the term PEO for all values of M_W.
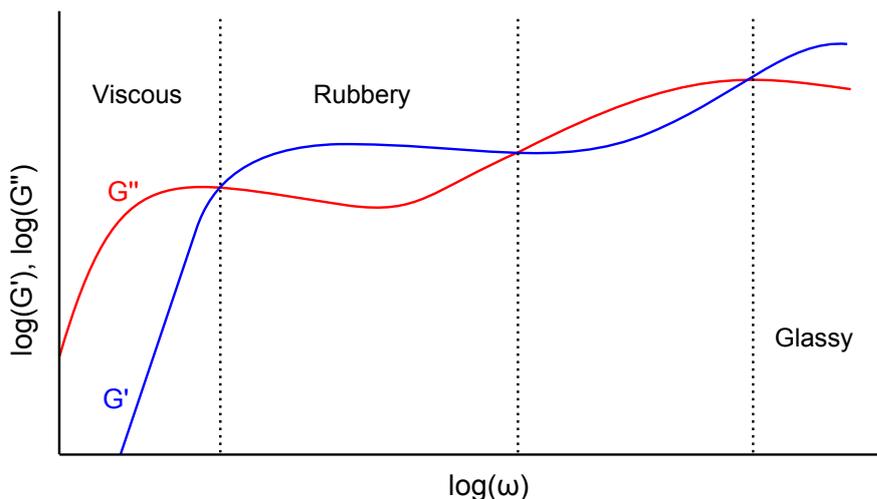
Figure 2.22: Plot of typical G' and G'' curves as a function of oscillation frequency for a polymeric fluid.

best shows the uniqueness (and strangeness) of PEO in terms of its solubility when compared with its homologues poly(methylene oxide), poly(acetaldehyde), poly(propylene oxide) and poly(trimethylene oxide) [41, 42].

Polymer name	Chemical structure	Soluble in water at room temperature
Poly(methylene oxide)	$HO\text{---}\!\!\left(\!CH_2\text{---}O\right)_n\!\!\text{---}H$	No
Poly(ethylene oxide)	$HO\text{---}\!\!\left(\!CH_2\text{---}CH_2\text{---}O\right)_n\!\!\text{---}H$	Yes
Poly(acetaldehyde)	$HO\text{---}\!\!\left(\!\begin{array}{c}CH_2\text{---}O\\ \vert \\ CH_2\end{array}\!\right)_n\!\!\text{---}H$	No
Poly(propylene oxide)	$HO\text{---}\!\!\left(\!\begin{array}{c}CH_2\text{---}CH_2\text{---}O\\ \vert \\ CH_2\end{array}\!\right)_n\!\!\text{---}H$	No
Poly(trimethylene oxide)	$HO\text{---}\!\!\left(\!CH_2\text{---}CH_2\text{---}CH_2\text{---}O\right)_n\!\!\text{---}H$	No

Table 2.1: Details of solubility in water at room temperature of several poly(ether) structures.

Oxygen groups are hydrophilic, whereas CH_2 groups are hydrophobic, therefore one would expect that the ratio between these groups would be the important factor in defining solubility. However, one should notice that the polymer with the

highest oxygen-methyl group ratio is PMO, an insoluble polymer, which suggests there is another factor to take into account. Kjellander and Florin [42] studied this solubility discrepancy extensively and concluded that the configuration of PEO is the critical factor. The oxygen-oxygen distance in the PEO backbone is 4.7Å, which is exactly equal to the next nearest neighbour distance between random water molecules [40, 42, 43]. Because of this, the oxygen units can hydrogen bond to two water moloecules without disrupting the water structure. The water then effectively "dresses" the PEO chain with no increase in the entropy of the system. Fig.2.23 is a diagram showing the likely arrangement of the PEO chain in solution with two water molecules bonded to each oxygen unit. Assuming very
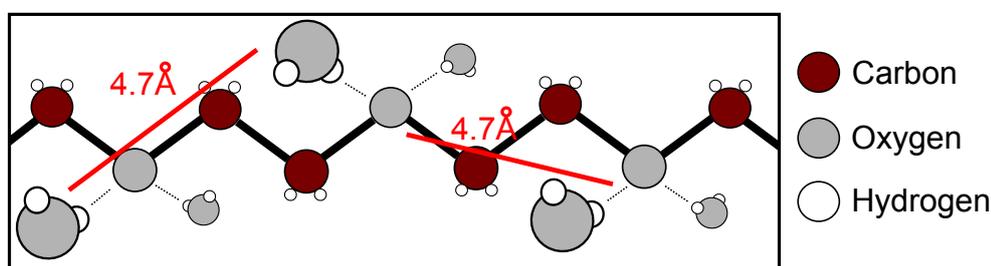
Figure 2.23: Schematic of a simplified view of the likely arrangement of a PEO chain dissolved in water. The distance between water molecules and the next nearest neighbour is exactly equal to the inter-oxygen distance along the PEO backbone.

little interaction between distant points on the polymer backbone, the dressing of the polymer is not expected to vary with chain length. This has been confirmed experimentally by Shikata et. al. who found that the number of water molecules per ethylene oxide monomer required to dissolve PEO chains remains constant at ~ 3.7 at all chain lengths in the range $7000 > M_{\mathrm{W}} > 1.5$ kg/mol [44]. Interestingly, this water "dress' picture then also predicts that as the temperature and therefore the water-water distance is increased, this effect will be lost and lead to a high temperature phase transition. This transition point is known as the lower critical solution temperature, or LCST, which has been observed experimentally as clouding of the solution above a critical temperature [45].

Furthermore, Cook et. al. showed that by increasing atmospheric pressure, PEO solutions go through a phase transition similar to the clouding effects of high temperature [46]. Fig.2.24 is the LCST plot of PEO as a function of temperature and pressure for mass fraction $c_0 = 0.1\%$ and $M_{\mathrm{W}} = 270$ kg/mol. Increasing pressure reduces the distance bewteen random water molecules and therefore
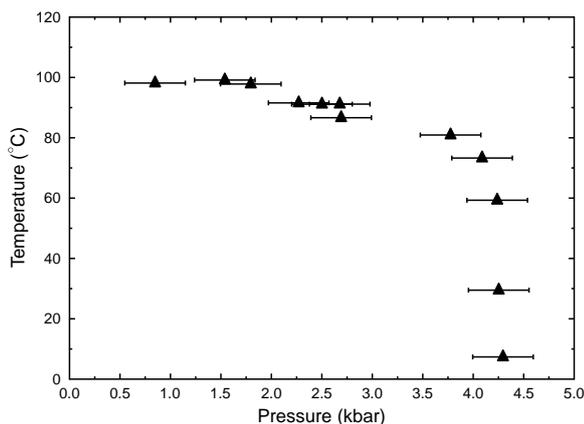
Figure 2.24: Plot of lower critical solution temperature (LCST) values for PEO solution (c_0=0.001g/g $M_W = 270$ kg/mol) as a function of pressure and temperature. Data published by Cook et. al. [46].

reduces the water dressing effect, reducing PEO solubility. This argument is enhanced by viscosity measurements of PEO with increased pressure as shown in Fig.2.25, which shows that as pressure is increased viscosity reduces. From the Flory relationship [46]:

$$\eta \propto \frac{R_\eta}{M_W} \tag{2.40}$$

where $R_\eta = R_G^{2/3} R_h^{1/3}$. This shows that the dissolved polymer coil size is reducing with increased pressure, which would be expected as a polymer transitions from good solvent (swollen coil) to poor solvent (collapsed globule) behaviour.

This behaviour is observed to be only dependent on molecular weight and not on concentration, however these experiments were restricted to dilute solutions, therefore removing any possible effects of polymer interactions, overlap or entanglements.

Hammouda expanded on the "water dress" model of PEO solvation by exploring the solubility in ternary solutions, specifically mixing PEO-water solutions with either methanol, ethanol or ethylene glycol [40]. Through small angle neutron scattering experiments, which gives solubility as an inverse relation to scattering intensity, he showed that PEO dissolves better in solvent mixtures than either solvent on their own, which is surprising. Ethanol for example is not a solvent for PEO at room temperatures, so at first glance one would expect adding ethanol to a water-PEO solution (and remembering that PEO happily dissolves in water at
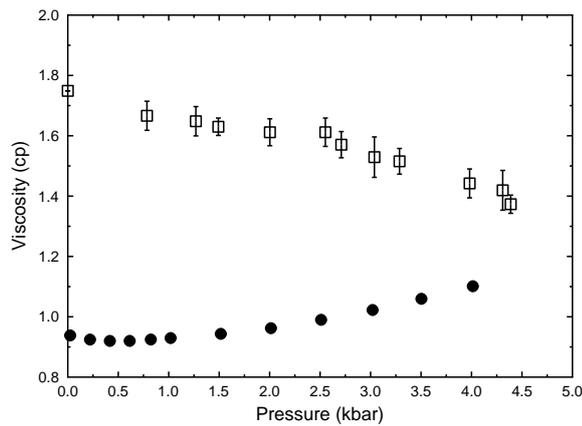
Figure 2.25: Viscosity measurements with increased pressure for water [47] (filled circles) and PEO solution, $M_W = 270$ kg/mol $c_0 = 0.1\%$ (hollow squares). Data published by Cook et. al. [46].

room temperature) would reduce the solubility. However, Fig.2.26 is a plot of the solvation scattering intensity for PEO-water-ethanol ternary solutions of varying water-ethanol fractions, $M_W = 48$ kg/mol, temperature and PEO concentration kept constant at 50°C and $c = 4\%$ respectively. This plot shows that solutions
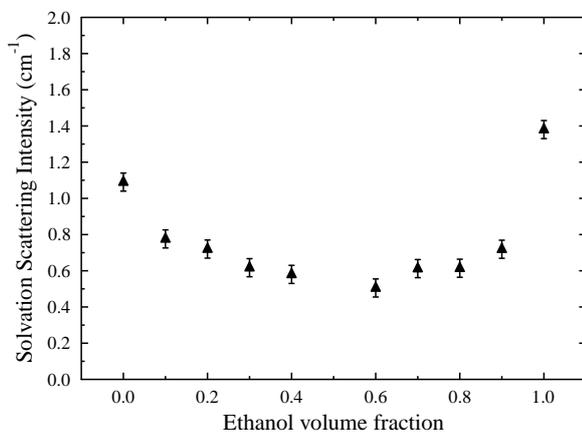
Figure 2.26: SANS measured solvation intensity for the case of 4% PEO in various volume fraction d-water/d-ethanol mixtures. Data published by Hammouda et. al. [40].

seem to dissolve best at equal volume fractions. The reader should note however that because these measurements were performed at 50°C, it is not a direct prediction of PEO-water-ethanol solvation characteristics at ambient conditions.

2.4.2 Clustering

Despite water being a good solvent for PEO, complete dissolution of PEO is not often observed experimentally. As well as the dissolved phase, a small portion of the total mass fraction of polymers forms undissolved polymer "clusters" (or aggregates), the origin of which is still under contention. The following is a list of several hypotheses on the origin of these clusters:

- Impurities [48]. Devanand carefully purified water prior to polymer dissolution and found that at high molecular weights clustering can be effectively eliminated. However, Polverari et. al. found through dynamic light scattering experiments that after hours or even days post mixing aggregates reform [49].

- PEO crystallisation [50]. PEO crystallizes below 60°C and above concentrations of 50% [51], so this would not be expected at low concentrations in ambient conditions. Despite this, Hammouda et. al. further increased the unlikelihood of this explanation by showing that these clusters remain undisturbed by varying the temperature of the system [52].

- Low temperature phase transition [53]. De Gennes proposed a second type of phase separation in which at ambient conditions below $c = 50\%$, the solution becomes highly concentrated with swollen coils, and dilute with collapsed coils. However, no physical explanation is offered for this phase separation.

- Chain ends effect [52, 54]. Hammouda et. al. show that PEO does not always strictly have an OH group on the end as shown in Table. 2.1. Alternatively a CH_3 could make up the end group. They show that clustering strength (i.e. the dynamic light scattering intensity of the clusters) increases by a factor of ~ 4 between PEO with two OH end groups and PEO with two CH_3 end groups.

- Cross linking [55]. Hydrogen bonds could form between oxygen sites on neighbouring polymers, or distant oxygens on a single polymer, thus disrupting the water "dress" as discussed previously. One would therefore expect clustering to increase with both concentration and molecular weight as the likelihood of neighbouring oxygen sites to come into close proximity

of each other increases. Clustering would also be an effect of the random configuration of the polymers as they are mixed with the solvent. In this case we would not expect clusters to form spontaneously from polymers that are already dissolved as the water "dress" would prevent inter polymer hydrogen bonding.

When PEO reaches its saturation concentration, either through temperature or concentration changes, it undergoes a 1st order phase transition from solution to semi-crystalline spherulites, which is a type of molecular ordering specific to polymers that demands its own subsection to explain.

2.4.3 Semi-crystallinity

Unlike most elemental solids which exist in a perfectly crystalline state with full three-dimensional positional order, molecular ordering in polymers often comes in the form of semi-crystalline spherulites, with small ordered regions in a larger less ordered material. In the case of polymers, the degree of ordering is highly dependent on the cooling rate as the molecules take time to rearrange themselves into an ordered state, which can be very long for macromolecules. Fast cooling leads to very little time for the polymers to rearrange into a crystalline structure, and instead they become "frozen" into a glassy state. This is sometimes known as "quenched disorder" as the polymers do not have time to crystallise, but do not have the thermal energy (or room, as is often the case with with highly entangled or highly branched polymers such as Dextran which will be described in section 3.7.1) to rearrange themselves further. Alternatively, different phase behaviour observed when cooling more slowly is sometimes referred to as "thermal annealing", which is when the polymer is given sufficient time at a high enough temperature to rearrange itself and reach equilibrium.

The basic unit of the semi-crystalline structure is the chain-folded lamella as shown in Fig.2.27. The regions between individual lamella are amorphous, and any given polymer can contribute to either the lamella, the amorphous region, or both.

To understand the transition from the highly disordered liquid state to the quasi-ordered semi-crystalline state we must first understand the process of crystal
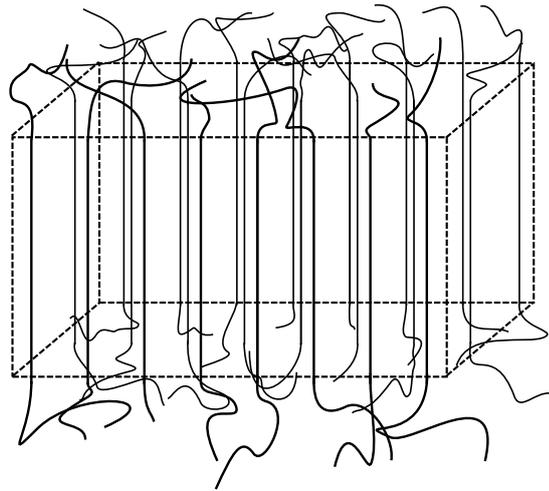
Figure 2.27: Diagram of a chain folded lamella, the basic unit of the semi-crystalline polymer structure. Individual polymer contour lengths are much longer than the thickness of the ordered region.

nucleation. The crystalline phase transition temperature T_c is defined as the point at which the system becomes unstable and the process of crystallisation will result in a reduction of the free energy of the system. However, as we will see in the next chapter, the formation of an interface has a specific energy cost depending on the interfacial tension between the solid and liquid phase γ_{sl}. The total change in free energy is a balance between the negative contribution to free energy as a result in the phase transition, which increases linearly with the crystal volume, and the positive contribution to the free energy as a result in the formation of an interface, which increases linearly with the surface area of the crystal:

$$\Delta E(r) = \frac{4}{3}\pi r^3 \Delta E_v + 4\pi r^2 \gamma_{SL} \tag{2.41}$$

This means that above a critical size radius r^*, the phase transition is stable and the crystalline region will grow outward radially from the nucleation point. Below this critical size, ordered crystal regions will be unstable and melt. This is schematically plotted in Fig.2.28.

This nucleation process is the same for perfectly ordered crystal regions such as water ice or salt crystals as it is with semi-crystalline polymer regions. Lamellae form from single nucleation points and arrange themselves into spherulite structures as shown in Fig.2.29. These spherulites are birefringent, and when viewed under cross polarizers show a signature "Maltese cross" structure. Spherulites
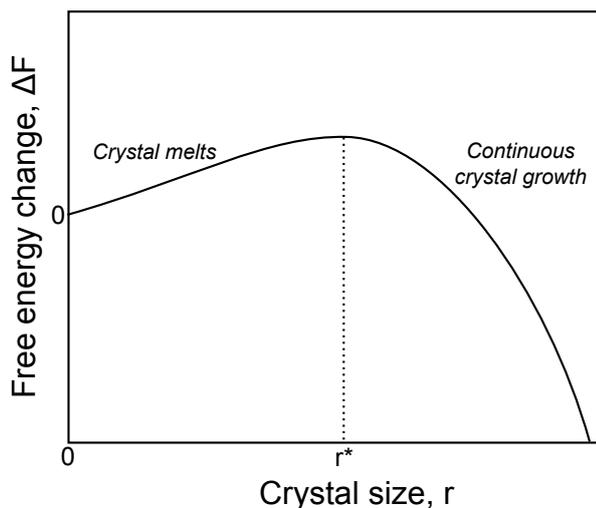
Figure 2.28: Schematic plot of the change in free energy as a function of crystal size.

continue to grow radially outward until either the boundary of the spherulite meets the advancing boundary of a second spherulite, or a single spherulite fills the entire system. However, one may ask the question, how do these spherulites form at all when at $r = 0$ the change in free energy of crystalline growth is positive? One would expect the spontaneous formation of a small interface due to a phase transition in the bulk to be unlikely. Indeed, nucleation is an activated process, which means it can only occur if thermal fluctuations in the bulk result in a local increase in the free energy. The chances of this occurring are increased significantly by the presence of dust particles or, in the case of a droplet, imperfections on the substrate. The number of spherulites that form are highly dependent on such impurities or imperfections.

2.4.4 Further PEO Properties

The viscosity of PEO-water solutions as a function of concentration and molecular weight has been studied extensively by Ebagninin et. al. [56]. Figures 2.30 and 2.31 are plots of their results from shear flow and oscillation experiments respectively. From the shear flow viscosity measurements it was concluded that the viscosity can be used as a sensitive indicator of the concentration regime (dilute, semi-dilute unenetangled, semi-dilute entangled or concentrated). This could therefore be used to predict the dynamic fluid properties PEO solution will exhibit over the course of increasing concentration due to evaporation. The oscil-
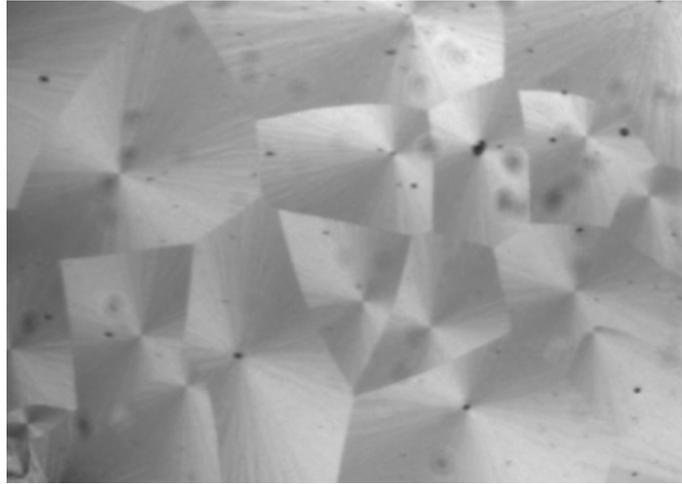
Figure 2.29: Image of spherulites captured during the late stages of drying in droplets of PEO-water solution ($c_0 = 2\%$ $M_\mathrm{W} = 100$ kg/mol). Nucleation occurred heterogeneously, often nucleating at dust particles.

lation results show more interesting visco-elastic properties of solutions dependent on frequency, molecular weight and concentration. Indeed, at molecular weights below 1000 kg/mol, in the concentration and frequency range observed, the solutions showed higher values of G'' compared with G', telling us that the solutions are predominantly viscous rather than elastic. However, two additional points can be made from these plots. Firstly, at 4000 kg/mol there is indeed a clear crossover from viscous to elastic behaviour, with a crossover point that decreases in concentration as frequency is increased. Secondly, in the whole molecular weight and concentration range, as frequency is increased the ratio between the storage and loss moduli (G''/G') decreases. This suggests that there may indeed be a cross-over timescale from viscous to elastic behaviour above the frequency range of their measurements for all molecular weights and concentrations. It may be useful therefore to fix M_W and c_0 and vary frequency to find the cross-over between viscous and elastic behaviour.

If the polymer concentration is increased further beyond the limits of the experimental results of Ebagninin et. al., eventually when the solution reaches the saturation concentration ($c = c_\mathrm{sat}$), the polymer will transition from the liquid phase to the semi-crystalline phase in the form of heterogeneously nucleating spherulites, which occurs at $c_\mathrm{sat} \approx 50\%$ for aqueous PEO solutions [52]. Beech et. al. have examined the rate of spherulite growth in PEO solutions and found that
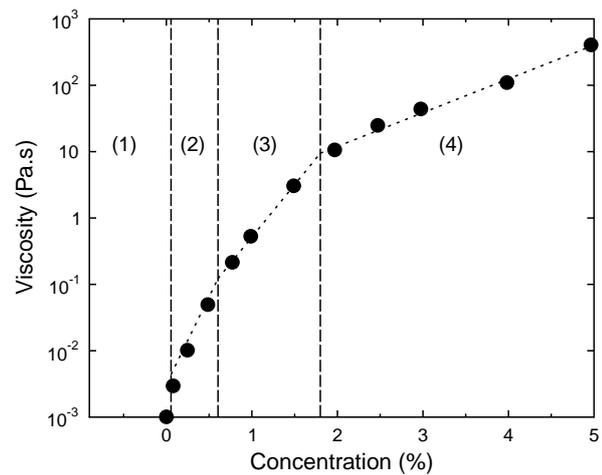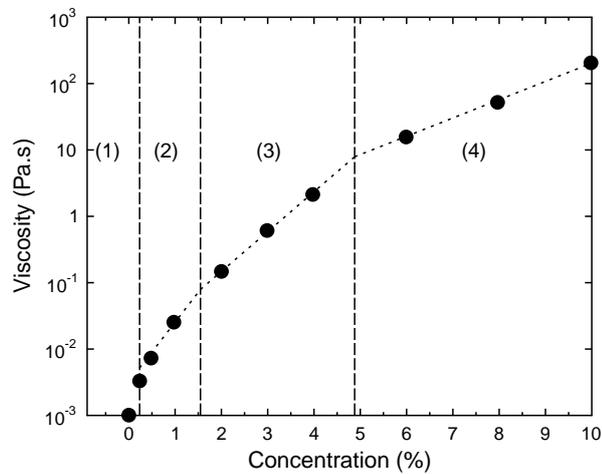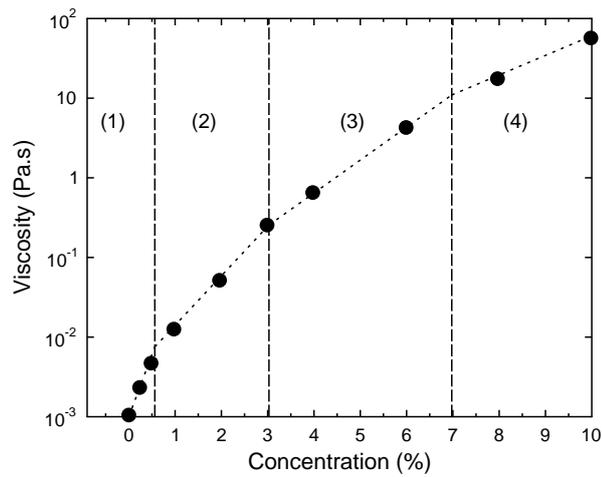
Figure 2.30: Zero shear rate viscosity η_0 plotted against mass fraction for 3 different molecular weights 400, 1000 and 4000 kg/mol (from top to bottom). The concentration regimes are split into (1) dilute (2) semi-dilute unentangled (3) semi-dilute entangled and (4) concentrated. Data taken from publication by Ebagninin et. al. [56].
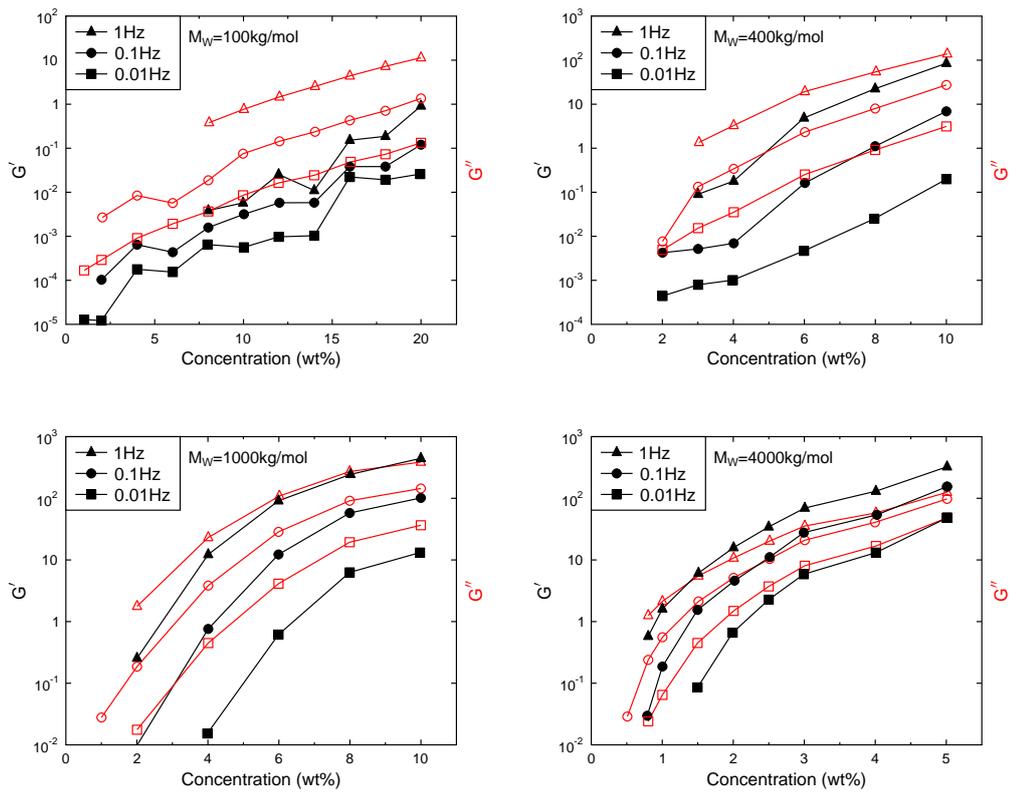
Figure 2.31: Variation of loss and storage moduli (hollow red and solid black shapes respectively) as functions of mass fraction at various oscillation frequencies for PEO solutions of $M_{\mathrm{W}} = 100$, 400, 1000 and 4000 kg/mol. Data taken from publication by Ebagninin et. al. [56]

it is dependent on temperature only, but not on molecular weight [57], as shown in Fig.2.32. Interestingly they also found that the free energy of spherulite nucle-
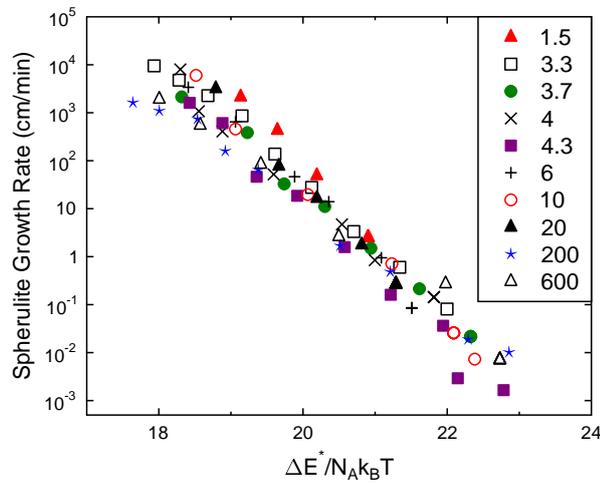
Figure 2.32: PEO Spherulite growth rate as a function of $\Delta E^*/N_A k_B T$ (where ΔE^* is the free energy of the nucleation of a spherulite with critical size r^* and N_A is avagadros number) for various values of molecular weight, labeled in the key in units of kg/mol. Data taken from publication by Beech et. al. [57].

ation does not vary with chain length. This is in stark contrast with experimental findings with polymers such as polyethylene, poly-isoprene and poly(tetramethyl-p-silphenylene siloxane) [58], in which the free energy of nucleation increases with M_W. No satisfactory explanation of this discrepancy is offered by Beech et. al. to accompany these interesting findings.

But words are things, and a small drop of ink,
falling like dew, upon a thought, produces that which
makes thousands, perhaps millions, think.

GEORGE BYRON

Chapter 3

Droplets

Droplets are everywhere. Most often, droplets are associated with rain, or condensation on the glass window on a cold morning, or the single beads of sweat that form on our brows on particularly hot days. But why do droplets form at all? Why not a thin liquid film? And if spherical shapes are preferrable to films, why do large volumes of water such as puddles or lakes not also ball up in this manner? Water of course is not the only liquid available. Oils and alcohols for example show surface spreading behaviour completely different to that of water, but what mechanism drives these behaviours? The answers to many of the troubling questions concerning droplets were first proposed by Thomas Young in 1805, whose insight of simple liquid behaviour has stood up to rigorous testing ever since. However, with the increasingly complex non-Newtonian liquids and textured surfaces used in industry today, the ideas proposed by Young are no longer adequate to fully explain droplet behaviour, and so research continues today with the aim of exanding on Young's brilliant ideas.

Evaporation is an equally common and ignored phenomena. Yet where would we be after a long game of squash without the evaporative cooling effect of sweat? Hot, is the answer. To many scientists, particularly those in the printing industry, evaporation is indeed a troublesome phenomena. What is commonly known as the coffee-ring effect, which causes suspended grains in a drop of coffee to be redistributed around the perimeter of the drop as it evaporates, also occurs in nanolitre sized droplets deposited from ink-jet printers. While ink-jet printing may be one of the most promising methods for deposition of functional materials,

until this outward radial flow can be controlled, evaporation will continue to remain a barrier to increasing printing precision.

In this chapter I will discuss wetting (the ability of a droplet to spread on a surface), evaporation effects (such as radial flows, evaporative cooling and convection currents), and the methods for which these effects have been utilised in order to control solute distribution in a deposited droplet. This will lay the first half of the literature groundwork for my research into a particular drying droplet system, where many of these phenomena have been observed, and very often, reliably controlled.

3.1 Interfacial Forces

3.1.1 Molecular Cohesion

The Oxford dictionary definition of a liquid is "having a consistency like that of water or oil, i.e., flowing freely but of constant volume". This is in fact a fairly restrictive definition as anyone who has ever played with honey or glue will attest to. Indeed in non-Newtonian liquids the borderline between solid and liquid becomes blurred depending on the situation, polymeric substances discussed in the previous chapter being prime examples. For the purposes of this chapter I will for now define a liquid as a disordered, condensed state of matter in which the molecules are mobile and the cohesive forces acting between molecules are greater than the effect of the thermal agitation [59].

The fundamental molecular interactions that lead to cohesive forces acting between molecules in a liquid can have several origins. Water is a good example of molecules with a high cohesive force. This can be attributed to the specific arrangement of the oxygen and hydrogen atoms which make up the molecules, as shown in Fig.3.1. Because the oxygen is more highly electronegative than Hydrogen (in layman's terms, this means the oxygen holds onto electrons more strongly than hydrogen), the molecule is slightly positive (δ^+) around the hydrogens and slightly negative (δ^-) around the oxygen [60]. A molecule with this kind of charge distribution is known as *polar*. This polarity has a knock-on effect between molecules as the positive pole of one water molecule will be attracted
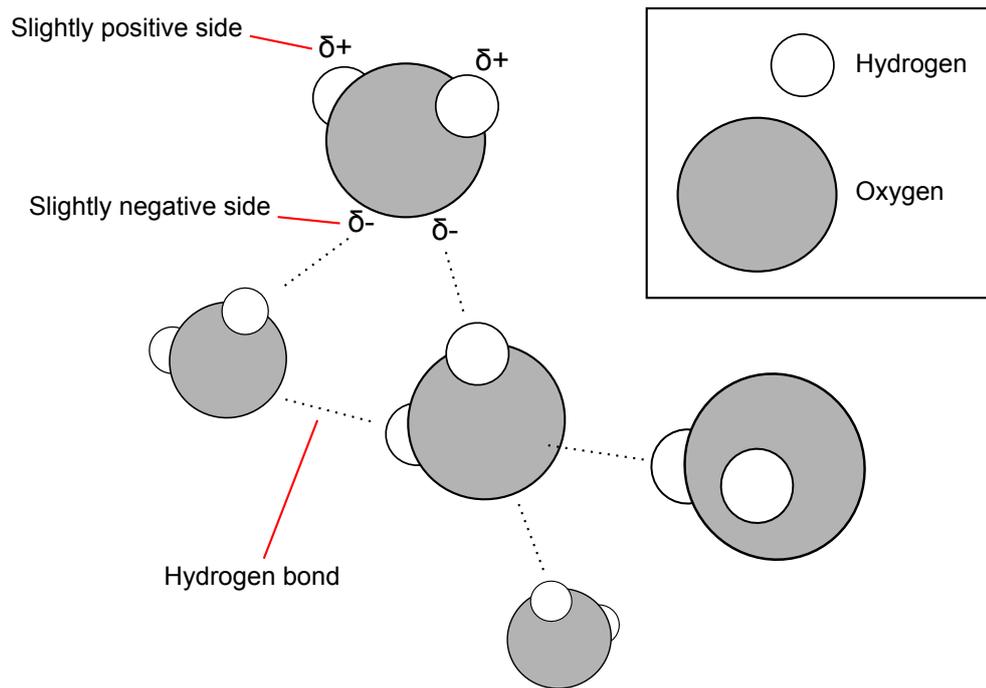
Figure 3.1: Random arrangement of liquid water molecules. The more strongly electronegative Oxygen causes an uneven charge distribution around the molecule, or polarity. The attraction this polarity causes between water molecules is known as hydrogen bonding.

to the negative pole of another. Polar attractions occur between many different types of substances, but in the case of a hydrogen atom covalently bonded to a highly electronegative atom, the polar attractions are very strong, and for this reason given their own specific name - *hydrogen bonding.* As a general rule, the more polar groups in a molecule, the stronger the intermolecular attractions. Fig.3.2 is a phase diagram of water as a function of temperature and pressure. Unlike most liquids which freeze when pressure is increased, ice will actually melt with increased pressure due to the strong hydrogen bonding effects in the liquid phase. Where the three phases meet on the diagram is known as the triple point, and is the temperature-pressure combination at which all three phases can exist. The critical point also labeled is where the pressure-temperature combination at which becomes impossible to distinguish between liquid and gas, and the phase transition disappears. No such phase transition vanishing exists between liquid and solid.

The free energy of a surface is quantified by the disruption of intermolecular bonds that occur when a surface is created. In water for example, the free energy
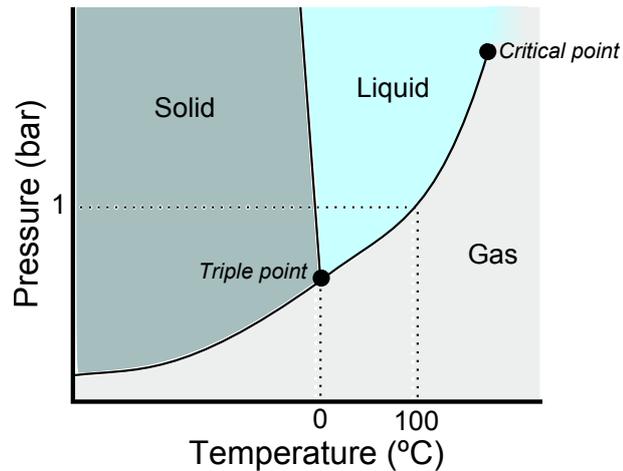
Figure 3.2: Phase diagram of water as a function of pressure and temperature

at the surface is caused by the available unused hydrogen bonds. The surface free energy can be defined as the excess energy at the surface of a material compared to the bulk.

3.1.2 Surface Tension

Even with small amounts of liquid there are many intermolecular attractions occurring simultaneously. Fig.3.3 is a schematic of the many attractions between molecules caused by this cohesion [59]. In the bulk of a liquid, the attractive pull between the many molecules will act equally in every direction, resulting in a zero net force. However, at the surface of the liquid, if we assume very little interaction between the liquid and air molecules, the lack of an outward pull would result in a net inward pull at the interface, with units of force per unit length. This surface pulling force is most commonly known as surface tension, and tends to reduce the surface area of a liquid, causing all liquids to be spherical when suspended in air. This surface tension can also be viewed in terms of energy, which is often most useful. Because of the high free energies associated with cohesive attraction, the lowest energy state for a molecule of water occurs when it is surrounded on all sides by other water molecules. High energy states are much more unstable than low energy states, so the liquid will attempt to reduce its total energy by limiting the number of exposed molecules by reducing its surface area.
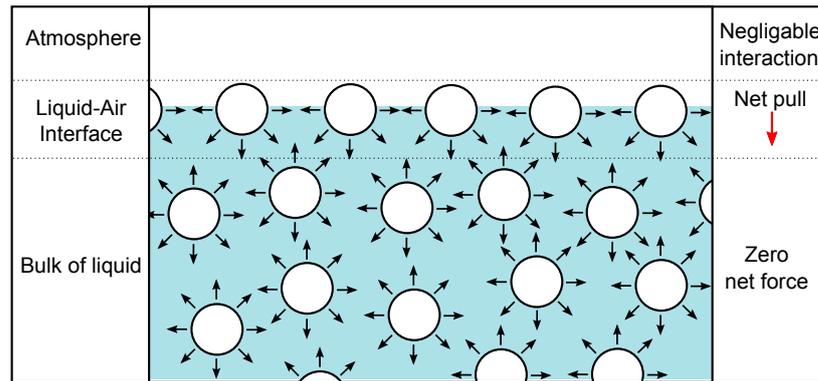
Figure 3.3: Diagram of the intermolecular cohesive forces acting between liquid molecules in both the bulk and at the surface of the liquid, resulting in a net inward pull at the interface, or surface tension.

It should also be noted that the relative effect of the intermolecular forces are highly dependent on the thermal energy of the system. As temperature increases, and molecules become more agitated, they effectively "hold on" to each other less and less, and the relative effect of surface tension is reduced. The general trend is that surface tension decreases approximately linearly with the increase of temperature [61]. However, only empirical laws have been found for this inverse proportionality due to the complexity of the changes in molecular interactions with energy, especially for non-polar liquids, or at temperatures approaching 0K. For this work, such complexities are not important, so we can assume that the dependency of temperature on surface tension is given by the Eötvös rule:

$$\gamma = \frac{k(T_\mathrm{C} - T)}{V_\mathrm{mol}^2/3} \tag{3.1}$$

where k is a constant ($k = 2.1 \times 10^{-7}$ J/Kmol$^{2/3}$ for almost all substances), T_C is the critical temperature and V_mol is the molar volume [61].

Surface tension is responsible for a wide range of everyday phenomena, including the ability of certain insects such as water striders to walk on water [62] or the spontaneous breakup of a cylindrical stream of water into a series of spherical droplets [59] in order to reduce the total surface area of the liquid. This stream break up can be easily seen by running the tap in the bathroom. Water exits the tap as a steady stream, but at some point between the tap and the sink, this stream breaks up and hits the sink as a pattering of droplets. For this transition to cause a reduction in surface area, the radius of the droplets must be at least

1.5× the radius of the cylindrical stream [59]. Any liquid, with any value of surface tension will tend to maintain a spherical shape when in contact with atmosphere only. However, when a second interface is introduced (rain drops stuck to a windshield for example), we can observe some interesting behaviour depending on the free energies of the various interfaces, such as spreading into either a thin film or a spherical cap droplet. The study of droplet spreading on a surface is known as *wetting*.

3.1.3   Cohesion versus Adhesion

To understand wetting it is preferable to take the definition of surface tension of a substance as the amount of energy required to increase its surface area by a single unit. From this we can say that a change in surface area results in a similar change in the free energy, scaled by the surface tension:

$$dE = \gamma dA \qquad (3.2)$$

A liquid with low cohesive attractions will require less energy to increase the surface area than a liquid with high cohesiveness. While it may be easier to picture surface tension as a contraction force per unit length, for a solid this is impractical as contraction forces will be dominated by the elastic properties of the bulk of the material. So for consistency, I will refer to substances with high or low surface tension as high-energy or low-energy surfaces.

Much like liquids, a solid with a high surface energy is one in which the chemical binding energy between molecules is high. High-energy materials are typically metallic or covalently bonded.* Low-energy materials on the other hand are made of molecules which have a low binding energy. Examples of these are molecular crystals or plastics. Again, for the purpose of simplicity it is assumed that the binding energy between the solid and the air is low, resulting in high free energy per unit area at the interface, with an equivalent surface tension denoted by γ_S. We now have terms for the free energy of liquid in air and solid in air, which do not vary. From this, in order to predict the wettability of a liquid on a solid surface, i.e. whether a large (flat puddle) or small (spherical droplet) contact

---

*Generally, glass is considered a high energy surface which highly wets water. This is often not the case depending on the specific structure of glass. As you will see from my later experimental findings, glass cannot be strictly defined this way

area between the solid and liquid will reduce the free energy, we need to know the adhesive forces acting between liquid and solid, or rather, the free interfacial energy between the two substances.

As we have seen already from equation 3.2, reducing the surface area results in the reduction of the free energy of the substance. However, when there are 3 substances in contact, which surface contact area will minimize and which will maximize depends on the interplay between all three surface energies [63]. As mentioned in section 3.1.1 cohesiveness is often a property of the polarity of the liquid. Indeed, if the liquid is less polar than the solid, the adhesiveness between solid and liquid will win out over the cohesiveness between the liquid molecules, and liquid will spread out onto the surface into a nanoscopically thin film [59,64]. This is why most liquids will spread completely on highly polar metallic surfaces (with the exception of mercury, which is metallic itself!). This is known as *total wetting*, and I will discuss this phenomena no further as the main focus of this research is in the alternative case, known as *partial wetting*.

3.2 Sessile Droplets

3.2.1 Partial Wetting

In the case where the free-energy of the liquid is comparable with the free-energy of the solid substrate then the liquid will not spread out and form a film, but rather form a spherical cap. The Young's relation characterizes the droplet shape through a simple calculation of the sum of the x-components of the interfacial forces acting at the contact line [59,65], as shown in Fig.3.4:

$$\gamma_{\mathrm{S}} = \gamma_{\mathrm{SL}} + \gamma_{\mathrm{L}}\cos\theta_{\mathrm{E}} \tag{3.3}$$

where θ_{E} is the equilbrium contact angle and γ_{S}, γ_{SL} and γ_{L} are the interfacial tensions at the solid-air, solid-liquid and liquid-air interfaces respectively. The droplet will be stable when the two opposing forces acting on the contact line of the droplet are equal. Through simple geometry we can calculate the equilibrium contact angle of the droplet from this force balance diagram. This result is identical if we approach the droplet from the perspective of minimizing the solid-air, solid-liquid and liquid-air contact areas.
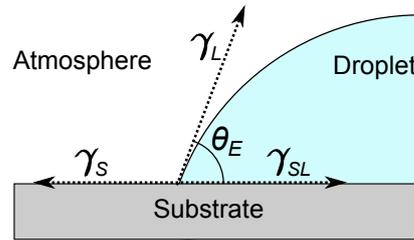
Figure 3.4: Diagram of the directional forces acting at the three interfaces between solid, liquid and air in a sessile droplet. Young's relation is found by equating the solid-air interfacial tension γ_S with the sum of the solid-liquid interfacial tension γ_{SL} and the x-component of the liquid-air interfacial tension $\gamma_L \cos\theta_E$.

In reality, calculating all 3 interfacial free energies in order to predict the equilibrium contact angle is difficult, particularly with respect to the solid, but let's start with the simplest method for measuring the surface tension of a liquid-air interface, which is most commonly done using the Wilhelmy plate method. In this technique a fully wetting thin plate (typically roughly textured platinum[†]) is lowered until it comes into contact with the liquid surface. The liquid will then climb vertically up along the surface of the plate in the form of a meniscus as shown in Fig.3.5. As the plate is then submerged and slowly extracted, the force
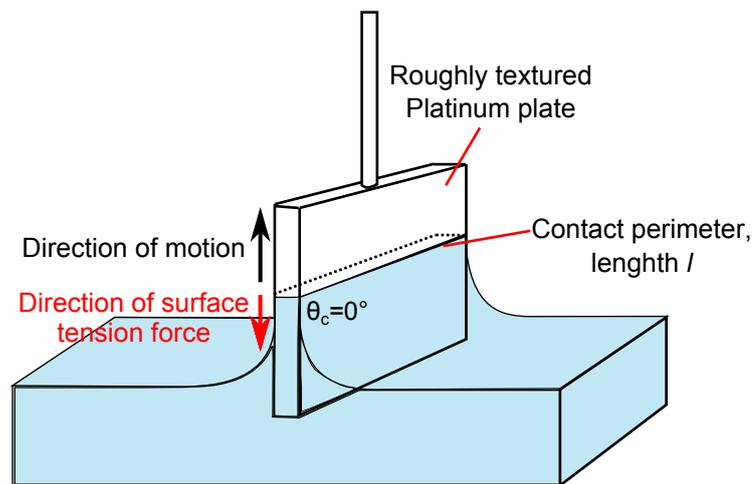
Figure 3.5: Diagram of the Wilhelmy Plate Method for calculating the surface tension of a liquid.

[†]The importance of surface roughness will be discussed in section 3.2.3, but in this situation, it should be noted that surface roughness simply improves wettability

exerted on the plate by the liquid goes through a maximum when the surface tension is acting only parallel and in opposition to the direction of the plate, i.e., when the contact angle reaches zero. At this point the force exerted is the product of the perimeter length of the contact line and the surface tension of the liquid, γ_{L}.

As mentioned previously, the elastic energy of a solid would dominate any direct measurements of cohesive forces acting between solid molecules. However, the interfacial energy between a solid and air can still be measured using the JKR test [66]. In this test a large sphere with radius R_{S} and a flat plane of the same solid material are brought into contact as shown in Fig.3.6. Provided the solid is
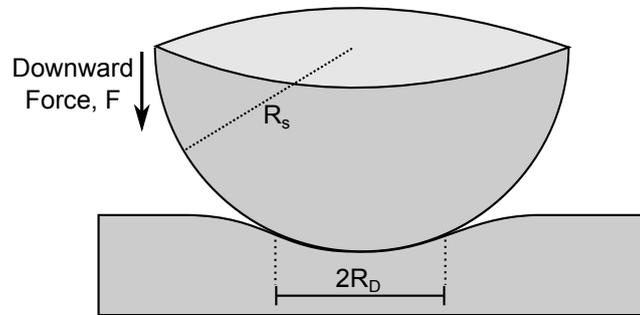
Figure 3.6: Diagram of JKR test, a method for calculating the surface tension of a solid.

soft enough, the contact between sphere and solid will not be a single point but a disk of radius R_{D}. The disk arises due to the competition between the interfacial energy (which is in favour of a large contact area), and the elasticity of the solid (which opposes a large contact area) [67]. By measuring the contact radius for a range of different sphere radii (R_{S}), and plotting R_{D}^3 against R_{S}^2, the gradient gives twice the interfacial free energy. This method works equally well submerged in a liquid, and so gives values for the interfacial energy between solid and liquid also.

Contact angles of droplets are measured independently by capturing profile images of the droplet and fitting an appropriate curve to the surface. Several different curve fitting methods exist, each with different suitable θ_c ranges [68]. Non-profile fitting methods also exist, such as optical reflectometry [69], which by measuring the reflected angle of a collimated beam of light, as shown in Fig.3.7, gives an estimation of θ_c:
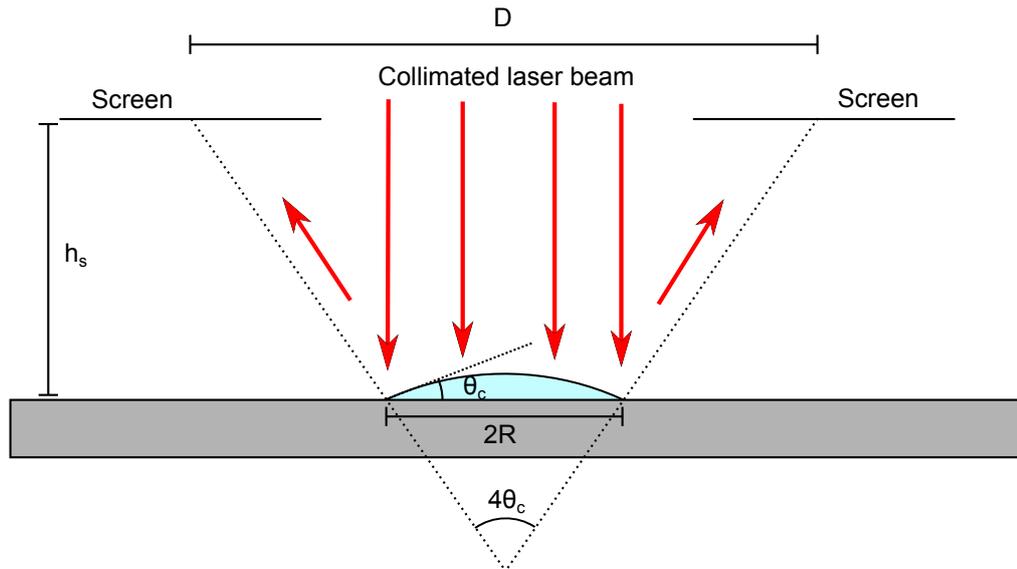
Figure 3.7: Diagram of optical reflectometry method for calculating the contact angle of a deposited droplet, for droplets with $\theta_c < 45°$

$$\tan(2\theta) = \frac{D - 2R}{2h_s} \tag{3.4}$$

This method is limited to when $\theta_c < 45°$.

While these methods are not applicable in every liquid, solid and air interface (such as if the solid is too hard, the contact area between sphere and flat surface will not be sufficiently large to measure R_D through microscopy, therefore no value of γ_S can be measured using the JKR test), these procedures give completely independent measurements of every term in equation 3.3, and directly validates Young's relation.

3.2.2   Hydrophobic and Hydrophilic surfaces

Surfaces are often defined by their ability to wet water, which may seem like a very specific case when we consider the wide array of liquids available to us, except that this is useful due to the ubiquity of water in everyday life. By convention, a surface is known as hydrophilic (this word comes from the Greek words *hydros*, meaning water, and *philia*, meaning love) if water has an equilibrium contact angle $\theta_E < 90°$, and hydrophobic (this time using the Greek word *phobos*, which means fear) when $\theta_E > 90°$, as shown in Fig.3.8.
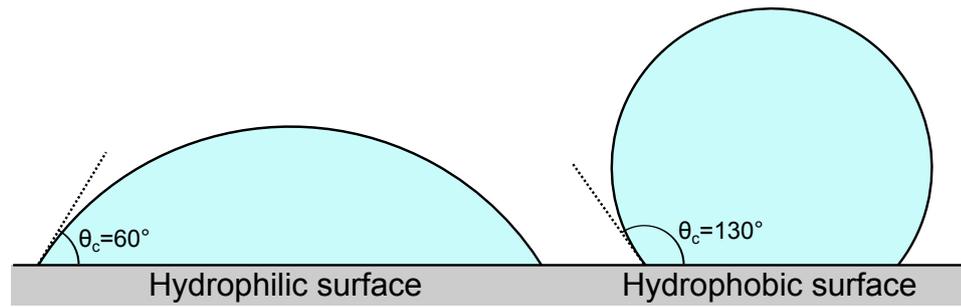
Figure 3.8: Diagram of side by side comparison of two equal volume water droplets on hyrdophilic and hydrophobic surfaces.

An example of a chemically hydrophobic surface is PTFE (most commonly known as Teflon), which has an equilibrium contact angle of $\approx 110 \pm 10°$ with water (high uncertainty from various contradictory measurements of θ_E in literature [70]. Unreliable results are most likely due to hysteresis effects which will be discussed in section 3.2.4). Other examples include lipids, which is a broad term describing many fats and waxy substances, and oils. A natural example of a hydrophobic surface is earwax, a substance evolved for the specific purpose of repelling water from the inside of the ear canal [71]. Most forms of glass are considered to be high energy surfaces, and therefore highly hydrophilic, but this can be altered with the addition of a hydrophobic monolayer, such as Granger's solution [72], a water based water proofing detergent designed as an additive for improving water repellency of many materials such as clothes and other fabrics by fluorinating the surface.

3.2.3 Structured Surfaces and Superhydrophobicity

Outside of the lab, nature has found ways to improve water repellency even further, not through increasingly hydrophobic molecules, but with complex physical structures. The most famous example of this is the sacred lotus leaf [73], which is known as a superhydrophobic surface. To understand this superhydrophobicity we have to move away from ideal smooth surfaces, and introduce micro or nanoscale physical structures. As we have seen already, a droplet in contact with a smooth surface will exhibit an equilibrium contact angle θ_E. However, if we introduce a regular structure of equally sized pillars to the surface, then the contact angle is adjusted, and the direction and magnitude of this adjustment depends

on one of two possible wetting states:

- Wenzel state. The liquid fills the gaps between pillars and wets the entire surface. In this case the cosine of the apparent contact angle is given by:

$$\cos\theta_{\text{App}} = \frac{A_{\text{3D}}}{A_{\text{2D}}}\cos\theta_{\text{E}} \qquad (3.5)$$

Where A_{3D} is the real contact area and remains fixed by the Young's relation and A_{2D} is the apparent 2D surface area as shown in Fig.3.9. The
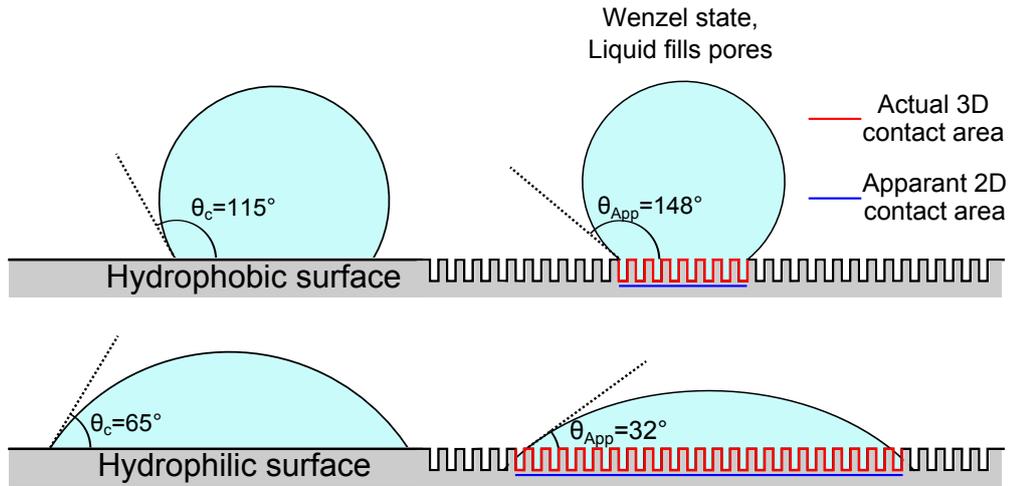
Figure 3.9: Diagram of Wenzel state wetting. The liquid fills the pores, and the apparent contact angle is either increased if the original smooth surface was hydrophobic, or decreased if it was hydrophilic. Calculated apparent angles for the case when $A_{\text{3D}} = 2A_{\text{2D}}$

consequence of this is that as long as the surface is completely wetted with no air pockets, then the apparent contact angle will increase when $\theta_E > 90°$ and decrease when $\theta_E < 90°$ [74] [75].

- Cassie-Baxter state. The liquid rests on the tips of the pillars, leaving small pockets of air trapped beneath the surface. The ability for liquid to penetrate the pores in the surface depends highly on the wettability of the surface and the dimensions of the pores. Indeed for a hydrophobic porous surface, the droplet does not necessarily fill the pores. Young's relation still remains true locally at each asperity, but the trapped air pockets further promotes the hydrophobicity of the surface, as shown in Fig.3.10. For a droplet to be in the Cassie-Baxter state the asperities must be of a certain critical height, and the surface forces around the perimeter of the asperities
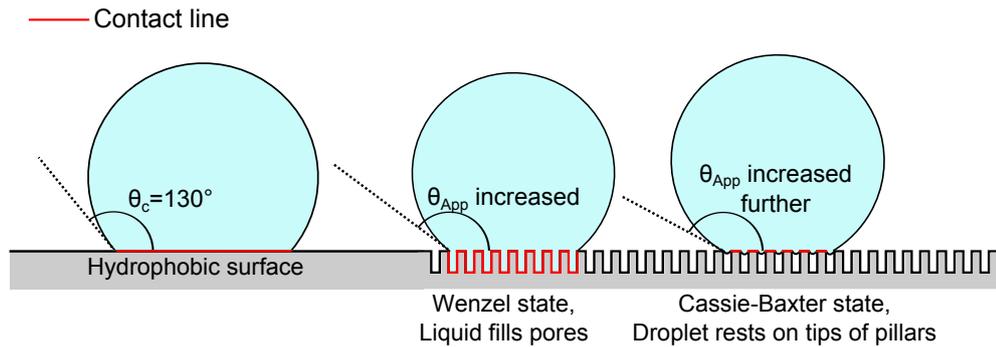
Figure 3.10: Diagram of comparison between wetting on a hydrophobic smooth surface and the effect of Wenzel and Cassie-Baxter state on the contact angle of a water droplet

must be greater than and in opposing direction to the gravitational pull on the droplet [76].

This effect has been utilized for the production of syperhydrophobic surfaces such as with PTFE coated carbon nanotube forests [77], which highlights the importance of air pockets as initial experiments (before treatment with PTFE) yielded values of θ_E with water of 161° (Cassie-Baxter state), but this high contact angle only remained stable for a few minutes until the water seeped in between the nanotubes (Wenzel state). The initial high contact angle was only stable for long periods if coated with PTFE before droplet deposition.

3.2.4 Hysteresis

Up until this point it has been assumed that a given liquid droplet-solid combination will have a fixed contact angle θ_E. However, anyone who has ever watched rain slide down the side of a car window will know that droplets often become stuck and bulge downwards due to the pull of gravity. This hints that in fact θ_E is not always fixed, but there is a wide range of values around the value of θ_E predicted by Young's relation at which the droplet remains stable. This wide margin of stable contact angles is known as *hysteresis*.

We have already seen that regular surface structures can affect the equilibrium contact angle of a droplet. This also goes for irregular surface roughness and defects, or even wettability changes due to chemical stains on the surface. Indeed,

on a non-ideal surface, a droplet can be inflated significantly before the droplet contact line advances. This does not imply that Young's relation does not hold, but rather it is limited to an ideal case. Imagine a smooth slightly hydrophobic surface, which has an equilibrium contact angle of 100° with water. However, before droplet deposition we add several small defects to the surface. These defects will increase the contact angle locally as discussed in section 3.2.3, but what of the regions where the surface remains smooth? In this arrangement, the droplet will be partially stable at the equilibrium contact angle, and partially stable at an increased contact angle. Now, rather than defining θ_{E} it becomes more useful to define the upper and lower limits of the stable contact angle. If one was to deflate a droplet by removing volume after it has reached equilibrium, the contact angle would reduce, until a point at which it is no longer stable when the contact line will dewet and recede. This critical point is known as the *receding contact angle* θ_{R}. Similarly, the upper contact angle the droplet can reach before it becomes unstable and the contact line advances is known as the *advancing contact angle* θ_{A}. At any value of θ_{c} between these two values the droplet is said to be *pinned* to the substrate.

Contact line pinning is in fact a complex phenomenon, depending on not only the density, size and distribution of defects, but also on suspended particles within the droplet [78, 79]. This effect however may require evaporation of the solvent, which is a complication to wetting that will be discussed in detail in section 3.3, with particular emphasis on solute "self-pinning" in section 3.4. Dust and debris in the atmosphere is also very well dissolved by solvents such as water. These unwanted contaminants could lead to 2 possible side effects:

- Reduction in the surface tension of water. Surface tension alterations are an an intrinsic property of surfactants, which will be discussed in section 3.2.5.

- Enhanced contact line pinning leading to greater hysteresis, much like in the case of suspended particles in the solvent (see section 3.4).

3.2.5 Surfactants

We have seen that the wetting properties of a droplet can be greatly varied by surface roughness, chemical stains, suspended particles and contaminants, most of which are undesirable effects. We have also seen that the hydrophobicity of a substrate can be altered by the addition of a fluorinated polymer layer. Similarly, the surface tension of a liquid can be reduced with the addition of a surface active agent, or *surfactant*, to the liquid [80].

For a compound to be a surface active agent for a specific solvent it must be amphiphilic, which means that it must have a component which "likes" the solvent, and a component which "dislikes" the solvent. Usually surfactants are used to reduce the surface tension of water, for example in detergents, emulsifiers and foaming agents [80]. For this reason I will focus on water active surfactants. While the chemical structure of surfactants take on increasingly complex forms, the simplest picture is that a surfactant is made up of a polar, hydrophilic "head" and a non-polar, hydrophobic "tail" as shown in Fig.3.11. While the head will happily dissolve in water, the tail will not. This solubility imbalance leads to two common effects:

- Adsorption of the surfactant at the liquid-air interface, with the tail pointing out of the solution and the head remaining submerged. The surfactant has replaced the water molecules at the surface, and because the tail is non-polar, and therefore has no "unused" bonds, the free energy of the surface is reduced, lowering the surface tension. The total reduction in surface tension is unsurprisingly related to the change in concentration of water at the interface and the free energy of the surface containing the surfactant.

- Formation of colloidal aggregates of surfactant molecules, or micelles, where the hydrophobic tails collect together surrounding themselves with a "shield" of hydrophilic heads as shown in Fig.3.11. Micelle formation only occurs above the "critical micelle concentration" [80]. Below this concentration molecules remain individual in solution.

There are other types of amphiphilic molecules which do not have this head and tail arrangement, and so are typically not considered "true" surfactants, but display many of the same properties. A key example being PEO, as discussed
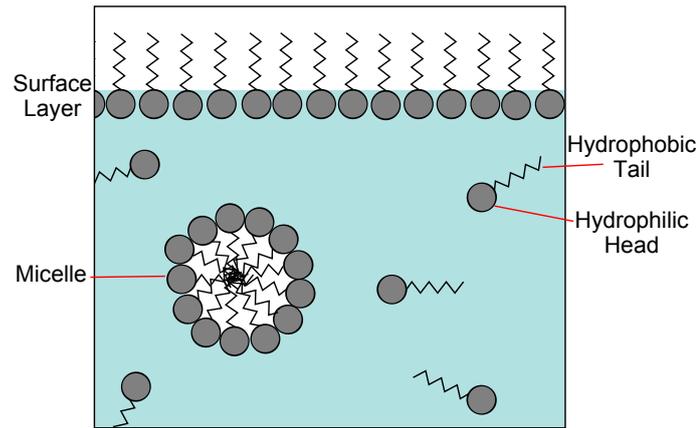
Figure 3.11: Diagram of the arrangement of surfactants in water

in the previous chapter, which consists of a repeating CH_2CH_2O backbone, the carbon groups being hydrophobic, while the oxygen groups are hydrophilic. The role of the polymer as a surfactant is shown simply in Fig.3.12. Unlike the usual
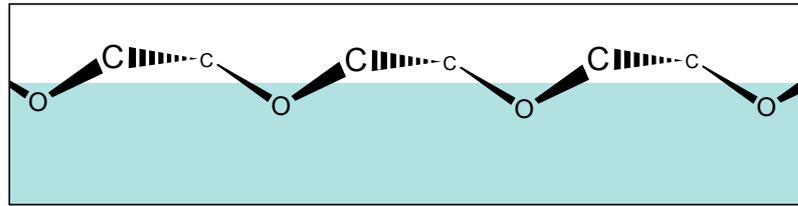
Figure 3.12: Diagram of the arrangement of a PEO molecule over the surface of water

head and tail arrangement of surfactants, PEO tends to lie along the surface of water, with the oxygen units submerged and the carbon units exposed [81, 82]. This picture is further complicated by increasing the concentration. At a critical value, the entire surface will be coated in carbon groups. Above this concentration the polymer chains bunch up together and start to dangle down into the bulk of the liquid as shown in Fig.3.13. While this does not alter the free energy of the surface as total number of exposed carbon groups is unaltered, this does create a polymer "skin" which alters flow behaviour [82]. Cao et. al. [83] measured the reduction in surface tension against PEO concentration for a range of molecular weights, as plotted in Fig.3.14. Interestingly, this seems to suggest that at high concentrations $c_0 > 0.1\%$, PEO with molecular weight $M_W = 85$ kg/mol has a reduced surface tension compared with both lower and higher chain
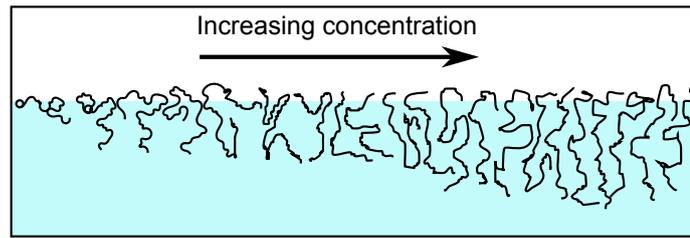
Figure 3.13: Diagram of arrangement of PEO chains at air-water interface with increasing concentration [82]. Single chains preferentially lie along the surface at low concentrations. They begin to bunch up and dangle into the liquid as concentration is increased.

lengths which is explained as a result of the formation of a dense surface polymer monolayer, which only occurs in a narrow molecular weight range. This point will be considered again in the final results chapter of this thesis in which polymer molecular weight is the focus.
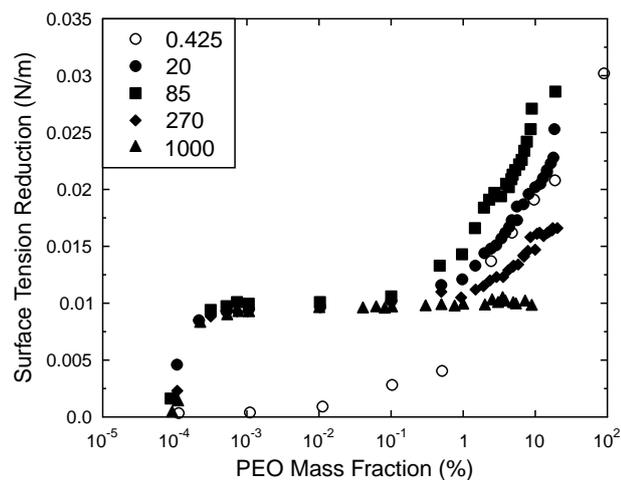
Figure 3.14: Plot of the change in surface tension against PEO concentration for a range of molecular weight. Different molecular weights distinguished by key in units of kg/mol. Plotted data taken from publication by Cao [83].

3.2.6 The Capillary Length

Until now, the effect of gravity has been ignored. One would imagine that in the absence of surface tension, gravity would completely flatten out any droplet. At the other extreme, in the absence of gravity, one would expect surface tension to
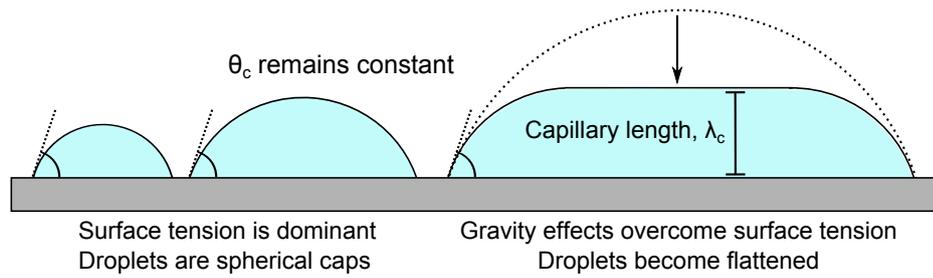
Figure 3.15: Diagram of increasing sized water droplets. Above a certain height, gravity is sufficiently strong to overcome surface tension and the droplet is flattened.

dominate at any volume of liquid, causing puddles of water left by rain to form large spherical cap structures. Clearly this is not the case. In fact, the cross over between spherical cap droplets and flat puddles is due to the competition between the effects of surface tension, which increase linearly with the surface area of the droplet, and gravity, which increase linearly with the volume of the droplet [84]. Once this is understood it becomes clear that because surface area scales with the square of the droplet radius, R^2, and volume goes with R^3, at a certain size gravity will dominate. The length scale at which gravity begins to dominate is known as the *capillary length*, the definition of which is:

$$\lambda_{\mathrm{c}} = \sqrt{\frac{\gamma_{\mathrm{L}}}{\rho g}} \tag{3.6}$$

where ρ is the density of the liquid and g is the acceleration due to gravity. Larger droplets become flattened at the top, but maintain their equilibrium contact angle, as shown in Fig.3.15. Equation 3.6 gives the capillary length of water as $\lambda_{\mathrm{c}} \approx 2$ mm. In order to increase this capillary length and have much larger spherical cap water droplets one must reduce the effects of gravity (for example by taking the droplet into orbit, using optical, acoustic or diamagnetic levitation - which is discussed in detail in chapter 4 - or more simply by placing the water droplet in an immiscible fluid with density close to that of water [84].

3.3   Drying

3.3.1   Aerosols - One Component Drying

To understand evaporation, let us first consider a suspended aerosol droplet evaporating in a one component system. This being in either a vacuum, or a gas phase that is made entirely of the vapour of the droplet. Firstly, evaporation (or condensation) occurs when liquid and vapour are not in equilibrium. That is to say that the vapour density is not equal to the saturated vapour density. If the vapour density ρ_v is greater than the density at which the gas phase is saturated with vapour, ρ_{sat}, excess vapour will condense into liquid droplets, whereas if $\rho_v < \rho_{sat}$ water in the liquid phase will evaporate. Furthermore, transfer across a liquid-vapour interface is a two way process. When $\rho_v = \rho_{sat}$, (this is known as the "dew point") water still escapes from the liquid droplet, but it re-enters the droplet at exactly the same rate. This means evaporation occurs when the water transfers faster from liquid to gas phase than in the opposite direction [85]. The rate of evaporation is proportional to the difference between the vapour density and the saturation density m]eaning drying rates slow down as ρ_v approaches ρ_{sat}.

As evaporation occurs the vapour density directly above the surface of the droplet must increase. In any given atmosphere, pressure homogenization is fast, and in a one component atmosphere pressure and concentration are proportional. Therefore, when evaporation occurs in this type of system, where all molecules in gas and liquid phase are identical, the concentration gradient of the vapour that builds up directly above the droplet very quickly homogenizes with the rest of the atmosphere, effectively maintaining the concentration gradient at zero [85][‡]. This means that the transfer rate across the liquid-gas phase boundary is controlled simply by the time-step required for a single molecule to escape (or re-enter in the case of condensation) the surface. The interface between the liquid and vapour phase is the only limiting step for evaporation, and therefore the total evaporation rate is proportional to the surface area of the droplet:

$$-\dot{V} \propto A \tag{3.7}$$

[‡]The speed at which the concentration gradient disperses here is important. Because pressure homogenizes at the speed of sound, the local evaporation rate j must be greater than the speed of sound in order to build up a concentration gradient over the surface.

Furthermore, because $V \propto R^3$ and $A \propto R^2$, $\frac{dR}{dt}$ is constant. The local evaporative flux j, which is the evaporation rate over a single unit of area:

$$j = -\frac{\dot{V}}{A} \tag{3.8}$$

is proportional to the receding velocity of the interface $\frac{dR}{dt}$ as volume loss from a given area must cause the droplet to shrink, and we have already shown this receding velocity to be constant. The actual value is defined by the Hertz-Knudsen relation:

$$j = \alpha \sqrt{\frac{k_B T}{2\pi M}} \frac{\rho_{\text{sat}} - \rho_{\text{v}}}{\rho_{\text{L}}} \tag{3.9}$$

where ρ_{L} is the liquid density, α is the "accommodation coefficient", which in simple terms is the probability of transfer between liquid and vapour phase, k_B is the Boltzmann constant, T is the temperature, and M is the mass of the liquid molecule [85].

3.3.2 Aerosols - Evaporation In Air

In the case where the liquid is evaporating into an atmosphere not consisting of the liquid vapour, the escaping vapour molecules must slowly diffuse through the atmosphere. Much like in the one component system, pressure of the atmosphere very quickly homogenises, but in this case pressure and concentration are not equivalent. This means that a concentration gradient builds up above the surface of the droplet, controlled by the continual evaporation and slow diffusion of vapour molecules into the atmosphere, with the vapour density directly above the surface being equal to the saturation density, and some other lower value ρ_∞ at a large distance r away from the centre of the droplet. If the boundaries of the atmosphere are sufficiently distant from the droplet (effectively at $r = \infty$), the vapour will diffuse outwards away from the droplet at a constant rate defined by the self diffusion coefficient of the vapour D_{v}. This means that the concentration gradient that very quickly builds up around the droplet will remain constant for the duration of drying [85]. To define j we must now introduce the diffusion coefficient of vapour molecules in atmosphere D_{v}, and the concentration gradient that has built up due to evaporation. This is given by Fick's law [86]:

$$j = -D_{\text{v}} \frac{d\phi}{dr} \tag{3.10}$$

where ϕ is the vapour volume fraction.[§] Rewriting the concentration in terms of the fractional vapour density compared with the liquid density and the gradient in terms of the vapour density change between the drop surface ($r = R$) where $\rho_\mathrm{v} = \rho_\mathrm{sat}$ and some distance away where $\rho_\mathrm{v} = \rho_\infty$, this can be rewritten:

$$j = -\frac{D_\mathrm{v}}{\rho_L}\left.\frac{d\rho_\mathrm{v}(r)}{dr}\right|_{r=R} \tag{3.11}$$

$$j = \frac{D_\mathrm{v}}{R}\frac{(\rho_\mathrm{sat} - \rho_\infty)}{\rho_\mathrm{L}} = -\frac{dR}{dt} \tag{3.12}$$

$$-\int R\,dR = \frac{D_\mathrm{v}(\rho_\mathrm{sat} - \rho_\infty)}{\rho_\mathrm{L}}\int dt \tag{3.13}$$

$$-\frac{R^2}{2} = \frac{D_\mathrm{v}(\rho_\mathrm{sat} - \rho_\infty)}{\rho_\mathrm{L}}t \tag{3.14}$$

D_v, ρ_sat, ρ_∞ and ρ_L are all constants, so now we can see that R^2 will reduce linearly with time. This is known as the D^2 law (because despite my tendency to discuss drop radius, the literature writes this in terms of the drop diameter). A more important result however is found by multiplying the local evaporative flux j by the total surface area of the droplet ($4\pi R^2$), giving the total evaporation rate proportional to the radius:

$$-\dot{V} = D_\mathrm{v}\frac{(\rho_\mathrm{sat} - \rho_\infty)}{\rho_\mathrm{L}}4\pi R \tag{3.15}$$

Experimental measurements of evaporation rate versus droplet radius gives good agreement with this result [87]. It must be noted that for these descriptions of single component and free atmosphere drying, several assumptions have been made:

- The temperature is homogeneous. This is in fact a fairly weak point in the theory as evaporation would lead to a temperature decrease at the surface via evaporative cooling [88]. This will affect the saturation density, and therefore the evaporation rate. Additionally, a temperature gradient would lead to surface tension and density gradients, which as we will see in section 3.5 can lead to unforeseen effects such as Marangoni flows or Bénard convection cells.

[§]Fick's law is not limited to the diffusion of vapour molecules, but any system with a concentration gradient, where j is a measurement of an amount of a given substance flowing through a unit of area in a given unit of time.

- The atmosphere is quiescent, meaning zero air currents. This assumption is often stated as reasonable in the literature if the chamber is appropriately sealed off, but is not so small that the walls interfere with the vapour diffusion. In the presence of an air draft advection becomes more important than diffusion (encapsulated by a high atmospheric Péclet number) and these scaling arguments break down [85].

- Droplets are at a large distance from other droplets. Overlapping vapour concentration gradients from separate evaporating droplets will complicate the theory.

- The radius of the droplet is tiny compared to the distance between the walls of the drying environment.

3.3.3   Sessile droplets

Now let us consider a sessile droplet in free air. To begin with we will assume low hysteresis and define the droplet base radius as R. When a pinned droplet evaporates, the height will decrease until the contact angle (which is linked to height and radius by $\frac{h}{R} = tan\frac{\theta}{2}$) reaches θ_{R}, at which point the contact line will recede. The evaporation rate is still vapour diffusion limited, and so one may jump to the conclusion that the radius of curvature R_{c} reduces linearly with time, much as an aerosol droplet. However, we have already seen that Young's equation dictates that a droplet receding contact line maintains a fixed contact angle close to that of the receding contact angle. If one was to picture a sessile droplet as simply being a section of an aerosol droplet as shown in Fig.3.16, the linear decrease in radius of curvature squared (R_{c}^2) would cause a similar decrease in the contact angle with time. Instead, the contact angle remains fixed, and the square of the base radius (R^2) reduces linearly with time. From this point we will define the droplet base radius as the crucial parameter R, rather than the radius of curvature. To summarise, any freely receding spherical droplet (assuming it is drying in quiescent air and not on a heated substrate) will follow the D^2 law, but the definition of radius depends on whether it is an aerosol or sessile droplet.
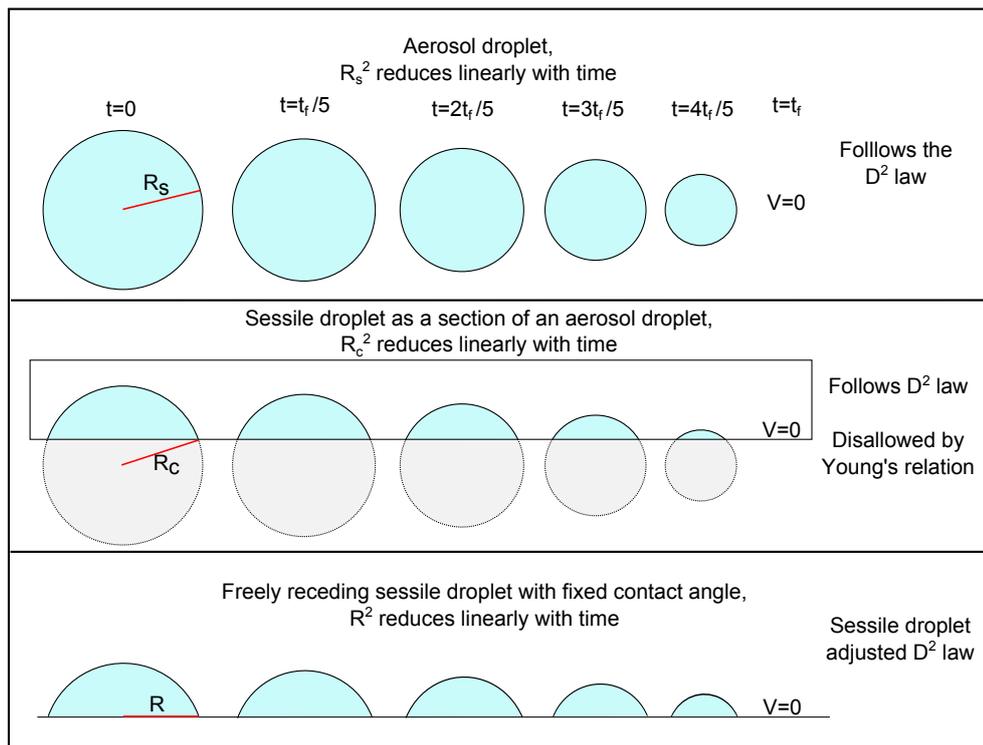
Figure 3.16: Comparison between a shrinking aerosol droplet, a sessile droplet pictured as a spherical cap section of an identically curved aerosol droplet, a freely receding sessile droplet which obeys Young's relation for a drop with zero hysteresis, with constant contact angle θ_c and linearly decreasing R^2 with time, and a pinned droplet, with a fixed base radius.

3.3.4   Evaporative Flux Profile

To further complicate the issue of a drying sessile droplet, when $\theta_c \neq 90°$ the local evaporation rate (j) profile over the surface of the sessile droplet varies with position, unlike with an aerosol droplet where evaporation rate is uniform. When we consider that we have already shown that the receding of sessile droplets follows the D^2 law, this may not seem important. However, a non-uniform evaporation rate will have profound implications for particle deposition and internal convection currents which will be discussed in sections 3.4 and 3.5.

To understand the evaporative flux profile profile over the surface of a sessile droplet, the convention is to compare with the equivalent electrostatic potential around a biconvex lens shaped conductor [1,89]. The biconvex shape being identical to the shape of a sessile droplet combined with its reflection. The electrostatic problem will not be discussed in great detail here, but essentially the electric field strength around the conductor diverges at the apex. In an evaporating droplet, the local evaporative flux follows the same divergence towards the contact line, as shown in Fig.3.17, despite not actually having a turning point due to the presence of the substrate. The evaporative flux profile along the surface of the droplet
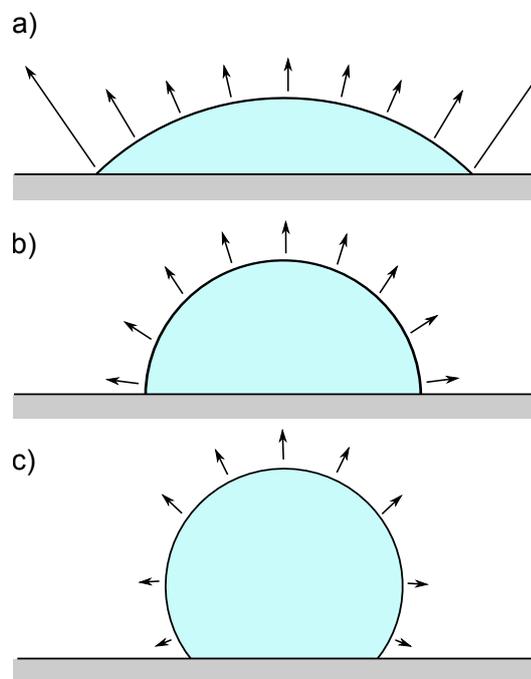

Figure 3.17: Diagram of the evaporative flux profile over the surface of a drop for when a) $\theta_c < 90°$, b) $\theta_c = 90°$ and c) $\theta_c > 90°$

close to the droplet perimeter is given by [85]:

$$j(r) \propto (R - r)^{-\lambda_\theta} \qquad \text{where} \qquad \lambda_\theta = \frac{\pi - 2\theta_c}{2\pi - 2\theta_c} \qquad (3.16)$$

In a droplet with a 90° contact angle, every point along the surface (r) will be equidistant from the centre of the droplet $(r \equiv R)$, giving a uniform evaporation rate profile. This can also be understood as the combined droplet and its reflection is now a perfect sphere, with aerosol evaporative flux profile. However, lowering the contact angle will increase the divergence, as shown in Fig.3.17.

Fig.3.18 shows the evaporative flux profile close to the contact line plotted against surface position r relative to droplet radius R for various values of θ_c between 10 and 90°. Additionally, when $\theta_c > 90°$ the local evaporation rate will be at
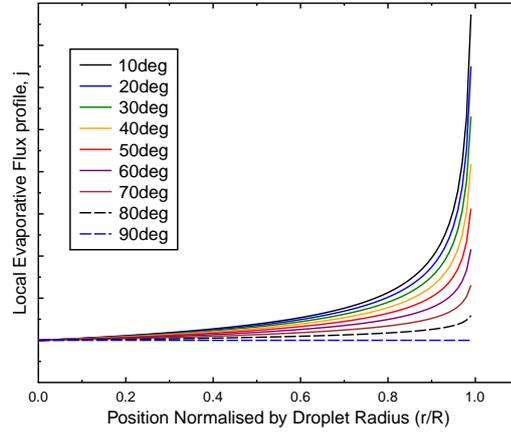
Figure 3.18: Evaporative flux profile over the surface of a sessile droplet against position r for various values of θ_c between 10° and 90°

a minimum at the contact line. This is easy to visualize as the vapour escape trajectory at the contact line will be hindered by the substrate when $\theta > 90°$, as shown in Fig.3.17 c).

In a drying pinned droplet where the contact line is fixed, and θ_c and droplet height h reduce with time, we might expect the evaporation rate would increase as the radius of curvature increases. However, the combined effects of reducing surface area and diverging local evaporative flux results in the evaporation rate simply scaling with droplet base radius R [85]:

$$-\dot{V} \propto R \qquad (3.17)$$

We should note however that this theory cannot take into account the very late stages of drying as θ_c approaches zero, in which evaporation profiles would transition from droplet to thin film behaviour.

3.3.5   Wettability and Drying

To further complicate the issue, Shin et. al. [90] have shown that the pinning forces in a drying droplet of water are highly dependent on the hydrophobicity of the surface. By observing 5 μl water droplets for the duration of drying on glass (hydrophilic), octadecyltrichlorosilane (OTS) (hydrophobic), and alkylketene dimmer (AKD) (superhydrophobic) they found 3 different drying regimes summarised in Fig.3.20 and 3.19:
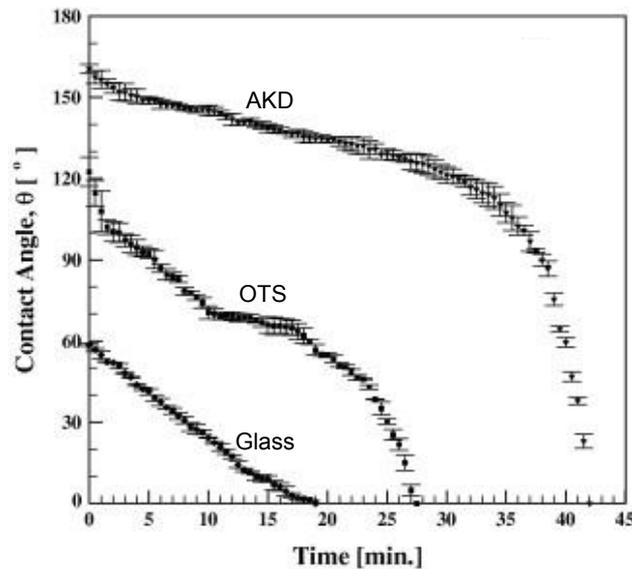
Figure 3.19: Plot of contact angle against time for equal volume water droplets on hydrophilic, hydrophobic and superhydrophobic surfaces. Figure taken from publication by Shin et. al. [90].

- Hydrophilic surface ($\theta_c(t = 0) = 58.6 \pm 0.6°$) - Droplet remains pinned for majority of drying time. Contact angle decreases linearly for the total duration of drying, and takes $\approx$ 19 minutes to fully dry. In the late stages where θ_c approaches zero, dR/dt accelerates very quickly and R drops from $\approx$ 70% of its initial value to zero in the final 5% of the total drying time.
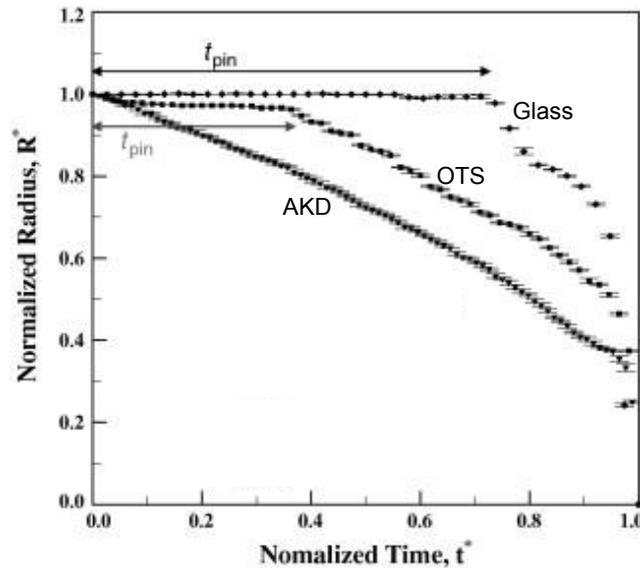
Figure 3.20: Plot of droplet radius normalised by its initial value against time normalised by total drying time for equal volume water droplets on hydrophilic, hydrophobic and superhydrophobic surfaces. Figure taken from publication by Shin et. al. [90].

This is explained by the evaporation no longer following droplet behaviour, but as that of a thin film.

- Hydrophobic surface ($\theta_c(t = 0) = 122 \pm 5°$) - Droplet remains pinned for only 40% of total lifetime. After this point droplet radius decreases linearly until the very late stages of drying, where much like on glass it accelerates and R very quickly drops to zero, in a total drying time of ≈ 27.5 minutes. Interestingly, there seems to be an intermediate stage in the contact angle. θ_c reduces linearly during the pinned stage, then levels off for almost a third of total drying time, and then begins to reduce again, all occurring during the linear reduction in radius with time.

- Superhydrophobic surface ($\theta_c(t = 0) = 161 \pm 2°$) - Droplet is completely unpinned for total drying time, radius decreases linearly until the very late stages, and takes a total of ≈ 42 minutes to dry. No intermediate stage in contact angle is observed here. Contact angle simply slowly reduces linearly until it reaches $\approx 110°$, and then rapidly drops off.

Perhaps the three most important observations in this paper are that in the late stages of drying there is a transition from droplet to thin film behaviour, the

radius decreases linearly in contrast with Cazabat's earlier predictions of a linear decrease in R^2 with time [85], and the total drying time for same volume droplets increases with hydrophobicity, as predicted from the proportionality between $\dot{V}$ and R. This same effect has also been observed fo+r droplets of ethanol on surfaces with varying degrees of hydrophobicity, in which M. Shanahan and K. Sefiane found that by increasing either the wetting or the pinning properties of the substrate, the lifetime of the droplet is reduced [91]. This has possible applications in cooling devices, as faster evaporation will lead to faster evaporative cooling [88].

3.4   The Coffee Ring Effect

We have seen that the evaporation rate profile over the surface of a sessile droplet is often non-uniform. We have also seen that droplets can display strong pinning forces, allowing for a fixed contact line and constant R during evaporation. Let us consider the case where $\theta_c < 90°$, and the evaporation rate is greatest at the perimeter. In the absence of pinning or internal flows, logically this would lead to a layer of liquid removed from the surface of the droplet as shown in Fig.3.21. The droplet would recede inwards with a linear decrease in R^2 with time. Now let us pin the droplet and fix the radius. In order to maintain the contact line and prevent shrinkage, liquid must flow radially outwards to replenish solvent loss at the perimeter as shown in Fig.3.21, with an average speed of replenishing flow proportional to the local evaporative flux j at the perimeter [1]. This means that two factors lead to outward radial flow: a pinned contact line and enhanced evaporation at the perimeter. While only the former case - a pinned contact line - is necessary for outward radial flow, this flow is enhanced by the higher evaporative flux at the contact line. Despite the outward flow, surface tension dictates that the droplet cannot alter its spherical cap shape, and so the droplet appears to simply lose height. If we now add suspended particles to the droplet, this outward replenishing flow will drag the particles radially outwards and deposit them at the perimeter of the droplet. This is most commonly observed in everyday life when a droplet of coffee is spilled on a surface and dries into the tell-tale coffee ring stain, as shown in Fig.3.22. Deegan et. al. [1, 79, 87] have studied this in depth and have evaluated the build up of particles into this ring with time. They showed that while at early times the mass of the disk builds up
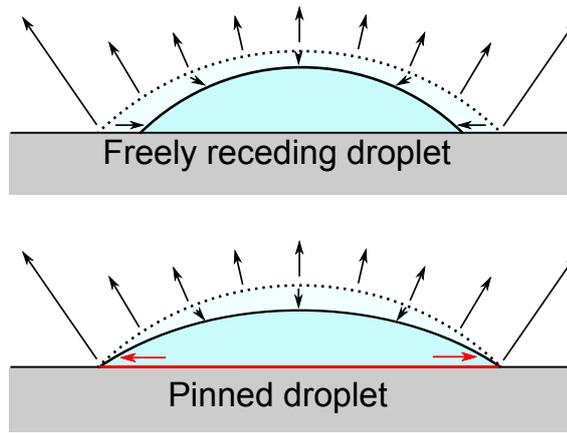
Figure 3.21: Pinned contact line induces outward radial flow (red arrow) to replenish solvent loss at the perimeter.

as a power law:

$$m_d \propto t^{2/(1+\lambda)} \tag{3.18}$$

where λ_θ is a function of the contact angle as shown in equation 3.16, at late times when the droplet height approaches zero, small changes in θ_c have negligible effect on λ_θ, and the growth rate of the ring is expected to diverge and lead to 100% of remaining solute to be very quickly deposited at the perimeter [87].

Evidence for these two growth rate timescales of the coffee-ring has been found by using a scanning electron microscope (SEM) to observe the small scale ($\approx 50\mu$m) ordering of the microspheres after drying. Marín et. al. [2] demonstrated a sharp order to disorder transition in the ring-stain (experiments performed with 3μl droplets, 0.5-2μm diameter red-fluorescent spheres). From the outermost edge of the ring toward the centre, a hexagonal to square to hexagonal packing trend was repeatedly observed. However, after this second hexagonal crystalline structuring, the arrangement very quickly becomes extremely disordered over a range $\approx 3\times$ the length scale of the ordered phase as shown in Fig.3.23. To explain this, Marín proposed a late stage "rush-hour" effect, in which as the height of the droplet approaches zero, radial flow diverges and packs the particles at the contact line too quickly for ordering to take place, while at early times, flow to the contact line is sufficiently slow to allow for crystallisation, thus supporting the theoretical predictions by Deegan et. al. of the coffee-ring growth rates.

Additionally, Riegel et. al. [92] showed that by imaging the diffusion of microspheres in sealed (non-evaporating) and open (evaporating) microarrays, an
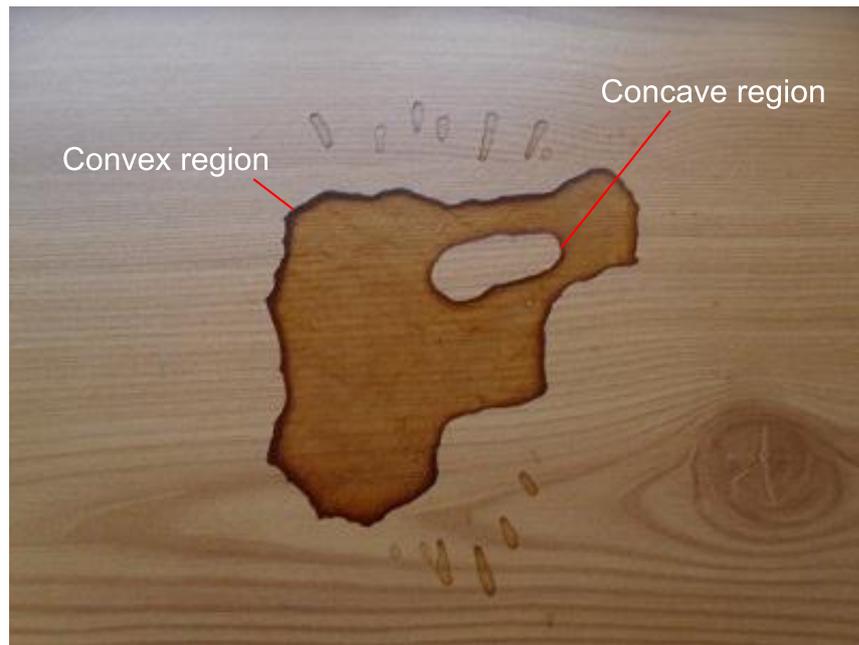
Figure 3.22: Example of the ring-stains left by drying coffee. Majority of suspended coffee grains are deposited at the edge of the solution during evaporation. Convex perimeter regions have a higher coffee grain concentration than concave regions.

outward radial velocity component can be extracted from the particle trajectories. Indeed, when the droplet is not allowed to evaporate, particles are no longer swept to the droplet perimeter.

Further aspects of the coffee-ring effect which should be mentioned include

- Anchoring of the contact line. The enhanced pinning caused by suspended particles appears to be the result of the coffee ring effect. The build up of particles at the contact line results in an additional energy barrier the contact line must cross in order to recede, effectively fixing the droplet radius at R_0. Indeed, it has been shown that a single microsphere attached to the surface is sufficient to increase the pinning of the contact line [93]. Late stage dewetting only occurs when remaining liquid surrounded by the solute ring reduces in height to a thin puddle. Assuming all particles have not already been swept to the droplet perimeter, small narrow ring-stain structures can form within the central region of the droplet. Dry nucleation sites appear along the inner edge of the ring, and spread into a visible "hole" in the liquid. This hole continues to spread due to surface tension forces appearing at this newly formed contact line. However, after a short time,

Droplet perimeter   Centre ⟶
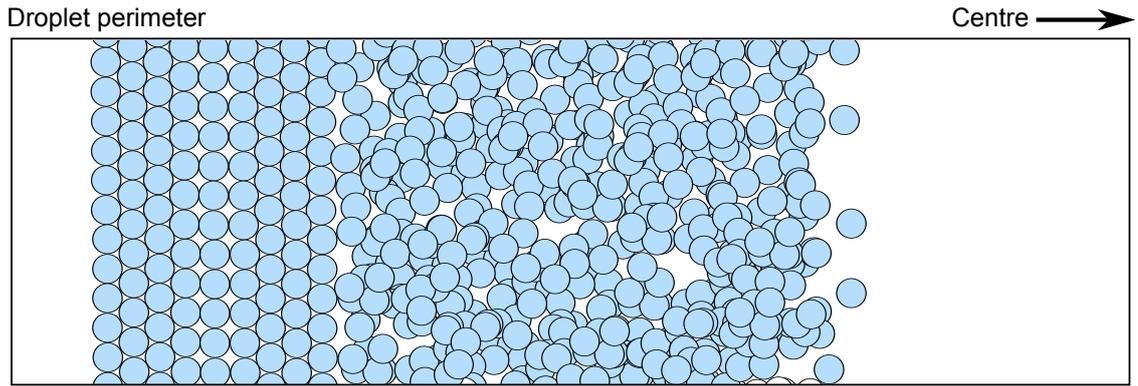
Figure 3.23: Diagram of ordering of microspheres in ring-stain. Clear order-disorder transition found supporting a late stage "rush-hour" effect.

due to enhanced evaporation at this new contact line, particles can begin to accumulate at the hole perimeter and halt its advancement [79] as shown in Fig.3.24. This occurs at multiple sites until the droplet is fully dried, leaving a thick ring deposit around the perimeter of the initial droplet, enclosing many smaller narrower ring structures. This phenomena was been observed with droplets of 2% volume fraction polystyrene microspheres [79], and shows an alternative late stage drying behaviour to that observed in the "rush-hour" effect.

- Non-uniform coffee-ring thickness in non-circular droplets. Fig.3.22 shows an example of a droplet with both convex and concave regions at the perimeter. Following the previous argument of the random walk of water molecules as the driving mechanism behind variation in the local evaporative flux, the concave regions would be expected to dry more slowly and convex more quickly. The final deposit does indeed support this theory, being thickest in the convex regions and thinnest in the concave [1].

- Coffee ring thickness w_d scales with initial volume fraction ϕ [94]:

$$w_\mathrm{d} \propto \phi^{0.67 \pm 0.05} \tag{3.19}$$
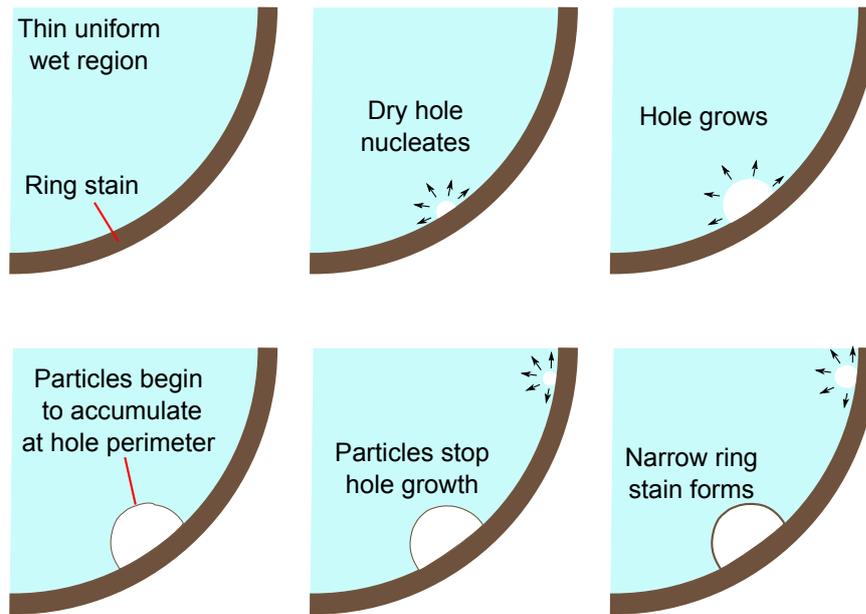
Figure 3.24: Dry holes nucleate in the late stage of drying leading to the formation of multiple narrow coffee-ring type stains in the centre of the droplet.

3.4.1   Limits of The Coffee-Ring Effect

Theoretically there may be constraints on the size of the microspheres that will display the coffee-ring effect. The upper size limit will be controlled by sedimentation time, while the lower limit controlled by diffusion effects.

Clearly, in order for all the suspended particles to be dragged to the contact line, the time required for a single particle to migrate from the centre to the perimeter of the droplet (distance R) must be less than the time required for a particle to sediment and become stuck in place on the substrate. Sedimentation is a gravitation effect, with the crucial parameter being a factor called the "gravitational length" L_g, which is a ratio of the relative effects of random motion induced by thermal energy, and the downward pull of gravity [95]. Clearly a large mass will be pulled down by gravity more strongly and sediment quickly, whereas a small mass will be governed mostly by thermal effects. However, because only one of these effects is directional, effects of gravity can never be completely cancelled out, instead we find a concentration profile of particles with respect to height h:

$$\phi(h) = \phi(h = 0)\exp\left[\frac{-h}{L_g}\right] \qquad (3.20)$$

where:

$$L_{\mathrm{g}} = \frac{k_B T}{mg} \tag{3.21}$$

When the height difference is equal to the gravitational length, the particle concentration decays to e^{-1} (~ 0.36) its initial value. In the atmosphere, air molecules are small enough that this decay is on the order of the thickness of the atmosphere, which is why we don't have to crawl around on the floor in order to breathe! A bag of footballs however have a much higher mass per "particle" and therefore this length is tiny, and the balls will all fall, or sediment, very quickly to the bottom of the bag. Colloidal particles however often span the mass range in which we see a transition between these behaviours. The important factor again is the gravitational length, which if it is much larger than the size of a droplet, means that sedimentation effects are negligible, whereas if this length is very small compared to the size of the droplet, sedimentation can become, but only if the sedimentation time is shorter than the lifetime of the droplet. This is important as we would expect a large particle which feels the downward pull of gravity very strongly would be less affected by the outward replenishing flow of the coffee-ring effect, and in a slowly evaporating droplet, smaller particles have more time to sediment to the substrate. Therefore there should exist a maximum sphere size limit on the coffee ring effect for a given evaporation rate. For example, a 10nm diameter particle suspended in water at room temperature, assuming it has the density of polystyrene (1.06 g/cm^3), $m = 5.6 \times 10^{-22}$ kg which gives a gravitational length of $L_{\mathrm{g}} \sim 76$ cm. Therefore it is pretty safe to assume concentration remains uniform over a sessile droplet. Whereas if we took this in reverse, a gravitation length scale of 0.5mm (a rough estimate of the minimum length scale required for sedimentation to become important in a droplet) would be found with a particle of 0.1 μm diameter. However this does not necessarily mean sedimentation will have time to occur, so we must now estimate the sedimentation velocity of such a particle by balancing the downward pull of gravity with the viscous drag of the fluid:

$$\frac{4}{3}\pi R_{\mathrm{S}}^3 \Delta\rho g = 6\pi\eta_{\mathrm{s}} R_{\mathrm{s}} v \tag{3.22}$$

where $\Delta\rho$ is the difference in density between the particle and fluid (which must be greater than zero or buoyancy effects will counter sedimentation) and v is the velocity of the particle, which is calculated as ~ 1.3 nm/s. So in a drop of water approximately 0.5 mm in height, the time required for all polystyrene particles to sediment would be approximately 4.4 days, which is well above the lifetime (~ 1

hour) of a typical water drop. Again, working in reverse, the particle diameter required for sedimentation to be complete within the 1 hour evaporation window is estimated as $\sim 2\mu$m. This of course also assumes no convective flow within the drop (which would tend to redistribute the particles and prevent sedimentation), which as we will see later from OCT imaging may not be a reasonable assumption to make.

Furthermore, the diffusion coefficient of these particles has not been taken into account. We would expect that diffusion effects would drive the particles to homogenize within the droplet, negating the effects of outward radial flow. The self diffusion coefficient of a sphere suspended in a liquid can be calculated from the Stokes-Einstein equation [96]:

$$D_\mathrm{s} = \frac{k_B T}{6\pi\eta_0 R_\mathrm{S}} \tag{3.23}$$

where η_0 is the solvent viscosity and R_S is the microsphere radius. Because the diffusion coefficient is inversely proportional to the sphere radius, we would expect a minimal size at which the random motion of the particle will be sufficiently fast to overcome any drag effects from the outward flow of the solvent. However, experimental results of drying droplets of nanoparticles are contradictory. While Askounis et. al. [97] used AFM to accurately measure the ring structure formed after drying droplets of TiO_2 nanoparticles suspended in ethanol, Shen et. al. found that reducing particle size below 60nm removes the coffee-ring effect [98](This is discussed in section 3.4.2). Furthermore, observations of drying salt solutions have yielded some interesting patterns including: ring-stain like deposits, fractal patterns, concentric rings, dendrites and single crystals [99]. To understand these patterns one must consider the effect of phase transitions. Up until now suspended particles have been inert and non-interacting with each other. However, when salt reaches its saturation concentration, it will precipitate in the form of highly ordered solid crystals. Because of the tiny sizes of salt molecules, it is difficult to image their motion during drying, and so determining whether the salt molecules are being dragged to the contact line via the coffee-ring effect, or if they simply crystallise here because of the enhanced evaporation rate is inconclusive. Either way, the result is that after sufficient solvent loss, salt crystallisation occurs at the droplet perimeter, which depending on the concentration and contact angle of the droplet once precipitation begins, leads to various different crystalline structures [99].

It has also been observed by Parisse and Allain that when drying a droplet of solution which has a very high concentration of nanosized colloidal silica particles ($c_0 = 24\%$ by volume, particle diameter = 15 nm), precipitation begins immediately after droplet deposition and the particles form a solid-like "gellled foot" around the perimeter of the droplet [8]. Despite the small size of these particles, the high initial concentration dampens diffusion effects, and therefore deposition occurs at the point of highest evaporation rate. This gelled foot behaves as a single growing solid structure, which as evaporation continues, shrinks, cracks, bends and unsticks from the substrate due to an increasing elastic modulus [100].

From an industrial point of view, the coffee-ring effect is a nuisance. In ink-jet printing for example, the outward flow in a drying droplet has the consequence of depositing the majority of ink into a small ring, rather than the desired uniform dot, thus lowering printing precision. A great deal of experimental research has been focused on suppressing the coffee-ring effect. Several lines of research which have found methods to successfully achieve this goal will be discussed here.

3.4.2 Supressing the Coffee-Ring Effect

Yunker et. al. discovered experimentally that by elongating the microspheres into ellipsoidal particles, the coffee-ring effect can be completely suppressed [3]. To understand this effect we must consider the effect the ellipsoid geometry has on the liquid-air interface. When a spherical particle encounters the liquid-air interface, it becomes trapped and deforms the interface [101] as shown in Fig.3.25. Typically, another distant particle can only interact with this trapped particle when it "feels" the interface deformation caused by the trapped particle [101,102], the stronger the deformation of the interface, the stronger the interaction. A spherical particle that comes into contact with a liquid interface becomes trapped, with a fixed contact angle as shown in Fig.3.25 (this assumes we ignore hysteresis effects). Because the particle is perfectly symmetrical, this would appear the same no matter what side it is viewed from. However, with ellipsoidal particles this is not the case. Again, the particle comes to rest at the liquid air interface. Now, because of the axis dependent curvatures (Fig.3.25 shows the two extremes), it is not possible to maintain a constant contact angle without deforming the interface. This deformation now results in an increase in the surface area of the

Spherical particle

No deformation of
liquid-air interface

Symmetry leads to a constant contact
angle with no liquid surface deformation

Deformation

y-axis   x-axis

Non-uniform particle curvature means liquid must deform
to maintain constant contact angle
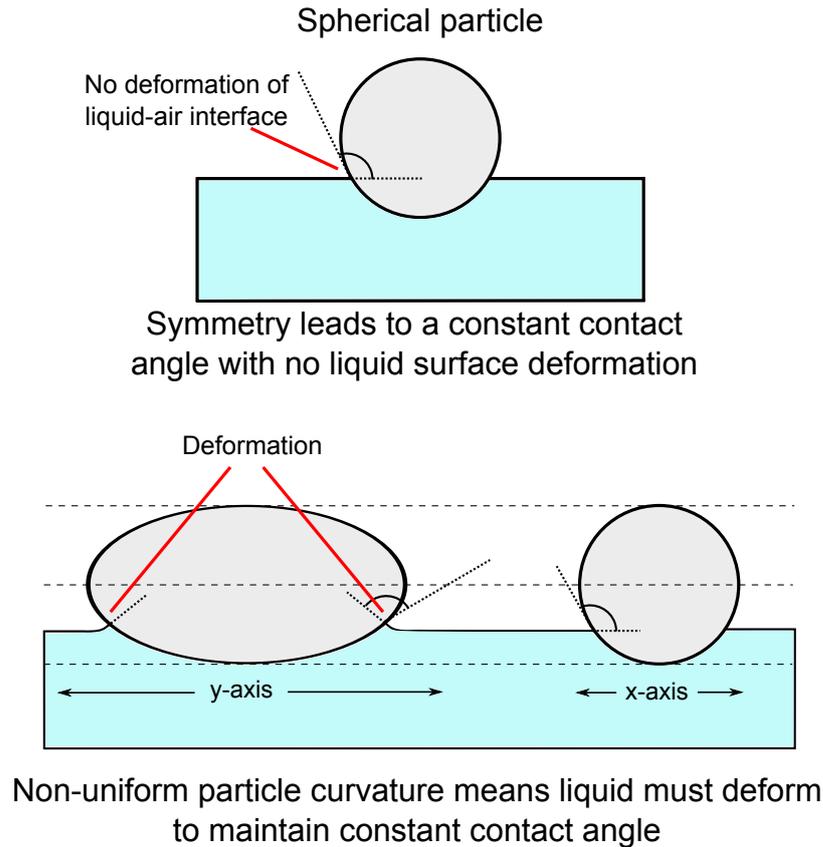
Figure 3.25: Diagram of air-water interface caused by the adsorption of a particle. Spherical particles deform the interface uniformly, whereas ellipsoidal particles cause a strong axis-dependent deformation [101].

interface, which surface tension forces would tend to minimize. This unfavourable increase in surface area results in long range capillary forces between ellipsoidal particles in order to minimize this deformation, and thus minimize the surface area [103]. This attractive force between ellipsoids at the interface leads to large loosely packed structures [3,104], which produces a surface viscosity greater than the bulk viscosity. These large structures resist the radial outward flow induced by the coffee-ring effect, and thus prevent the coffee-ring stain from forming, leading to a disordered uniform deposit. Further evidence that this suppression is caused by long range inter-particle attractions is through the addition of a surfactant. As observed by Yunker et. al. by introducing surfactants, this effect is reduced [3]. Surfactants reduce the surface tension, and thus reduce the energy required to deform the interface. This effectively removes the attractive forces between ellipsoids at the interface, and once again ellipsoids collect at the droplet perimeter via the coffee-ring effect.

As briefly mentioned previously, Shen et. al. showed that if relative humidity, contact angle and particle concentration are kept constant, there is both a minimum particle size and a minimum droplet volume, below which the coffee-ring effect does not occur [98]. Increasing relative humidity lowers the minimum droplet volume, and suggests that the limiting factor is the total drying time of the droplet. Indeed, the paper proposes two important time scales for determining whether a coffee-ring will form. The first of which being the total evaporation time (which we will define as t_0), the second being a time step required for two random particles to come into contact with each other ($t_{particle}$), a step they suggest is essential for the particles to form a monolayer at the base of the droplet and pin the contact line, which induces outward flow. If the contact angle is able to reach θ_R before the particles can collect together and pin the droplet, the contact line will recede and no coffee-ring can form. By analysing these two timescales in terms of: the total drying rate $-\dot{V}$; the initial and receding contact angle; the diffusive distance between two random particles L_m; and the self diffusion coefficient of the particles D_s, they found that the lower critical radius for coffee-ring stains follows:

$$R_c = -\dot{V}\frac{2L_m^2}{\pi^2(\theta_0 - \theta_R)D_s} \tag{3.24}$$

Interestingly, this predicts not only that reducing the evaporation rate through increasing humidity will reduce the minimum coffee-ring radius, but also that increasing the concentration and therefore decreasing L_m, will decrease the minimum radius. However, because $D_s \propto 1/R_p$ and $L_m \propto R_p$, this equation also predicts that the relation between the minimum droplet radius and the particle radius will go as $R_c \propto R_p^3$. This is in stark contrast to their experimental findings as they showed that with droplets of 20nm spherical particles, rather than the typical coffee-ring structure, a uniform "pancake" deposit was observed. This possibly suggests that the increase of the diffusion coefficient of the particles with decreasing radius plays a much more significant role in suppressing the coffee-ring stain than this prediction can account for.

Hydrophobicity has also been shown to play an important role in particle deposition. Uno et. al [105] observed the evaporation rate of water droplets with dispersed latex microspheres on hydrophobic and hydrophilic surfaces. Their findings in droplet radius and contact angle with time agreed very well with earlier results of pure water droplets discussed in section 3.3.5, in which on hydrophilic

surfaces the contact line remained fixed, whereas on hydrophobic surfaces the contact line was able to depin and recede. This led to the particles accumulating at the droplet perimeter in the hydrophilic case, but not in the hydrophobic case. Instead the particles remains dispersed until a critical concentration was reached, at which point they began to accumulate together into large aggregates. These aggregates then either sedimented, or adsorbed to the water-air interface, leaving small localised clumps of particles after drying.

Another method for removing the coffee-ring effect was by removing droplet pinning through electrowetting. Eral et. al. [106] showed that by by applying AC voltage across a conducting substrate, and varying the frequency, the wetting properties of the liquid become dynamic. Provided that the electrowetting force that drives the movement of the contact line is greater than the pinning force, the contact line would be constantly in motion matching the frequency of the alternating voltage. This effectively removed outward radial flow, resulting in the suspended particles depositing only at the very late stages of drying in a small localised area at the centre of the droplet.

Finally, it has also been shown that for coffee-stains to form, Marangoni effects *must* be suppressed [9]. The origin and complications that arise due to Marangoni flows is complex, and will be discussed in much detail in section 3.5.2.

3.5 Convection Currents

The importance of internal convection currents in drying droplets on the particle deposition patterns is becoming increasingly apparent. Surface tension, temperature and density gradients will invariably cause instabilities within a droplet, which often lead to circulatory flows that can negate the coffee-ring effect. Observations of density and surface tension driven instability flows go back almost 200 years, with the commonly observed Rayleigh-Bénard convection (or Bénard cells) in a heated pot of fluid [107], and Marangoni flows in a glass of wine [108].

3.5.1 Rayleigh-Bénard Cells

Rayleigh-Bénard convection is a type of buoyancy driven flow that occurs in a thick horizontal layer of fluid that is heated from below. This is most commonly observed when heating up a pan of soup. As heat is input from below, and the temperature increases, the density of the liquid at the base of the pan is reduced. This leads to an instability as a less dense material at the base of a liquid will be displaced upward by the more highly dense layer of liquid above due to buoyancy effects. This can be understood simply in terms of gravity pulling downward on the denser materials more strongly, thus displacing the less dense objects in the opposite direction. As the less dense liquid at the base rises and more dense liquid at the top sinks, the constant application of heat from below will continually reverse the direction of the sinking liquid. This very quickly sets up metastable convection cells as shown in Fig.3.26.
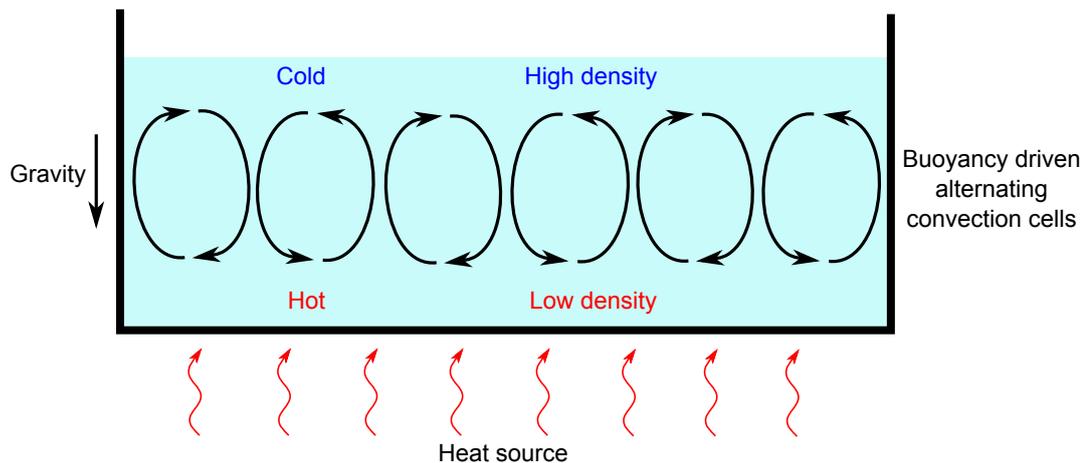

Figure 3.26: Diagram of Bénard cells in a thick layer of fluid heated at the base

In fact, if the temperature gradient is too small it may not be sufficient to set Bénard cells in motion. Viscous damping forces will resist this flow, as convection cells induce shear gradients (the velocity of fluid fluid around the perimeter of a cell is higher than at the centre). In order for a density gradient to induce a Bénard cell, its effect must overcome that of viscous damping. The transition between which effect is dominant is characterized by the dimensionless Rayleigh number, Ra, which in the case of a horizontal plane of liquid with thickness L is

given by:

$$Ra = \frac{\rho^2 g \beta c_{\mathrm{p}}}{k \eta_{\mathrm{D}}} (T_{\mathrm{t}} - T_{\mathrm{b}}) L^3 \qquad (3.25)$$

where: β is the thermal expansion coefficient, which is a measure of the substances tendency to change in volume in response to a change in temperature; η_{D} is the dynamic viscosity; k is the thermal conductivity; ρ is the average density; c_{p} is the specific heat capacity; and T_{t} and T_{b} are the respective temperatures at the top and bottom of the liquid layer [107]. This type of instability has been shown to only occur in thick layers of liquid, whereas in thin films, a typical example being hot oil in a pan, a similar surface tension gradient (Marangoni) driven instability is the result [109]. As this is the subject of the next section, it is important be be clear that both instabilities can occur in heated liquid films, which is often why these two terms are coined together into Bénard-Marangoni convection.

To further complicate the matter however, in solvent-solute mixtures, the density gradient will be enhanced due to evaporation. Firstly, evaporative cooling will reduce the temperature and thus increase the density at the surface, and secondly, solvent loss will increase the solute concentration at the interface and, assuming the solute is more dense than the solvent, as is usually the case, will increase the density of the solution further. To account for the possibility of buoyancy driven instabilities in an evaporating solution, it may be more useful to have a term which includes a density gradient as a function of both temperature and concentration.¶

3.5.2 The Marangoni Effect

Unlike Rayleigh instabilities driven by density gradients, the Marangoni effect is a surface tension gradient driven flow, the first recorded case of which being Thomson's observations of tears of wine [108], which he proposed to be an outcome of the evaporation of wine which contains two solvents (water and ethanol), each with differing vapour pressures and surface tensions. To fully understand the mechanism that drives this particular case we must have a through understanding of the competing vapour pressures of solvent mixtures, which will be

---

¶Non-planar fluid systems have not been discussed here. The effects of the Rayleigh number in a spherical cap drying drop would become even less clear due to the curved surface and non-uniform depth profile.

discussed in depth in section 3.6.1, but for now I will give a simplified description of the process.

First, two quantities must be known for both water and ethanol: the surface tension (γ_w and γ_e) and the vapour pressure, which is a measure of the volatility of a given fluid. At a given temperature, two equally sized droplets of ethanol and water will evaporate at differing rates depending on the relative vapour pressures. High vapour pressure leads to fast evaporation, low vapour pressure leads to slow evaporation. The relationship between the change in vapour pressure and temperature is given by the Clausius Clapeyron equation:

$$ln\left(\frac{P_1}{P_2}\right) = \frac{\Delta H_{\text{vap}}}{R}\left(\frac{1}{T_1} - \frac{1}{T_2}\right)$$
(3.26)

where P_1 is a known vapour pressure at given initial temperature T_1, P_2 is the value of vapour pressure after altering the temperature to T_2, ΔH_{vap} is the heat of vaporisation and R is the ideal gas constant. From this we can see that when $T_2 > T_1$, $P_2 > P_1$.

As a general trend, because thermal energy and therefore vapour pressure increases with temperature, and at boiling point the vapour pressure is exactly equal to ambient pressure ($P \approx 1$ bar), the vapor pressure of a liquid at ambient temperatures will be higher for a liquid with a lower boiling point. With the boiling points of water and ethanol being 100° and 78.4°C respectively, we would expect ethanol to dry faster. Indeed, the room temperature (20°C) vapour pressures of water and ethanol are 0.023 and 0.0583 bar respectively, giving ethanol a faster evaporation rate.

The azeotrope of a solvent mixture is the point at which the mass fractions of the two solvents are balanced in such a way that the ratio does not change despite the differing evaporation rates. Put simply, as ethanol evaporates faster than water, the droplet must have a higher fraction of ethanol than water in order to maintain a constant water:ethanol ratio. The azeotrope of ethanol and water is 95.5% ethanol and 4.5% water by mass [110], therefore with wine, which has a much lower ethanol fraction ($\approx 8\%$ by mass), the ratio of water:ethanol will shift in favour of water with time.

The tears of wine phenomena is explained as follows: water has a higher surface tension than ethanol (at $T = 20\pm0.1$°C, γ_w and $\gamma_e = 72.86$ and 22.39 mN/m $\pm0.4\%$ [111]), therefore as the liquid evaporates and the relative water content at

the interface increases, the surface tension will also increase, while in the bulk it remains unaltered, leading to a surface tension *gradient*. This in turn leads to the region of low ethanol content at the surface pulling itself away from the region of high ethanol content. This pull causes a film of fluid to climb away from the bulk of the wine up the side of the glass, and will continue to climb until the weight of fluid is sufficient that gravity pulls it back down in the the distinctive teardrop shapes as shown in Fig.3.27.
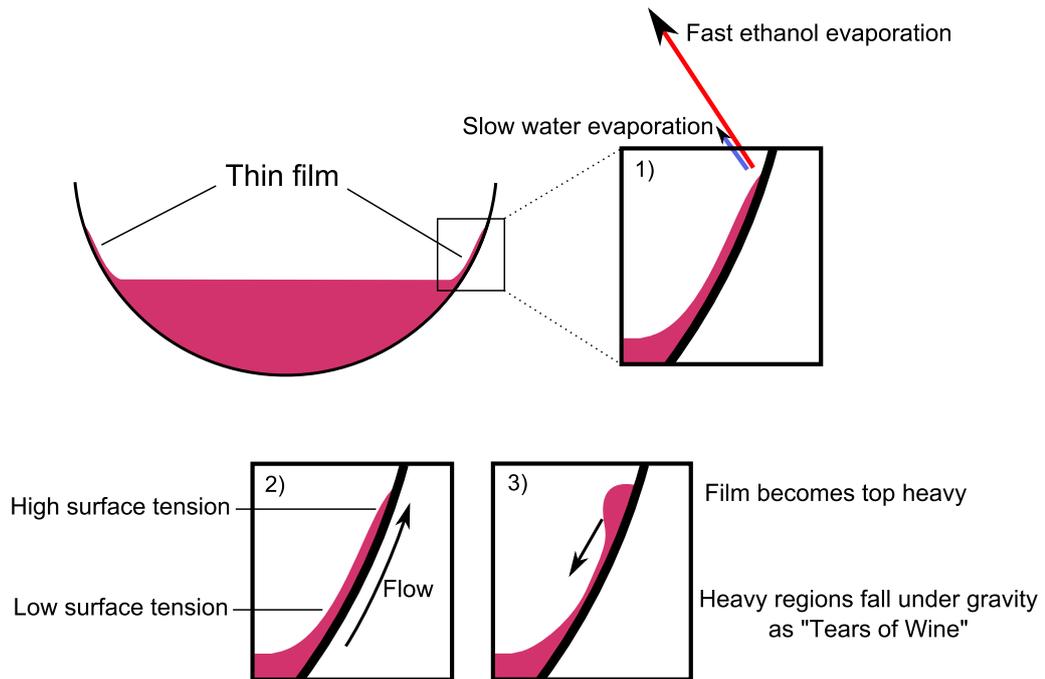

Figure 3.27: Diagram of the "Tears of Wine" effect induced by Marangoni stresses in an evaporating glass of wine.

This Marangoni effect can also be easily demonstrated by depositing a drop of high ethanol content (vodka for example) onto a thin film of water. The two liquids are completely miscible, so they readily mix. However the high surface tension perimeter of the thin film quickly pulls itself away from the low surface tension ethanol region, leaving a gap where the alcohol was deposited. This outward pulling stops when the two solvents are completely mixed and no surface tension gradient remains.

3.5.3 Marangoni Convection in Drying Droplets

As briefly mentioned earlier, Hu et. al. [9] proposed that Marangoni effects must be suppressed in order for coffee-ring stains to form. This conclusion was made based on observations of drying droplets of fluorescent PMMA particles in two different solvents: water and octane. They discovered that particles suspended in octane flow around the droplets following clear convection currents, circulating in a downward direction in the centre of the droplet and upward along the interface, as shown in Fig.3.28.
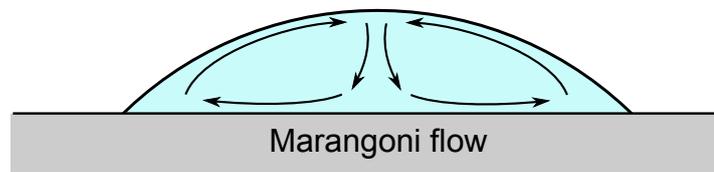

Figure 3.28: Diagram of Marangoni stress induced convection currents in a drying droplet of octane [9]

.

They propose that these flows are induced by the evaporative cooling effects at the interface. The evaporation leads to a temperature profile within the droplet, with lowest temperature at the droplet peak. As discussed earlier, the Eötvös rule predicts that a decrease in temperature would result in an increase in surface tension. This surface tension gradient then exerts an upward pull on the outer layer of liquid, resulting in a Marangoni driven flow up along the surface. This flow then sweeps the particles up along the interface and deposits them preferentially in the centre, leading to a large clump of particles in the middle of a flat uniform fully dried deposit. By comparing this with the known ring-stain forming water droplets, which with the same particle tracking method they observed to have very weak convection currents, they conclude that Marangoni flows must suppress the coffee-ring effect. However, their numerical calculations predict that a drying droplet of water should also have a sufficient temperature decrease at the interface to induce Marangoni flows. The explanation they propose for the lack of agreement between theory and observations is that water is highly soluble to contaminants, and as little as 300 contaminant molecules per μm^2 is sufficient to lower the surface tension to a value at which Marangoni flows would not be expected [112–114]. They do not suggest the origin of these contaminants, or a

method to eliminate their effects.

The difficulty with understanding the effects of evaporation on temperature changes in a drying droplet is that not only must we take into account a non-uniform evaporation rate profile (which would logically lead to a non-uniform temperature profile), but we must also consider the thermal conductivity of both the liquid and the substrate, and the size of the droplet. Cazabat proposes that temperature gradients in a slowly evaporating droplet will equilibrate very quickly on a highly heat conducting substrate, whereas volatile droplets on a surface with low conductivity will very quickly develop a temperature gradient, with lowest temperature at the peak [85]. Hu and Larson used numerical modelling and analytical calculations to show that assuming the droplet and substrate are at room temperature before deposition, and the conductivity and thickness of the substrate are greater than the respective conductivity and height of the droplet, a temperature gradient should develop in an evaporating droplet of water on a glass substrate with a temperature difference of $\approx 0.02°$C between base and peak with a droplet [112]. This small temperature gradient is too small for current infra-red imaging techniques to observe, which has a precision of $\approx 0.1°$ [115]. They also conclude that as the droplet dries and reduces in size, the relative thickness of the droplet compared to the substrate would shrink, and temperature gradients should reduce. Therefore Marangoni flows should be more significant in a droplet with a high initial contact angle. Similar results were found in simulations by Girard et. al. in small heated water droplets [116], however neither approaches accounted for non-uniform evaporation rate profiles. Clearly, if a droplet evaporates from the contact line faster than at the peak, evaporative cooling would be greatest at the perimeter. It would seem that in order to to progress further with our understanding of cooling effects in a drying droplet and the resulting Marangoni flows, we must either account for non-uniform evaporation rates in simulations, or observe experimentally the temperature gradients that develop inside an evaporating droplet with greater precision than current Infra-red imaging techniques allow.

3.6   Evaporating Binary mixtures

3.6.1   Azeotropes

Let us consider a mixture of two solvents A and B. In an ideal system, the evaporation rate would simply decrease linearly as the fraction of the more volatile component is decreased. A liquid which follows this behaviour obeys Raoult's law [117]:

$$P_{\text{total}} = P_A c_A + P_B c_B \tag{3.27}$$

where P_A, P_B, c_A and c_B are the respective vapour pressures and mass fractions of solvents A and B. In this type of mixture the adhesive forces acting between different molecules is equal to the cohesive forces between identical molecules.

Azeotropes, which as mentioned previously are the mixture compositions at which the combined different evaporation rates and volume fractions lead to a concentration that does not change with time, exist when the liquid deviates from Raoult's law. Taking ethanol and water for example, water and ethanol both have a stronger cohesive force than the adhesive force between water and ethanol, which results in the molecules being more readily available to escape the mixed liquid phase and into the vapour phase than they would be individually. This is known as a positive deviation from Raoult's law. Negative deviations also exist in the case where adhesion is greater than cohesion, and multiple azeotropes can exist for solutions of three or more solvents or in solutions that are not completely miscible, but these will not be discussed further.

Fig.3.29 is an exaggerated plot of the vapour pressure with concentration of a solvent mixture that follows a positive deviation from Raoult's law. Note that there is a region in the plot (shaded) in which the vapour pressure is greater than the vapour pressures of the individual pure components. This means that the boiling point of the mixture will be lower at a certain ratio than either of the pure solvents respective boiling points. The point at which the boiling point reaches a minimum is the azeotropic point (for ethanol and water, the respective boiling points are 78.4 and 100°C, with an azeotropic boiling point of 78.1°C [117]). Fig.3.30 is an exaggerated plot of the boiling point of ethanol-water against concentration by mass. Also plotted is the vapour composition that a given mixture will give off as it evaporates.
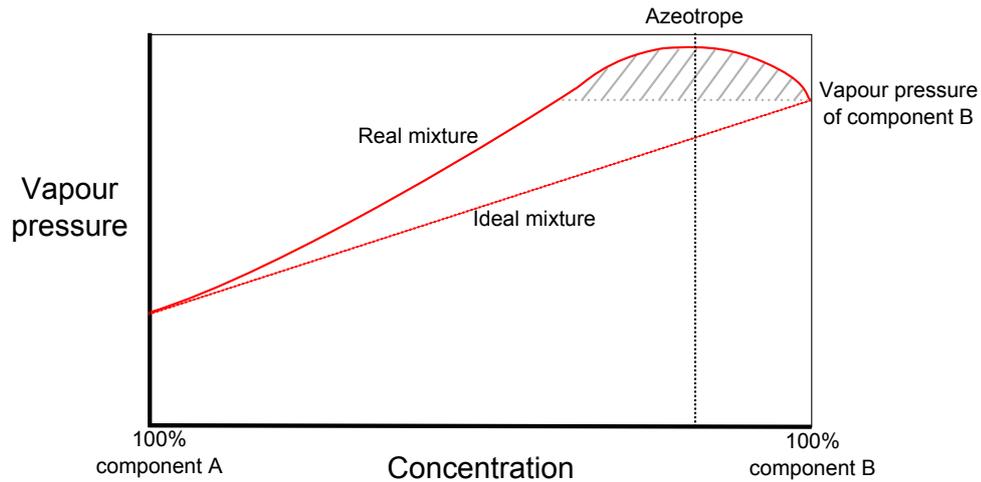
Figure 3.29: Diagram of vapour pressure with concentration for a mixture of two solvents with a positive deviation from Raoult's law. Shaded region represents concentration at which the vapour pressure, and therefore evaporation rate, is higher than both the constituent vapour pressures

Typically, this property of water-ethanol mixtures is utilized for the dehydration of water through distillation. By boiling a given mixture that has an ethanol mass fraction below the azeotropic point, it will give off a vapour that has a higher ethanol concentration than the original liquid, as shown by the dotted lines in Fig.3.30. Then this higher ethanol concentration vapour is condensed back into a liquid in a separate chamber, and reboiled. This process is repeated until the vapour reaches the azeotropic concentration of 95.6% ethanol by mass. At this point, the ratio will not change with further boiling and ethanol purification can not continue. We must note here that during successive boilings, the vapour is removed from the system.

What is not considered here is the liquid left behind after evaporation, which is most useful when considering evaporating droplets. If we consider a steadily evaporating solution, one in which the vapour that is given off is removed from the system the system, if the initial concentration of ethanol is below the azeotropic point, the ethanol content in the droplet will progressively decrease as shown in Fig.3.31. The vapour this mixture gives off will also progressively decrease in ethanol concentration until all ethanol is lost to the vapour phase and the remaining liquid is 100% water. Similarly, a mixture with a concentration above the azeotropic point will move in the opposite direction, with water content decreasing with time until only pure ethanol is left. If we ignore the evaporation
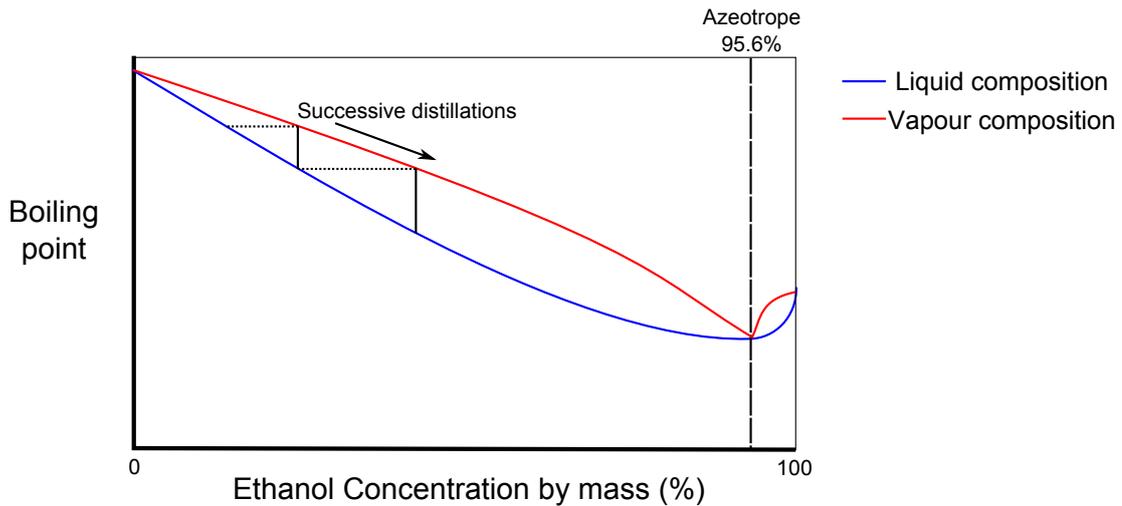
Figure 3.30: Exaggerated plot of the boiling point of water-ethanol mixtures against concentration. Dotted lines show the corresponding vapour concentration a given liquid concentration will evaporate. Successive distillations allow one to collect the higher concentration vapour, and progressively increase the concentration up until the azeotropic point.

rate and plot the ethanol concentration as a function of the change in mass, the evolution of the solution concentration from start to finish for various initial concentrations is plotted in Fig.3.32. It is also assumed here that the solution is always in equilibrium with the vapour, and the solution remains homogeneous. This type of plot would not be a very accurate description of the concentration evolution of a drying droplet for example as evaporation rate varies with concentration, the diffusion of the vapour into the atmosphere has not been considered, and as we will see in the next section, a completely homogeneous solution may not be a fair assumption to make.

3.6.2   Water and Ethanol

We have already discussed the Marangoni effect that is induced through evaporation from large volumes of water and ethanol mixtures, but what of a drying droplet? Sefiane et. al. explored the wetting behaviour of water-ethanol mixtures, and showed that the initial contact angle of a binary mixture droplet has a non-linear dependence on the concentration of both components [118]. On a rough PTFE surface, water and ethanol have $\approx 90°$ and $30°$ contact angles re-
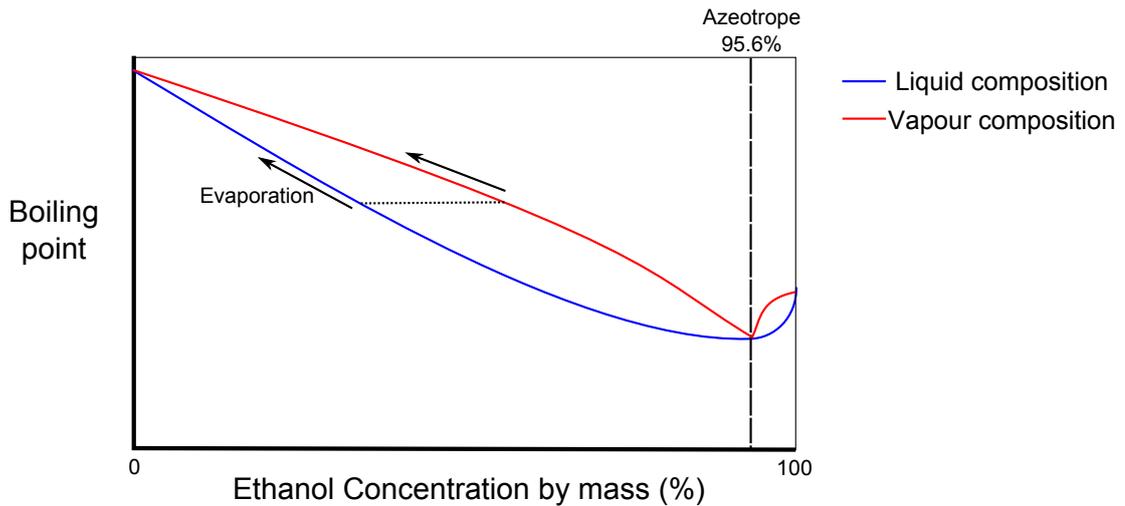
Figure 3.31: Exaggerated plot of the boiling point of water-ethanol mixtures against concentration. Dotted lines show the corresponding vapour concentration a given liquid concentration will evaporate. Progressive evaporation decreases both the ethanol content in the droplet and the ethanol content in the vapour given off by the liquid.

spectively, however a 50:50 mix does not have a contact angle that lies directly half way between, but rather at 42°, much closer to the initial contact angle of pure ethanol. This could be due to ethanol dominating the surface properties at early times, or could be simply due to the complication which arises due to altering the two components (γ_L and γ_{SL}) in Young's equation.

After observing evaporation of droplets with various water-ethanol ratios, they found some interesting results. Firstly, after normalising volume, radius and contact angle with their initial values (V_0, A_0 & θ_0) and time with total drying time (t_0) (thus removing the effects of wetting and volatility), the behaviour of the pure solvents collapsed onto identical curves. However, with mixtures of the two solvents, the evaporation sequence did not behave as either of the two pure components, rather, they showed a 3 stage evaporation process:

- Stage 1. The more highly volatile component evaporates more quickly and dominates the concentration of the surface of the droplet. The wetting and evaporation rate suggest that the droplet is behaving as a droplet of pure ethanol. The contact line is pinned and contact angle reduces with time.

- Stage 2. As the ethanol content is lost to the atmosphere, the water content at the surface increases, raising the surface tension of the droplet and thus
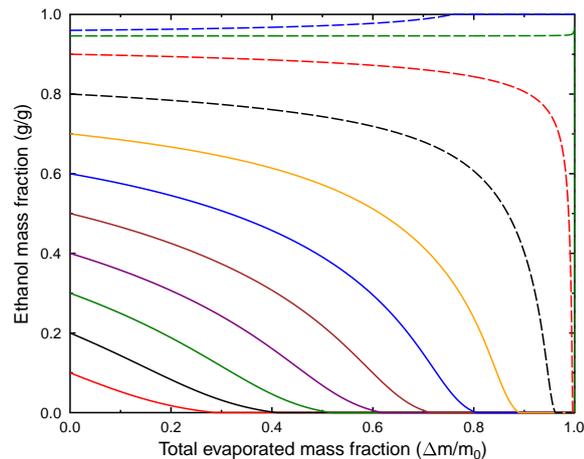
Figure 3.32: Plot of the evolution of the ethanol concentration from a given volume of solution with constant evaporation rate.

increasing the contact angle.

- Stage 3. The droplet is almost entirely water, and behaves as such, with simultaneous decrease in volume, radius and contact angle. While we may have expected the contact line to become pinned again as with water droplets at early times, or for the contact angle to remain constant as the contact line recedes, it seems that both shrink simultaneously. No explanation is given as to why the droplet seems to not follow Cazabat's constant contact angle receding argument. It is possibly due to the relative size of pinning sites increasing with respect to the size of the shrinking contact line of the droplet, thus enhancing the pinning force and lowering the receding contact angle as evaporation continues.

This result is surprising as we have already discussed a case in which water and ethanol simultaneously evaporate (tears of wine [108]), which led to Marangoni-stress induced flows. The already discussed Marangoni effect would predict that the water content at the interface should immediately increase as ethanol is lost to the atmosphere, however these findings suggest that the concentration of ethanol at the surface *increases* during the early stages of drying [118,119]. This perhaps suggests that concentration changes in a sessile droplet behave very differently compared to that in a large cylindrical volume of fluid. Perhaps the radial flow to the contact line or the relative speed at which all the ethanol escapes such a small

volume alters this behaviour. Or perhaps in a large volume of wine convection currents self-mix any concentration gradients in the bulk, limiting the ability for all of the ethanol to migrate to the interface. Similar results were also found with water-methanol mixtures [119].

Sefiane et. al. then further explored this binary system by seeding the droplets with 1μm diameter fluorescent microsphere in order to image internal flows within the droplets [120]. The particles were imaged using a microscope in focus within a single plane at the base of the droplet. 3 dimensional flows were extrapolated by analyzing the particle trajectories. They observed randomly oriented vortices during the first stage of drying where ethanol migrates to the surface of the droplet, a decay in the vortices as the droplet transitions to a purely water droplet during stage 2, and finally zero vortices with simple radial flow patterns as predicted by the coffee-ring effect during stage 3. However, because this method relies on imaging a single plane at the base of the droplet, and extrapolating z-direction flows, it is less reliable than imaging flows in the z-direction directly.

3.6.3 Bénard Convection in Drying Droplets

Kang. et. al. [121,122] have directly observed very different convection currents in sessile droplets of water-ethanol mixtures ($V = 3\ \mu$l, $R \approx 1$ mm), by adding fluorescent tracer particles to the mixture before deposition and illuminating a plane in the x-z direction with an Nd:YAG ($\lambda = 532$ nm) laser. At 5% initial ethanol concentration, they observed that two convection currents build up with upward fluid motion in the centre and down along the surface as shown in Fig 3.33, with the complexity of the flow patterns increasing with initial ethanol concentration. They propose that the increased evaporation rate of ethanol increases the water concentration and thus the fluid density at the droplet surface (as the densities of ethanol and water are 789 and 1000 kg/m^3 repectively), inducing buoyancy driven convection. They further confirm that the direction of the flow is driven by gravity by inverting the droplet and finding that the direction of convection is once again upwards in the centre and downward along the surface, as shown in Fig.3.33. However, they also propose that Marangoni flows due to increased surface tension at the interface should play a key role. Possibly by reducing the size of the droplet, and therefore reducing the effect of gravity compared to that
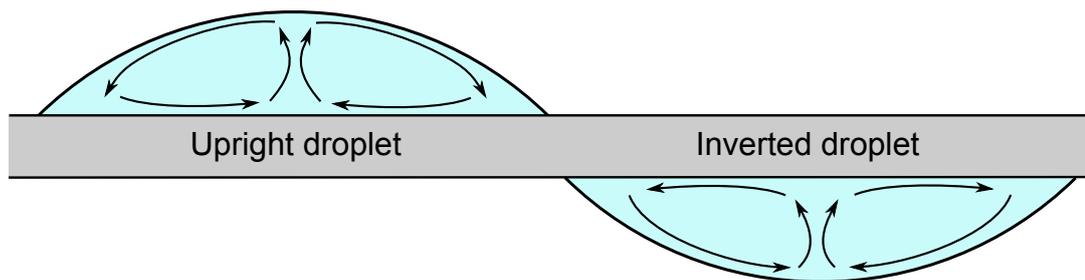
Figure 3.33: Convection currents observed in a drying droplet of water-ethanol mixture. When inverted, the direction of the convection remained upwards in the center and down along the surface, confirming that buoyancy is the driving mechanism behind these flows.

of surface tension, we would see different flow patterns.

These observations are in stark contrast with the discussed findings of Sefiane et. al. who proposed that ethanol dominates the surface concentration in the early stages of drying, and as the density of ethanol is lower than that of water (789 and 1000 kg/m^3 respectively [123]), we would not expect the buoyancy driven convection observed. This kind of contention shows that the evaporation dynamics of binary solutions are not well understood, and warrant further investigation.

Finally, now that an in depth review of the current lines of thought concerning both polymers in solution (with specific emphasis on PEO) and evaporating droplets has been discussed, we can start thinking about the system that is at the focus of this research - drying PEO droplets. First however, there is one well cited example of another drying droplet system, that we will see is both similar and different to our research - Dextran droplets.

3.7 Drying Polymer Droplets

3.7.1 Dextran

Pauchard and Allain may be the first researchers to thoroughly explore the behaviour of drying polymer droplets [7,124,125], with particular emphasis on Dextran, a water soluble highly branched polysaccharide. Their approach was to systematically vary initial mass fraction c_0, relative humidity RH and initial con-

tact angle θ_0 and observe the changes in droplet morphology over the course of evaporation. The fully dried structures were novel enough to warrant putting a great deal of thought into understanding and explaining this system, some examples of which shown in Figures 3.34 and 3.35.
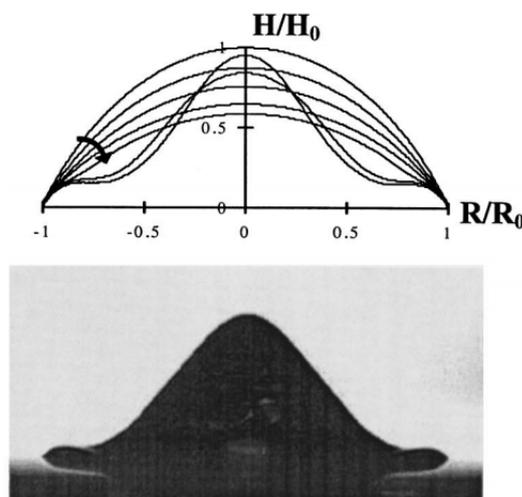

Figure 3.34: Profile image of fully dried Dextran solution droplet with plot of droplet surface profile with time. Image taken from publication by Pauchard [124].

The proposed explanation for how these unusual "Mexican hat" or "doughnut" like structures form is one of a structural instability nature, or "skin buckling" as they refer to it. This line of thought can be summarised as follows:

- During the early stages of the droplet lifetime, evaporation is uniform over the surface of the droplet. Remember from earlier in this chapter that this is a fair assumption when $\theta = 90°$, but opinion varies as to the evaporative profile over the surface of the droplet at lower contact angles.

- This uniform evaporation induces an outward flow to the droplet surface, and results in the formation of a highly concentrated polymer layer, or "skin" over the surface, as shown in Fig.3.36.

- As the concentration increases further, this polymeric skin undergoes a phase transition to a glassy state. Due to the highly branched nature of Dextran, reordering into a crystalline or semi-crystalline state would require much longer timescales than those associated with droplet drying.
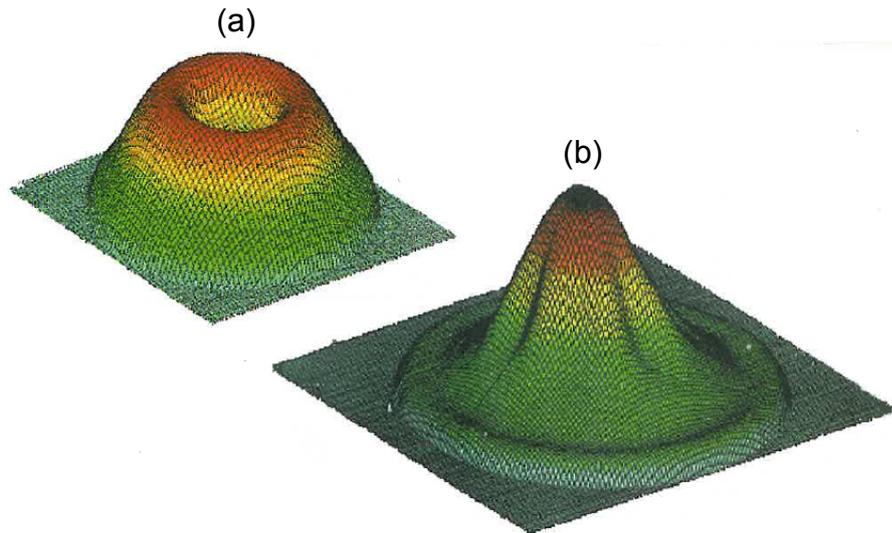
Figure 3.35: 3D maps of fully dried Dextran droplets measured with mechanical profilometer: (a) $RH = 50\%$, $\theta_0 = 70°$ and (b) $RH = 30\%$, $\theta_0 = 40°$. Image taken from publication by Pauchard [125].

- The glassy skin is then incompressible (i.e. cannot reduce in surface area), but water permeable, and so evaporation continues.

- Because the surface area is fixed and the volume within the interior of this glassy shell is reducing due to evaporation, an instability occurs, and the skin buckles inwards to accommodate volume loss.

This is a nice, simple picture for how unusual droplet structures form. The different morphologies come down to combinations of effects such as how quickly
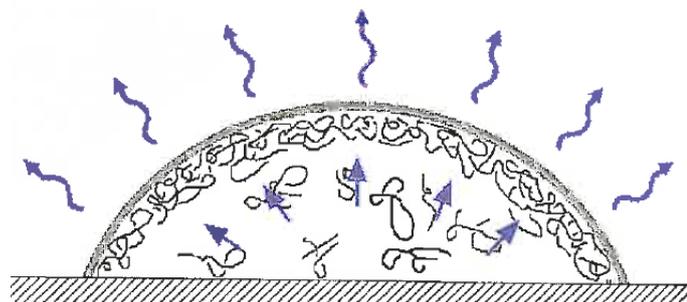

Figure 3.36: Diagram of the proposed mechanism behind the formation of an incompressible, water-permeable glassy skin over the surface of a drying Dextran droplet. Image taken from publication by Pauchard [125].

the skin builds up with respect to droplet lifetime, the shape of the droplet when the incompressible skin is formed, and the amount of polymer remaining in the non-skin state after buckling begins.

However there are some assumptions made here that may be too simplistic. Firstly, uniform evaporation over the droplet surface which as we have seen earlier in this chapter may not be a reasonable assumption to make when $\theta \neq 90°$. Quite how a non-uniform evaporation rate would affect the proposed glassy skin is unknown. Secondly, these Dextran droplets remain pinned ($R(t) = R_0$) for the duration of their lifetime, yet no account for the well established coffee ring effect, which one would expect to induce radial flow and deposit the polymers at the contact line rather than uniformly over the droplet surface, is made. Indeed, with large branched polymers perhaps the modes of flow are different to those of coffee grains. However, considering that the skin build up is proposed to be induced by outward solvent flow (which up until now we have considered to be usually in the direction of the droplet perimeter, not the surface), the coffee-ring effect should also be taken into account. Indeed, Kajiya et. al. found that by using fluorescent microscopy and lateral profile observation of drying droplets of fluorescent polystyrene dissolved in ethanol, the outward flow of the polymers due to the coffee ring effect could clearly be observed [126]. It must be noted however that these polymers were dissolved in ethanol, which has a lower surface tension than water and thus giving the droplet a lower initial contact angle, which as we have seen would act to enhance the evaporation rate at the droplet perimeter. Finally, the development of a "glassy skin", which is proposed to be the fundamental precursor to the formation of these strange final structures, has not been observed experimentally. While this may seem an obvious downfall of the glassy skin hypothesis, the lack of such an observation in likely due to the nature of the glassy transition. Unlike most phase transitions there is no reordering of the molecules, they simply become fixed in place, making it a typically difficult transition to observe.

Okuzono et. al. approached solving the problem of predicting whether a polymeric skin could form at an interface by analytically and numerically solving for the concentration build up at an interface as a function of diffusive and evaporative flux effects [127]. They propose a Péclet type number as the key factor in

the concentration build up at the interface:

$$Pe = \frac{hj}{D} \tag{3.28}$$

Where j is the evaporative flux, h is the length of the system in the direction of the evaporative flux, and D is the diffusion coefficient. High values of Pe lead to quick build up of polymer at the interface and therefore skin formation, whereas low values of Pe mean fast diffusion and zero concentration gradients. However, because this is a 1D solution, and assumes unidirectional evaporative flux, using this result as a basis for predicting the skin build up over the 3D interface of a droplet is not simple. To progress with this drying polymer droplet understanding, it would perhaps be beneficial to repeat the experiments of Pauchard and Allain, but instead replace Dextran with a polymer that undergoes a crystalline phase transition when $c = c_{\text{sat}}$ rather than a glassy transition, in order to improve the visibility of the reordering of the molecules, and therefore observe directly the local regions high in polymer concentration.

PEO, a linear chain water-soluble polymer described in depth in the previous chapter, is a prime candidate for such research. The ubiquity of PEO in research makes the lack of research into evaporating PEO-water droplets surprising, which is one of the reasons why the research in this thesis will be focused entirely on this system. The main reason however, is not that no one else has done it before, but because it is interesting!

The Scientific Method is a wonderful tool as long as you don't care which way the outcome turns.

Cristina Marrero

Chapter 4

Methods

In this chapter I describe the particular experimental methods which I have used in the rest of the thesis, justify them scientifically, and quantify any associated errors.

4.1 Droplet Preparation

4.1.1 Solution mixing

The first task was to mix various aqueous PEO solutions. A range in PEO molecular weight (M_{W}) was provided by Sigma-Aldrich and Polysciences as detailed in Table 4.1. Wherever provided by the supplier, the polydispersity of the PEO provided is included in the molecular weight uncertainty. Some suppliers have not detailed the polydispersity of their product, and so these uncertainties are not listed, but are probably at least 25%.

Solutions spanning a range of initial mass concentrations, c_0 from 1% to 50% were mixed by hand using distilled, deionised water and were left to equilibrate for at least 24 hours before use. Mass fractions were carefully measured using a Kern ALJ160-4NM mass balance to within 0.1 mg, and were mixed in high enough quantities ($\approx$10 g) to limit the impact of instrumental and measurement errors. In some solutions, particularly at high values of M_{W} and c_0, the mixing process led to the formation of a thick layer of high viscosity solution which impeded

Supplier	Product code	Molecular weight (kg/mol)
Sigma	P4338	3.35±0.3
Sigma	P4463	8±1
Sigma	95172	20±4
Sigma	P4646	≈35
Aldrich	181986	≈100
Polysciences	06104	100±50
Polysciences	17503	200±100
Sigma-Aldrich	182001	≈300
Polysciences	06105	300±150
Polysciences	06106	600±300

Table 4.1: Details of range of PEO molecular weight used and their respective suppliers

further dissolution. These solutions were then placed on a Stuart SRT60 Roller-mixer for at least 24 hours to encourage further mixing. Faster methods were not used to avoid possibility of shear induced molecular damage, and due to this mixing limitation, the most concentrated solutions obtainable are lower at high values of M_{W} due to the increased viscosity. Solutions were stored in 15ml sample tubes and sealed with Nescofilm to limit changes in concentration due to solvent evaporation. Water loss due to evaporation between successive opening and sealing the sample tube was quantified by measuring the mass of a test sample as it is opened and resealed 4 times a day over the course of two weeks. Total opening time was kept constant at approximately 20 seconds, as this is an estimate of the average time required to extract a droplet from the sample. This led to a total mass loss of ~ 0.005 ml from the 5ml sample (0.1%). Therefore I concluded that unwanted evaporation effects during storage and from opening the sample tube are negligible.

In the molecular weight range below 100 kg/mol solutions remained clear and colourless for the entire time they are kept within their sealed tubes (up to 3 months before disposal) at any value of c_0 below c_{sat} (the *saturation* concentration $\approx 50\%$). Whereas at high molecular weight ($M_{\mathrm{W}} \geq 100$ kg/mol) this is not the case as solutions appeared cloudy immediately after mixing and remained cloudy given any amount of dissolution time or prolonged mixing. This high M_{W}

cloudiness can be attributed to small ($\approx$3 μm in diameter) irregularly shaped undissolved clusters, which are easily viewed with microscopy as shown in figure 4.1. The origin of these non-soluble clusters remains under contention [48, 49, 52,
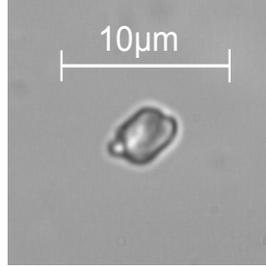

Figure 4.1: Undissolved PEO cluster as viewed under 100$\times$ magnification.

53, 55] as discussed in section 2.4, but it must be stressed that these solutions are *not* saturated. In an attempt to further dissolve these clusters I used a Silverson high-shear mechanical stirrer for 24 hours, however they remained unaffected. In experiments which use solutions of $M_{\mathrm{W}} \approx 100$ kg/mol these clusters were removed via the careful use of an adjustable speed Harvard Apparatus 11Plus filtration pump and Minisart single use filters (pore size, $a \approx 0.45$ μm). Due to high viscosities, filtration was performed slowly (flow rate, $Q \approx 0.1$ ml/hr) to avoid high pressure build up in the filter and to reduce shear damage to the polymer. If we assume that flow through the filter is the same as flow through an array of equally spaced and sized tubes as shown in Fig.4.2 then the average shear rate can be estimated from the following equation:

$$\dot{e} = \frac{4Q}{\pi a^3 N} \tag{4.1}$$

where N is the total number of pores. To estimate the number of pores an image was acquired of the filter membrane at 2000$\times$ magnification using a scanning electron microscope (SEM) as shown in Fig.4.3. To perform this SEM scan the membrane was first coated with a layer of gold particles using an Emitech K575X sputter coater. To calculate average size I used the particle size function in ImageJ, which gave an average pore size of 0.6 ± 0.3 μm (mean $\pm$ standard deviation) and pore number density of 0.51 μm^{-2}. The size of the filter membrane is approximately 7×10^8 μm^2. Therefore, we calculate an estimate of the average shear rate during filtration as $\dot{e} = 0.5$ s^{-1}, which is much less than the shear rates required to damage PEO as found in the literature [128]. However, Fig.4.3 shows that the array of tubes assumption may not be reasonable, and so further evidence that the shear is not sufficient to damage the polymers is required.
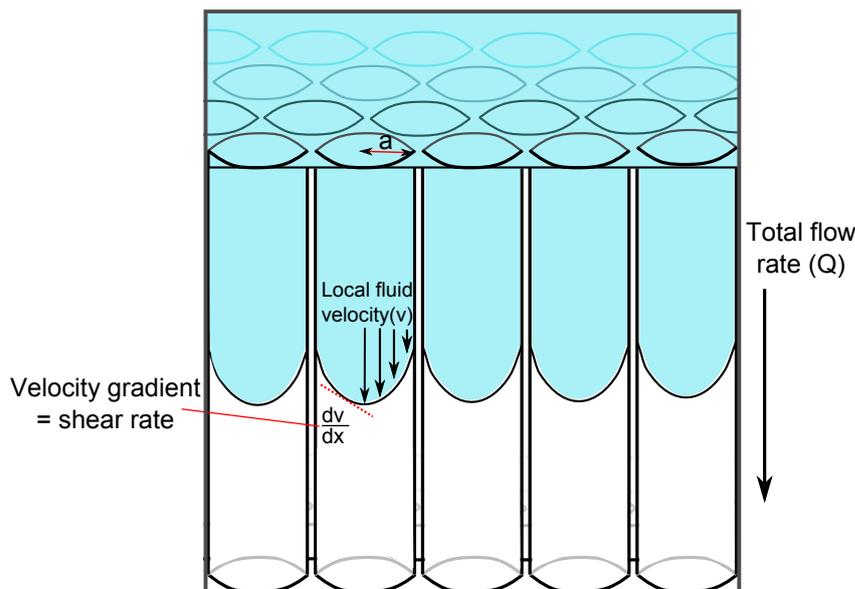
Figure 4.2: Diagram of shear induced from flow through array of tubes.

It is well documented that high shear stress can induce polymer scission [128–130]. To account for any possibility of shear induced damage to the polymer, viscosity and density of the solutions were measured prior to and post filtration. Density was measured using an Anton Paar DMA 4500 Density Meter giving values accurate to 0.1 kg/m^3 and control of temperature to within $\pm 0.2°$ and used to calculate the concentration post-filtration. Care was taken to ensure no bubbles were present in the sample volume of the density meter. Viscosity was measured using Brookfield viscometer DV-II + Pro with a cone and plate geometry (Cone diameter $d = 4.8$ cm and $\theta = 0.8°$) as a function of increasing and decreasing shear rate from 0 up to 900 s^{-1}, limited to a maximum shear stress of 2.5 Pa. In this shear stress range Newtonian fluid behaviour was observed, and the viscosity of the solution could be extracted from the good linear fit to the shear stress versus shear rate plot, to within $\pm 5\%$, and plotted against the values of concentration calculated from the density measurement. The concentration-viscosity curves in Fig.4.4 show that after using the density measurements to account for the reduction in concentration during filtration, we see no change in viscosity to within $\pm 5\%$. This is an important result as it shows that the polymer chains remained unbroken. If 100% of polymer chains had been broken in exactly half, the density of the solution would be unaffected, but the molecular weight would reduce by a factor of 2. In a good solvent, the Mark-Houwink equation
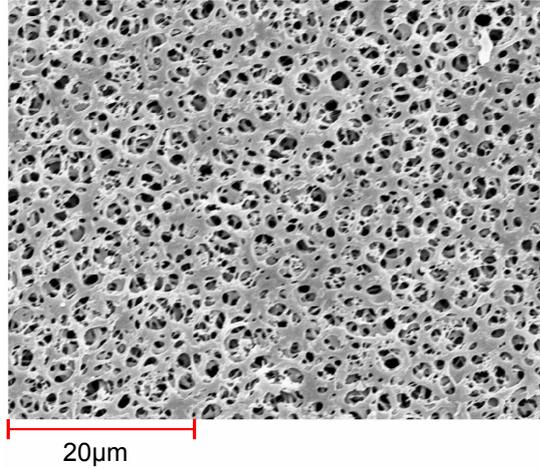
Figure 4.3: 2000x magnification SEM image of Minisart 0.45μm filter membrane

gives the relationship between molecular weight and the intrinisic viscosity of the solution [10]:

$$[\eta] \propto M_{\mathrm{W}}^{4/5} \tag{4.2}$$

and the intrinsic vicosity is related to the measured viscosity of the solution η by:

$$\eta = \eta_{\mathrm{s}}(1 + c[\eta]) \tag{4.3}$$

Where c is the concentration and η_{s} is the solvent viscosity. From Fig.4.4, we can see that at just 1% concentration the measured viscosity is approximately 2.5 Pa.s, which is $\sim 2500\times$ higher than the viscosity of water at room temperature ($\eta_{\mathrm{s}} \approx 1 \times 10^{-3}$ Pa.s). Therefore, the solvent viscosity contribution is small, and we can rewrite equation 4.3 as:

$$\eta \approx \eta_{\mathrm{s}}c[\eta] \propto \eta_{\mathrm{s}}cM_{\mathrm{W}}^{4/5} \tag{4.4}$$

Therefore, if molecular weight is reduced by a factor of 2, we would expect reduction of $\sim 34\%$ in the measured viscosity. However, because viscosity has no apparent change to within $\pm 5\%$ we can conclude that shear rates induced during filtration were only sufficient to damage a maximum of 15% of the polymer chains. From this point forward I will assume that if any chains were indeed broken, they were not in sufficient quantities to affect experimental findings. Alternatively, chromatography could have been used to accurately measure the average molecular weight (and indeed the polydispersity) before and after filtration. This
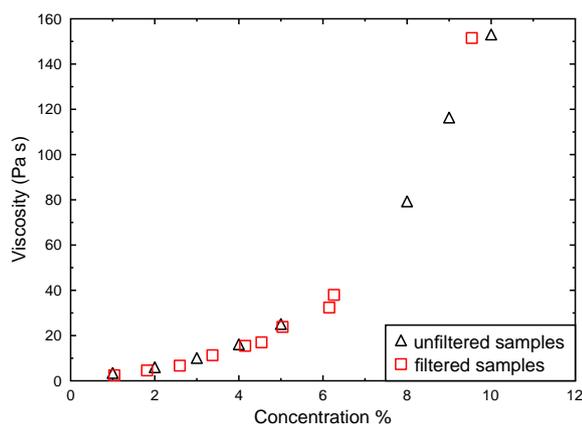
Figure 4.4: Viscosity against concentration before and after filtration

method was not used in this research. Filtration of higher M_W PEO solutions proved experimentally too difficult, and so in all experiments which involve values of $M_W \geq 200$ kg/mol these clusters were not removed.

As well as purely aqueous solutions, water-ethanol-PEO mixtures were made. At room temperature PEO is significantly less soluble in almost all solvents than in water (for example, to dissolve in ethanol temperatures must be raised above $T = 50°\text{C}$ [40]). To account for this, the mass fraction of water mixed was greater than or equal to the mass fraction of PEO. When the fraction of water was less than that of PEO, regardless of the ethanol content, the polymer becomes partially insoluble and sedimented to the bottom of the container. These mixtures were omitted.

4.1.2 Droplet Deposition

Droplets were deposited using a Gilson M10 MICROMAN, an adjustable positive-displacement pipette with volume control between 1 and 11 μl to within 0.1 μl. Unlike typical syringes which are filled entirely with air before use, positive-displacement pipettes contain an adjustable piston which removes the air cushion between the liquid and the pipette prior to sample aspiration [131]. This is important for highly viscous samples as the pressure forces acting between the air and liquid in the syringe would otherwise lead to the spontaneous formation of bubbles, or cavitation, in the liquid. The standard initial volume for the majority

of experiments in this thesis was 10 μl, deposited on TAAB thin borosilicate glass coverslips (dimensions: 24×50 mm, 0.085 to 0.13 mm thick). All glass slides were carefully cleaned with ethanol to remove dirt and debris prior to droplet deposition. To deposit the droplets, they were suspended at the tip of the micro pipette and lowered until they came into contact with the substrate and spread into a sessile droplet. By depositing the droplets this way, as opposed to dropping them from a height, any possibility of impact splashing was removed. Initial contact angles were therefore close to the advancing contact angle ($\theta_0 \approx 90°$). Due to the high hysteresis of PEO solution droplets on glass microscope coverslips (measured receding contact angle $\theta_r \approx 10°$), control of the initial droplet contact angle was easily achieved. To reduce the initial contact angle a higher volume of liquid than required was initially deposited onto the substrate, and given 30 seconds to equilibrate and for the contact line to pin. After this equilibration time the volume of the droplet was reduced to the desired volume of 10 μl using the micro pipette. Because the receding contact angle is very low, this method allowed easy control over the contact angle from the initial volume deposited. To increase the initial contact angle, droplets were also deposited on various other hydrophobic fluoropolymer substrates including: Cytop, an amorphous fluoropolymer with an equilibrium contact angle of 110° with water; Teflon (or PTFE), a semi-crystalline fluoropolymer with an approximate equilibrium contact angle of 114° with water (Cytop and Teflon substrates were provided by the University of Edinburgh); and glass slides coated in Granger's solution, a water based water proofing detergent (contact angle with water depends strongly on Granger's application method). This hydrophobic layer was added by submerging glass slide coverslips in aqueous Granger's solution (5% concentration) for approximately 30 minutes, and then placing the glass slides in an 80°C oven for 3 hours to dry and activate the Granger's layer.

4.1.3 CCD Imaging

To simultaneously image the droplet from the side and above the droplet was placed on the substrate as shown in the experimental apparatus setup in Fig.4.5. Two digital USB monochrome CCD cameras from ImagingSource (model number DMK 41BU02.H, 1280×960 pixels) with LINOS 0.3× magnification lenses were placed above and to the side of the droplet and interfaced to a computer with IC
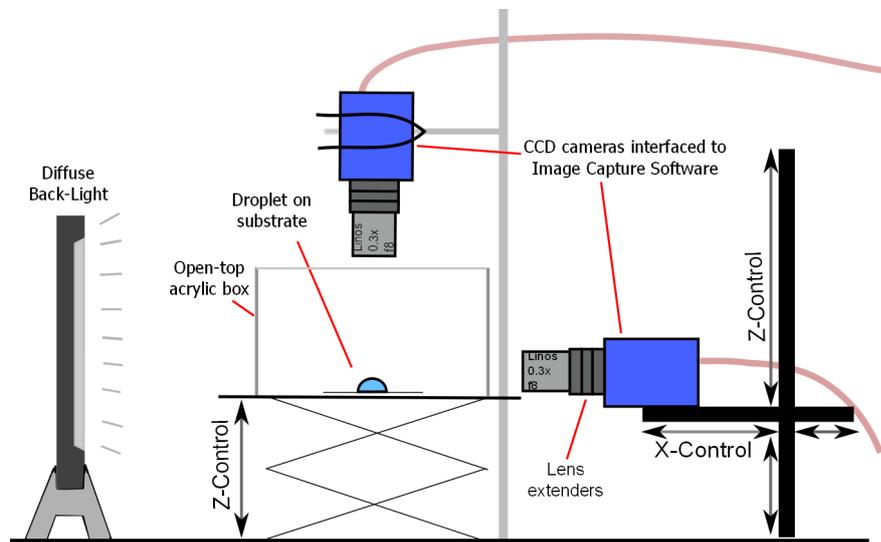
Figure 4.5: Experimental setup for imaging a droplet in ambient conditions, side perspective
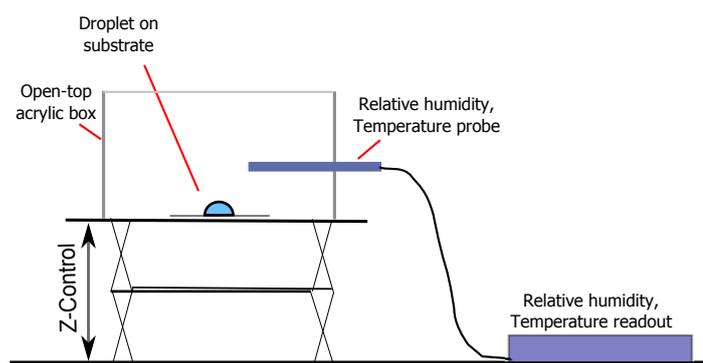

Figure 4.6: Experimental setup for imaging a droplet in ambient conditions, front perspective

Capture software. To easily focus both images the camera positioned above the droplet was kept stationary, the substrate was placed on a z-controllable platform, and the profile-view camera was attached to a mount with control in the x-z plane. A StockerYale diffuse back light (ML-0405) was used to illuminate the droplet and provide good contrast between the droplet surface and the background. By the addition of Thorlabs lens tube extensions, screwed in place between the lens and the CCD camera, the field of view could be adjusted to fit the acquired image size to the size of the droplet. Imaging of a droplet with initial volume $V_0 = 10$ μl was found to be best with the addition of 3×0.5 cm extension tubes. The droplet was also placed inside an open-top box ($15 \times 15 \times 15$ cm) to remove any effects of net air flow in the lab, without creating a sealed chamber. If this box had been sealed, the effect of droplet evaporation would increase the local relative humidity, which will in turn alter the vapour pressure of the droplet. At ambient conditions, the dew point ($RH = 100\%$) is reached when there is approximately 15 g of water vapour per 1 kg of air [132]. If the volume of the drying chamber used was ≈ 0.003375 m^3, and the density of the air at ambient conditions is ≈ 1.2 kg/m^3, then this chamber can hold a maximum of 6×10^{-5} kg, or 60 μl, of water vapour. Therefore, a 10 μl droplet evaporating into a sealed $15 \times 15 \times 15$ cm chamber will increase the relative humidity of the chamber by $\approx 17\%$. If the box remains open however, it is reasonable to assume that the size of the atmospheric chamber (in this case the lab) is large enough that the relative humidity will remain relatively unchanged by the evaporating droplet.

An Omegaette relative humidity (RH) and temperature (T) probe was slotted into a circular hole in the side of the box to record any changes in temperature and humidity with time. With an open-top box in ambient conditions only small changes in RH ($\pm 0.5\%$) and T ($\pm 0.2\%$) were observed within the time frame of a single experiment. Fig.4.6 is a diagram of the same experimental setup but from as viewed from the side (with one or two pieces of apparatus removed from the diagram for clarity) to show the positioning of the humidity/temperature probe. After droplet deposition images were sequentially recorded every 10 seconds from above and from the side using IC Capture software.

4.1.4   Image Analysis

From the time-lapse profile images of the droplet it was possible to calculate physical quantities such as droplet volume (V), surface area (A), height (h), liquid radius (R) and contact angle (θ_c). Typically, the volume and surface area of a droplet are calculated by fitting the Young-Laplace equation to the curve.

To calculate V, A and h, the surface profile was extracted by folllowing these steps:

- Combine the still images into a single sequence using the *import image sequence* function in ImageJ..

- If the substrate was tilted rotate the image so that the contact line is horizontal.

- Crop the sequence so that only the droplet remains.

- Convert the image sequence into binary by setting a threshold to better define the droplet-air surface, whilst being careful not to lose any profile data. For this step good image contrast between droplet surface and background is critical. Fig.4.7 shows the difference the quality of the original image can make when taking a threshold.
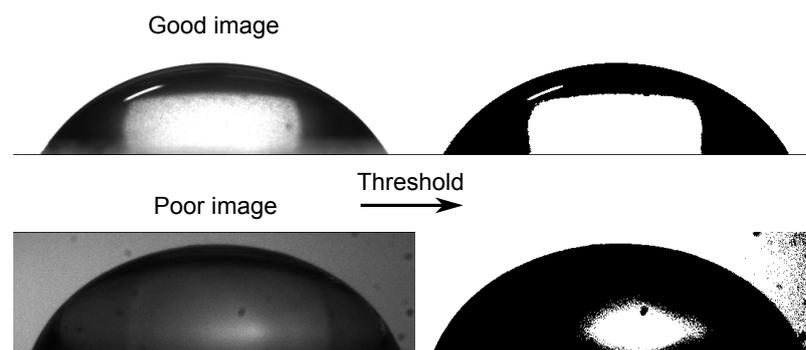

Figure 4.7: Representation of the damaging effect a poor quality image has on the threshold step in using ImageJ to extract the droplet profile.

- Run a macro which implements the *Do Wand* tool and extracts the droplet surface profile as a series of x-z pixel co-ordinates and saves each individual series to a new text file.

- Run a program in MATLAB which uses the profile co-ordinates to calculate V, A, R and h for each image and append each to a new text file as a series of values against image number.

These last two steps are entirely automated, and the steps performed by the MATLAB program can be summarised as follows: First the height is calculated from the maximum pixel z-coordinate $h = z_{\max}$. Then the position of maximum height is defined as the centre of the droplet $z(x = 0) = z_{\max}$. The program then calculates A and V by rotating each surface co-ordinate around this central axis and numerically integrating under the resulting continuous curve.

This process is automatically repeated for each image, with each successive set of measured values appended to a text file. These values are then imported into an excel file and plotted against time. This step could have easily been included into the MATLAB code, however the time interval between images was sometimes adjusted depending on the evaporation rate of the droplet, and so this adjustment to the volume and surface area measurements was added manually at a later stage. $V(t)$ and $A(t)$ are very sensitive to variations in the position of this axis, caused by changes in the maximum point. To account for asymmetry in the profile the MATLAB code calculates V and A given by the half profiles to the left and right of the axis (as shown diagramatically in Fig.4.8), then averages the left and right values to obtain the mean, and uses half the difference for the uncertainty. As a comparison with $V(t)$, in some experiments the droplet mass $m(t)$ was also continually monitored using the Kern mass balance interfaced to a computer using LabVIEW. During the early stages of drying, where the droplet is a perfectly spherical cap, volume and mass normalised by their initial values are equivalent.

Figure 4.8: a) Profile image b) Profile image converted to binary c) Schematic of how the volume and surface area of rotation are calculated by using maximum point as the axis of rotation. Errors quantified as the difference between the rotation of the left side of the axis and the right.

To measure $R(t)$ and $\theta_c(t)$ more care needed to be taken. Fig.4.9 a) and b) are images of symmetrical, spherical-cap droplets during pinned drying, and in this case $R(t)$ can be easily measured as half the base length as shown in f) and g). However, c), d) and e) show more irregular droplet shapes in which we need a more explicit definition of $R(t)$. From this point forward I will define R as the
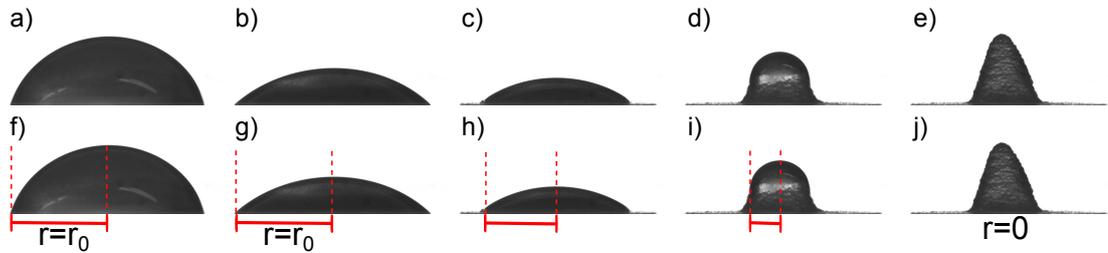

Figure 4.9: Diagramatical definition of *liquid base radius*, $r(t)$, at different stages of drying.

liquid base radius, which is measured as half the horizontal distance between the left and right 3 phase (liquid-solid-air) contact lines as highlighted in Fig.4.9 f) to j). Measurements of $r(t)$ can be made from above or from the side when $\theta_c \leq 90°$. However, when $\theta_c > 90°$, the base radius is obscured by the droplet above it. Because of this, measurements of $R(t)$ were predominantly taken from the profile images. To measure θ_c I used the ImageJ plugin *DropSnake* [133], which fits a spherical cap to a plotted surface, with contact angles measured on the left and right side (denoted as *CA Left* and *Right*) as shown in Fig.4.10. Blue and red represent two different methods the DropSnake plugin uses to calculate the contact angle. Results are given as the average of these two measurements, with half the difference as the uncertainty. For accurate measurements this contact
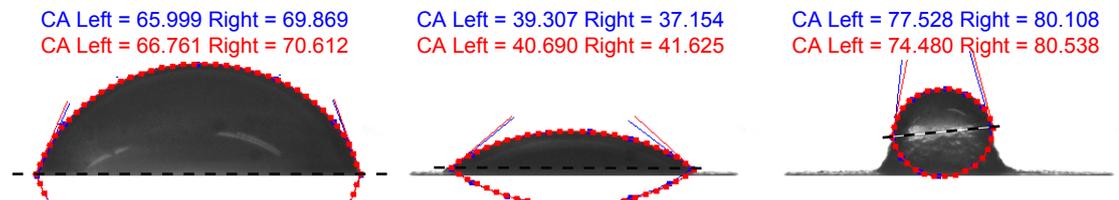

Figure 4.10: Screen shots of contact angle measurements using the 'Snake the curve' tool in DropSnake. Dashed black line added to aide visualisation of chosen 3 phase contact line.

angle measuring tool requires careful positioning of the droplet contact line. Due

to the subjectivity of positioning the 3-phase contact line in highly irregular droplets, such as the far right image in Fig.4.10, this method yielded results with very high uncertainties, and so were mostly omitted. With the exception of θ_c, all measurements taken by this point have been calculated in units of pixels. The camera-lens setup used until this point has a very narrow in-focus working region (~ 1 mm), so if droplets are always kept in focus, we can assume the pixel-cm conversion ratio remains constant. Therefore calibration from pixel number to a real physical length scale for all in-focus droplet images requires just a single snapshot of a known length, in this case a ruler as shown in Fig.4.11. This image was captured through a sheet of acrylic of equal thickness to the walls of the acrylic chamber which the droplets are placed inside (0.5 cm) to ensure consistency in the focal length.
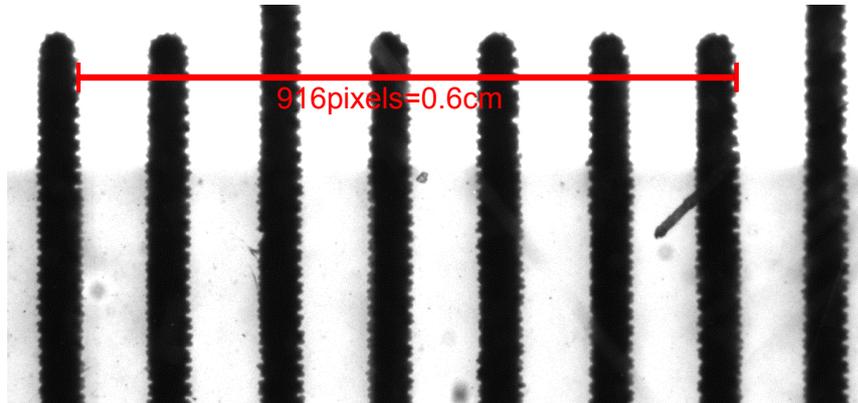

Figure 4.11: Image of ruler captured at same focal distance as droplet images for conversion from pixels to cm.

4.1.5 Droplets On An Incline

As already discussed in Chapter 3, gravity plays an important role in both the shape of the droplet and the direction of convection currents. In this set of experiments I varied the angle of inclination of the substrate in order to observe the effect of the direction of gravity with respect to the contact line. Fig.4.12 is a diagram of the experimental setup prior to droplet deposition. A series of glass substrates were stuck down onto an adjustable bed, each with a different angle of inclination between 0 and 90°. The importance of an adjustable bed is that depositing a droplet onto an already inclined plane is difficult. By first lifting the
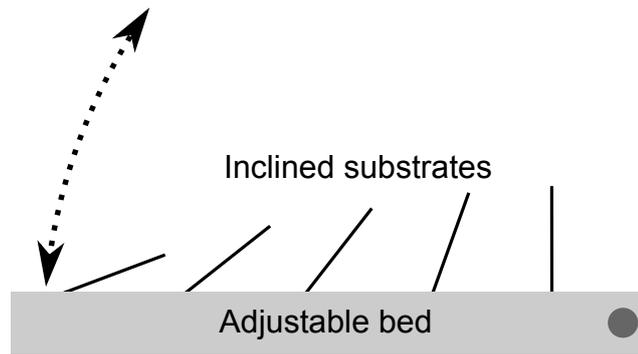
Figure 4.12: Experimental setup for drying droplets on an incline.

bed until the substrate is positioned such that gravity acts in perpendicular to the plane of the substrate, the droplet can be deposited without risk of the droplet dripping down the substrate before it becomes pinned. Once the droplet was deposited and given approximately 10 seconds to become pinned to the substrate, the bed was lowered back down, and the droplet then evaporates at an incline without falling or sliding down the substrate.

4.2 Atmospheric conditions

One of the major experimental aims of this thesis is to observe and explain how preliminary atmospheric conditions affect the final fully dried droplet structure. In this section I describe how atmospheric pressure P, relative humidity RH and temperature T were carefully controlled and measured during evaporation. Previously it was stated that when recording droplet drying, images were acquired every 10 seconds. However, this standard image frequency proved to be unsuitable for very fast and very slow drying rates. Therefore, image capture frequency was individually adjusted.

4.2.1 Reduced Pressure

To reduce the pressure in the atmosphere, the droplet was first placed inside a small steel cylindrical chamber (radius ≈ 4.5 cm, length ≈ 4 cm, thickness ≈ 2 cm) with transparent 0.5 cm thick acrylic windows as shown in Fig.4.13 and 4.14,
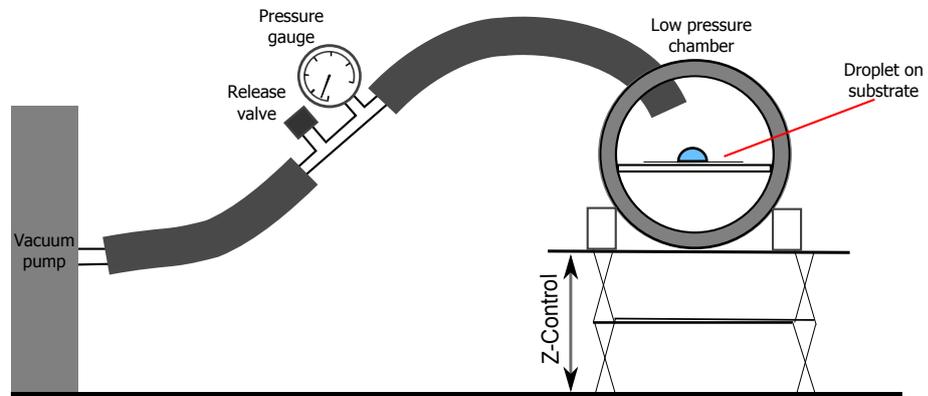
Figure 4.13: Experimental setup of imaging a droplet in partial pressure conditions, front perspective.
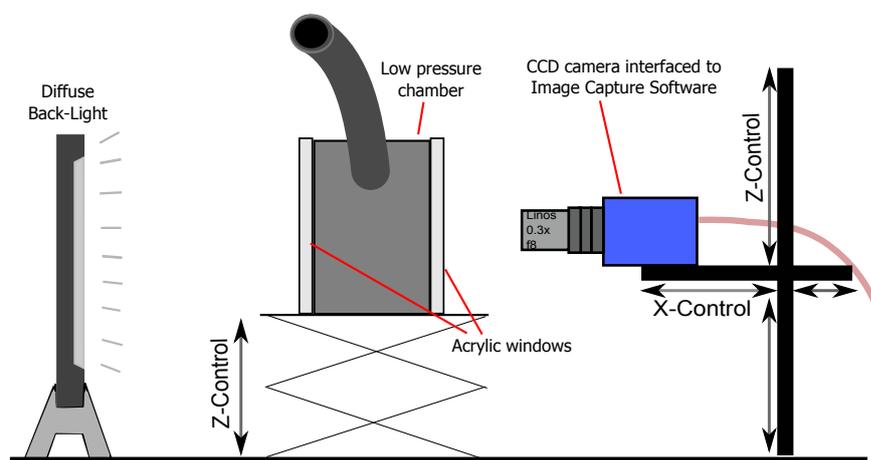

Figure 4.14: Experimental setup of imaging a droplet in partial pressure conditions, side perspective.

and connected to one of two available vacuum pumps: a Vacuubrand MD4NT diaphragm pump; and an Edwards E2M5 oil diffusion pump. The diaphragm pump gave a minimum partial pressure of ≈10 mbar, and by using a manually controlled release valve and a pressure gauge, pressure was controllable between 10 and 1000 mbar with an average uncertainty of ±10 mbar due to the inaccuracy of the needle position. The oil diffusion pump connected to the same chamber was capable of further reducing the pressure to 0.1 mbar. However, preliminary experiments showed that aqueous PEO droplets freeze at ≈ 2 mbar due to the latent heat causing localised cooling: although an interesting phenomenon as it appears that only a thin crust forms which then insulates the remaining liquid droplet, no further studies were performed on freezing droplets. Because of this effect the low partial pressures achievable with the oil diffusion pump were not explored, and the diaphragm pump was the preferred method of pressure reduction. Furthermore, the oil diffusion pump can potentially lead to drop contamination through oil backstreaming. As this could interfere with the drop drying process, and is typically a difficult problem to both observe and overcome (without the use of a molecular sieve), again the diaphragm pump became preferable.

A problem found with drying at low pressures ($P < 100$ mbar), is that bubbles would often spontaneously appear and interfere with the drying process as shown in Fig.4.15. Several possibilities were suggested as the origin of these bubbles
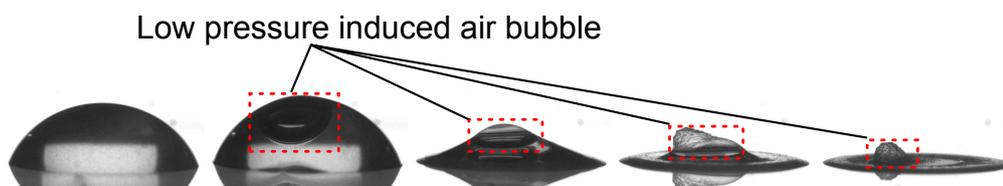
Figure 4.15: Spontaneous bubble growth at low atmospheric pressure ($P = 100$ mbar) disrupting the droplet drying process ($M_{\text{W}} = 300$ kg/mol, $c_0 = 5\%$).

including: dissolved gases coming out of solution; micro bubbles trapped on the substrate growing due to the reduced pressure; or solution boiling. Boiling can be easily dismissed due to the non-repeatability of this phenomenon. Indeed, repeat experiments rarely led to the same outcome with regards to bubbling. To investigate whether the bubbles were from dissolved gases coming out of solution, large quantities of solution were degassed prior to droplet deposition. This step had little effect on droplet bubbling, and so I concluded that these bubbles become

trapped between the droplet and substrate during droplet deposition. Due to the seemingly random occurrence of these bubbles no effort was made to remove the bubbling effect, instead experiments were repeated until I had collected sufficient quantity of recordings in which bubbling did not occur.

4.2.2 Humidity control

The easiest method for increasing relative humidity to a fixed % is with the use of a saturated salt solution bath [134]. The principle behind this technique is simple. If a water bath is added to an enclosed system, it will evaporate until either all the water has transitioned to the gas phase, or the atmosphere has reached the dew point, at which time water will transition from the liquid to the gas phase at exactly the same rate vapour transitions from the gas phase to the liquid phase. in section 4.1.3, a crude estimate was made for the maximum water mass required for a $15 \times 15 \times 15$ cm chamber to reach the dew point. Let us assume that the water bath added to the chamber is well over this quantity. If however, the water is mixed with a non-volatile substance such as salt, the vapor pressure is proportional to the mass fraction of water in the solution (Raoult's law [117]). This is because at a given temperature, the same number of particles are at the surface in both pure water and the salt solution. However, in the solution, only the water molecules can escape into the vapour phase. Because these represent only a fraction of the total number of particles present at the surface, the presence of salt effectively lowers the vapour pressure of the water. The importance of the solution being saturated is that as water escapes, the concentration of salt will increase. However, the concentration in the liquid phase cannot increase further as it is at the saturation concentration already. Therefore solvent loss leads to crystallisation at the exact same rate as evaporation (in units of grams per second). Therefore, because the liquid phase concentration can not change, the mass fraction of water at the interface is fixed, and from Raoult's law we know that the vapour pressure of the solvent component is proportional to its mole fraction in solution, the vapour pressure of the solvent is both reduced and fixed. As with any solvent, evaporation will continue until the rate of water escape equals the rate of vapour reentry into the liquid phase. In the case of a solution however, this will happen at a lower value of relative humidity than in the pure case simply due to the reduction in the vapour pressure of the solution. An

alternative way to understand this is by thinking in terms of chemical potential. When a molecule transitions from one phase to another (such the migration of water molecules from solid to liquid in melting ice), it is because the molecules are moving from a high chemical potential to a low chemical potential. In the case of a non-evaporating drop where there is an equilibrium between the gas and the liquid phase, their chemical potentials are in balance leading to zero net migration of molecules from one phase to the other. By adding salts to the liquid phase we are altering the chemical potential of the solution, but not the gas, and so they will reach equilibrium at a different value of vapour density.

This is of course a simplified view of how introduction of salts can reduce the maximum water content of the atmosphere, but the technique is a highly useful one as the relative humidity at which the solution and vapour phase reach equilibrium is highly sensitive on the specific salt used.

To observe the effect of relative humidity on the droplet drying behaviour, I introduced several saturated salt baths around the substrate, as shown in Fig.4.16. Clearly if the environment is too large the water will evaporate away entirely
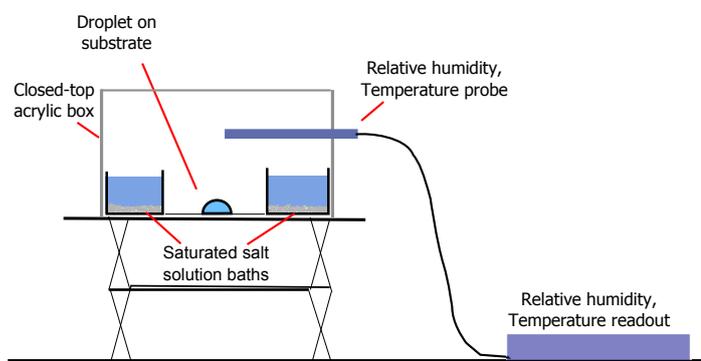
Figure 4.16: Experimental setup of relative humidity control.

before the humidity is altered appreciably. To account for this, the experimental procedure used here was very similar to that used in Fig.4.5 and 4.6, except that the acrylic chamber lid was closed to reduce the size of the environment that the salt solution baths had to evaporate into, the salt solution baths were allowed to equilibrate with the environment for at least 2 hours prior to droplet deposition (as this seemed to be the time required for the relative humidity read-out from the probe to level off), and only a small opening in the chamber was created to allow for droplet deposition, remaining open for a maximum of 10 seconds. To

vary the relative humidity two different salt solutions were used: Sodium Chloride (NaCl) and Potassium Sulphate (K_2SO_4), giving approximately 75±2 and 81±2% respectively, measured independently of predicted relative humidities of 77±1.3 and 98±1% from literature [135]. Discrepancies between literature and measured values could possibly be due to the acrylic chamber not being entirely air-tight. At the time of exploring the effect of RH on droplet drying, ambient conditions were consistently $RH = 55 \pm 5\%$ and $T = 22 \pm 1°$C.

The effect of reducing the relative humidity was also explored by replacing salt solution baths with silica gel beads. These beads effectively extract the the water vapour from the atmosphere (to a limited extent. One bead of course cannot dry out an entire lab!). Preliminary tests with leaving the silica gel in lab conditions showed that the colour changed from a maroon like colour to a much lighter orange colour. Assuming they do not become saturated with water, these silica gel beads should absorb and trap all water vapour and reduce the humidity to 0%. However, independent measurements using the Omegaette RHT probe showed that this water absorption process was too slow compared to the drying rate of the polymer droplets ($\approx$ 1 hour). Ideally, it would be preferable to create a completely dry environment before depositing the droplet. Experimentally this proved difficult as the process of introducing a droplet often lead to the atmosphere in the acrylic chamber quickly equilibrating with the lab, and therefore low relative humidity drying observations were limited to $25 \pm 4\%$. One possibility would be to blow nitrogen gas over the droplet throughout the experiment, creating a 0% humid environment. However, this would mean that the assumption of a quiescent atmosphere discussed in the previous chapter is no longer valid, and so this was not attempted.

4.2.3   Temperature

To observe the effect of temperature the droplets were placed in a ceramic oven (AX series from Progen Scientific) varying temperature between 25 and 65°C. The dried deposits were imaged post-experiment from above. However, due to the constraints of the ceramic oven in-situ droplet imaging was not possible, and so an alternative method of varying temperature was used with a Stuart CC162 hot-plate to create oven-like conditions in a transparent container as shown in

Fig.4.17. By varying the temperature of the plate between 50 and 150°C, and allowing half an hour for the temperature to equilibrate, I had control over the temperature of the atmosphere between 20 and 70°C independently measured with the Omegaette RHT probe. The discrepancy between plate temperature and atmospheric temperature could be due to the chamber not enclosing the entire hot plate and the chamber not being entirely air-tight. To ensure the plate-atmosphere temperature gradient did not interfere with the droplet drying, the substrate was placed on a raised platform with the RHT probe positioned as close to the droplet as possible. Preliminary experiments found the melting temperature of PEO ($M_W = 100$kg/mol) powder to be between 65 and 70°C, and so 60°C was chosen as the upper limit in drying temperature.
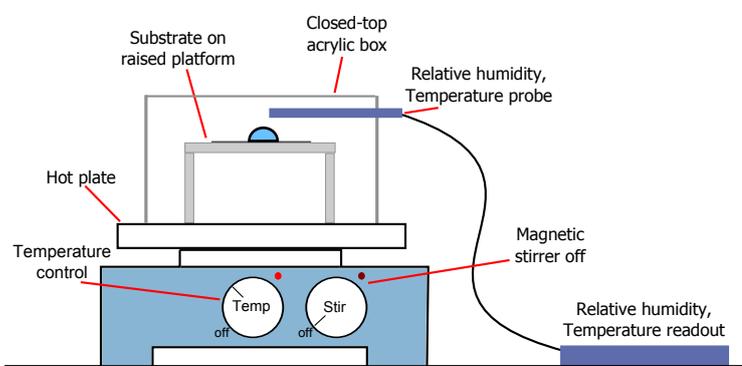
Figure 4.17: Experimental setup of temperature control with Stuart CC162 hot-plate.

4.3 Other Imaging Methods

4.3.1 Microscopy

To view the structure of the semi-crystalline PEO precipitate in higher detail during and post-drying, I used one of two microscopes available: a Nikon Eclipse TE2000-S inverted transmission microscope with 2×, 10×, 60× and 100× magnification lenses; an Olympus BX51 in reflection microscope with 5×, 10×, 20× and 50× magnification lenses. These were connected to ImagingSource cameras DMK 41BU02.H (black and white) and DBK 41AF02 (colour) and interfaced to a computer with IC Capture software. To capture the PEO phase transition time between liquid and semi-crystalline I inserted two polarizing filters in the Nikon

microscope (one at the light source and one at the camera), rotated at 90° to each other. Typically cross polarised filters will block out all light from a white light source and lead to no image being acquired. However, if an anisotropic crystalline material (such as semi-crystalline PEO solid) is placed between the two filters, the orientation of the light is twisted as it passes through the material. This is due to the intrinsic property of anisotropic crystals of having direction dependent symmetry, and thus a directionally dependent refractive index. Because of this twisting the second polarized filter can not block out all the light, and an image of the anisotropic crystal can be seen. With a white light source, the refractive index is also wavelength dependent, leading to the semi-crystalline structure appearing to have position dependent colour. Any material that can twist light so that it may be viewed through cross polarised filters is known as *birefringent*. This method allowed for simple imaging of the crystallisation transition time of PEO in drying droplets.

4.3.2   Optical Coherence Tomography

OCT is a tool designed for in-situ non-invasive imaging of internal structures of objects [136]. Most commonly it is used for imaging the inside of the human eye without the necessity of invasive surgery [137]. The principle behind OCT is very similar to ultrasound, in that it emits a wave (light in this case rather than sound) and detects the wave which is bounced back. However, due to the very high speeds of light, using the time delay method of measuring fine details in small samples is impractical. Instead, OCT uses interferometry to measure fine (sub-millimetre) details of surfaces.

The setup in Time-domain OCT is as shown in Fig.4.18. A broad band white light source emits a beam of light which is then split into two paths, one towards the sample, and one towards a movable reference mirror. Light is then reflected and scattered back by the mirror and sample, recombined to create interference, and collected at the detector, usually a photodiode, which measures the intensity of the interfering light. If the light source was monochromatic then the coherence length, which is the maximum path difference in space (or time) between the two beams of light in which an interference pattern can be observed, is infinite. This means that the intensity of the interference pattern between the two beams
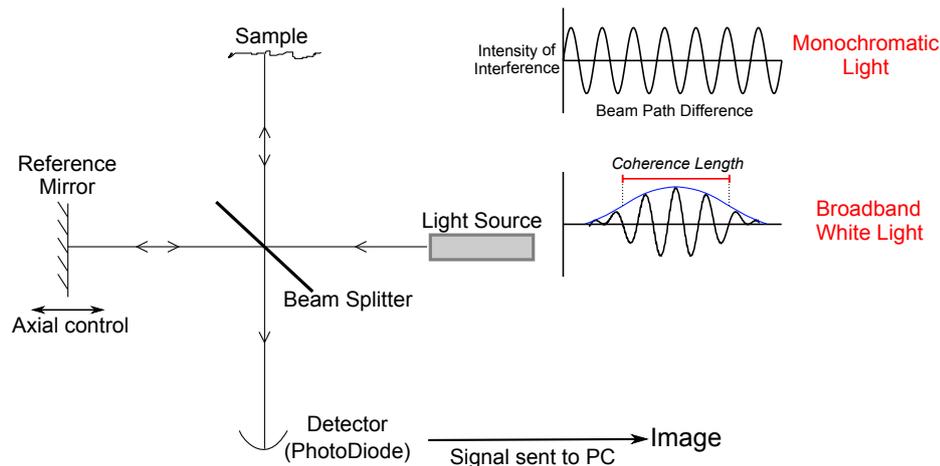
Figure 4.18: Setup of Time-Domain OCT

of light reaching the detector would be cyclic with path difference and give very little information about the sample, as shown in Fig.4.18. Broad band white light however has a short *coherence length*, and so as long as the path difference between the two beams is within this coherence length, the level of interference can be used to measure fine details within the sample. By then moving the reference mirror axially the position at which the two beams of light show interference will shift accordingly, and a depth profile of the sample can be collected over time. This type of OCT has high precision, but high scanning times due to the requirement of mechanical translation of the reference mirror. An alternative method to this is Frequency-Domain OCT (otherwise known as Fourier-Domain or Spectral-Radar OCT), which utilises the fact that the level of interference is not only a function of difference in path length (or time), but of the frequency of each constituent light wave. By replacing the photodiode with a spectrometer, and performing a Fourier transform on the acquired frequency data, a similar image can be constructed as with Time-Domain OCT but without the slow process of moving the reference mirror.

The aim of these experiments was to perform non-invasive imaging of the depth profile of drying PEO droplets in order to track internal convection currents using Fourier-Domain OCT. The device I used was a Thorlabs Spectral-Radar OCT, which consists of a Michelson interferometer, a broadband white light source with central wavelength of 930 nm and full width half maximum bandwidth of 100 nm and a spectrometer. The interferometer and scanning mechanism are located

within a handheld probe and the spectrometer and light source are located in a separate base unit connected to the hand-held probe by an optical fibre. The x and z resolution were 9 and 6.5 μm respectively, with a fixed depth range of 1.6 mm [138]. The handheld probe was secured to a motorised micrometer stage for remote control over probe position in x, y and z directions. Due to this narrow depth range, 5 μl was the standard droplet size. As previously mentioned imaging requires light scattering sources. Droplets with $M_W \leq 35$ kg/mol are completely transparent and colourless, and have an atomically smooth curved surface, leading to very little backscattering of light to the detector. To image the convection currents ≈ 30 μl of aqueous 4.3 μm diameter copolymer microspheres (2% solution) were added to every 5 ml of PEO solution, giving around 0.01% by volume of spheres in solution. These microspheres acted as point source light scatterers and provided a novel method for recording convection currents with time during droplet drying. Microsphere motion was tracked and plotted using the ImageJ particle tracker plugin, which implements the feature point detection and tracking algorithm as described in the work by Sbalzarini and Koumoutsakos [139].

At high molecular weight ($M_\mathrm{W} \geq 200$ kg/mol) PEO solutions remained cloudy due to undissolved clusters as discussed in section 4.1.1, and so copolymer microspheres were not added, instead undissolved clusters acted as point light scatterers under OCT. OCT imaging was also performed on an inverted drying droplet to show the effect gravity has on internal convection currents.

Using OCT for tracking internal convection currents has several limitations:

- Secondary scattering artifacts. Light that is scattered multiple times within the sample will travel a longer distance and lead to the detection of a non-existent surfaces. Care must be taken to distinguish between the real object and these artifacts.

- Image acquisition frequency. For good signal to noise ratio when imaging microspheres suspended in a droplet, the limit on image acquisition was approximately 1 image per second. This rate was too slow for image acquisition of microspheres in pure water. However this was more than sufficient for PEO solutions due to the high viscosities and slow flow rates.

- Refractive index. The OCT software outputs an image as a function of the
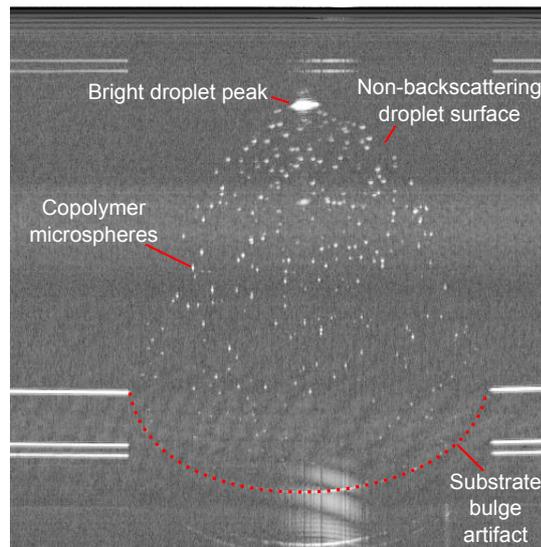
Figure 4.19: Raw OCT imaging of droplet with added copolymer microspheres

time it has taken for light to travel between the emitter and the sensor, and makes the assumption that the light has travelled through air only, with a refractive index $RI = 1$. If a portion of the light travels through a medium with a much higher refractive index (for example water, $RI = 1.33$) then the light will take longer to return from the scattering surface than if travelling through air alone, and so the surface appears to be at a greater distance from the detector than it is. This becomes clear when imaging a droplet as the contact line between droplet and substrate appears to bulge downward as shown in Fig.4.19 .

This "bulge" can be used to our advantage as a novel method for measuring the refractive index of the droplet. The simplest method of determining the refractive index is to take the ratio between optical height and the corresponding physical height ($RI = h'/h$), assuming no bubbles or other material between the droplet and the flat substrate, and assuming refractive index is constant for the entire path length through the droplet [138], as shown in Fig.4.20.

4.3.3 Confocal Microscopy

Another method I used for tracking micron sized particle motion in a drying droplet is confocal microscopy. A confocal microscope detects structures by fo-
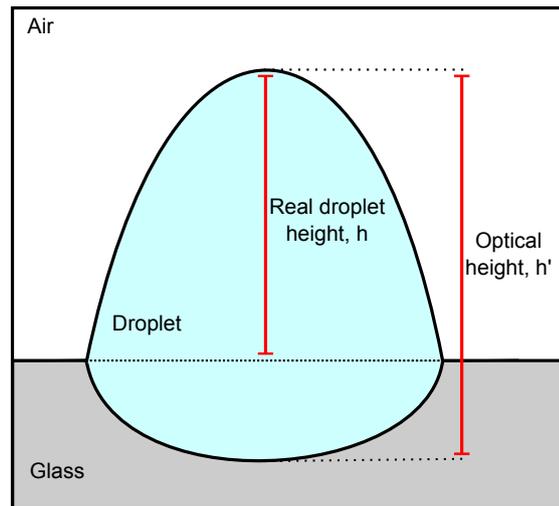
Figure 4.20: Calculating refractive index of a droplet from OCT image

cusing a laser on a single point in space (the focal point) and scanning both laterally across the focal plane and vertically by adjusting the focal length [140]. Both reflected and fluorescent light from the object then passes through the objective lens, which is then with the use of a beamsplitter refocused to a single point, the *confocal point*. A pinhole aperture is then positioned at the confocal point to block out all out-of-focus light, as shown in Fig.4.21, resulting in the detection of all objects in the focal plane only. This technique differs from typical fluorescence microscopes which floods a specimen with light from a single source and excites all particles simultaneously resulting in the detection of all particles, including a large out of focus background. The device then adjusts the focal plane and rescans, resulting in a stack of images which can be compiled into a 3D image. Due to this, confocal microscopy has a much higher optical resolution (typically of the order of a few hundred nanometres [141]) than typical fluorescence microscopy, but requires much longer scanning times.

In preparation for these measurements, I added 30 μl of 1% concentration green fluorescent polystyrene microspheres (Duke Scientific, 1.9 μm diameter) to 5 ml of 10% concentration PEO solution (M_W = 100 kg/mol), giving a final sphere volume concentration of $\approx 0.006\%$. Using a Leica TCS SP5 II confocal microscope with a focused cyan laser, 20$\times$ magnification lens and the provided LAS AF software, I captured a stack of $775 \times 775 \times 10$ μm (x,y,z) images of the perimeter of either a 5 μl or 10 μl droplet, encompassing the total scannable height range of the droplet, and repeated until the droplet was fully dried. Ideally I would
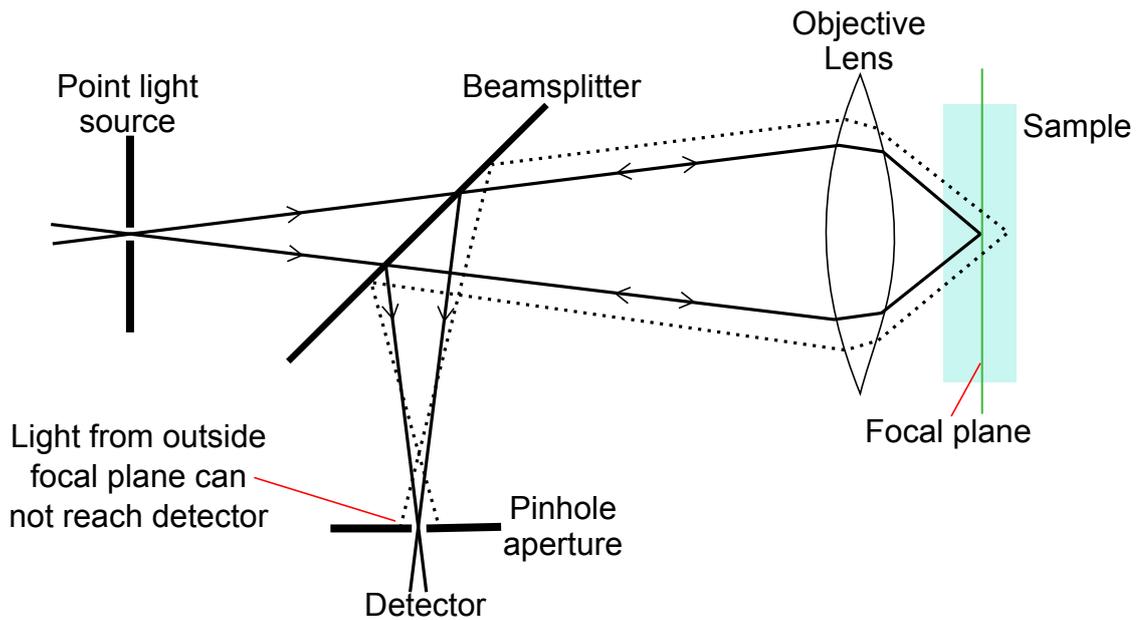
Figure 4.21: Principle of confocal microscopy

have imaged the entire droplet, however this was not possible at these volumes
due to the constraints of the imaging process, and so the perimeter of the droplet
was chosen as the point of imaging as this would give key information on the
direction on direction of convection currents with respect to both the perimeter
and the centre of the droplet. The time required to scan the total height range of
the droplet reduced as the droplet lost height due to evaporation, and so z range
was manually adjusted every 10 stacks to match this change.

4.3.4   Diamagnetic Levitation

One of the obstacles with 3D modeling of a drying sessile droplet is that the con-
tact between droplet and substrate complicates the drying process as discussed
in depth in Chapter 3. A pinned contact line will lead to outward flow via the
coffee-ring effect, and the non-uniform evaporation rate could lead to tempera-
ture and density gradients over the droplet surface, inducing convection currents.
However, if the substrate were removed from the system by evaporating in zero
gravity conditions, these various complications could be removed. I achieved zero
gravity (on a microscopic level [142]) drying droplet conditions through the use
of diamagnetic levitation. Diamagnetism is an intrinsic property of specific sub-

stances (such as water) which causes it to produce a magnetic field in opposition to an externally applied magnetic field. To use this repulsion effect to levitate a droplet of water a high field gradient is required with a local field minima - a magnetogravitational potential trap. Any diamagentic material will naturally repel the region of high field strength, and be attracted to the region of low field strength. This effect is very small compared to the most common form of magnetism, ferromagnetism, which requires very little field strength to produce a visible force. To levitate water the product of the strength of the magnetic field and the gradient in the magnetic field required to induce a force great enough to overcome the effect of gravity is given by the following equation:

$$B\frac{dB}{dz} = \frac{\mu_0 g \rho}{\chi} \tag{4.5}$$

where χ is the magnetic susceptibility, ρ is the liquid density and μ_0 is the permeability of free space. Assuming a completely symmetric magnetogravitational potential trap and no air currents along the z-direction, the minimum $B\frac{dB}{dz}$ required for water is ≈ 1400 T^2/m.

This experiment was performed in collaboration with Richard Hill at the University of Nottingham using a superconducting solenoid magnet with a near room temperature vertical bore (diameter = 5 cm) [142] for levitating PEO droplets with $R \approx 0.5$ cm. Such large droplets are a necessity when depositing a droplet into the magnetogravitational potential trap as without gravity or a substrate it is difficult to remove a droplet from the end of the pipette. The droplets were suspended approximately 80 mm above the geometric center of the solenoid, where the diamagnetic force is equal in magnitude and opposite in direction to the gravitational pull on the droplet [143]. The magnetic field strength and vertical field gradient were $B \approx 12$ T and $dB/dz \approx 120$ T/m respectively at the levitation point.

Fig.4.22 shows the experimental setup for imaging the levitating droplet as it evaporated in the bore. The CCD camera was required to stay at a significant distance away from the bore due to the high magnetic field. Images of the droplet were captured from the side and above, however due to the different path lengths the light must travel between the droplet and camera for the two droplet images shown in Fig.4.22, both views could not be simultaneously captured in focus, and so the side-on view was chosen as the in-focus image for the duration of the experiment. Additionally, preliminary experiments showed that as the droplet
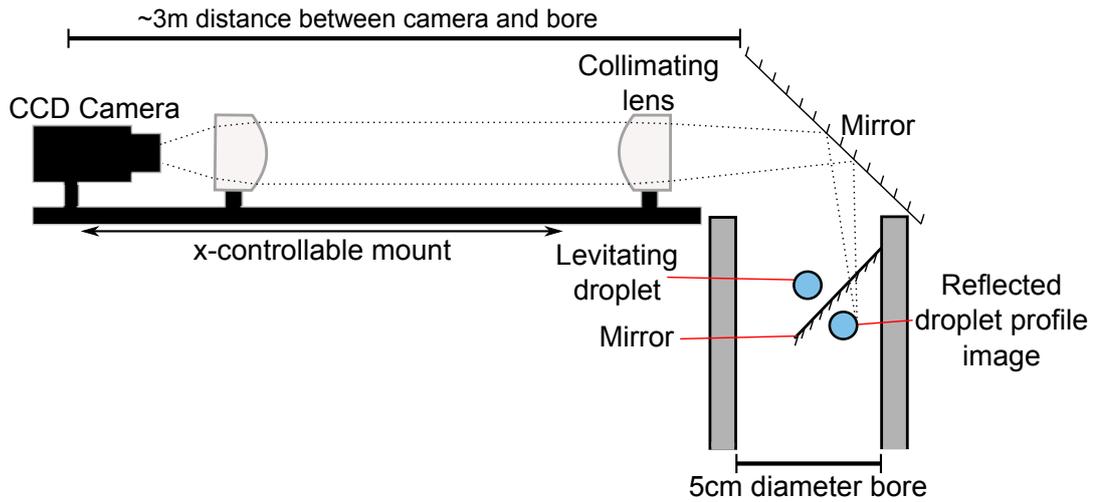
Figure 4.22: Diamagnetic levitation setup

dries and loses volume the droplet position drifts slowly down into the bore, possibly due to the different magnetic susceptibility of PEO to water [144]. This means imaging from above becomes slowly out of focus over time, whereas profile images will remain in focus for the entirety of the experiment. The known width of the mirror inside the bore (2.5 cm) was used as a reference length for measuring droplet $V(t)$ from the captured images. Despite the droplet being confined to a spherical magnetogravitational potential trap, both the surface tension and diffusivity of the vapour molecules are not expected to be affected by the magnetic field, so assuming no air currents the field should not alter the evaporation rate. However, because the bore is slightly cooler than room temperature ($T_{\text{bore}} \approx$ 15°C), a downward air draft is set up inside the bore, and as discussed in Chapter 3 a quiescent atmosphere is one of the prerequisites for a diffusive controlled evaporation profile. Therefore we would now potentially expect the evaporation rate to scale with the drop surface area ($V \propto A$) rather than drop radius ($V \propto R$). This predicted alteration to the drying behaviour, while interesting and warranting further examination, is not investigated in this thesis.

4.4 Non-droplet measurements

4.4.1 Rheology

As discussed in section 2.3.2 complex fluids such as polymer solutions can exhibit both *viscous* and *elastic* responses under shear stress, depending on the timescale of the applied force. When considering an evaporating droplet of polymer solution, shrinkage due to volume loss could be seen as deformation of a complex fluid under stress with an associated timescale - the evaporation rate. It is possible that the complex component of the fluid (the polymer entanglements) could exhibit either a viscous flow or elastic stretching response to this evaporative flux. To this end, in this section I discuss how I measured the cross-over point between G' and G'' (the storage and and loss moduli) against frequency for PEO solutions with various values of c_0 and M_W to find the local evaporative timescales required to induce an elastic response.

To characterise the viscoelastic behaviour I used an oscillating cone and plate technique as described in section 2.3.2. By using a rheometer we can control the oscillation variables of amplitude and angular frequency. By then measuring the applied force required to induce the specified shear rate, the rheometer can calculate the storage modulus G' and the loss modulus G''. Oscillation experiments were performed with a Carri-Med CSL2-100 rheometer, Brookfield CPE-40 cone spindle ($R_S = 2.4$ cm, $\theta = 0.8°$) and peltier plate (Temperature set at 10° to reduce the rate of evaporation) with the gap manually set at $d = 46$ μm and Volume $V = 0.65$ ml. An amplitude sweep was performed to find the central point of the $\tan(\delta)$ plateau region. This value was often found to be at ≈ 0.2. Setting $\tan(\delta)$ at 0.2, an angular frequency sweep was performed in the range 0.01 to 250 rad/s.

4.4.2 DSC - Differential Scanning Calorimetry

Differential scanning calorimetry (DSC) is a thermoanalytical technique in which the amount of heat required to increase the temperature of a known mass of a given substance is compared with a reference pot which is maintained at the same temperature, as shown in Fig.4.23. The heat input program is designed so that
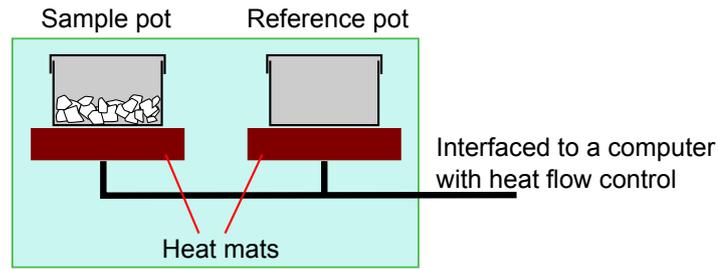
Figure 4.23: DSC sample and reference pot

the temperature ramp remains the same in both the sample and reference pot. The basic principle underlying this technique is that when the sample undergoes a phase transition, more or less heat is required to maintain the constant rate of change of temperature depending on whether the transition is endo or exothermic. For example, as a solid sample melts to a liquid, it will require additional thermal energy in order to break the highly ordered solid structure and maintain the same temperature as the reference pot, which is why at $T = T_\mathrm{m}$ there is a peak in Fig.4.24. Conversely, as a sample undergoes crystallization, thermal energy is released from the sample during the molecular ordering process, and therefore less heat is required to maintain the temperature increase. The difference in heat flow between the sample and reference during a linear temperature increase or decrease will show what type of phase transition is occurring, and how much energy this transition absorbs or releases. Fig.4.24 is a schematic of the typical curves DSC will produce as a sample goes through glass (T_g), crystallisation (T_c) and melting (T_m) phase transitions.
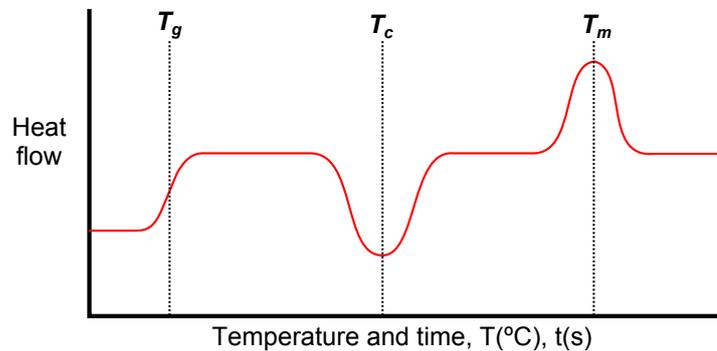
Figure 4.24: DSC phase transition curves

To compare the degrees of crystallinity between structures of dry PEO I placed

a known mass (weighed individually with a Kern ALJ160-4NM mass balance to within 0.1 mg) of each separately into the DSC device as shown in 4.23 and performed multiple scans over the temperature range 30 to 80°C, covering the known melting point of $M_W = 100$ kg/mol PEO, $66 < T_m < 75$°C [145].

The most exciting phrase to hear in science, the one that heralds new discoveries is not "Eureka!", but "That's funny"...

ISAAC ASIMOV

Chapter 5

PEO Droplet Pillaring

This chapter presents an in-depth examination of the drying behaviour of PEO-water droplets with particular focus on the effects of concentration, contact angle and volume on the fully dried structure, while the solvent, atmospheric conditions and molecular weight are kept constant. These droplets appear to exhibit four distinct stages during evaporation, including: pinned drying, where volume, surface area and height decrease while base radius remains pinned; pseudo-dewetting, where polymer precipitation at the contact line drives the liquid phase to retreat inwards; boot-strap building, where the liquid appears to be lifted upwards by the polymer precipitate and form a novel tall central "pillar" that is unlike anything observed in other drying polymer systems; and late stage contraction in which the pillar slowly shrinks in size as remaining solvent is lost. Possible driving mechanisms behind the formation of these unusual structures are discussed, including: skin-buckling; autophobism; and mechanical squeezing from a contracting semi-crystalline collar. The first two options, while well established effects in dewetting and polymer drying systems [7, 146], appear to be unlikely candidates when the experimental observations presented in this chapter and the next are taken into account. Pillar formation is unaffected by initial droplet volume, but highly dependent on initial concentration and contact angle, with a minimum value in either case below which pillar formation stops and typical coffee-ring type formation begins. These minimum concentration and contact angle criteria are explained as a consequence of the geometry of the droplet when precipitation begins ($t = t_{\mathrm{p}}$).

The reader may notice that these results chapters are not structured in a typical manner compared with other theses. While most thesis results chapters follow a similar structure to a peer reviewed paper, to write this body of work in that manner would not do the investigative process justice. The slow progression of observations and various hypotheses explored are as crucial to this work as the final conclusions. After all, any researcher should always remember that there may be evidence contrary to your theories just around the corner, so to simply forget a hypothesis which was eventually disproven does a disservice to the scientific method. With that in mind I have attempted to write these three chapters as a story, starting with the initial results of varying concentration, the conclusions made from these results, and the ongoing progression in terms of experiments, hypotheses and tests made from that point forward.

By the end of this chapter, I also hope to have inspired the reader to double check what fully dried structures have formed the next time they find an old spillage to clean up, and then to ask themselves "can I explain that?".

5.1 The Drying Process

5.1.1 10% Concentration

To begin with, PEO solutions of 10% polymer mass fractions were chosen as the standard solutions for drying droplet observations. This is because preliminary experiments showed that $c_0 = 10\%$ is both significantly higher than the minimum concentration required for pillar-like structures to form ($\sim 3\%$), but is also not so high that structural instabilities occur during drying ($\sim 25\%$), both of which are behaviours that will be discussed later. Fig.5.1 is a time-lapse sequence of profile images captured from a single $c_0 = 10\%$ droplet over the course of drying. $M_W = 100$ kg/mol and $V_0 = 10$ μl were chosen for similar reasons: preliminary experiments showed that 100 kg/mol seems to be a narrow region in which the interesting pillar formation process occurs, and 10 μl is large enough that some details of the drying process can be seen by eye, but are not so large that the droplet height exceeds the capillary length, at which point gravitational effects become important to the droplet shape. Furthermore, unless otherwise stated, relative humidity and temperature are constant at $RH = 55 \pm 5\%$ and $T =$

$22\pm1°$C respectively. This statement is true of all three results chapters. From the
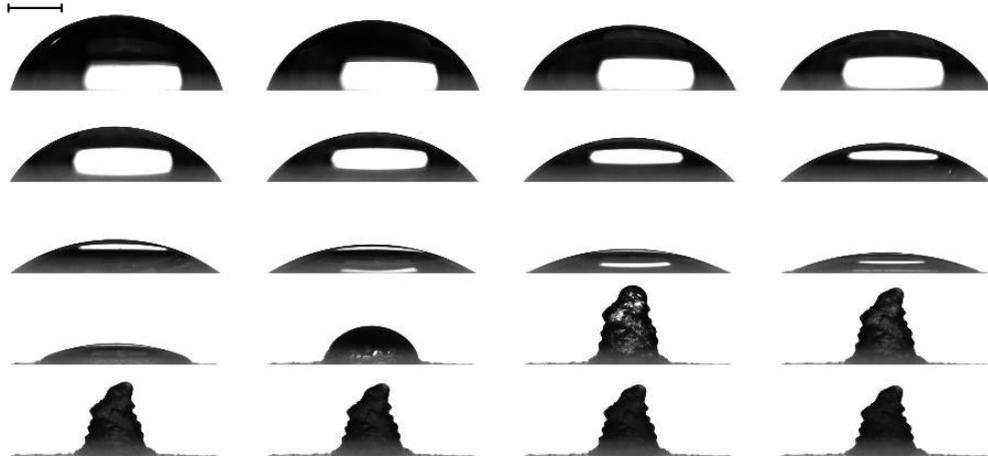
Figure 5.1: Time-lapse sequence of profile images of a drying PEO droplet ($c_0 = 10\%$, $V_0 = 10 \ \mu l$) with 5 minute time step between images, in order from left to right and top to bottom. Scale bar represents 1mm.

first 3 rows, the droplet seems to be displaying simple pinned droplet behaviour, in which the contact line and droplet radius R are fixed while the volume V, height H and contact angle θ_c reduce almost linearly. However, by the fourth row, something unusual happens which leads to the formation of the irregular structure in the last 6 images. At a certain time, the liquid droplet appears to become unpinned from the substrate and recede inwards with a steadily increasing contact angle, and eventually solidifies into a tall central structure.

Fig.5.2 is the same droplet as viewed from above using the observation methods detailed in Chapter 4. The bright light reflections in the early images are an unfortunate but unavoidable consequence of the diffuse back-light used for acquiring good quality profile images. From this set of images it should become clear that during the stage where the droplet appears to become unpinned and recede inwards in the profile images, a thin layer of solid PEO is deposited where the droplet was previously wetting the substrate. Because prior to this receding stage the droplet has not reached its receding contact angle (measured independently at $\theta_r \approx 10°$), and because precipitation is always a precursor to droplet receding, it would appear that precipitation drives the receding stage rather than typical contact line dewetting.

Fig.5.3 is a time-lapse sequence of images of the solid layer formed during precipitation as viewed under a $2\times$ magnification lens with cross-polarising filters.
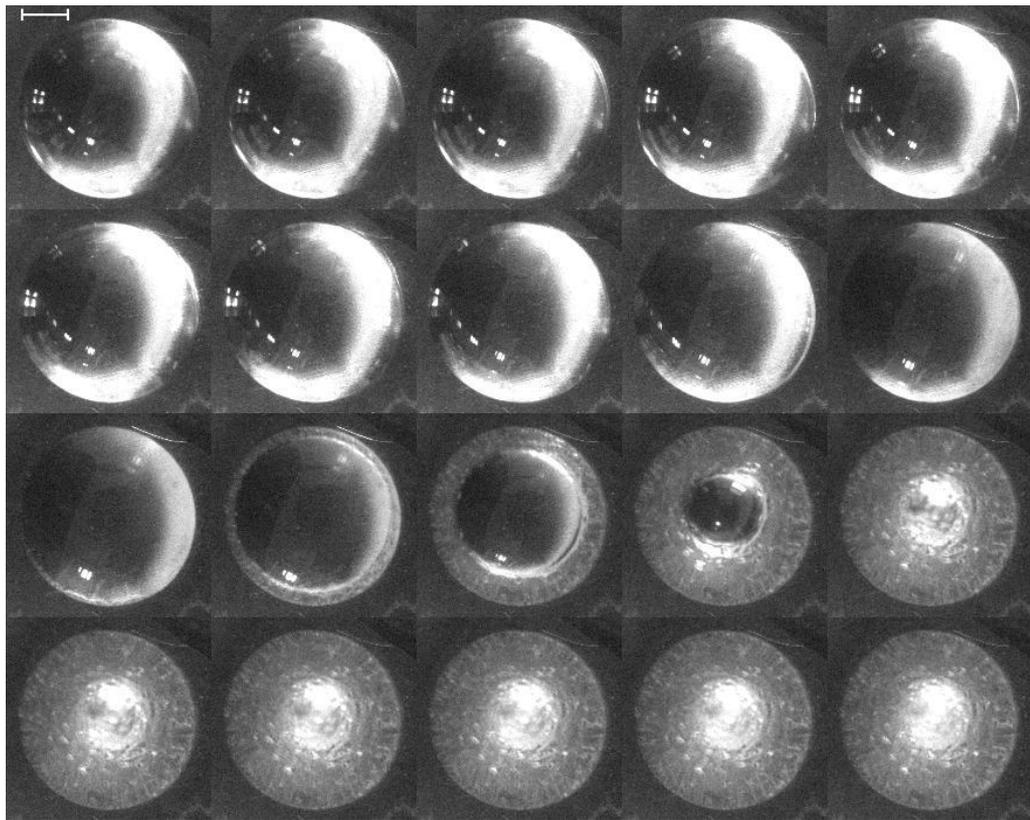
Figure 5.2: Time-lapse sequence of images of a drying PEO droplet ($c_0 = 10\%$, $V_0 = 10$ μl), with 5 minute time step between images captured from above, in order from left to right and top to bottom. White scale bar represents 1 mm.

The images remain dark until precipitation begins which shows that this growing solid layer is birefringent. This strongly suggests that the solid layer is made of a large number of spherulites, and it is the nucleation of these small semi-crystalline spherulites around the droplet perimeter which leads to the retreating of the liquid phase. Furthermore, capturing these images from below led to the
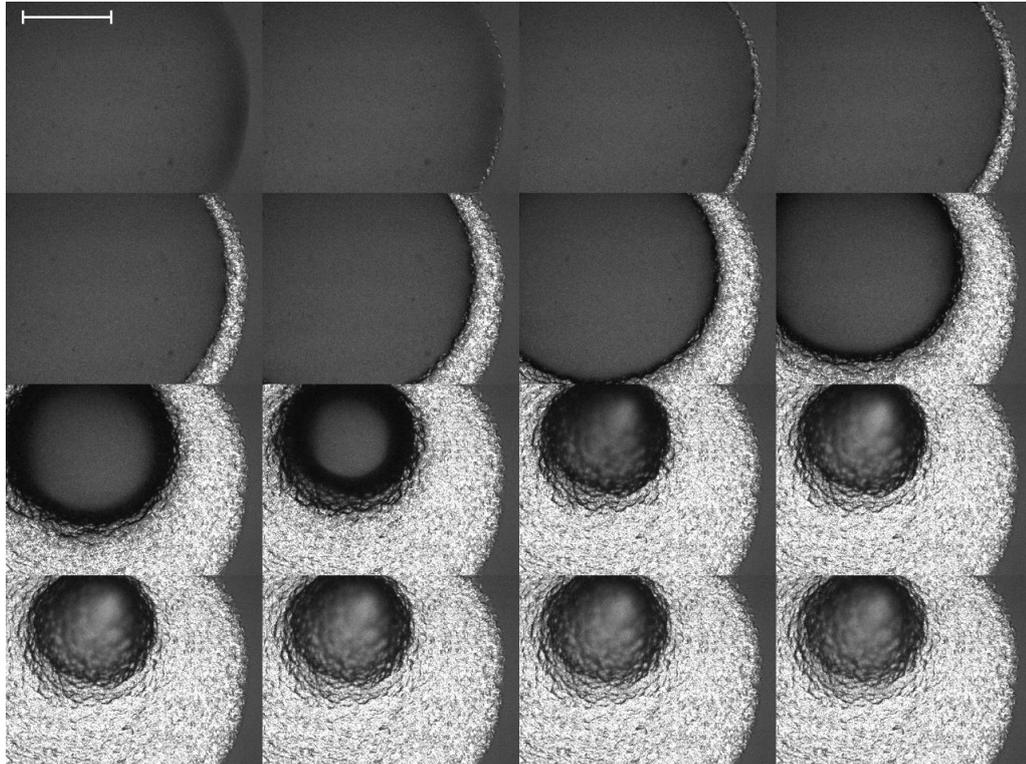
Figure 5.3: $2\times$ magnification images of 10% PEO droplet, captured from underneath through cross-polarized filters. Time step between images 2.5 min. Scale bar represents 1 mm.

observation that the central region is not entirely dry as the tall solid structures form, but rather encloses a large amount of liquid. With a careful eye, the reader should also see that the last few images of Figures 5.1 and 5.2 show that after the solid spherulite layer has fully formed over the surface of the remaining liquid, the tall pillar structure gets progressively opaque and smaller as time goes on. This suggests that the solid region is both permeable to the evaporation of the remaining water enclosed within and compressible as volume loss does not lead to surface buckling.

5.1.2   The Four Stages

As detailed in Chapter 4, with good quality side on images and the use of a computer interfaced mass balance, measurements of droplet surface area A, volume V, height h, liquid base radius R and mass m could be taken as the droplet dries. Fig.5.4 is a plot of these measurements from a standard $c_0 = 10\%$ PEO droplet, with each measurement normalised by its initial values A_0, V_0, h_0, R_0 and m_0. The vertical dotted lines represent key points in time at which changes in droplet
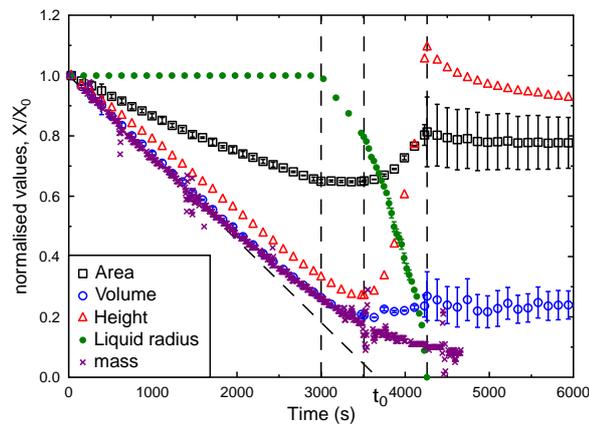
Figure 5.4: Plot of normalised surface area, volume, mass, liquid radius and height against time for a single PEO droplet, initial concentration $c_0 = 10\%$ calculated from droplet profiles. Vertical dashed lines separate time into four stages: pinned drying; pseudo-dewetting; boot-strap building; and late stage contraction. Diagonal dashed line represents volume and mass trajectory from initial drying rate and crosses horizontal axis at $t = t_0$.

behaviour occur. These four distinct behaviours can be observed from both the raw images and the normalised plots. Fig.5.5 is a diagram of the four stages, with
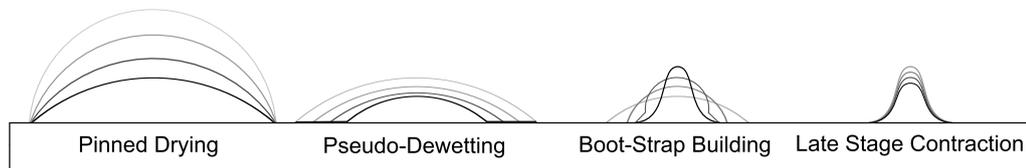
Figure 5.5: Digram of the droplet surface profile changes with time during the four stages of drying: Pinned Drying; Pseudo-Dewetting; Boot-Strap Building; and Late Stage Contraction.

each stages given its distinctive name: Pinned Drying; Pseudo-Dewetting; Boot-

Strap Building; Late Stage Contraction, and are described in detail as follows:

Pinned drying

The normalised plots show that during this stage the droplet height and volume appear to decrease almost linearly. The dashed line marks the initial linear trajectory of the volume and mass curves, which only deviates away from the measurements over the final quarter of the pinned stage. It would be expected for the evaporation rate to remain constant for the duration of the pinned stage as the droplet radius is fixed, and as shown in Chapter 4 that $\dot{V} \propto R$. The early mass and volume plots show good consistency between mass balance and profile image analysis methods of measuring the evaporation rate of the droplet. The deviation away from the dashed line towards the end of the pinned drying stage are possibly due to concentration effects, which are discussed in more detail in section 5.2.2. This stage ends when the concentration at the droplet perimeter reaches the saturation concentration c_{sat}, which is also known as the precipitation time, $t = t_{\text{p}}$.

Figure 5.6: Time-lapse profile images of drying droplet during stage one - pinned drying. Total duration 50 minutes. Scale bar represents 1 mm.

Pseudo-dewetting

This stage is named as such due to the appearance of a freely receding, or dewetting, contact line. However, we have already shown this is not true dewetting as it is driven by polymer precipitation, and true dewetting leaves no trace behind, whereas here a thin layer of solid PEO is being deposited. During this stage the liquid base radius reduces, the surface area appears to remain constant and the height continues to reduce. This stage is often short lived, and as we will see later, sometimes skipped. Precipitation seems to always begin at the perimeter, which drives motion of the liquid phase away from the precipitating region. Perimeter precipitation is highly reminiscent of the previously discussed coffee-ring effect,

in which suspended grains are swept to the contact line due to pinned drying induced advective flow to the perimeter. I have also shown in Chapter 3 that an enhanced evaporative flux at the contact line should influence this advective flow, and therefore we would expect this to play a role in the polymer contact line precipitation. A simple test for this is to observe the final structures that form from of an array of PEO droplets. The close proximity of many droplets in the centre of the array will create a localised highly humid region around the centre of the array, which in turn will create a region of reduced evaporation rate. Therefore, any given droplet at the perimeter of the array will dry fastest in the direction away from the region of high humidity, which we would therefore expect to lead to earliest precipitation at the outermost edge of these droplets. If precipitation truly drives the liquid to recede away from the solid region, then the final pillar structures should then point toward the centre, which is is exactly what is shown in Fig.5.8.

Figure 5.7: Time-lapse profile images of drying droplet during stage two - pseudo-dewetting. Total duration 8 minutes. Scale bar represents 1 mm.
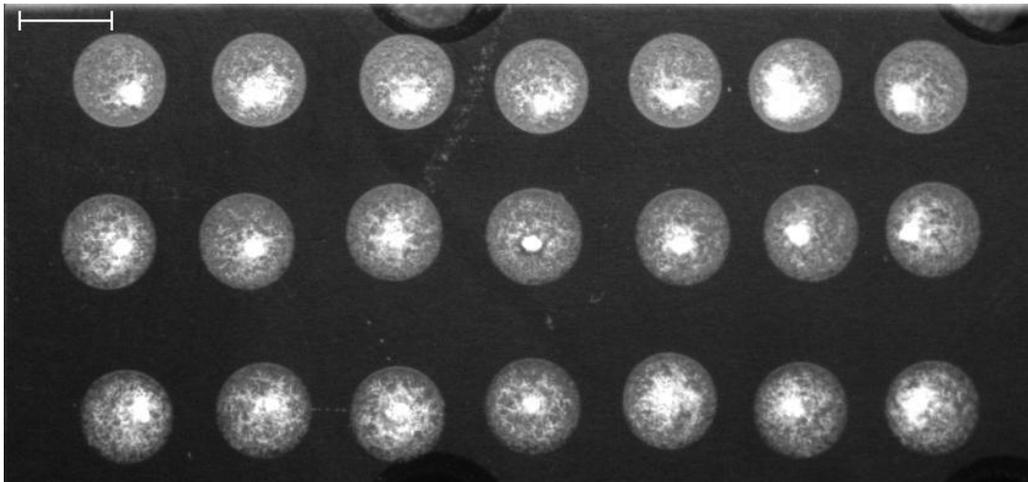

Figure 5.8: Image of the final structures formed from a 3×7 array of PEO droplets. The most central droplet formed a highly symmetric pillar, whereas the pillars formed from the outermost droplets point towards the centre of the array. Scale bar represents 4 mm.

Boot-strap building

The driving force behind this stage and the previous stage are identical: spherulite formation. However, there is a key difference which can be clearly seen in the normalised data, which is a necessary factor for pillar formation: height increase. At some point the effect of the receding contact line, which would tend to increase height in a fixed volume droplet, overcomes the height reducing effects of evaporation. This stage of height increase has been coined "boot-strap building" due to the unusual self-lifting properties, as the liquid is being lifted up by its own deposit. This height increase continues until the spherulites have completely encased any remaining liquid. Additionally, from the normalised plot it can be seen that not only does the height increase but the surface area also increases. This is an important observation as we will see later.

Figure 5.9: Time-lapse profile images of drying droplet during stage three - boot-strap building. Total duration 13.5 min. Scale bar represents 1 mm.

Late stage contraction

All remaining liquid is now encased in a semi-crystalline layer of unknown thickness. This layer is somewhat permeable to water, and the inner volume reduces with time, leading to a late stage shrinking of the structure. The total duration of this stage is difficult to measure as the late stage evaporation rate is very slow, as shown in the normalised mass data. This evaporation rate is possibly a function of the increasing thickness of the semi-crystalline layer, which is difficult to measure dynamically without disturbing the drying process.

Figure 5.10: Time-lapse profile images of drying droplet during stage four - late stage contraction. Total time lapsed in images 50 minutes. Scale bar represents 1 mm.

5.2   Effect of Concentration

As briefly mentioned earlier, initial concentration can vary this behaviour by either removing the pillaring effect entirely at low concentrations, or causing highly asymmetric and structurally unstable morphologies at high concentrations. In this section the effect of c_0 on both the drying process and the fully dried structures are discussed.

5.2.1   Below The Pillaring Concentration

At low concentrations, I have observed both flat uniform deposits and structures that highly resemble the common coffee-ring stain, with one or two key differences. The lower concentration limit to pillar formation lies at approximately $c_0 = 3\%$ (at ambient conditions $T = 22 \pm 1°C$ and $RH = 55 \pm 5\%$, independent of droplet volume). Figures 5.11 and 5.12 are image sequences of the same 3% droplet captured from the side and above.

Figure 5.11: Time-lapse profile images of the drying process of a PEO droplet, $c_0 = 3\%$. Total duration 1hr 12mins.

Despite leaving an almost uniform deposit, the images captured from above (particularly the seventh image) show that the droplet still exhibits the pseudo-dewetting stage as a result of PEO precipitation at the droplet perimeter. However, precipitation occurs much later in the droplet lifetime, as one would expect with a lower initial concentration. This means that both the height and the
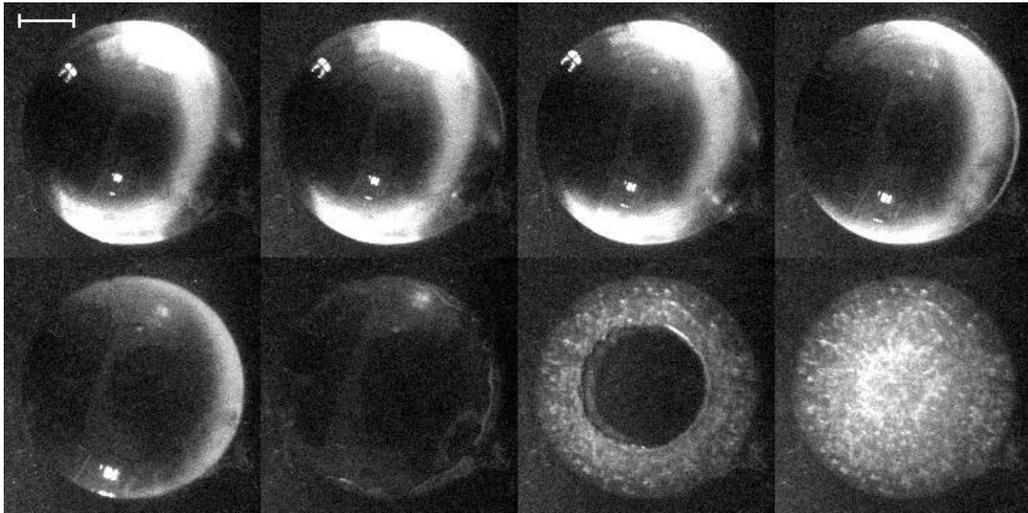
Figure 5.12: Time-lapse images of the drying process of a PEO droplet, $c_0 = 3\%$, as viewed from above. Total duration 1hr 12mins.

contact angle when the droplet reaches the precipitation time t_p is significantly reduced. This seems to have the effect of removing the boot-strap phase entirely.

Reducing concentration further leads to similar behaviour, as shown in the series of images focusing on the pseudo-dewetting stage of a 2% initial concentration droplet in Fig.5.13. Unlike at 3%, here the liquid base radius abstruptly stops retreating part way between $R = R_0$ and $R = 0$, and leaves an apparently empty central region surrounded by a thick coffee-ring like stain. Using cross
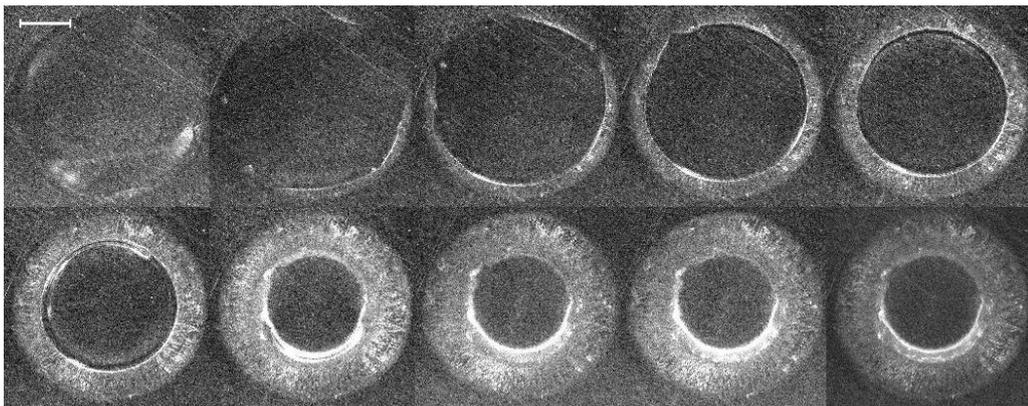
Figure 5.13: Time-lapse images of the pseudo-dewetting stage of a 2% initial concentration droplet, captured from above. Total time 6.5 minutes.

polarized filters through a 2× magnification lens, it was actually found that this central region is not devoid of precipitate, but rather formed a very thin layer of

large spherulites as shown in Fig.5.14. Note that although similar in appearance, Figures 5.13 and 5.14 are not the same droplet.
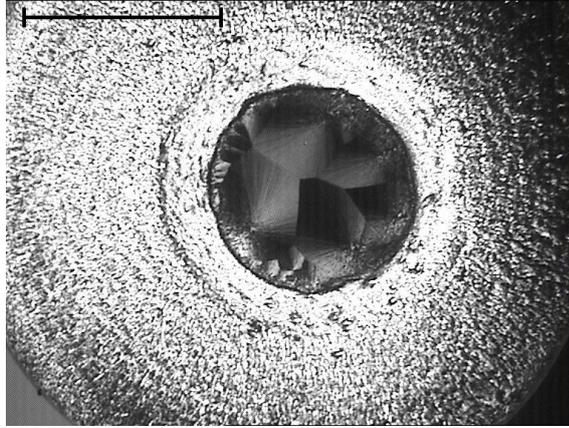
Figure 5.14: Image of a fully dried 2% droplet captured with a $2\times$ magnification lens through cross polarised filters showing that the "empty" central region contains well defined semi-crystalline spherulites. Scale bar represents 1 mm.

Fig.5.15 is a plot of the surface profile of a fully dried 2% initial concentration droplet in a single x-z plane as extracted via surface profilometry. This gives a measure of the thickness of the thin central region at $h_c \sim 23 \pm 3~\mu$m, which as can be seen from Fig.5.15 is around the order of $5\times$ smaller than the thickness of the outer layer deposited during the pseudo-dewetting stage. Note also that the thickness of the outer region is greatest nearer the centre, whereas typical coffee-ring stains are thickest at the perimeter. This is evidence for the contracting collar theorem that will be discussed later in this chapter and then again in the next.

Reducing the concentration to $c_0 = 1\%$ led to a narrowing of the coffee-ring like structure, and thus a larger "empty' region, and allowed for better imaging of the spherulites that form from the central thin film. Fig.5.16 is a time-lapse sequence of images of the fast growth of spherulites as the thickness of this thin wet film diminishes.

5.2.2   Above The Pillaring Concentration

Fig.5.17 is a time-lapse sequence images of the pseudo-dewetting and boot-strap building stages of drying droplets with initial concentrations $c_0 = 5, 10, 15, 20,$
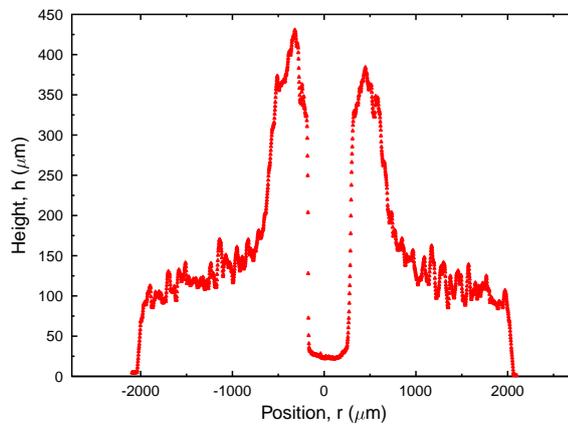
Figure 5.15: Height profile of a fully dried PEO droplet ($c_0 = 2\%$) in a single x-z plane as measured via stylus profilometry.
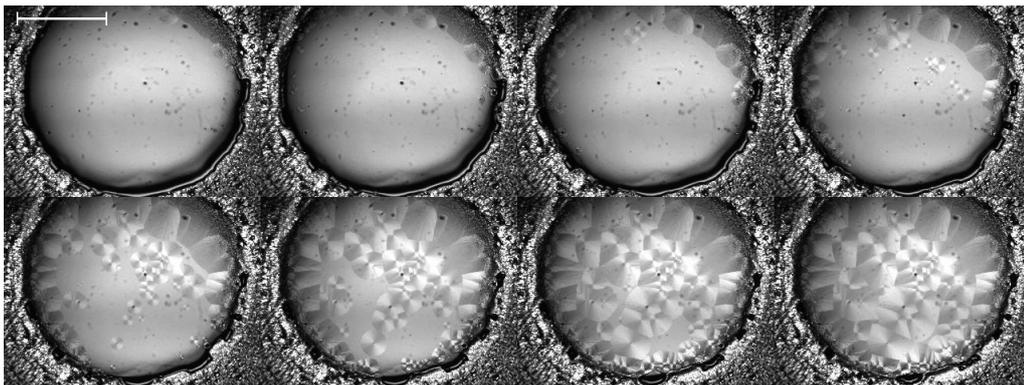

Figure 5.16: Time lapse images of the growth of spherulites in the thin central region of an almost fully dried 13 μl droplet ($c_0 = 1\%$), captured under $2\times$ magnification through cross polarized filters. Total duration 21 s. Scale bar represents 1 mm.

25 and 30%. While from top to bottom, each column represents the total time taken between t_p (the precipitation time) and t_f (the time at which the surface of the structure has fully solidified), this does not mean that the time step between individual images is the same. Indeed there seemed to be some random variance in the duration of the second and third stages, possibly due to random fluctuations in ambient conditions. Over 10 repeats, this total $t_f - t_p$ timescale remained fairly constant ($\approx 1190 \pm 120$ s), and so these relative time steps are aligned in this figure.

From the first four columns it would appear that the tall central structures simply increase in size with initial concentration, which is not too surprising as the initial quantity of polymer per droplet increases. However, at 25%, the structures no longer remain cone shaped but formed highly asymmetric tall pillar structures, which often during the growth stage will show regions in time in which the liquid phase spills over the side of the solid region, as shown in the last two images in the far right column in Fig.5.17. Also worth noting is that the contact angle at the time of solid precipitation t_p increases with initial concentration. This is simply due to the region at the perimeter of the droplet requiring less time to reach the saturation concentration $c_{sat} \approx 50\%$ as c_0 is increased.

These are just a select few of the initial concentrations experimentally observed. To further examine the apparent four stages these droplets exhibit, the volume, surface area, height and radius were measured with time from the profile images. Fig.5.18 shows 8 plots of these measurements normalised with their initial values as a function of time for droplets with initial concentrations $c_0 = 4, 5, 7, 10, 12, 15, 20$ and 25%. Higher than 25% led to erroneous results due to the toppling over of the droplet during the boot-strap stage, and so only data prior to toppling was extracted, which has not been included in this figure. At this point the labels t_g and t_f have been added to the plots as the times at which vertical growth begins and finishes respectively.

Several observations can be made from this plot:

- $t_f - t_p$ does not have a clear dependence on concentration. Furthermore, the average receding speed was extracted from these measurements and plotted against initial droplet concentration as shown in Fig.5.19. This shows that receding speed, which we assume to be equivalent to radial spherulite growth
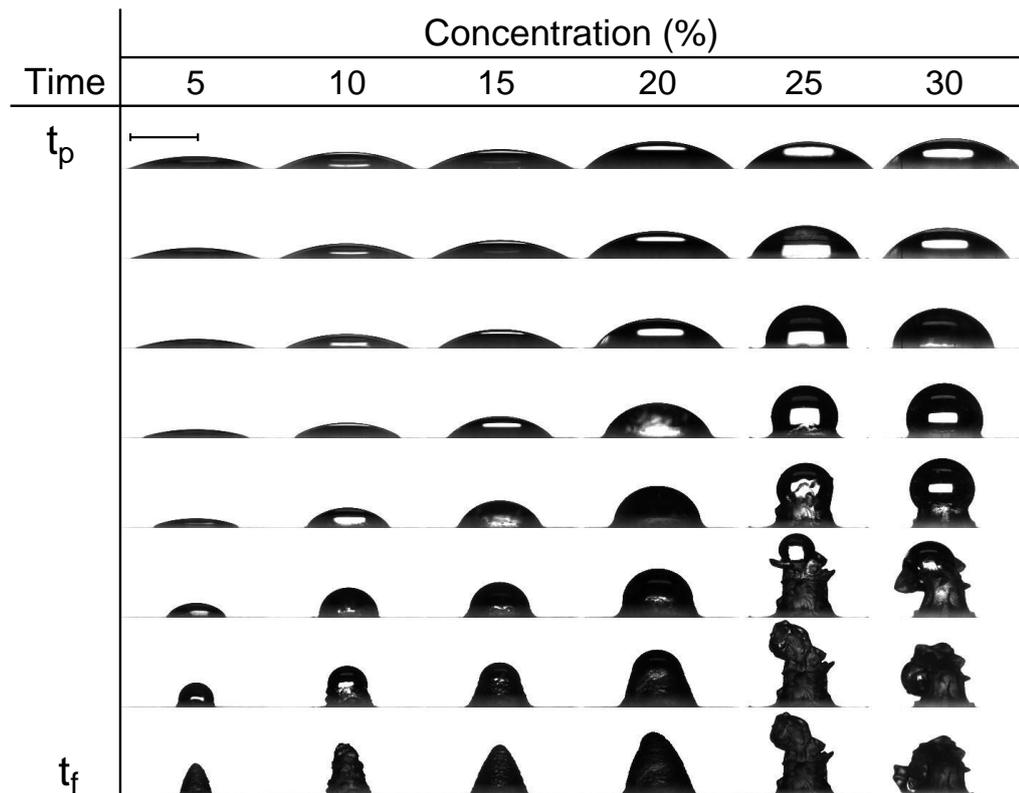
Figure 5.17: Six vertical time-lapse droplet image sequences captured during the pseudo-dewetting and boot-strap building stages. From left to right, initial concentration $c_0 = 5$, 10, 15, 20, 25 and 30%. From top to bottom is the time axis, with total time taken equal to the difference between the precipitation time and the time at which surface crystallisation stops ($t = t_{\mathrm{f}} - t_{\mathrm{p}}$). Scale bar represents 2 mm.
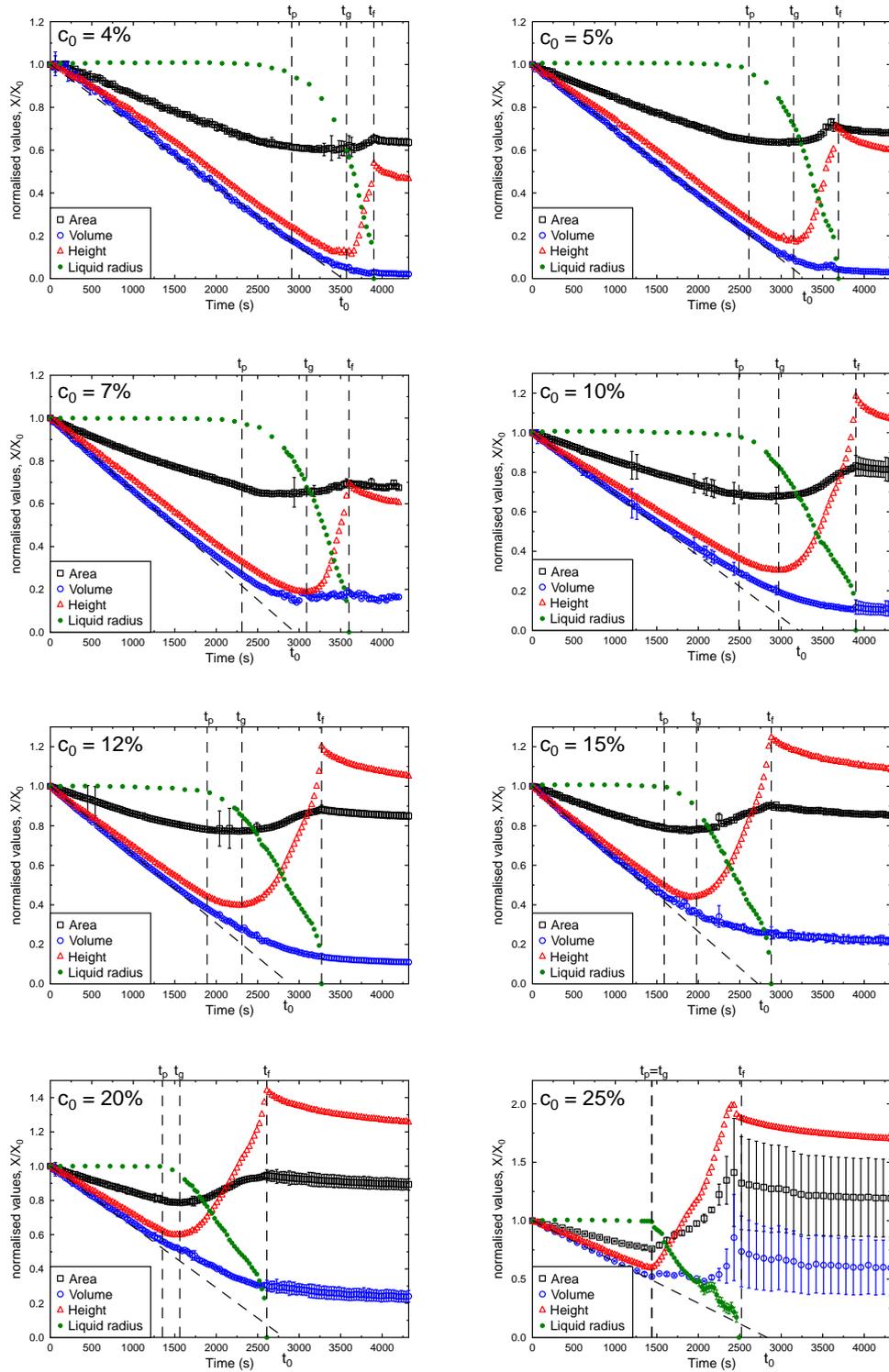
Figure 5.18: Plots of normalised surface area, volume, liquid radius and height against time for droplets of various initial concentrations.

rate, is fairly constant with no dependency on initial droplet concentration. The weighted average value of $\dot{R}$ was calculated at -1.6 ± 0.3 μm/s.
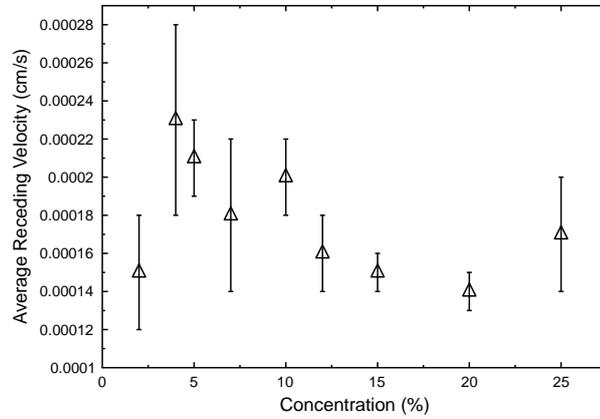
Figure 5.19: Plot of the average receding speed during stages 2 and 3 as a function of initial concentration.

- During the pseudo-dewetting stage in which the remaining liquid both re-cedes, loses volume and height, the surface area remains constant. This seems to be a repeating factor for all droplets irrespective of the initial conditions.

- Surface area shows a significant increase during the boot-strap building stage. Fig.5.20 is a plot of the normalised surface area for $c_0 = 5, 10, 15$, 20 and 25% plotted against time normalised by t_0, the total drying time as extrapolated from the linear fit to the initial evaporation rate, $\dot{V}$. Each plot has been off-set in the y-axis for clarity.

- Precipitation time (t_p) decreases with concentration. This is the least sur-prising results as one would expect that the higher the initial concentration, the less time required for the concentration at the perimeter to reach the saturation concentration $c_{\mathrm{sat}} = 50\%$. In the next chapter we will use these data points more carefully to extract an estimate of the diffusion coefficient of the polymer in solution.

- $t_\mathrm{g} - t_\mathrm{p}$ decreases with concentration, and indeed vanishes when $c_0 = 25\%$. This means that droplets which exhibit all four stages lie in an intermediate range in concentration $3\% \leq c_0 \leq 25\%$. When $c_0 \leq 3\%$ boot-strap growth vanishes, and when $c_0 \geq 25\%$ pseudo-dewetting vanishes.
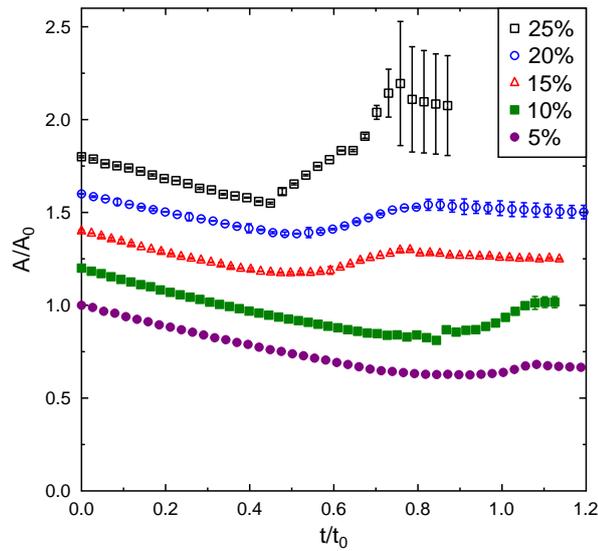
Figure 5.20: Plots of A/A_0 against time normalised by t_0 for various initial concentrations. Each successive plot is offset in the y-axis by 0.1.

Fig.5.21 is a plot of evaporation rate $\dot{V}$ against c_0 over a large number of repeats and shows no systematic variation with initial concentration. This a slightly sur-
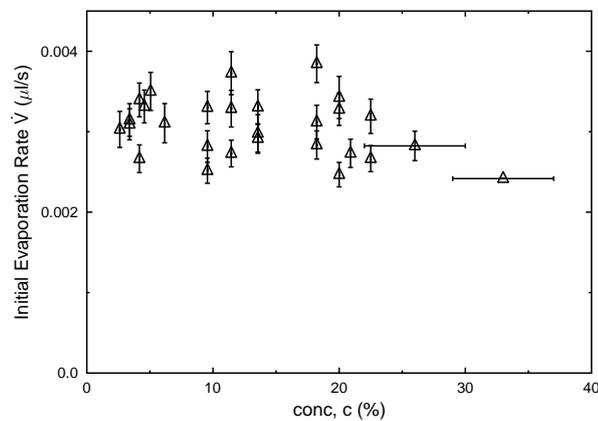
Figure 5.21: Plot of initial evaporation rate $\dot{V}$ against initial droplet concentration.

prising result as higher polymer concentration means lower water concentration at the surface and therefore a lower evaporation rate would be expected. Indeed, the amphiphilic properties of PEO mean the hydrophobic CH_2 units will preferentially go to the interface and the O units will hydrogen bond with the water. As shown in Fig.3.14, at concentrations above $\sim 0.1\%$, surface tension decreases

with increasing concentration, which suggests that not only is the concentration of the bulk increasing, but the local concentration of at the interface is also increasing. Possibly there is a subtle decrease in evaporation rate with increasing concentration, which is supported by the normalised volume curves in Fig5.18, which show a slow deviation away from the linear fit to the initial evaporation rate. Perhaps slight variations in temperature ($T = 22 \pm 2$°C), relative humidity ($RH = 55 \pm 5\%$) and radius ($R_0 = 0.20 \pm 0.02$ cm) were significant enough to skew the evaporation rate versus concentration data plot. With this in mind, we will explore the effects of droplet size on both the fully dried structures and the evaporation rate in the next section. Atmospheric conditions will be considered in much greater detail in Chapter 6, but for now these results seem to suggest that initial concentration does not affect $\dot{V}$. This result agrees with the assumption that evaporation is limited purely by vapour diffusion as discussed in Chapter 3, rather than being limited by the rate of escape of water molecules from the droplet surface. We would therefore expect evaporation to increase proportionally with the droplet base radius [85].

5.2.3   Volume effects
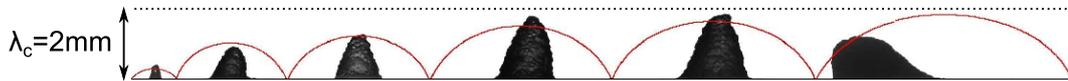
Figure 5.22: Effect of initial volume on the PEO structures at $t = t_\mathrm{f}$. Solid red lines are the initial droplet profiles. From left to right $V_0 = 0.4$, 5, 10, 20, 30 and 50 μl. Dotted line represents the maximum droplet height limit given by the capillary length $\lambda_\mathrm{c} \sim 2$mm.

Fig.5.22 shows the structures formed at the end of the boot-strap building stage for droplets with initial concentration $c_0 = 10\%$ for a range of initial volumes $V_0 = 0.4$, 5, 10, 20, 30, 50 μl. This point in time (t_f) was chosen for consistency rather than images of the fully dried structures as the time at which all the water has evaporated is not well defined. The maximum volume chosen was 50μl as at this volume the droplet height approached the capillary length of water ($\lambda_\mathrm{c} \sim 2$ mm), as shown by the dotted line in the figure. Above this point, gravitational effects cause the droplet to flatten at the peak thus losing their spherical cap shape and can no longer be satisfactorily described as droplets at all, but rather

small puddles.

Fig.5.22 shows that provided the droplet has a height below $\sim 0.8\lambda_c$, initial volume has no observable effect on the drying process. As droplet height approaches the capillary length however, gravity effects become important. The final structure is the result of the liquid phase toppling over during the growth stage, which led to the asymmetric structure shown. However it should be noted that the toppling over does not necessarily correlate with the height approaching λ_c, but is clearly more related to the structure during the growth stage. It may be fortuitous that the droplet size at which the interface is deformed by gravity is also the volume at which growing structures become unstable.

5.2.4 Droplet Evaporation Rate

The evaporation rate has been extracted from both the mass and volumetric data acquired from a large range of droplets at various values of c_0 and V_0. In section 3.3.4 it was shown that evaporation rate should be proportional to droplet base radius. Fig.5.23 is a plot of $\dot{V}$ (calculated primarily from $V(t)$ measurements from droplet profiles) against R_0, and is in good agreement with linear dependency predictions of a vapour diffusion limited evaporation model. The dotted lines represent the upper and lower errors on the gradient based on the weighted average linear fit to the data.

It would seem that the evaporation rate is proportional to the radius, but this does not answer the question of whether this proportionality remains during the pseudo-dewetting stage. Calculations of the evaporation rate during this phase are difficult for several reasons. Firstly, measuring the gradient between each point on the volume curve is not a reliable method of extracting the evaporation rate due to the random fluctuations in measurements. While these fluctuations appear small in Fig.5.18, they are compounded when measuring the difference between every volume value to extract evaporation rate. Secondly, during the second and third stages of drying, large uncertainties are often introduced due to asymmetry in the droplet structures. To validate the expression that evaporation rate remains proportional to the radius even during the precipitation stages, let us perform the following integral of the evaporation rate:

$$\dot{V} = -KR \tag{5.1}$$
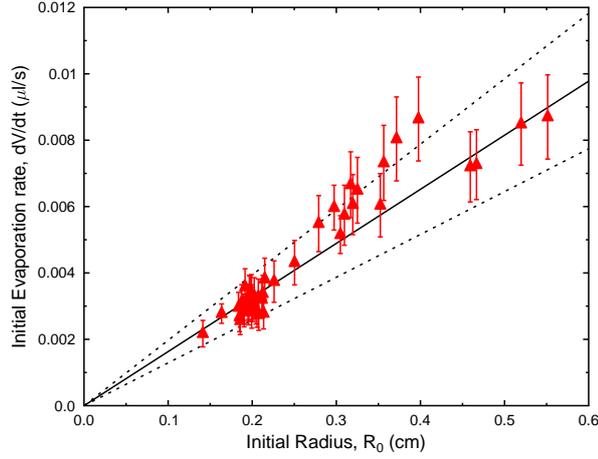
Figure 5.23: Evaporation rate for a wide range of initial concentrations and volumes, plotted against initial droplet radius R_0.

$$\int_0^t \dot{V} dt = -\int_0^t KR dt = -K \int_0^t R dt \qquad (5.2)$$

where K is the proportionality between evaporation rate and radius. The value of K is estimated from the gradient in Fig.5.23 as $K = (1.7 \pm 0.2) \times 10^{-5}$ cm^2/s. If the radius was constant then this would be rewritten:

$$V(t) = V_0 - KRt \qquad (5.3)$$

However, radius is indeed changing with time, so to calculate the area under the radius-time curve, we simply take the sum of the discrete radius measurements and rewrite this equation as:

$$V(t) = V_0 - K\Delta t \sum R \qquad (5.4)$$

where Δt is the time step between measurements of radius, and $\sum R$ is the total sum of the radius measurements at time t. As mentioned, converting differences in volume measurements into a plot of evaporation rate with time becomes tricky during the second stage, not only because of structural asymmetry, but also due to the unknown density of the solid deposit. Therefore droplet mass was used here as a measure of water loss here instead. Equation 5.4 can now be rewritten:

$$m(t) = m_0 - \rho K\Delta t \sum R \qquad (5.5)$$

Where ρ is the density of water. Now by measured $m(t)$ values from two different droplet experiments (with same initial volume, but differing initial base radius)

against $m_0 - \rho K \Delta t \sum R$ as shown in Fig.5.24, we see good agreement between measurements and predictions for total mass for two droplets with equal initial volume and different values of θ_0. Therefore it can be concluded that evapora-
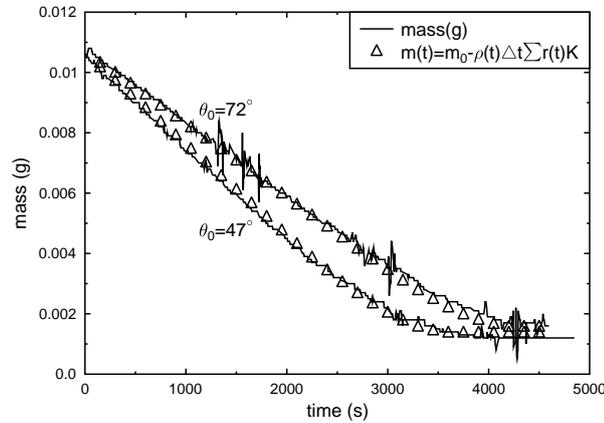
Figure 5.24: Solid lines represent measured mass versus time curves for two droplets with same initial volume V_0 and differing initial radius R_0. Triangles represent the summation of the discrete radius measurements multiplied by the time step Δt and the constant of proportionality between radius and evaporation rate (K), subtracted from the initial volume and converted into mass by multiplying with the density of water. Agreement between solid line and triangles throughout droplet lifetimes confirms that $\dot{V}$ remains proportional to R during the receding liquid stages.

tion rate remains proportional to liquid radius throughout drying, until the very late stages in which liquid droplet radius vanishes, and evaporation must occur through a thick layer of solid PEO.

It may strike the reader as somewhat counter-intuitive that the evaporation rate should scale with drop radius rather than surface area, but as discussed in Chapter 3, this is explained in the literature (with experimental evidence to support the proportionality [85]) as being a consequence of a vapour diffusion limited evaporation rate, with the vapour concentration profile quickly set up above the droplet being the time limiting step for evaporation, rather than the time required for water molecules to escape the drop surface. In a non-quiescent atmosphere these assumptions break down (as the concentration profile is no longer constant), so we would expect that without the drying chamber the evaporation rate would scale with surface area rather than the radius. Furthermore, with highly volatile fluids thermal plumes in the vapour phase and temperature gradients within the drop lead to a non-quasi-steady state, and thus the arguments made by the dif-

fusive model become less convincing for solvents such as ethanol which we will examine later. For now at least, our results seem to agree with those in the literature which show that for water droplets the diffusive model works well [85].

5.2.5 Initial Contact Angle

Fig.5.25 is a sequence of droplet images at $t = t_\mathrm{f}$ for $c_0 = 10\%$, $V_0 = 10 \pm 1$ μl over a range of initial contact angles. The first five images in this figure are droplets deposited on a glass coverslip, and show that there seems to be a critical minimum contact angle, below which pillar formation stops. Surprisingly however there does not seem to be a gradual reduction in pillar size, as we would have with reducing concentration, but instead pillars remain fairly constant in size in the 45-90° initial contact angle range, but at some point around $\theta = 40°$ there is a dramatic cutoff. The final image is a droplet deposited on a glass substrate coated in a layer of dried Granger's solution to increase hydrophobicity (as discussed in Chapter 4). This image suggests that increasing the contact angle by introducing a hydrophobic substrate simply leads to a slightly taller final structure. However,
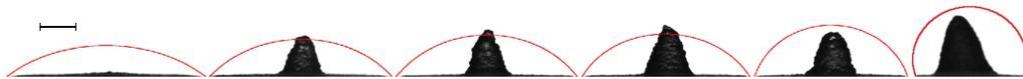
Figure 5.25: Effect of initial contact angle on the PEO structures at $t = t_\mathrm{f}$. Solid red lines are the initial droplet profiles. From left to right $\theta_0 = 40, 47, 54, 57, 70$ and 110°. Scale bar represents 1 mm.

Figures 5.26 and fig:5pcCytop are series of images of PEO droplets ($c_0 = 10$ and 5% respectively) drying on a Cytop substrate, which shows slightly different behaviour including a true surface tension driven dewetting phase in which the contact line recedes without precipitating solid PEO (at 5%) and a late stage unsticking of the solid deposit from the substrate (in both cases). Red dotted lines are added to images to aid comparison between initial droplet diameter and the diameter immediately prior to precipitation.

These images suggest that contact line pinning is a crucial requirement for the formation of tall central pillar or conical structures. On certain highly hydrophobic surfaces, it would appear that a low concentration of PEO leads to low pinning forces, and therefore low hysteresis. This means that unlike on glass, these
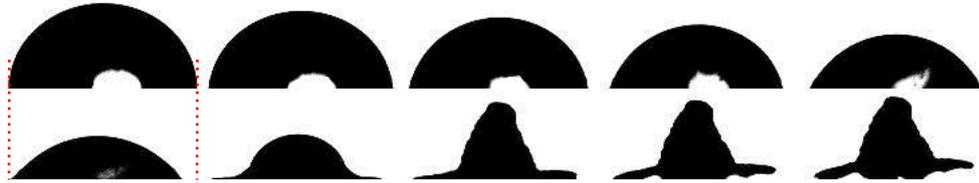
Figure 5.26: Profile images of a $c_0 = 10\%$, $V_0 = 10$ μl droplet on a Cytop coated substrate. Red dotted lines added to aide clarity to the comparison between initial radius and droplet radius immediately prior to precipitation. At late stages of drying the droplet peels itself away from the substrate. Images courtesy of Manon Granjard from the University of Edinburgh.


Figure 5.27: Profile images of a $c_0 = 5\%$, $V_0 = 10$ μl droplet on a Cytop coated substrate. No pinned stage observed, rather the droplet freely recedes until it precipitates uniformly leading to large central solid clump. Images courtesy of Manon Granjard from the University of Edinburgh.

droplets reach their receding contact angle before the concentration at the droplet perimeter reaches c_{sat}, which in turn leads to a freely receding contact line stage followed by the PEO solidifying almost uniformly into a large central clump. While the final image in Fig.5.27 does not look entirely different from the tall central pillars usually observed, it is in fact a completely depinned asymmetric clump of solid PEO, which differs from the usual deposit both by not being pinned and not being surrounded by a thin solid layer. Furthermore, the stage in which the solid deposit peels itself away from the substrate tells us that not only does the liquid phase not pin as strongly with Cytop as with glass, but the adhesive forces between the solid PEO spherulites and Cytop are weaker than those between PEO and glass.

Although interesting, the presence of a freely receding contact line complicates the drying process, and these effects will be investigated no further, yet the reader should note this as one of the various restrictions on pillaring, several more of which will be discussed in depth as this thesis progresses.

5.3 Pillaring Predictions

As hinted at in the previous section, one of the main focuses in all three research chapters in this thesis is to define the limiting requirements for pillar formation. We have observed that there is a minimum concentration ($c_0 \sim 3\%$) and contact angle ($\theta_0 \sim 40°$), and no effect from droplet volume in the range observed ($0.4 < V_0 < 50\ \mu$l), but no explanation thus far has been given to explain or predict these pillar-flat deposit boundaries.

One thing to test prior to examining the pillar-flat cutoff is to ensure that the phase of the solid in the peak is the same as that of the flat disks. Microscopy has shown that the flat disks are comprised of semi-crystalline spherulites, however the tall central pillars are more difficult to examine due to their structure. Furthermore, the spherulites could simply be too small to observe under a microscope. To test that the phase transition that occurs during precipitation of the thin uniform outer region is the same transition ocurring during the bootstrap building of a tall central pillar, these dry PEO structures were seperated post-drying and analysed using differential scanning calorimetry (DSC). For com-

pleteness, these results were compared with the data from the other form of dry PEO available, the unmixed powder.

Scans were performed between 30 and 80°C and back again at 3°C per minute. Fig.5.28 is a plot of the heat flow as a function of temperature, and shows that all three forms of dry PEO follow similar melting (peaks) and crystallisation (troughs) temperatures.
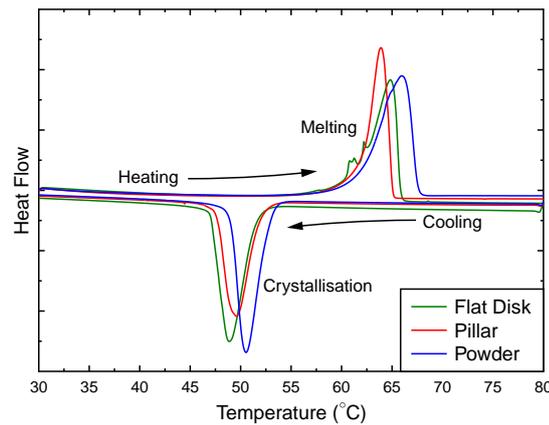
Figure 5.28: DCS scans of solid PEO from flat disks, tall central pillars and pure unmixed PEO powder.

Repeats of experiments with just the pure powder led to variance in size and position of the peaks and troughs similar to that in this figure. Therefore it is concluded that shifts in position and size are due to unknown sources of random error in the DSC measurements, and therefore all three morphologies are in the same semi-crystalline phase.

In this section I will discuss a purely geometric constraint on the boundary between pillaring and flat disk formation, which takes into account effects of initial concentration and contact angle.

5.3.1 Evaporation Versus Receding

First let us consider the competition between the effects of evaporation, which continuously reduces the volume of liquid phase, and spherulite growth which effectively works to push all remaining liquid to the centre. Without describing

the driving mechanism behind this pushing force (which is the emphasis of the next section), it is possible to put constraints on the ability for this receding phase to form a pillar at all when it is in competition with evaporation. We know from section 5.2.2 that once precipitation begins, the receding speed of the liquid phase is fairly constant with no dependency on concentration. We also know that the evaporation rate remains proportional to the liquid radius. With these factors in mind, I propose that after precipitation begins if the linear trajectory of $\dot{R}$ reaches zero before the volume reaches zero, then at the end of the receding phase there will be a region of liquid at the centre of a flat solid deposit. However, if the volume reaches zero first, then pillaring can not occur, instead the central region will lose all volume while the contact line is receding, and will form a ring-like structure.

Fig.5.29 is a diagram showing the two outcomes of this model. The diagram is
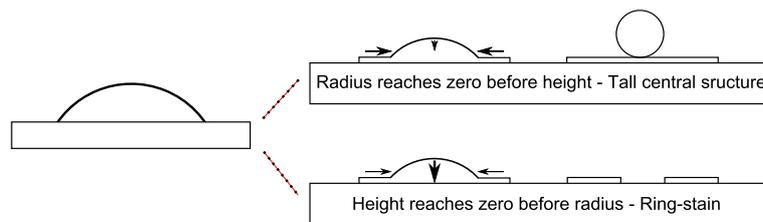
Figure 5.29: Diagram of the competing effects of precipitation driven radial receding and evaporative driven shrinking. The two outcomes show that if the radius reaches zero before the height, there will be a large central liquid region remaining once the receding stage has finished, and thus a tall central deposit, whereas if the height reaches zero first the receding phase will stop abruptly and leave behind a coffee-ring stain like deposit.

actually fairly unrealistic, as the precipitation does not only work to reduce the radius of the contact line, but in fact continually grows up the surface of the liquid, which leads to the final deposit having a different structure to that described in this model (which would essentially be a liquid sphere sat on a flat uniform deposit with radius R_0). However, despite this clear difference, this picture may yet give key insight into the upper/lower boundary of flat disk/tall pillar formation as functions of initial solution concentration and droplet geometry.

To calculate the restrictions on the pillaring process, we follow these simple analytical steps to solve for the changes in volume and radius with time after precipitation begins. First let us start with the basic proportionality between

evaporation rate and droplet radius:

$$\dot{V} = -KR \tag{5.6}$$

The radius at any given moment is given by the initial radius R_0, the rate of change in radius $\dot{R}^*$ and the time elapsed since precipitation began t:

$$\dot{V} = -K(R_0 + \dot{R}t) \tag{5.7}$$

Integrating with respect to time gives:

$$\int \dot{V} dt = -K \int (R_0 + \dot{R}t) dt \tag{5.8}$$

$$V = -KR_0 t - \frac{K\dot{R}t^2}{2} + A \tag{5.9}$$

and when t=0 (start of precipitation) $V = V_{\mathrm{p}}$, so:

$$V = V_{\mathrm{p}} - KR_0 t - \frac{K\dot{R}t^2}{2} \tag{5.10}$$

This is the equation for the volume at any given time during the receding phase, but we want a measurement of the volume at the time when $R = 0$, which will occur (given a constant value of $\dot{R}$) when $t = -R_0/\dot{R}$. Therefore:

$$V = V_{\mathrm{p}} + \frac{KR_0^2}{\dot{R}} - \frac{KR_0^2}{2\dot{R}} \tag{5.11}$$

$$V = V_{\mathrm{p}} + \frac{KR_0^2}{2\dot{R}} \tag{5.12}$$

Which will be positive, and therefore form a pillar, when:

$$V_{\mathrm{p}} > -\frac{KR_0^2}{2\dot{R}} \tag{5.13}$$

From figures 5.19 and 5.23 K and $\dot{R}$ are estimated as $K = 1.7 \pm 0.2 \times 10^{-5}$ cm^2/s and $\dot{R} = -1.6 \pm 0.3$ μm/s. Therefore, if the initial droplet radius is $R_0 = 0.2 \pm 0.01$ cm, then the minimum volume required at the start of precipitation is $V_{\mathrm{p}} \approx 2.1 \pm 0.5$ μl. The minimum concentration droplet found to form pillars (as shown in the $c_0 = 4\%$ plot in Fig.5.18) has a volume at $t = t_{\mathrm{p}}$ of 1.8 μl, which is slightly below the predicted value, but well within the uncertainty. The

---

*Here it is assumed that $\dot{R}$ is not a function of time as evidenced by the somewhat constant receding speeds plotted in Fig.6.28. This assumption has several limitations, which will be improved upon in the next chapter

discrepancy could be due to the assumption of a constant value of $\dot{R}$ with time, which will be improved upon in the next chapter. Indeed the $c_0 = 4\%$ radius profile is distinctly less linear than the majority of the other droplets in Fig.5.18. The initial slow decrease in radius could be due to uneven spherulite formation around the droplet perimeter at $t = t_p$. This is seen clearly from above as shown in Fig.5.30. This effect could cause either an over or underestimate in liquid
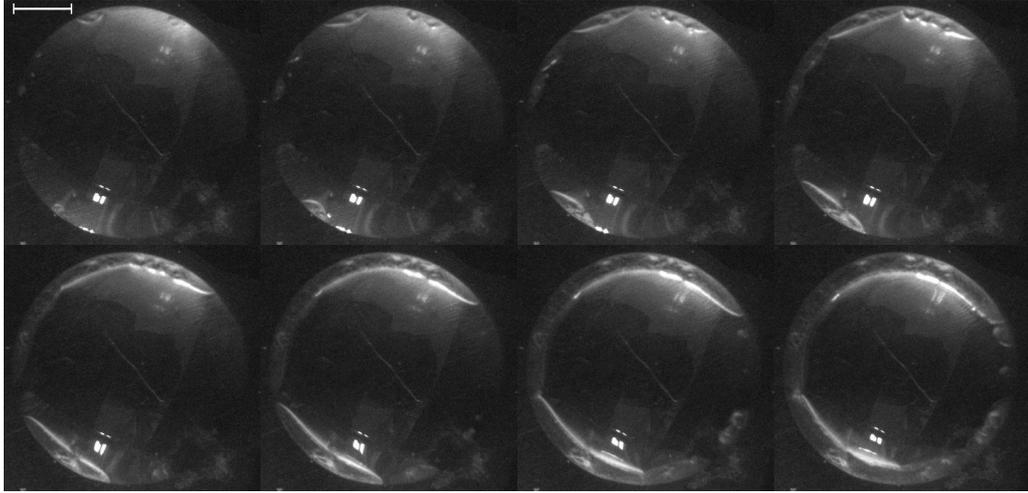
Figure 5.30: Time-lapse sequence of images showing that occasionally precipitation begins non-uniformly around the perimeter of the droplet. Scale bar represents 1 mm.

radius values compared with the true average liquid radius depending on the position of the camera.

To visualise this competition between receding and evaporation on the final structure graphically, first we need the equation for volume as a function of radius and height, which is equal to the volume of a spherical cap given by [147]:

$$V = \frac{\pi}{6}R^3\left(X^3 + 3X\right) \tag{5.14}$$

where:

$$X = \frac{h}{R} = tan\left(\frac{\theta}{2}\right) \tag{5.15}$$

Now, by setting the decrease in radius as constant (with $\dot{R} = -1.6 \pm 0.3$ μm/s), and using equations 5.12 and 5.14 to numerically calculate volume and height with time respectively, we can plot the change in the predicted droplet parameters between the onset of precipitation and the point at which receding stops (either when R or $V = 0$). Fig.5.31 is a selection of radius, height and volume plots predicted by this model for various droplet volumes at $t = t_p$. R_0 and V_0 are

fixed at 0.2cm and 10 μl respectively. From left to right $V_\mathrm{p} = 1.5$, 2.5, and 3.5 μl. In the far left plot, V_p is sufficiently low that both the liquid height and volume reach zero simultaneously well before the radius reaches zero, and would form a ring stain, with thickness marked by the difference between R_0 and the value at which the dotted line crosses the y-axis. The second and third plots however show that both the radius reaches zero before the volume and the structure will undergo an increase in height, which would therefore be expected to form a tall pillar structure. Of course these volume curves only account for the volume of the solvent. The total volume would be the sum of this predicted solvent volume and the volume of the polymer in solution which has not been precipitated at the contact line.
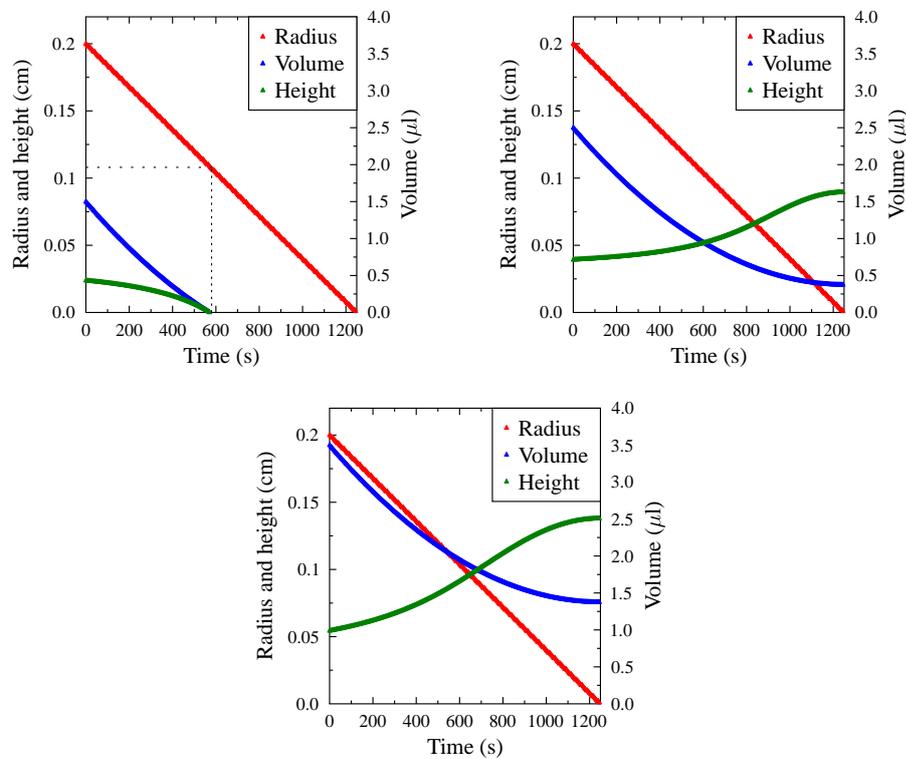
Figure 5.31: Plots of volume, radius and height curves calculated numerically from equation 5.14 during the receding liquid stage for 3 different droplet volumes at the precipitation time. From left to right $V_\mathrm{p} = 1.5$, 2.5 and 3.5 μl. When $V_\mathrm{p} = 2.5$ or 3.5 μl, the radius reaches zero while volume remains and the droplet height increases. Whereas when $V_\mathrm{p} = 1.5$ μl, the volume reaches zero before the base radius, and we would expect a coffee-ring type stain with thickness equal to the difference between R_0 and where the dashed line crosses the vertical axis.

At $c_0 = 3\%$ (which did not form a pillar) the precipitation volume was measured

at $V(t = t_\mathrm{p}) \approx 1.5~\mu$l, which is smaller than the lower limit of the uncertainties in the estimate of the minimum pillaring volume. This suggests that while there are some shortcomings in the model, particularly that $\dot{R}$ is constant with time, and that pillar formation occurs if the base radius reaches zero (which would lead to a spherical droplet resting on a flat deposit rather than the tall pillar structures observed), this criteria for pillar formation gives a good indication of the relative effects of the competing evaporative and receding components that lead to the different fully dried structures, and gives a good estimate of the minimum requirements for a pillar to form.

5.3.2 Pillar Prediction Complications

There are some cases in which this model has failed to account for observations, particularly when varying initial contact angle. If θ_0 is varied while R_0, $\dot{V}$ and c_0 are kept constant, we can use this argument to make predictions on the minimum pillaring θ_0. From observations of droplets with initial concentration $c_0 = 10\%$ and radius $R_0 = 0.2$ cm, the time at which precipitation begins was found to be ≈ 2550 s, and the evaporation rate $\dot{V} = 0.00309~\mu$l/s. Taking all these initial conditions into account, a droplet with the minimum pillaring volume at the precipitation time ($V_\mathrm{p} = 2.1 \pm 0.5~\mu$l) would be given by an initial droplet volume of $V_0 = 9.9~\mu$l. Therefore from equation 5.14 we can estimate a minimum initial contact angle of $\theta_0 \approx 68°$, which is not in agreement with minimum initial contact angle observations ($40 < \theta_0 < 47°$) shown in Fig.5.25. However, these images were captured of droplets with fixed initial volume, *not* fixed initial radius. Up to now all measurements of $\dot{R}$ have been at a constant values of R_0 and $\dot{V}$, so to explore the effect of initial contact angle independent of V_0 and R_0, more experimental observations are required.

Additionally, while this model does account for the droplet having a non-zero height at the end of the receding stage, it does not explain how the liquid receding is driven by the formation of spherulites to begin with. For a complete understanding of the pillaring process, a description of the driving force during the second and third stages of drying must be included.

5.4   What Causes Receding?

Until now this research has been focused purely on the fully dried structures that form from drying PEO droplets, the initial conditions leading to these different morphologies, and what characteristics of the drying process can be extracted from the droplet profiles as they go through these drying stages. While all these approaches to understanding the pillaring phenomenon are important, they do not answer a crucial underlying question: how does the formation of spherulites at the contact line lead to a receding liquid phase, and ultimately, a tall central conical or pillar-like structure? Several hypotheses have been suggested...

5.4.1   Skin Buckling

As discussed in section 3.7.1, previous studies of drying polymer droplets have reported that fully dried droplets form donut or Mexican hat structures depending on initial concentration, contact angle and relative humidity. Fig.5.32 is a side by side comparison of two respective fully dried structures of Dextran and PEO, and it is clear there are distinct similarities in the structures.

Figure 5.32: Side by side comparison of the structures that form from droplets of water dissolved: (a) Dextran, $c_0 = 40\%$ (image taken from publication by Pauchard [124]) and (b) PEO, $c_0 = 20\%$.

The hypothesis put forward by these authors proposes that a skin buckling process, in which an incompressible glassy skin forms over the droplet surface which deforms and "buckles" inward due to continued evaporative driven volume loss, is the mechanism behind the formation of these unusual structures. This was initially considered a likely candidate for the structures that form from PEO droplets, however with some careful scrutiny, this mechanism was dismissed.

Firstly, it has been shown in this work that there is a clear precipitation driven receding stage that begins at the three phase contact line. This suggests that if there is indeed a region of high concentration, it is not uniform over the droplet surface as with the Dextran droplet polymer skin, but rather the polymer concentration is greatest at the droplet perimeter. Secondly, the buckling model requires the surface skin to be incompressible (or only slightly compressible) and thus have a constant surface area once buckling begins. Fig.5.20 is a plot of normalised surface area with time during the evaporation of a series of PEO droplets, which shows a clear increase during the boot-strap building phase. From this result alone we can conclude that the incompressible skin model is certainly not the case for PEO, and therefore the drying process of PEO droplets follows behaviour as yet unexplored in the literature. The increasing surface area measurements were the first crucial result that identified the drying behaviour of PEO droplets as fundamentally different from already published work and led to our first publication in *Physical Chemistry Chemical Physics* [148].

5.4.2   Autophobic Dewetting

One idea that was also suggested very early on in this research was that the amphiphilic properties of PEO could play an important role during precipitation, specifically causing autophobic driven receding of the liquid phase. Autophobic dewetting is defined as the non-wetting behavior of liquid droplets on their own monolayer [146], as it is a type of repellancy between two chemically identical substances of in different phases. Autophobic dewetting could be applicable to this work if the thin layer of solid PEO spherulites acts as a monolayer, which the remaining liquid phase can not spread on. The ability for PEO to show autophobic behaviour could be due to its amphiphilic properties and the specific helical structure the polymer forms in aqueous solution. If there is not a sufficient amount of water to "dress" the polymer entirely (as discussed in section 2.4), which would be the case when a significant quantity of water has evaporated from the droplet, then the effect of the hydrophobic CH_2 groups could become dominant, resulting in a repulsion between the polymer and the insufficient quantity of water. In other words, when the solid is precipitated, it forms a waxy surface which repels solutions of insufficient water concentration, causing a high interfacial tension between the precipitate and the highly concentrated solution. Proving this from

droplet contact angle measurements is difficult as one would need to measure the equilibrium contact angle between a solid PEO layer and a solution precisely at the saturation concentration, which is both difficult to push through a syringe due to the high viscosity, but also because this test requires an environment of 100% relative humidity in order to prevent any evaporation from the solvent.

There are many observations that do not support this hypothesis, however they will have to wait until the next chapter in which we examine in detail the next set of drying droplet variables explored - atmospheric conditions. For now we will move on to the third and final hypothesis of the driving force behind the receding of the contact line.

5.4.3 Contracting Collar

We have observed that precipitation always occurs first at the perimeter of the droplet, which as described in section 3.3.4 is the region of the greatest local evaporative flux, and the region to which suspended particles are swept during outward radial flow in a pinned sessile droplet. It follows then that because PEO droplets display pinned drying, a similar process to the common coffee-ring effect should be expected. Fig.5.33 is a diagram of this model in which toward the end of stage one, a region highly concentrated in polymer builds up at the perimeter. One could follow this line of thought and expect that this would mean
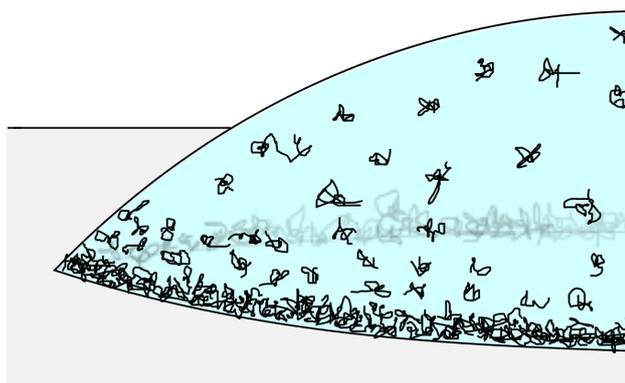

Figure 5.33: Diagram of polymer build up at the droplet perimeter via the coffee-ring effect during the pinned drying stage.

all the dissolved polymer chains would be dragged to the contact line and leave

a polymeric ring stain. Indeed, confocal microscopy observations of the motions of seeded fluorescent particles close to the contact line give clear evidence of this outward radial flow, as shown in Fig.5.34. The arrows in the figure indicate the trajectory of particles close to the contact line. The motion in the direction of the contact line are the predicted coffee-ring effect radial flows, whereas the downward arrow shows the motion of particles at the surface as the droplet shrinks due to evaporation. However, we have also shown that unlike coffee grains, at a certain
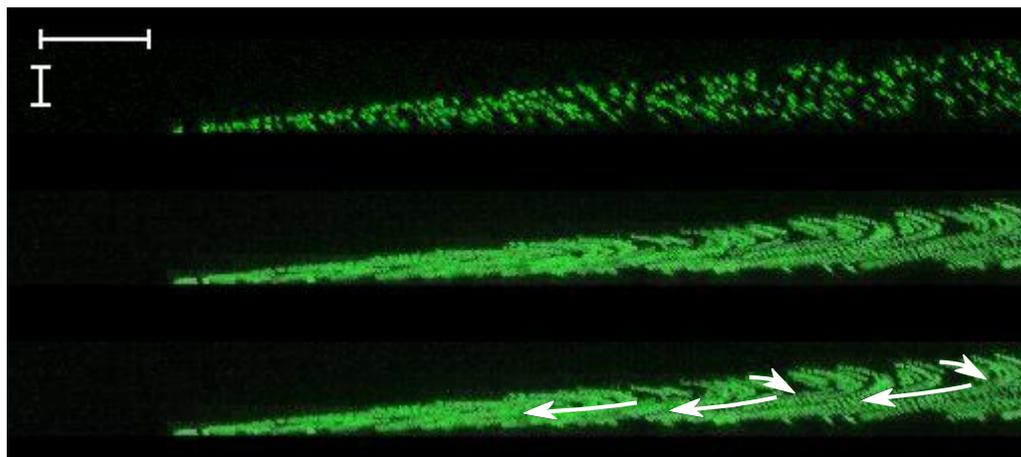
Figure 5.34: Set of images acquired through confocal microscopy and subsequent image analysis. The top image is the result of acquiring a set of 2D images of the droplet close to the contact line, stitching together and rotating through the z-axis with the use of the 3D project function in ImageJ. The second image is given by repeating this for a series of stacks in time, and through the Z-Project function in ImageJ projecting all images into a single image which shows the blurred trajectories of the particles with time. The bottom image shows the direction of these trajectories, which appears to be down into the droplet at the surface, and out toward the contact line in the bulk. Horizontal and vertical scale bars represent 50 μm and 200 μm respectively.

concentration ($c \approx 50\%$), the highly concentrated region will undergo a phase transition in the form of spherulite nucleation. We have observed that these spherulites not only nucleate at the contact line, but then proceed to nucleate up along the surface of the droplet as shown in Fig.5.35, leading to the appearance of an advancing crystallisation front, which ultimately encases the remaining liquid. Fig.5.36 is a diagrammatic representation of this advancing crystallisation front.

Fig.5.35 also shows the rather surprising result that not only do spherulites nu-
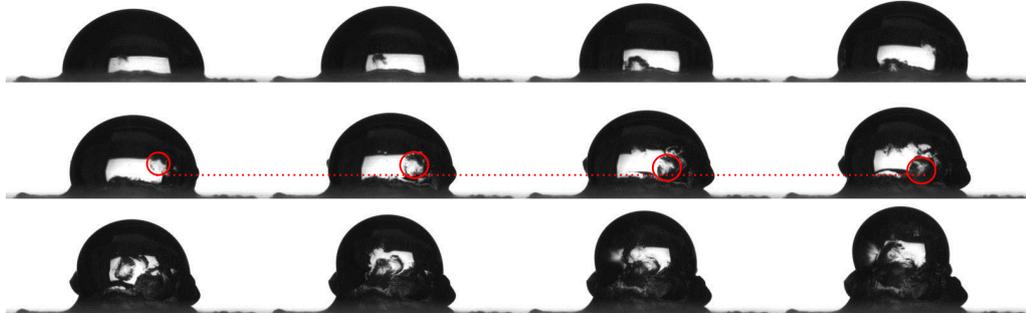
Figure 5.35: Sequence of images during the bootstrap building stage of $c_0 = 25\%$ droplet. The semi-crystalline region advances up the surface of the remaining liquid. Red circles highlight a single spherulite that initially grows until it comes into contact with another spherulite, and then appears to move down toward the substrate.
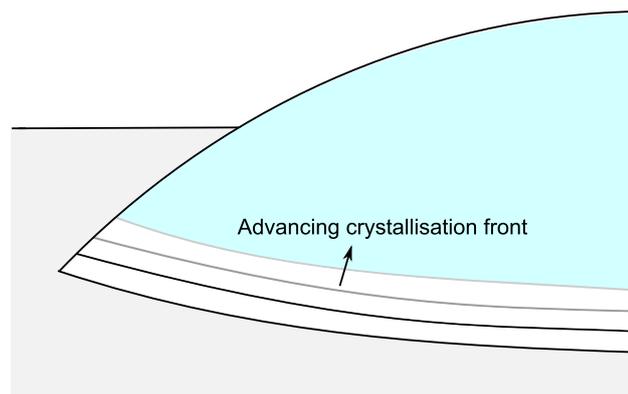
Figure 5.36: Diagrammatic representation of the crystallisation front advancing up the droplet surface.

cleate up along the liquid surface, but individual spherulite regions seem to fall back down towards the interface. I propose three possible causes of the downward motion of these spherulites:

- Gravity. These spherulites now have a sufficiently high density that gravity causes an appreciable downward pull on them leading to this downward motion. One may wish to estimate a spherulite sedimentation velocity to test whether this argument can be dismissed or not purely on the grounds of the time it would take to sediment versus the remaining lifetime of the drop. However, while the density of pure PEO powder is known, as we will see later that does not necessarily give an estimate of the density of these spherulites, which upon nucleation still contain a large amount of water. Furthermore, spherulites are not necessarily solo entities, but can be interlocked with other spherulites through entanglement of polymers between neighbouring lamellae (as discussed in section 2.4.3). Therefore we can not reliably estimate their size either, making sedimentation velocity calculations unreliable.

- Surface flows. It is possible that internal convection currents in the liquid phase work to push these spherulites together in the direction the liquid-substrate interface.

- Contraction. These spherulites form at approximately 50% concentration, but the concentration of water in the semi-crystalline phase is unknown. This means that there could be up to a 50% mass fraction of water contained within the solid region. Spherulite size is limited by the formation of other neighbouring spherulites. Therefore, once the boundaries of a single spherulite become fixed due to the presence of other spherulites, if it still contains water it must then contract due to further evaporation. The collective effect of a large number of tightly bound contracting spherulites would then lead to the appearance of this downward motion. This final suggestion, unlike the previous two, is actually downward motion of the entire solid phase, not downward motion of individual spherulites.

Later in this thesis evidence will be presented that make the likelihood of the first two explanations of this downward spherulite motion unlikely. For now let us simply continue under the assumption that this motion is due to drying

induced spherulite shrinkage. Now, we have the combined effects of an advancing crystallisation front, and a contraction of the spherulites due to volume loss. If the spherulites were allowed to freely contract equally in all directions then we would expect they would simply collect together in small bunches over the surface of the droplet. However, this is impossible as the semi-crystalline region is pinned at the contact line. Fig.5.37 is a diagram of the semi-crystalline collar
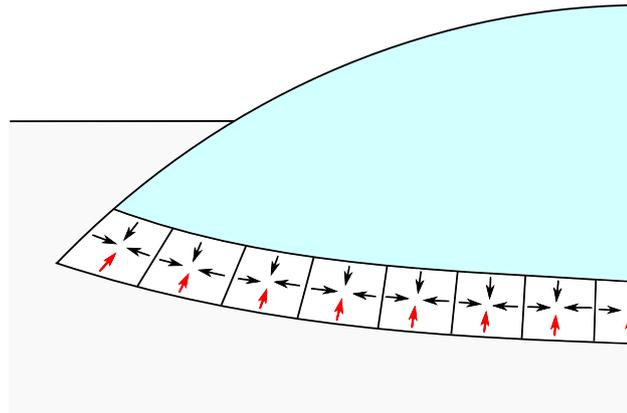
Figure 5.37: Diagram of the semi-crystalline "collar" surrounding the remaining liquid. Arrows represent the directions the spherulite boundaries must move to allow for volume loss from further evaporation from the semi-crystalline region. Red arrows represent the forbidden direction of contraction due to pinning with the substrate.

that surrounds the perimeter of the droplet. It has been split into small regions to aide the visualisation of this collar being consisted of small distinct contracting spherulite regions. Each of these regions wants to contract in the directions of the arrows shown, but the red arrow is forbidden due to being pinned to the substrate. Therefore, combined downward and horizontal contraction of this collar leads to the remaining liquid to be squeezed inwards as shown in Fig.5.38.

A prediction of this constricting collar model is that if the substrate was sufficiently flexible, the red arrows would not be forbidden, and we would expect the substrate to bend upwards once spherulite contraction begins. This is indeed what happens when a droplet of $c_0 = 10\%$ and $V_0 = 10$ μl dries on a 0.5 μm thick sheet of PDMS (provided with thanks by Nicasio Geraldi), as shown in Fig.5.39. This small scale investigation suggests it may be useful to repeat this experiment but on a PDMS strip or cantilever to enable calculations of the upward bending force induced on the substrate by the droplet. Conversations with the supplier of this flexible material Nicasio Geraldi suggests that this is indeed feasible, but
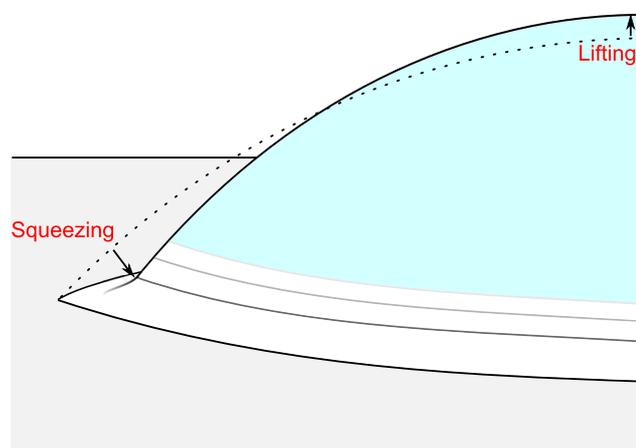
Figure 5.38: Diagram of contracting collar induced receding of the liquid phase.
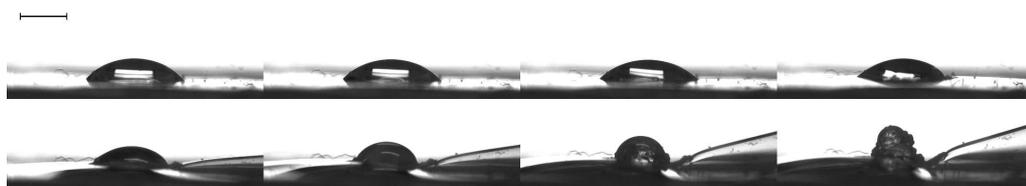
Figure 5.39: Time-lapse profile images of a PEO droplet drying on a thin sheet of PDMS. Once precipitation begins (in the fourth image), the substrate is pulled upwards by forces induced by the combination of a contracting PEO collar and a high pinning forces between the droplet and the substrate. Scale bar represents 2 mm.

is beyond the scope of this work. Indeed, there appears to be growing intrigue in the area of sessile droplet induced forces acting on soft substrates, illustrated by the work of Das et. al. in which they describe an unusual tangential force towards the centre of the droplet dissimilar to the normal force described by Young's equation [149]. With the understanding of surface forces acting on soft substrates still not well understood, it should not be surprising that I did not have time to explore the implications of this experiment further. However it may prove interesting to repeat this test with beam or drum bending experiments, which would give more information on the localised substrate deformation.

As the PEO drying droplet story of this thesis develops I will refer back to these proposed pillaring hypotheses, adding to the evidence for or against each one. The reader should keep in mind as this thesis progresses that despite the constricting collar hypothesis being the most likely culprit behind pillar formation, the fine line between cause and effect in this system makes proofs very difficult, which in many ways makes this research all the more interesting.

Logic will get you from A to Z; imagination will get you everywhere.

ALBERT EINSTEIN

Chapter 6

The Péclet Number

Dimensionless numbers crop up time and time again in fluid mechanics. Whether concerning buoyancy driven convection flows (the Rayleigh number [107]), the competition between inertial and viscous flows (the Reynolds number [150]), Marangoni flow due to surface tension gradients (the Marangoni number [109]), the rheology of viscoelastic fluids (the Deborah number [151]), or even the convective competition between the Lorentz force and viscosity (the Chandrasekhar number [152]), there seems to be an associated dimensionless number. The key dimensionless number I am going to introduce in this chapter is called the Péclet number.

The Péclet number describes the competition between the effects of advective fluid flow and diffusion down a concentration gradient [153]. This is often used in terms of the transport of heat or particles across a certain distance within a fluid, however in this chapter the Péclet number will be used purely in terms of its ability to transport a given polymer over a certain distance in a drying droplet.

In this chapter I will explore the effects of atmospheric pressure, temperature and relative humidity on the drying behaviour of PEO droplets. These effects are collapsed into the dimensionless Péclet number, which encapsulates the competition between the evaporation rate which works to carry the dissolved polymers to the contact line, and the polymer's self diffusion coefficient, which drives the polymers down the concentration gradient and homogenises the solution. High values of Pe leads to faster advective flow, earlier precipitation, and taller pillar structures, whereas low values of Pe leads to uniform precipitation and flat

"pancake" like deposits. Along the way a model for characterising the Péclet number in a drying droplet is developed, which shows some success at predicting the minimum pillaring condition ($Pe > 1$) for PEO droplets.

If one day I could add my own name to this myriad of dimensionless numbers, I will consider myself a success.

6.1   Atmospheric Conditions

6.1.1   Low Pressure

Reducing atmospheric pressure is a simple method of increasing the evaporation rate of a droplet without affecting the polymer diffusivity and fluid viscosity as one would if the evaporation rate was controlled through varying temperature. Although, it should be noted that it is very difficult to increase evaporation rate without also reducing the surface temperature via evaporative cooling effects. Let us therefore attempt to quantify this effect by calculating a rough estimate of the effect of evaporative cooling on the surface temperature of the drop at the high evaporation rates ($\dot{V} \sim 3 \times 10^{-5}$ μl/s) associated with the lowest pressures examined in this work ($P \approx 20$ mbar). For simplicity, let us assume that instead of a spherical cap of height h and base radius R the liquid is cylindrical in shape with identical height and radial dimensions to those given by the standard 10 μl droplets examined in this thesis ($R \approx 2$ mm, $h \approx 1.4$ mm), and that evaporation only takes place over the top surface. This drop will therefore continuously lose heat through evaporative cooling with a heat loss rate given by $dQ/dt = \dot{m}L_{\mathrm{v}}$ [154], where $\dot{m}$ is the rate of change in mass and L_{v} is the latent heat of vapourisation ($Lv \approx 2500 J/g$). The reader should notice that given a constant loss of mass this will give a continuous loss of heat and reduction in temperature with time. Clearly this does not happen or all drops would freeze after a given mass loss. Therefore we must balance this rate of heat loss with some other form of heat transport within the liquid. Let us assume now that the only method of replenishing this heat loss is through thermal diffusion from the bulk of the liquid. The heat diffusivity will tend to homogenise the heat profile through the liquid, with the rate of change of heat at a certain position in z is

given by the equation:

$$\frac{dQ}{dt} = -kA\frac{dT}{dz} \tag{6.1}$$

where k is the thermal conductivity and A is the contact area between drop and substrate [155]. If we assume that the substrate is sufficiently heat conducting that the bottom layer of the fluid remains at T_0 (20°C) at all times, and assume a linear vertical temperature gradient, then this can be rewritten:

$$\frac{dQ}{dt} = -kA\frac{\Delta T}{h} \tag{6.2}$$

where ΔT is the temperature change at the surface. Now if we equate the two terms for the rate of change in the heat, and assume that these two effects reach equilibrium quickly enough that there is very little change in h from mass loss, we will find the point at which the effects of latent heat of vapourisation and thermal diffusivity balance, and from this estimate the change in temperature at the surface ΔT. At ambient conditions, where $\dot{m} \approx 3 \times 10^{-9}$ kg/s, this gives a surface temperature change of ≈ 0.7 K, whereas at atmospheric pressures of 20 mbar, the rate of mass loss is around one order of magnitude higher and therefore we predict a reduction in surface temperature of around 7.2 K*.

In this work it will be assumed that the effects of the evaporative cooling on the final fully dried structures will be negligible compared with those caused by the change in the droplet evaporation rate. The dominant effects of reducing pressure in the formation of these pillar structures probably depends on some dimensionless number that encorporates evaporation rate, thermal diffusion and latent heat of vapourisation... The Baldwin number perhaps! Defining this competition is beyond the scope of this work, and only effects of evaporation rate will be considered.

Fig.6.1 is a sequence of profile images showing the drying behaviour of a PEO droplet ($c_0 = 10\%$) under a reduced atmospheric pressure of 50 ± 5 mbar. Unsurprisingly the t_0 is significantly reduced by reducing pressure (by a factor of ~ 10 from 1000 to 50 mbar). However, an increased evaporation rate seems to not only reduce the total drying time but also the fraction of the total drying time required for precipitation to begin. t_0 and t_p were measured as approximately 38 and 259 s respectively. Therefore, at $P = 50$ mbar $t_p/t_0 \approx 0.15$ whereas in

---

*For a more accurate estimate the complex combination of conduction (from substrate and atmosphere), convection, radiation, drop shape and evaporation profile must be taken into account.
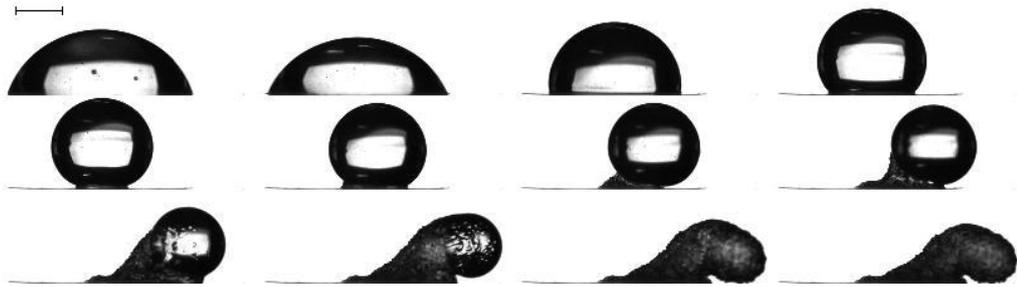
Figure 6.1: Time lapse profile images of PEO droplet, $c_0 = 10\%$, $M_W = 100$ kg/mol, at reduced atmospheric pressure of $P = 50$ mbar. Total time lapsed 9 minutes and 10 seconds. Scale bar represents 1 mm.

a similar droplet at ambient conditions $t_p/t_0 \approx 0.76$. This immediately suggests that not only is water escaping from the droplet at an enhanced rate, but the advective flow of the polymer to the contact line is increased, causing the fractional time for polymer concentration to reach the saturation concentration at the droplet perimeter to be reduced.

Earlier precipitation at the contact line means an increased droplet height, contact angle, and importantly, volume at $t = t_p$. Therefore we would expect from the geometric argument proposed in the previous chapter regarding the competition between the receding speed and the height loss due to the evaporation rate that the reduced value of t_p/t_0 would lead to larger pillar structures. The results suggest that this is indeed the case, however the structures become highly unstable during the growth phase, topple over sideways and continue to grow in the direction it toppled. This sideways growth is certainly a result of random toppling as no preferred direction was found over a large number of repeats irrespective of vacuum pump inlet position. Indeed, often the structures would grow in the direction either towards or away from the camera, resulting in out of focus imaging. We must note here that the conclusions made from the geometric argument proposed in the previous chapter assumed no evaporative flux effect on $\dot{R}$, which we will see later is not the case.

Pressure was varied between 20 and 1000 mbar as shown in Fig.6.2. This suggests that the growth instability begins at around $P \sim 200$ mbar, below which sideways growth is the likely result. This toppling effect is interesting as it sets a limit on the size of the fully dried droplets, however if this experiment was repeated in microgravity, the droplet will wet the substrate in the same manner, the evapo-

Figure 6.2: Fully dried profile images of droplets dried in the pressure range $20 \leq P \leq 1000$ mbar. $c_0 = 10\%$. Scale bar represents 1 mm.

ration profile will remain the same and so we would expect the same preferential precipitation at the contact line, and thus the same pillar forming process, but this tendency to topple over would be removed, and so we would expect highly symmetrical vertical structures. However it must be noted that removing gravity would remove the possibility of any buoyancy driven flows, which we will see later are highly prevalent in drying PEO droplets.

6.1.2   Pressure Versus Concentration

Similar behaviour is also observed at $c_0 = 5\%$ as shown in Fig.6.3. Interestingly,

Figure 6.3: Fully dried profile images of droplets dried in the pressure range 20 to 1000 mbar. $c_0 = 5\%$.

if the geometric argument is valid, and increasing the evaporation rate leads to an earlier fractional precipitation time, we would expect that at $c_0 = 2\%$, which previously has been shown to have too little volume at $t = t_\mathrm{p}$ to form pillars (and instead forms coffee-ring type deposits), should transition from coffee-ring to pillar behaviour if the precipitation time is reduced by increasing the evaparation rate $\dot{V}$, which is exactly what was observed as shown in Fig.6.4.

It is clear from the images in Fig.6.4 that, as expected, the initial evaporation rate is faster at lower pressures: the droplet drying at $P = 25$ mbar is noticeably smaller after $t = 100$s than any of the others. Also at $P = 25$ mbar droplet receding has already begun by $t = 200$ s, much earlier than any of the others. Intriguingly though, from this point onwards, low pressure droplets seem to evaporate more slowly. This may be due to the known dependence of evaporation rate
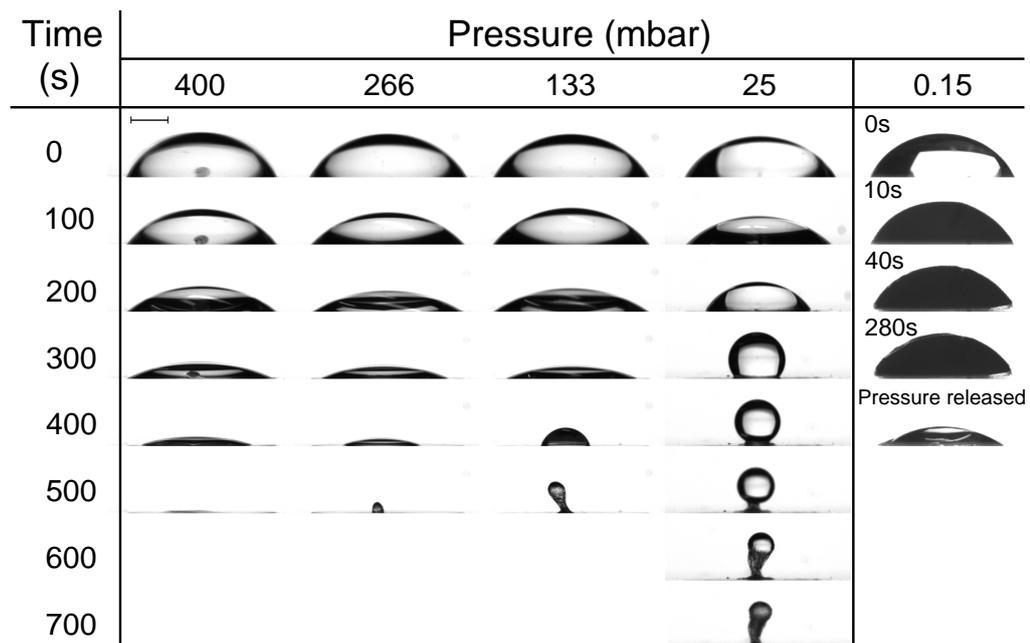
Figure 6.4: Time lapse images with time increasing in 100s intervals downwards, showing, in the first four columns, behavior for a range of $10 \ \mu l$ droplets with initial concentration $c_0 = 2\%$ and decreasing pressures (from left to right $P = 400, \ 266, \ 133, \ 25$ mbar). In the far right column the pressure is sufficiently low (< 0.15 mbar) that the outer layer of the droplet freezes, which if left under vacuum would continue to sublime. When the vacuum is released, as illustrated in the fifth image of the far right column, the frozen-crust melts. The scale, indicated by the 1 mm scale-bar in the upper left is the same for all images.

on liquid base radius $\dot{V} = -KR$. At $t = 300$ s the droplet base radius at $P = 25$ mbar is significantly lower than any of the others, which could explain the reduction in evaporation rate. However, we must also note that the proportionality between droplet radius and evaporation rate is only valid when evaporation is diffusive limited. At some reduced value of P, the mean free path in the atmosphere would be significantly large compared with the size of the droplet that this would no longer be the case. Instead evaporation would be ballistic meaning that the limiting time-step for evaporation is now the time required for a water molecule to escape from the droplet surface, rather than the diffusive time away from the droplet into the atmosphere. Ballistic evaporation therefore becomes proportional to the total interfacial area between the liquid phase and atmosphere.

The mean free path is the average distance a particle travels before a collision with another particle, and is given by the equation [156]:

$$\lambda = \frac{k_B T}{4\sqrt{2}\pi r^2 P} \tag{6.3}$$

where r is the radius of the particles and P is the atmospheric pressure. At ambient conditions ($P \approx 1000$ mbar, $T = 22°$C) the mean free path in air is approximately 68 nm [157]. At the lowest pressures observed in this work (~ 20 mbar), this gives an approximate mean free path of 3.4 μm ≈ 68 nm $\times 40$, which is more than 3 orders of magnitude smaller than the diameter of the droplet. Therefore it is assumed that the atmospheric pressures explored in this research are not small enough to induce ballistic type evaporative behaviour.

The two vacumm pumps available gave two different ranges. The rotary pump, which was used for the majority of experiments gave reliable control down to $P \approx 15$ mbar, as shown in the first 4 columns of Fig.6.4. With the oil diffusion pump however, pressures created were significantly lower, by at least two orders of magnitude. Using this pump it was found that when $P < 0.15$ mbar, as evaporative cooling removes heat from the droplet, the outer layer of the droplet freezes into a crust, as shown in the final column of Fig.6.4. When the valve is opened and the chamber returns to atmospheric pressure, the frozen crust quickly melts. By balancing latent heats of vaporization ($L_v \approx 2500$ J/g) and fusion ($L_f \approx 330$ J/g) and heat capacity for water ($C \approx 4.2$ J/gK), and assuming no heat flow from the environment, the fraction of a droplet at initial temperature ΔT above freezing which would need to evaporate in order to remove sufficient heat for the entire remaining droplet to freeze is $1 - L_v(L_v + L_f + C\Delta T)^{-1} \approx 15\%$.

The droplets observed here do not freeze entirely, only forming a frozen crust, so should require a smaller volume loss, in line with these qualitative observations. Crust-freezing disrupts the four-stage process and introduces a lower/upper limit to the pressure/evaporation rate at which we should expect pillars to form.

Fig.6.5 is a phase diagram showing, as a function of the experimental parameters c_0 and P, profile images of the dried structures. This is not an exhaustive
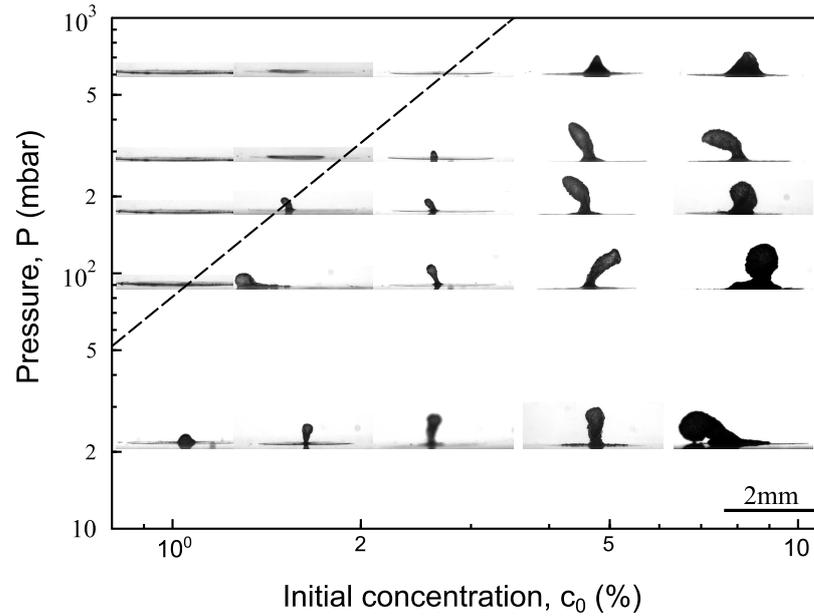
Figure 6.5: The shape of the solid deposit at the end of stage 3 plotted as a function of both initial droplet concentration c_0 and reduced pressure P on log axes. The dashed line is a guide to the eye dividing pillars (below) from flat deposits (above) and has the form $P \propto c_0^2$.

representation of all data, but a selection of twenty representative images chosen from over 50 experiments to indicate the dependence on the two experimental parameters c_0 and P. As expected, lower concentration droplets require lower pressures to achieve pillar formation. Higher c_0 leads to earlier PEO deposition and therefore larger and unstable final structures. A guide is drawn dividing flat deposits from pillarss although the distinction is not absolute, and has the form $P \propto c_0^2$.

6.1.3 Low Pressure Receding Speed

From this point we have enough experimental observations to draw conclusions of the effect evaporation rate has on the liquid receding speed during stages 2 and 3. Fig.6.6 is a plot of the average receding speed over the pressure range $20 - 1000$ mbar and initial concentrations $c_0 = 2$, 5 and 10%, as a function of K, the proportionality between evaporation rate and droplet radius. Before conclusions

Figure 6.6: Plot of the average value of $\dot{R}$ during the pseudo-dewetting stage as a function of K, the proportionality between evaporation rate and droplet radius. Data points extracted over the range of atmospheric pressures $P = 20$, 50, 100, 200, 500, and 1000 mbar and initial droplet concentrations $c_0 = 2$, 5 and 10%.

are drawn it must be stated that measurements of liquid base radius were limited to the region in which the measurable liquid base radius is in contact with the substrate. For example, in the $P = 25$ mbar column of Fig.6.4, $\dot{R}$ measurements would be stopped prior to the 6th image as at this point the droplet is being significantly lifted away from the substrate by a very narrow collar, at which point $\dot{R}$ reduces significantly. In this same column however, between images 2 and 6 $\dot{R}$ seems to remain fairly constant, and so this is the value plotted.

The best fit line has been plotted through the origin as it is clear that with zero value of K, evaporation would stop and no receding phase could occur. The dotted lines are given by the calculation of the error in the best fit line based on

the values weighted by their respective uncertainties. This seems to suggest that the magnitude of $\dot{R}$ increases linearly with K:

$$\dot{R} = -\frac{K}{l} = \frac{\dot{V}}{Rl} \tag{6.4}$$

Where l is the reciprocal constant of proportionality and has units of length and is calculated as $l = 1.64 \pm 0.03$ cm. No clear understanding of the physical origin of this characteristic length scale has been found in this work, except that it is not simply the thickness of the deposited layer, which from preliminary profilometry experiments has been measured at approximately 7.7 and 11 μm at atmospheric pressures $P = 200$ and 1000 mbar respectively.

However, it should be stressed that the initial droplet dimensions are kept constant in these experiments, which means that this length scale could be somehow related to initial the droplet radius ($R_0 \sim 0.20 \pm 0.01$ cm) or height ($h_0 \sim 0.135 \pm 0.005$ cm). Further observations of droplets with varying radius and height are required to better define l.

This result alters the geometric argument from the previous chapter. The expression for the minimum pillaring volume at $t = t_{\mathrm{p}}$ given in equation 5.13 can now be rewritten:

$$V_{\mathrm{p}} > \frac{KR_0^2}{2\dot{R}} = \frac{R_0^2 l}{2} \tag{6.5}$$

Despite this slight alteration to the form of the equation, it seems that this predicts that the evaporation should have no effect on the minimum pillaring volume. Therefore the difference in fully dried structures at a given initial concentration can be explained only as a result of the reduced value of t_{p}/t_0.

But why does increasing the evaporation rate reduce the fractional precipitation time? A lower value of t_{p}/t_0 means a lower average concentration in the droplet at the time of precipitation. Presumably, this is caused by the increased evaporative flux, which has a greater pull on the dissolved polymers to the contact line, leading to earlier build up, higher concentration gradients and earlier precipitation. So, here is an interesting thought experiment: What would happen if one were to initially dry a droplet at 20 mbar, but once precipitation begins increase the pressure back to ambient conditions ($P = 1000$ mbar). According to the geometric argument, changing pressure at this point will have no effect on the final structure as the effects of receding speed and evaporation rate cancel out. However, this assumes that if pressure is increased precipitation at the contact

line would continue. I suspect this would not be the case. If pressure is increased the high radial outward pull to the contact line induced by the high evaporation rate will diminish, and the remaining liquid may behave as a typical PEO droplet at ambient conditions which requires a much higher total concentration for precipitation to begin. In fact without the high radial outward flow induced by fast evaporation rates, the polymer which has already precipitated may diffuse back into the solution.

Fig.6.7 is a selection of images taken from a drying droplet experiment in which the pressure was reduced to the lower limits of the rotary vacuum pump (≈ 10 mbar) mid droplet drying, maintained for around 45 seconds, and released back to ambient conditions. As expected, the results show that when the pressure is reduced, fast precipitation driven pseudo-dewetting is the result. More interestingly however is the finding that when the pressure is again increased back to ambient conditions the polymer precipitate slowly diffuses back into the solution. This tells us that despite the geometric argument being unchanged by
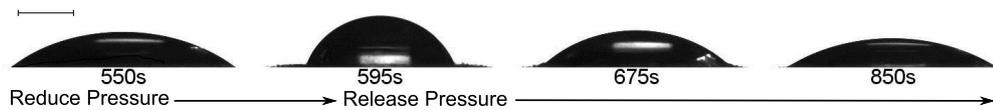
Figure 6.7: Results of inducing and releasing low pressure (~ 10 mbar) mid droplet drying ($c_0 = 10\%$, $V_0 = 10 \ \mu l$). The first image is the droplet after drying for 550 seconds under ambient conditions. At this point pressure is reduced to and maintained at ≈ 10 mbar for 45 seconds. The droplet very quickly precipitates and pdeudo-dewets resulting in the droplet shown in the second image. At this point pressure is released and without the enhanced outward flux of the high evaporation rate, the precipitate begins to redissolve back into the solution, and the liquid spreads back to its original radius after around 300 seconds. Scale bar represents 1 mm.

the evaporation rate, the concentration gradient at the contact line that leads to polymer precipitation is driven by a competition between the evaporation rate and the diffusion coefficient. For earlier precipitation one would need the effects of evaporation induced outward flow to be greater than the effects of polymer diffusion coefficient. Therefore the high evaporation rate must be maintained or the droplet precipitation time will revert back to one found at ambient conditions, which will lead to smaller final structures.

6.1.4 Relative Humidity

As well as atmospheric pressure the evaporation rate is also highly sensitive to the relative humidity, and as discussed in section 4.2.2, using either saturated salt solution baths or silica gel beads are well established methods of controlling RH. Fig.6.8 is a time-lapse sequence of profile images of a droplet drying at a reduced evaporation rate with $RH = 81 \pm 2\%$. Interestingly, as similar to the results
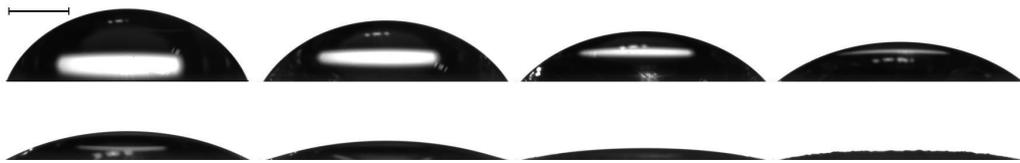
Figure 6.8: Time-lapse profile images of $c_0 = 10\%$ droplet drying at high relative humidity $RH = 81 \pm 2\%$. Total time lapsed 2 hours and 3 minutes. Scale bar represents 1 mm.

found at reduced pressures is that not only does the droplet dry more slowly, but the precipitation time as a fraction of t_0 is increased to $t_\mathrm{p}/t_0 = 0.87$, as compared with $t_\mathrm{p}/t_0 = 0.76$ at ambient conditions ($RH = 55 \pm 5\%$). This means that precipitation occurs (starting in image 7) when the volume is significantly low enough that pillaring no longer occurs.

Fig.6.9 is a sequence of the final profile images over a range of relative humidities, and shows that there is an upper/lower limit to the relative humidity/drying rate that can induce pillar formation.

Figure 6.9: Fully dried profile images of droplets dried in the relative humidity range 25-80%. $c_0 = 10\%$.

A pattern seems to be emerging regarding the evaporation rate and the normalised precipitation time, which gives clues about the polymer concentration gradient that develops in a drying droplet. The final method for varying droplet evaporation rate is through controlling the atmospheric temperature. From the

results of experiments varying P and RH, we would now predict that increasing $\dot{V}$ by increasing T, should lead to taller pillar structures.

6.1.5 Temperature

Fig.6.10 is a sequence of profile images of droplets at $t = t_\mathrm{f}$ at atmospheric temperatures $T = 30.5, 40.0, 51.2$ and $60.1°$C. The temperature of the atmosphere in this set of experiments was controlled as described in section 4.2.3. Fully dried images of similar droplets were captured from above as shown in Fig.6.27, however these droplets were placed inside a ceramic oven with no independent measurements of temperature, relative humidity or evaporation rate, which could explain the discrepancy between the deposits that form, particularly at $T = 40°$.

Figure 6.10: Fully dried profile images of droplets dried at atmospheric temperatures (from left to right) $T = 30.5, 40.0, 51.2$ and $60.1°$C. $c_0 = 10\%$.
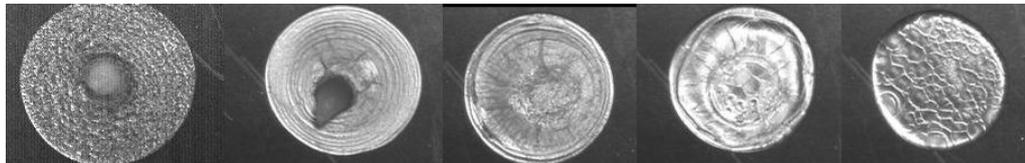
Figure 6.11: Fully dried images of droplets dried in an oven at temperatures (from left to right) $T = 21, 30, 40, 50$ and $60°$C captured from above. $c_0 = 10\%$.

This seems to suggest that there is an upper limit to the temperature at which pillars can form, which is not in line with the predictions from the previous section. On the one hand increasing the evaporation rate through reduction in pressure leads to earlier precipitation and taller pillars. However here we see that increasing evaporation rate by raising the temperature leads to flat uniform deposits. Indeed evaporation rate does increase with temperature as shown in Fig.6.12, so why does this behaviour not tie up with the low pressure results? The answer to this could lie in the diffusive behaviour of polymers in solution,
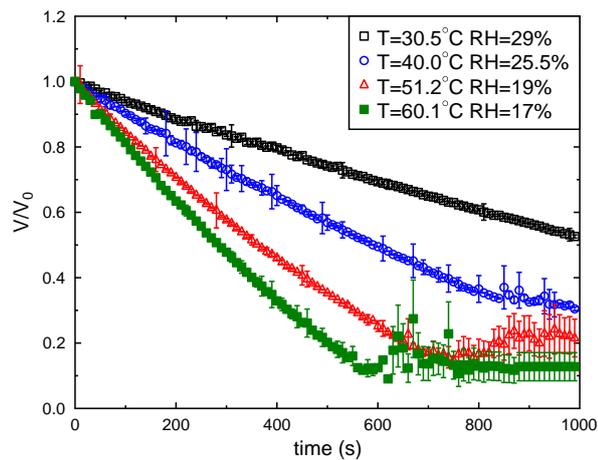
Figure 6.12: Normalised volume curves for droplets evaporating at various atmospheric temperatures. This plot shows that evaporation rate increases with temperature.

and it is at this point that the Péclet number must be introduced.

6.2   Evaporation Versus Diffusion

Following the argument proposed by Deegan et. al. concerning the coffee-ring effect, if a drying sessile droplet is pinned, there must be outward radial flow. Advection is a term used to describe suspended material being swept downstream, which is effectively the process occurring as coffee-grains are carried to the droplet perimeter as shown diagrammatically in Fig.6.13. Dissolved PEO would be expected to behave the same way and be swept to the droplet perimeter in exactly the same manner as is shown diagrammatically in Fig.6.14.

Now let us imagine that evaporation is switched off, or rather the effect of the evaporative flux is significantly smaller than the effect of Brownian motion. As discussed in section 2.2.2, a concentration gradient induces diffusive motion. The polymers that had collected at the perimeter due to the evaporation driven advection are now migrating back down the concentration gradient towards a perfectly homogeneous droplet as shown in Fig.6.15

When this behaviour is considered it becomes clear that the build up of a concentration gradient at the droplet perimeter is given only by a droplet in which
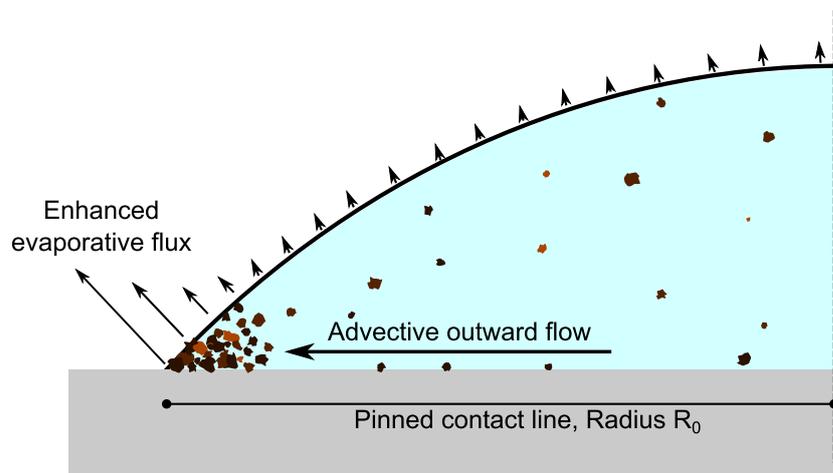
Figure 6.13: Diagram of the advective flow induced by the coffee-ring effect.
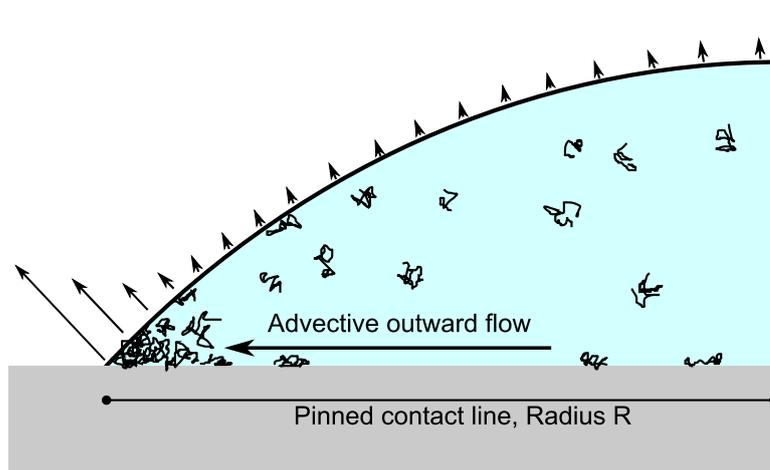
Figure 6.14: Diagram of the advective flow induced by the coffee-ring effect in a PEO droplet.
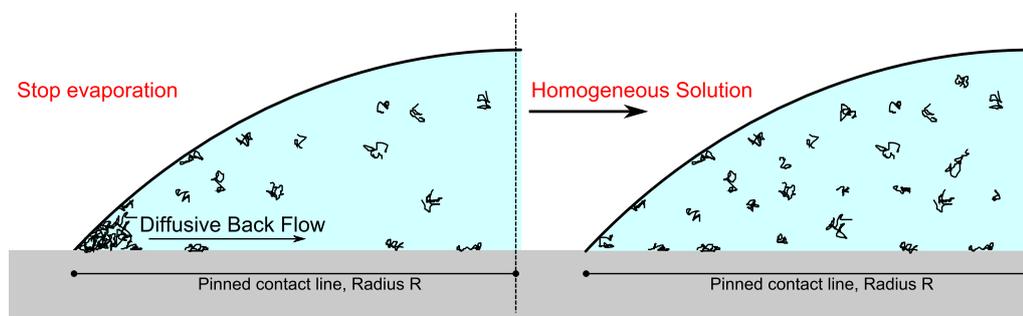
Figure 6.15: Diagram of the perfectly homogeneous system given by a droplet in which the diffusive effects outweigh the evaporative flux driven advective flow.

evaporative flux effects outweigh diffusive effects, and the gradient is given by the ratio of the two. The Péclet number describes this competition between advective build up and diffusive back-flow over a given distance.

6.2.1   A Model For The Péclet Number

To characterise this competition we need terms for the concentration build up at the contact line over time due to advective effects, and the diffusive back-flow given by these concentration gradients. The model discussed in this section for the competition between advective flow to the contact line and diffusive back-flow was developed by my collaborators Prof. Martin Shanahan from the University of Bordeaux and Prof. Khellil Sefiane from the University of Edinburgh, and led to my third publication [158]. As described in section 3.3.4, it is recognized that when $\theta \ll 90°$ the major contribution to evaporation occurs in a small region close to the contact line [85]. From this, let us first assume that all evaporation occurs in a narrow triangular wedge of width ϵ ($\epsilon \ll R$) at the contact line as shown diagrammatically in Fig.6.16.
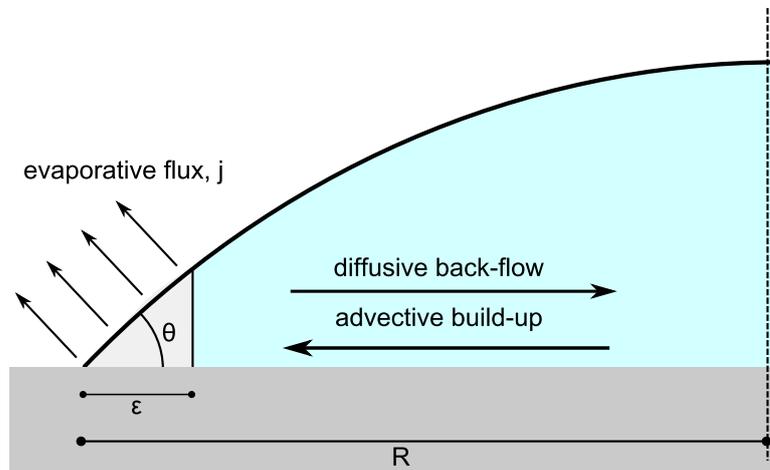
Figure 6.16: Diagram of the first major assumption of the Péclet number characterisation: the vast majority of evaporation occurs in a narrow triangular wedge close to the 3-phase line.

The droplet is now divided somewhat arbitrarily into two homogeneous regions, a large inner volume $0 < r < R - \epsilon$ in which evaporation is negligible and the concentration is assumed to remain at approximately c_0, and the narrow

outer annulus in which the majority of the evaporation occurs and the polymer concentration will increase. This triangular region has a cross sectional area of $\frac{1}{2}\epsilon^2\tan\theta$, and total surface area given by the surface area of a conical frustum (not including the top and bottom circular discs) as shown in Fig.6.17, where:

$$
\begin{aligned}
A &= \pi(R_1 + R_2)s \\
&= \pi(2R - \epsilon)\frac{\epsilon}{\cos\theta} \\
&= \frac{2\pi R\epsilon}{\cos\theta}\left(1 - \frac{\epsilon}{2R}\right)
\end{aligned}
$$

(6.6)

and because $\epsilon \ll R$:

$$
A \simeq \frac{2\pi R\epsilon}{\cos\theta}
$$

(6.7)
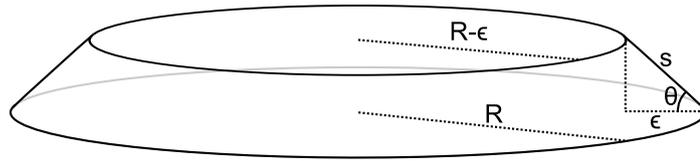
Figure 6.17: Diagram of the conical frustum over which the majority of evaporation occurs.

Since we have experimental values of overall evaporation rate, $\dot{V}$, we may estimate the evaporative flux per unit area (j) over the conical frustum as:

$$
j \approx -\frac{B\dot{V}\cos\theta}{2\pi R\epsilon}
$$

(6.8)

where B is the fraction of the total evaporation rate that occurs from this narrow region ($0 \ll B < 1$).

For the (idealised) quasi-static situation in which the cross-sectional area of the edge region does not vary with time (equivalent to constant contact angle), the water lost by evaporation from this region must be replaced by the arrival of liquid from the center of the droplet with equal volume. However, unlike the evaporate, the replenishing liquid will not be pure water but will also contain polymer at a concentration c_0. Now let us consider the total volume lost (and thus the induced volume flow) per unit length of the 3 phase line as shown in Fig.6.18. The evaporation rate through this section is simply the product of the average
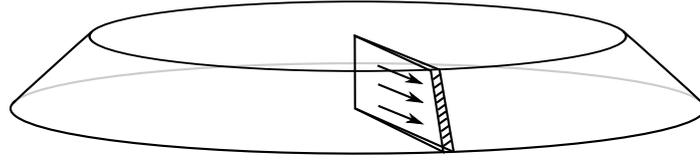
Figure 6.18: Diagram of the outward flow of polymer from the bulk of the droplet per unit length of 3 phase line.

evaporative flux across the frustum and the length of this section, $j\epsilon/\cos\theta$. This is essentially a 1D model of the polymer motion with time, originating somewhere in the middle of the droplet and travelling toward this section of the conical frustum. The incoming polymer volume reaching this region per unit time is given by the product of the evaporation rate over this section and the concentration of the solution, $j\epsilon c_0/\cos\theta$. Finally, the rate of increase in polymer concentration at the droplet perimeter due to advective flux, $\left(\frac{dc}{dt}\right)_{\text{adv}}$, is given by the rate of arrival divided by the cross sectional area of the triangular region shown in Fig.6.16:

$$\begin{aligned}\left(\frac{dc}{dt}\right)_{\text{Adv}} &= \frac{j\epsilon c_0}{\cos\theta}\frac{1}{\frac{1}{2}\tan\theta\,\epsilon^2}\\ &= \frac{2jc_0}{\epsilon\,\sin\theta}\end{aligned} \tag{6.9}$$

Combining with equation 6.8 for j gives:

$$\begin{aligned}\left(\frac{dc}{dt}\right)_{\text{Adv}} &= \frac{2c_0}{\epsilon\,\sin\theta}\frac{B\dot{V}\cos\theta}{2\pi R\epsilon}\\ &= \frac{B\dot{V}c_0}{\epsilon^2\tan\theta\,\pi R}\end{aligned} \tag{6.10}$$

As we have shown, this will be countered by a diffusional back flow due to the developing polymer concentration gradient. For very dilute polymer solutions, the gradient diffusion coefficient is equal to that given by the Stokes-Einstein relation for single molecule self diffusion D:

$$D = \frac{kT}{6\pi\eta_{\text{s}}R_{\text{h}}} \tag{6.11}$$

For more concentrated, entangled solutions, the gradient diffusion can be faster as the network entanglement length replaces R_{h} in the Stokes-Einstein equation [17]. Notwithstanding this dependence on concentration, as we do not vary the polymer length or solvent, and disregarding the small set of experiments in which temperature was varied, molecules in all droplets will have with the same limiting

value of the gradient diffusion coefficient, which will be some multiple of D. It is acknowledged that a more rigorous mathematical approach is required to allow for cooperative and reptative diffusion effects at high concentrations.

By using Fick's second law we can now estimate the rate of decrease in the concentration gradient with time due to purely diffusive effects, $\left(\frac{\partial c}{\partial t}\right)_{\mathrm{D}}$, from the spatial variation in the concentration gradient:

$$\left(\frac{\partial c}{\partial t}\right)_{\mathrm{D}} = D\left(\frac{\partial^2 c}{\partial x^2}\right) \tag{6.12}$$

The maximum effect diffusion could have would occur at the greatest concentration gradient, which is limited to $c = c_{\mathrm{sat}}$ at the contact line and $c = c_0$ at some distance away. Due to the nature of the advective flow through this narrow triangular region, let us assume that the gradient over the wedge at precipitation time is given by $(c_{\mathrm{sat}} - c_0)/\epsilon$.

To test whether the centre of the droplet remains at $c = c_0$ during the pinned stage we need a method of measuring the concentration in situ during evaporation. One such method would be through the use of optical coherence tomography, or OCT.

6.2.2 Bulk Concentration Changes

As discussed in section 4.3.2, OCT could be used to measure the average refractive index across vertical slices through the droplet by comparing the known height of the droplet, and the apparent optical height of the droplet ($RI = h'/h$). Unfortunately, due to the atomically smooth nature of the surface of the droplet only a small portion of the air-droplet interface reflects light in the direction of the detector (namely the droplet apex), and so only across this narrow central region could the vertically averaged refractive index be measured. The refractive index of water is highly dependent on wavelength, but with OCT, which uses a broadband light source centred at 930 nm, this method yields a value of $RI \approx 1.3345 \pm 0.001$ [138]. Whereas PEO has a refractive index of $RI = 1.4539$ (as provided by the suppliers Sigma-Aldrich). Therefore if the concentration in this region increases, we should observe a refractive index increase as time goes on. Fig.6.19 is a plot of RI against time normalised by the precipitation time (t/t_{p}) for a PEO droplet with initial concentration $c_0 = 5\%$, and shows that RI
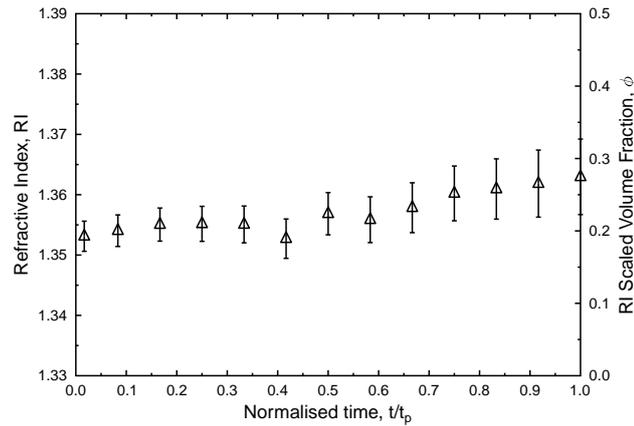
Figure 6.19: Average refractive index across the central vertical region of a PEO droplet ($c_0 = 5\%$, $M_W = 100$ kg/mol) plotted against time normalised by the precipitation time, t/t_p.

remains relatively unchanged for the first half of stage one, with a slow increase during the second half as the droplet prepares to precipitate. This suggests that, for a while at least, the assumption that concentration in the bulk remains constant is not entirely unreasonable. Puzzlingly however is the observation that the initial refractive index was found to be around $RI \approx 1.35$, which if we assume a linear proportionality between volume fraction and refractive index gives an initial concentration (by mass) of $18 \pm 2\%$. Clearly this is not the case, and a more thorough investigation of refractive index versus concentration is required. Furthermore, I found that if my measurement of either the optical or the real height from the OCT images is out by just one pixel (and consider that in the first image the optical height is estimated as 456 pixels, this is a small error indeed), this leads to a miscalculation of the concentration by around $\pm 3\%$. Clearly a better method of measuring the concentration during drying is required.

As we will discuss later, the assumption that the concentration of the bulk of the droplet remains at the initial concentration is not particularly likely, but this sets the upper limit of both evaporative flux and gradient diffusion effects. Next we will assume that the inner region is homogeneous, and the concentration gradient here is virtually 0, so the required second derivative can be estimated as the difference in the gradients divided by distance ϵ:

$$\left(\frac{\partial c}{\partial t}\right)_D = D\frac{c_{\text{sat}} - c_0}{\epsilon^2} \tag{6.13}$$

Now, the ratio of the concentration build-up due to advection and evaporation, and concentration reduction due to diffusion can be written:

$$\frac{\left(\frac{dc}{dt}\right)_{\text{Adv}}}{\left(\frac{\partial c}{\partial t}\right)_{\text{D}}} = Pe \approx \frac{B}{\pi}\frac{c_0}{c_{\text{sat}} - c_0}\frac{\dot{V}}{DR\tan\theta} \tag{6.14}$$

Clearly, if $Pe > 1$, the effects of advection should be dominant and net build-up is to be expected near at the droplet perimeter, whereas for $Pe < 1$, gradient diffusive effects should be dominant and polymer concentration should stay uniform throughout the droplet. With terms B and D assumed constant, it can be seen that the three crucial factors determining Pe are the initial concentration, the droplet shape and the evaporation rate. This is interesting as it shows that at ambient conditions, as considered in the previous chapter, the droplet shape should have an impact on the precipitation time, as high Pe means early polymer build up at the perimeter and thus a reduced value of t_{p}. This means that while the geometric argument previously proposed remains unaffected by evaporation rate, complete understanding of the pillaring behaviour of droplets with regards to contact angle and volume can not be complete without consideration of the Péclet number. Furthermore if we assume that the evaporation rate scales with the radius (R), temperature (T), relative humidity (RH) and pressure (P) as follows:

$$\dot{V} \propto \frac{RT(1 - RH/100)}{P} \tag{6.15}$$

then by recombining with equation 6.14 we have an estimate of the Péclet number factoring in atmospheric conditions:

$$Pe \approx \frac{B}{\pi}\frac{c_0}{c_{\text{sat}} - c_0}\frac{KT(1 - RH/100)}{PD\tan\theta} \tag{6.16}$$

However, it must be stressed that the proportionalities between atmospheric conditions and evaporation rate have limitations. Pressure, relative humidity and temperature are all intrinsically linked, so it is difficult to create a situation where just one of these factors could be altered, particularly in the case of a reduced pressure which not only alters the humidity of the environment, but by increasing evaporation rate also decreases the temperature of the drop through the latent heat of vapourisation. Essentially, the effects of the varying atmospheric conditions on evaporation rate are complex, so for simplicity it will be assumed that these proportionalities are valid for the range of experimental conditions examined in this thesis. I urge the reader however to think about these dependencies carefully if he or she should chose to replicate these experiments.

With this equation we now have some understanding of the effects of atmospheric pressure, relative humidity and temperature on whether pillar formation will occur, arising due to their respective dependencies on the droplet's initial Péclet number. A low Péclet number would lead to shallow concentration gradients, no preferential deposition at the edge and a flat uniform final deposit, whereas a high Péclet number would give very early crystallisation at the contact line, followed by a receding contact line and increasing height during stages 2 and 3, and a final pillar-shaped deposit provided V_p is large enough.

6.2.3   Predictions Of The Péclet Number

The predicted dependency of initial atmospheric and geometric conditions on t_p/t_0 is detailed below and compared with the results previously found. In all observations considered in this summary $c_0 = 10\%$, and any effects of concentration on the diffusion coefficient are not considered as the concentration profile at $t = t_p$ is assumed to be constant:

- **Relative humidity and pressure**. At constant concentration and temperature, D is constant. Increasing $\dot{V}$ by reducing pressure or relative humidity will increase Pe. Pillars continue to form, and under low pressures are significantly taller than at atmospheric pressure. Conversely, reducing $\dot{V}$ by increasing RH stops pillar formation, as expected for lower values of Pe.

- **Temperature**. From the literature [100] it is known that in the temperature range we are working at, total evaporative flux is linearly proportional to temperature: $\dot{V} \propto T$. However, the cooperative diffusion coefficient is a function of temperature and viscosity [19], $D_c \propto k_B T / 6\pi R_h \eta$, where η is the solution viscosity. Previous work studying the viscosity of PEO $M_W = 10$ kg/mol [159] shows that in the range of temperatures we have observed the solution viscosity is given by $\eta \propto T^{-\alpha}$ where α lies between 2 and 3. Combining these various dependencies on T (at constant concentration) gives:

$$Pe \propto T^{-\alpha} \qquad (6.17)$$

  Thus an increase in temperature will lead to smaller Péclet number, as the effects of faster evaporation are insignificant compared to the reduction in

viscosity and increase in diffusion, in agreement with observations shown in Fig.6.10.

- **Contact angle.** At constant initial radius and varying contact angle, we would expect the Péclet number to increase with reducing contact angle, which at first glance would appear to disagree with the observations of contact angle dependency on pillar formation from the previous chapter. However, it is difficult to make comparisons from this to the results shown in Chapter 5 (in which below $\sim 45°$ pillar formation stopped) for several reasons. Firstly, in this set of experiments both initial radius R_0 and contact angle θ_0 were varied while volume remained constant. Secondly, unlike atmospheric conditions which remain fairly constant throughout a given experiment, the contact angle reduces with time, which would lead to a steadily increasing value of Pe. Thirdly, while a value of Pe greater than 1 is necessary for build up at the contact line, it is not sufficient for pillar formation to occur, as we have discussed in the previous chapter, a geometric constraint (which intrinsically includes a contact angle dependency) is also required. Thereferore the dependency of θ_0 on pillar formation requires further investigation. Furthermore this approach is only valid for θ_0 intermediate between 0° and 90°: for low θ the droplet is more like a drying film in which only vertical, not horizontal flux is important; on the other hand, close to 90°, flux is uniform across the surface so the assumption that most evaporation takes place within ϵ of the 3 phase line breaks down.

  The Péclet argument does however predict that for a droplet with a contact angle above 90°, the Péclet number would be less than unity, $Pe < 1$, and therefore preferential precipitation at the droplet perimeter should not be possible, which is in agreement with our observations. On hydrophobic surfaces in which very little pinning took place, θ remained above 90° and precipitation appeared almost uniform. Whereas on hydrophobic surfaces with a high pinning force, θ was able to reduce below 90°, and contact line precipitation was observed. This prediction is also very much in line with the well established coffee-ring effect, which requires either a pinned contact line or enhanced evaporation at the 3-phase line for outward radial flow to be induced in the first place.

- **Volume.** Equation 6.16 shows that when the radial dependency on $\dot{V}$ is taken into account, the size of the droplet becomes unimportant to the

Péclet number. This is certainly in agreement with the results shown in the previous chapter which showed that as long as the droplet height is below the capillary length, pillar formation appears unaffected by V_0. Above this size, while the Péclet number may indeed remain unaffected as it only takes into account the advective and diffusive effects in the radial direction and not the droplet height, the geometric constraints which were showed to be significant to the pillar formation process in the previous chapter become altered somewhat. Therefore it becomes difficult to predict the final fully dried structures of large flat puddles. Because this research focuses on the drying of droplets and not puddles, these large volumes have not been investigated.

6.2.4   Quantifying Pe

To quantify the Péclet number we first need an estimate of the diffusion coefficient D. Again, we are assuming that the diffusivity is given by the very low concentration limit in which the polymer behaves as a solid sphere with radius R_{h} and is unaffected by increases in concentration. Using Ficks law, the local evaporative flux can be written as $j = D\nabla c$, where D is the gradient diffusion coefficient and ∇c is the concentration gradient. Again, as previously shown, the greatest effect of diffusion would be given by a droplet where $c = c_{\mathrm{sat}}$ at the perimeter and $c = c_0$ at some unknown distance away. In the previous section we considered this to be over a narrow wedge at the 3-phase line with distance ϵ. Fig.6.20 is a schematic plot of the concentration profile as a function of distance from the centre of the droplet r at the precipitation time $t = t_{\mathrm{p}}$.

In reality the concentration profile will be smooth, but for simplicity let us assume a linear decrease over distance ϵ and a sharp leveling off beyond this distance.

As with the work of Pauchard et. al. [7], now we will write the distance ϵ in terms of a diffusive length scale on the order of $\sqrt{Dt_{\mathrm{p}}}$. Fick's first law can now
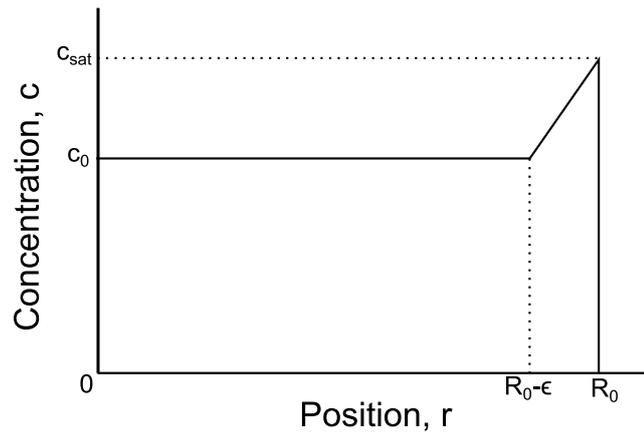
Figure 6.20: Schematic plot of the assumed concentration profile at $t = t_{\mathrm{p}}$.

be rewritten as:

$$
\begin{aligned}
j &= -D\frac{dc}{dx} \\
&= -D\frac{(c_{\mathrm{sat}} - c_0)}{\sqrt{Dt_{\mathrm{p}}}} \\
&= -\frac{\sqrt{D}(c_{\mathrm{sat}} - c_0)}{\sqrt{t_{\mathrm{p}}}}
\end{aligned}
\tag{6.18}
$$

In Fig.6.21 $j\sqrt{t_{\mathrm{p}}}$ is plotted against c_0 for a large range of droplets (from experiments at ambient conditions), with the best fit line crossing the horizontal axis at $c_{\mathrm{sat}} = 60 \pm 6\%$ in close agreement with literature values [160]. The square of the
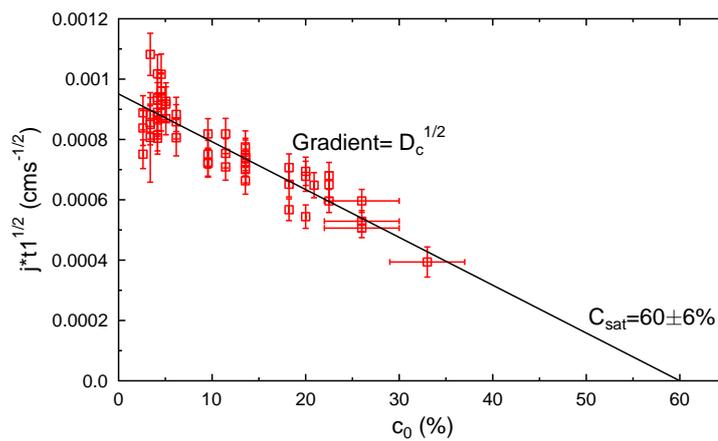

Figure 6.21: Plot of $j\sqrt{t_{\mathrm{p}}}$ plotted against concentration and a weighted best fit line. This gives $c_{\mathrm{sat}} = 60 \pm 6\%$ in close agreement with the literature [160] and $D = 25 \pm 10$ $\mu\mathrm{m}^2/\mathrm{s}$.

gradient gives an estimate of the diffusion coefficient as $D = 25 \pm 10$ μm^2/s. We can compare this with the estimate of the diffusion coefficient given by equation 6.11. PEO has a Kuhn length $b = 1.1$ nm and Kuhn mass $M_0 = 0.137$ kg/mol, giving a single chain with molecular weight $M_W = 100$ kg/mol in a good solvent a hydrodynamic radius of $R_h = 14.66$ nm. Therefore, in very dilute solutions this gives a diffusion coefficient of $D = 14.6$ μm^2/s, which is within the error bars of our estimate. The large error bars at high concentrations are due to the difficulty in measuring the density post-filtration for such high viscosity solutions, and so these concentration values are estimates.

However, for plotting this graph j was estimated as simply the total evaporative flux divided by the surface area of the droplet, thus assuming that j is uniform over the entire surface of the droplet, which is certainly not the evaporative flux profile proposed in the previous section. Furthermore, it may not be reasonable to assume a uniform concentration gradient, or that the centre of the droplet remains at $c = c_0$. In the polymer review chapter the dependencies of concentration on both the self and cooperative diffusion coefficient in dilute, semi-dilute and entangled solutions were discussed in depth. Despite this, it is difficult to know exactly what regime we are in as we are making assumptions about the concentration gradient close to the contact line. It is clear a more rigorous approach to calculating the diffusion coefficient is required, which is beyond the scope of this primarily experimental research. For now we will move forward with this estimate of D as, with the exception of experiments in which temperature was varied, and ignoring the unknown evaporative cooling effects at low pressures, D is expected to be a constant for the majority of experiments performed.

Fig.6.22, is a plot of the two dimensionless quantities $\dot{V}/DR$ against $c_0/(1 - c_0)$ on log axes, using $D = 25$ μm^2/s and indicates pillars by triangles and flat disks by circles. The dependency of $\tan\theta$ has been omitted from this plot due to the complicated relationship between pillar formation and θ_0 as described in the previous section.

As we have shown previously, the Péclet number is a necessary, but not sufficient requirements for pillar formation. Clearly if the Péclet number is dominated by diffusion ($Pe < 1$), no preferential precipitation can occur at the contact line, and therefore pillar formation would be impossible. Additionally, in the previous chapter we also discussed cases in which preferential deposition at the contact line
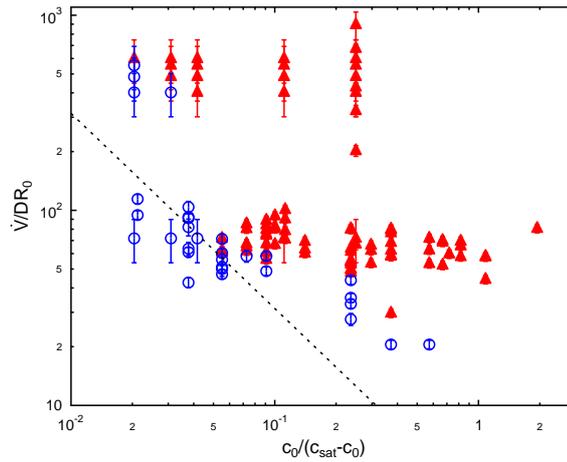
Figure 6.22: Phase diagram showing the nature of the final deposit, either a tall central pillar (filled red triangles) or a flat disk (hollow blue circles). The vertical axis combines evaporation rate, droplet radius and diffusion coefficient, and the horizontal axis is a function of initial droplet concentration c_0. Uncertainties are primarily due to difficulties in measuring evaporation rates when droplets dry rapidly in low pressure conditions. The dotted line is from the theoretical model, and corresponds to a value of $Pe = 1$.

still led to coffee-ring like stains due to the geometric constraints of the droplet at $t = t_p$ and in this plot no distinction is made between flat uniform deposits and coffee-ring type deposits. Therefore, it is difficult to use the calculated Péclet number to define a boundary between pillar and non-pillar formation. Despite this, by setting the fractional evaporative flux at the contact line to $B = 1$, and plotting the $Pe = 1$ boundary, we should find the condition below which pillar formation can not occur. This boundary is plotted as the dotted line in Fig.6.22 and shows good agreement with the theoretical minimum conditions that must be met before pillar formation is possible. Flat deposits above the line are possible due to the geometric conditions of the droplet once precipitation begins at the contact line.

6.3 Evidence For Contracting Collar

In the last chapter three possible explanations for the unusual receding liquid behaviour of PEO droplet drying were proposed. The first, buckling of a wa-

ter permeable incompressible polymer skin, was dismissed on grounds that the surface area increases during the boot-strap building phase. The validity of the remaining two, autophobic dewetting and mechanical squeezing from a contracting collar, remained unclear.

6.3.1   Levitation

Levitation offers a unique perspective in droplet drying as it removes the necessity of a substrate, which as we have seen in Chapter 3 introduce complications to the drying process such as non-uniform evaporation, advective flows and convection currents. Diamagnetic levitation in particular is an exciting prospect as unlike other levitation methods (such as acoustic levitation [161]) the fluid is levitated at a microscopic level (which means that every water molecule experiences an upward force greater than and in opposition to g) rather than being simply held up at the base of the droplet against the pull of gravity which tends to deform the droplet surface [142].

Fig.6.23 is a time lapse sequence of images of a drying PEO drop ($c_0 = 10\%$, $V_0 = 0.44$ ml) suspended in a magnetogravitational potential trap. The images show the drop as viewed from above (left) and from the side (right). The drop viewed from above seems to slowly move out of focus, whereas the images from the side show that the droplet is shifting to the left (down into the bore) with time. This is most likely due to the differing magnetic susceptibility of water and PEO ($\chi_{\text{water}} = -9.051 \times 10^{-9}$ m^3/kg [162], $\chi_{\text{PEO}} \approx -0.62 \times 10^{-9}$ m^3/kg [144] at 300 K and $M_{\text{W}} > 16$ kg/mol.) As the water concentration reduces, the magnetic susceptibility of the droplet reduces and therefore the repulsion force between the liquid and the high magnetic field reduces, causing the droplet to drift to a lower position in the magnetogravitational potential trap. It must be noted that despite removing the substrate, convection currents may persist. The machine that induces the high $B\nabla B$ involves supercooled fluids to allow for superconducting coils. These fluids then somewhat cool the air within the bore, which then could have the unwanted side effect of creating a temperature gradient vertically across the drop, which as we have seen can induce Bénard cells, Marangoni flow and evaporative flux gradients. Due to the time constraints with using this levitation device these effects were not explored any further.
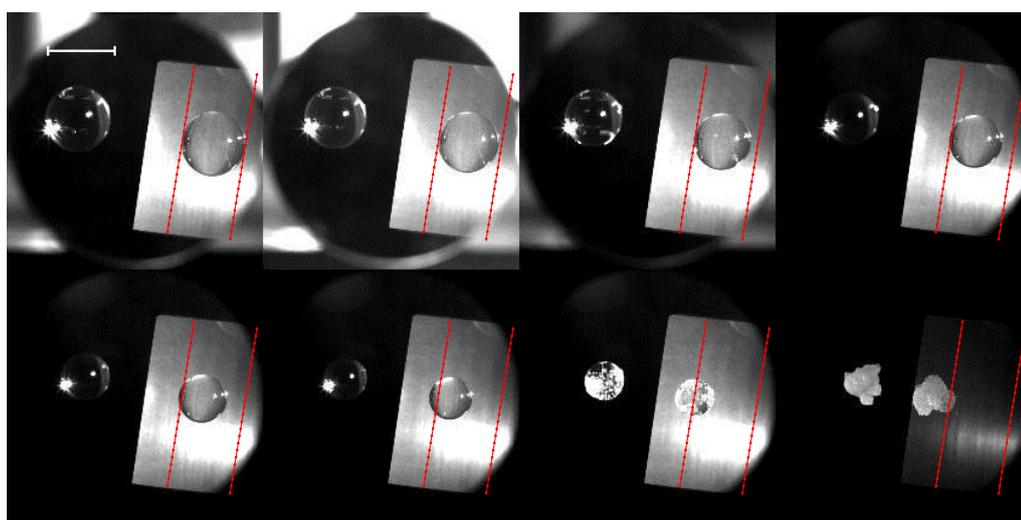
Figure 6.23: Time-lapse sequence of images of a diamagnetically levitating PEO droplet. Images show the drop as viewed from above (left) and from the side (right). The drop viewed from above seems to slowly move out of focus, whereas the images from the side show that the droplet is shifting to the left (down into the bore) with time due to the decreasing magnetic susceptibility of the solution. Late images show highly irregular structure after PEO precipitation. Total duration 9 hours 58 minutes and 12 seconds. White bar represents 1 cm. Red dotted lines added as guide to eye to show relative position of the droplet with time compared with the position at $t = 0$.

Immediately it can be seen that despite the removal of the substrate the final structure formed in the 8th image has a highly irregular structure. Fig.6.24 is a time-lapse sequence of images exploring the solidification process in more detail. While initially the spherulites appear to form uniformly over the droplet
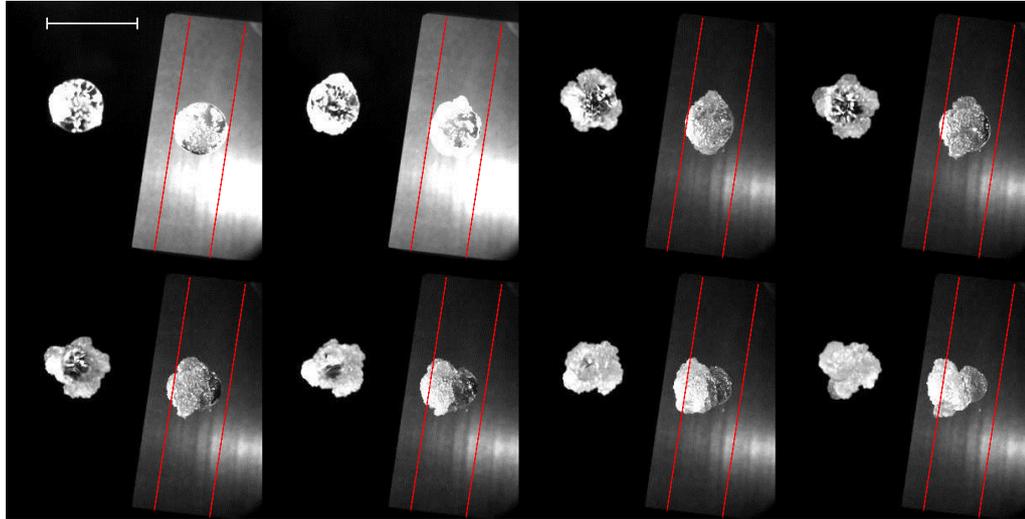
Figure 6.24: Time lapse sequence of images of a diamagnetically levitating PEO droplet after precipitation begins. Images show that precipitation occurs preferentially on one side of the droplet, which continues to contract and push itself away from the remaining liquid. Total duration 1 hour 16 minutes and 10 seconds. White bar represents 1 cm, red dotted lines added as guide to eye to show position of the solid and liquid surfaces with time relative to the droplet at $t = t_p$.

surface, they then collect together preferentially at the bottom of the droplet (left of profile images), possibly due to the reduced magnetic susceptibility of the spherulites compared with the water rich liquid phase. This is suppported by the observation that after the final image in Fig.6.23 the solid structure falls out of the magnetogravitational potential trap. The red dotted lines are added as a guide to the eye to show the change in position of the solid and liquid surfaces of the droplet in time with respect to the droplet position and the fixed reference mirror. Interestingly, when these spherulites have collected together they continue to contract. Ideally, for the contracting collar argument we would like to observe the remaining liquid to be extruded out from the solid interior. However, the nature of diamagnetic levitation keeps the liquid fixed in place while the contracting solid moves down into the bore, as shown diagramatically in Fig.6.25.
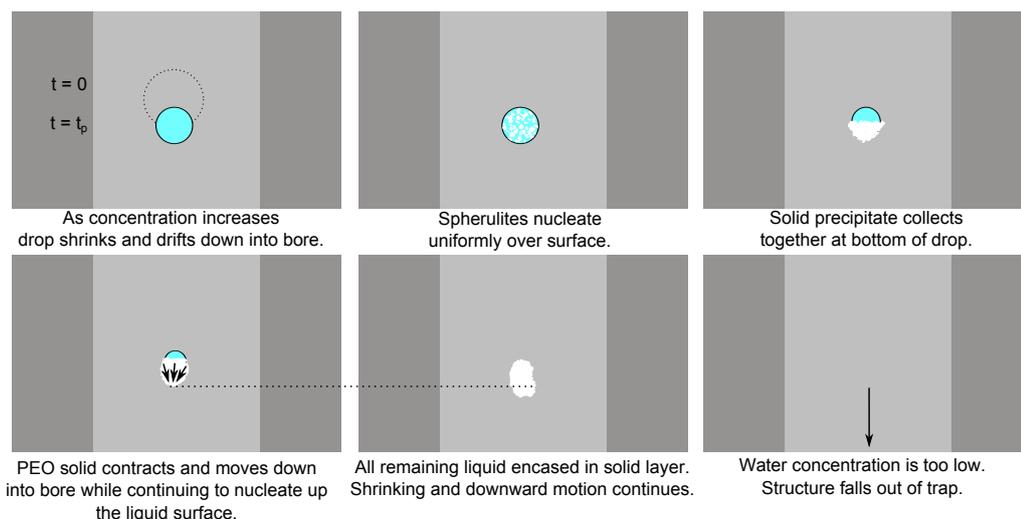
Figure 6.25: Diagram of the drying behaviour of diamagnetically levitating PEO droplets after precipitation begins. While nucleation occurs uniformly, these spehrulites collect together at the base of the drop. Spherulite nucleation continues in the direction away from the precipitate up the drop surface as the solid PEO contracts and moves down into the bore. Eventually the water content of the structure is too low and it falls out of the magnetogravitational potential trap.

Therefore while the solid shrinking adds evidence to the contracting collar argument, this cannot show that this contraction is sufficient to squeeze the liquid out of the volume it occupies.

6.3.2 Droplet Inflation

A key component of the contracting collar argument is that there must be a small wall-like structure around the remaining liquid during the receding stage. I have proposed that the combination of growth and contraction makes this wall difficult to observe directly from profile imaging. However, there could be a simple test to observe whether this spherulite PEO "collar" exists - droplet inflation. By lowering an automated syringe into the droplet at some point during the pseudo-dewetting stage and flooding the liquid phase with more PEO solution, its behaviour should give us key information about the structure and wettability of the deposit. If a contracting collar is indeed present, we would expect the droplet to inflate with a fixed base radius. This would continue until some point at which the volume is sufficiently high that the liquid spills over the top of

the spherulite collar and wets the already deposited thin PEO layer. This would effectively kill two birds with one stone. If the droplet inflates and spills over then it will add weight to the evidence of a solid collar around the liquid phase. But furthermore, if the liquid, once spilled, easily wets the solid it will add evidence against the autophobicity argument.

Fig.6.26 is a time-lapse sequence of images immediately prior to, during and after droplet inflation, and shows exactly what the constricting collar hypothesis suggests.
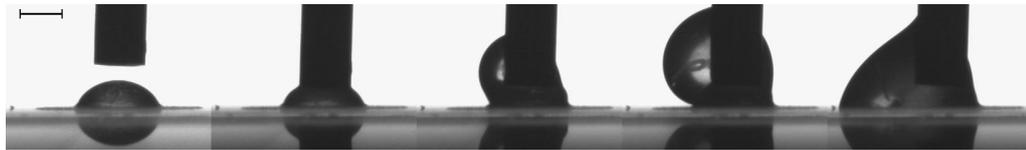
Figure 6.26: Series of profile images captured during the inflation of a PEO droplet with further PEO solution during the pseudo-dewetting stage. The influx of liquid leads to a build up in the centre with a fixed base radius. This continues until the volume is sufficiently large that it spills over the spherulite collar and wets the thin layer of deposited solid PEO. Scale bar represents 1 mm.

6.3.3 Droplets On A Slope

An interesting result found early in this research was that droplets on a slope, depending on the angle of inclination and initial concentration, can display a pillar formation process which leads to the final deposit preferentially growing against the direction of gravity. In a somewhat tongue-in-cheek manner this behaviour was coined "anti-drip paint" for its tendency to over compensate in countering the effects of gravity, as opposed to typical non-drip paint designed to simply resist the downward pull of gravity.

Fig.6.27 is a series of vertical time-lapse sequences of droplets with initial concentration $c_0 = 6\%$ drying at various angles of inclination. The last 2 or 3 images in each sequence show this upward motion clearly, particularly at $\theta_I = 50$ and $71°$ in which the upward motion of the lower liquid contact line is sufficiently fast that the remaining liquid appears to spill up over the top retreating contact line and wet the already deposited solid. Leaving the surprise at this "anti-drip
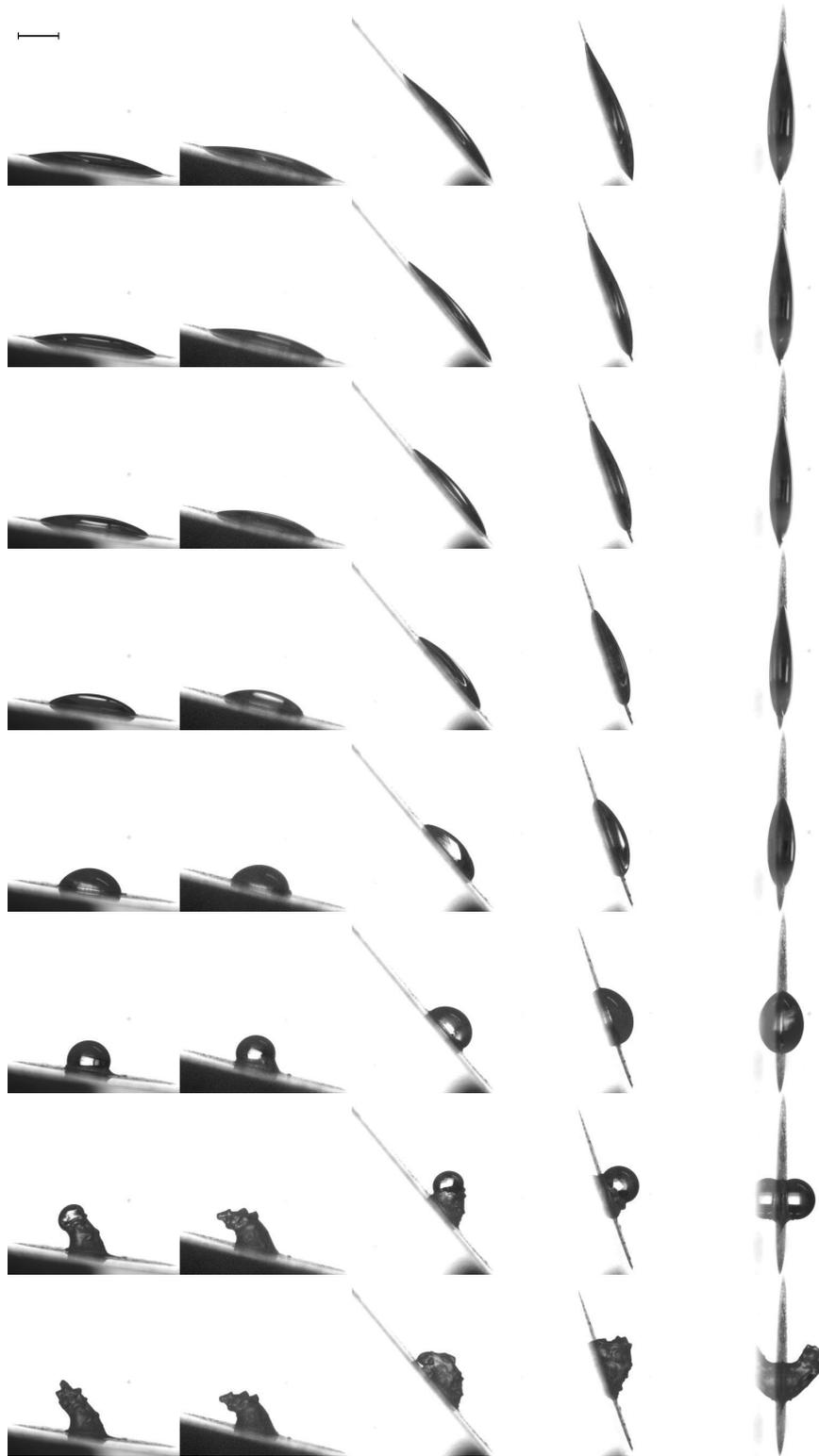
Figure 6.27: Time lapse images of droplets drying at varying angles of inclination, from left to right $\theta_{\mathrm{I}} = 9$, 15, 50, 71 and $90°$ encapsulating the time range from similar midpoints during the receding stage and the start of the late contraction stage. Initial concentration $c_0 = 6\%$. Total duration from top to bottom 17.5 minutes. Scale bar represents 1 mm.

paint" behaviour aside for a moment, careful analysis gives crucial clues as to the pillar forming process. Firstly, the final "toppling" images of the $\theta_I = 50$ and $71°$ sequences add weight to the dismissal of the autophobic argument, which would negate the possibility of the liquid phase wetting the solid deposit.

Fig.6.28 is a series of radius versus time plots for each angle of inclination. However, unlike other measurements of radius in which the total diameter was extracted from the images and divided by 2, here the radius is measured as simply the distance between the contact line at both the top and the bottom from the centre of the droplet, allowing for separate measurements of the receding speed from both the top and bottom of the droplet.

Two important observations can be made from these plots. Firstly, the droplet begins precipitation at the top first at every angle of inclination. This can be explained due to the droplet deformation under the influence of gravity. In previous experiments gravity had no effect on the droplet shape as the droplet height was kept below the capillary length of water ($\lambda_c \approx 2$ mm). However, on an incline the effective height of the droplet in the direction of gravity is greater than the distance between the substrate and the apex of the droplet as shown in Fig.6.29. When this effective height increases above λ_c, the droplet either slides down the substrate, which is indicative of the bottom and top droplet edges having the advancing and receding contact angles of the droplet respectively, or the droplet bulges down in the direction of gravity, resulting in a difference in the contact angle given by [163]:

$$\Delta\theta = \sin\theta_{\mathrm{T}} - \sin\theta_{\mathrm{B}} = \left(\frac{R}{\lambda_{\mathrm{c}}}\right)^2 \sin\theta_{\mathrm{In}} \tag{6.19}$$

This is shown diagrammatically in Fig.6.30[†]. This figure also shows the knock-on effect this has on the surface evaporative flux profile. As discussed in Chapter 3 the evaporative flux is enhanced at the droplet perimeter, and this enhancement is greatest for lower contact angles. Therefore, a droplet on a slope in which the effective height is greater than the capillary length will evaporate fastest from the top edge, which results in earlier precipitation at the top of the droplet than at the bottom.

Secondly, the bottom contact line recedes with a higher velocity than the top.

[†]The maximum effective height found at an incline of $\theta_{\mathrm{In}} = 90°$ is given by the droplet diameter, therefore these effects would not be observed in droplets with initial radius $R_0 < \lambda_{\mathrm{c}}/2$.
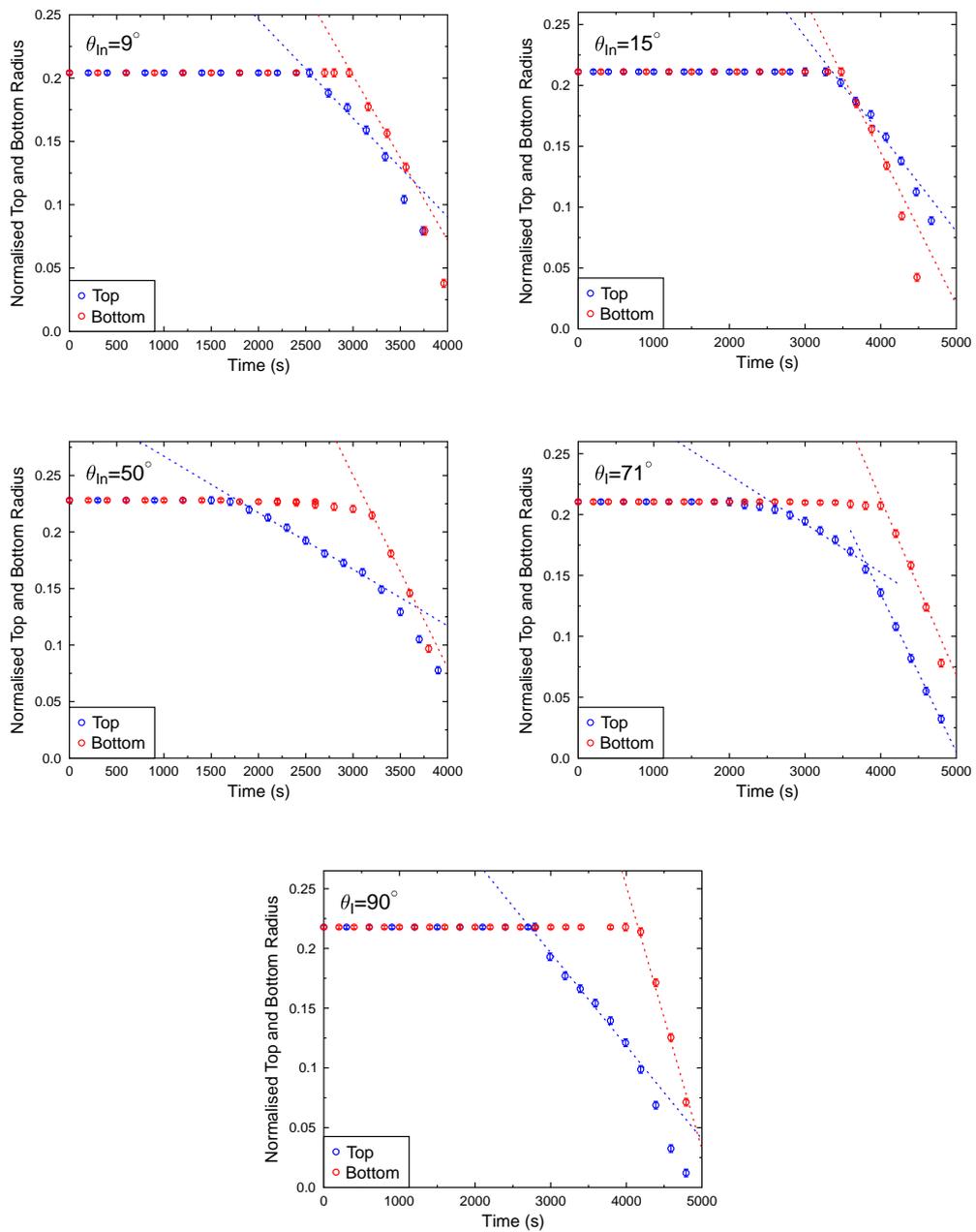
Figure 6.28: Series of radius versus time plots at angles of inclination $\theta_{\mathrm{In}} = 9, 15, 50,$ 71 and $90°$. The blue and red plots are measurements of the top and bottom radius as the distance between the centre of the initial droplet and the top and bottom 3-phase lines.
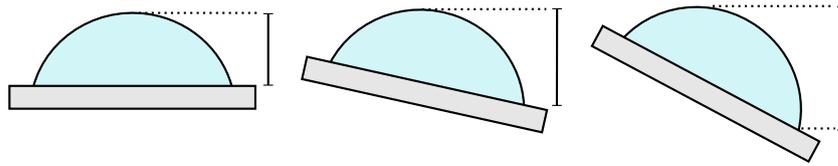
Figure 6.29: Diagram of the effective height increasing with the angle of inclination. When this effective height increases above the capillary length ($\lambda_c \approx 2$ mm for water), assuming high hysteresis, the droplet bulges down in the direction of gravity.
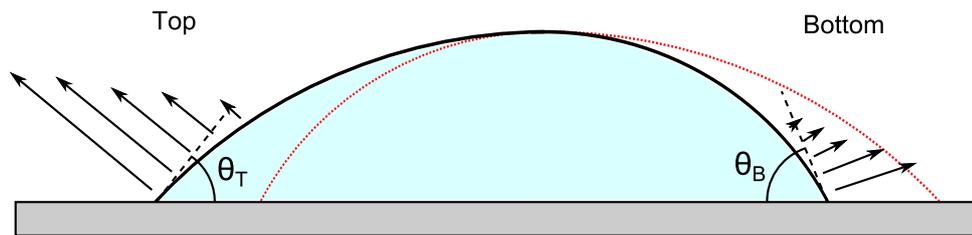
Figure 6.30: Diagram of a droplet on an incline with different contact angles at the top and bottom due to the influence of gravity. The dotted lines show the respective spherical cap shapes given by the radius of curvature at the top and bottom of the droplet.

The blue and red dashed lines in Fig.6.28 show the initial receding speeds from the top and bottom respectively, with the exception of $\theta_{\mathrm{In}} = 71°$ in which the receding phase from the top contact line has been split into two linear regions. In each plot, particularly at $\theta_{\mathrm{In}} \geq 50°$, the initial red dashed line has a much greater gradient than the blue. This is interesting as previously it had been shown that the receding speed increases with evaporation rate, whereas here the region of greatest local evaporative flux shows the slowest receding phase. However, the previous measurements which gave $\dot{R}$ as proportional to K were for droplets with fixed droplet radius. While this droplet does have this same fixed radius, the two contact angles are given by droplets of different radii of curvature as shown by the red dotted lines in Fig.6.30. The different radii of curvature could help to explain the disparity between the receding speeds, however this behaviour requires further exploration and comparison with receding speeds as a function of droplet radius. Furthermore, this "anti-drip paint" phenomenon appears to only occur in droplets with initial concentrations above 5% and below 10%, which thus far cannot be explained.

6.3.4   Low Pressure and High Humidity

Fig.6.31 is a time-lapse sequence of images during the vertical growth stage of a PEO droplet with $c_0 = 5\%$ at a reduced pressure $P = 100$ mbar. During this stage, as is often the case at low pressures, the growth structure is sufficiently large compared with the supporting solid region that it topples over and shifts from growing vertically to growing in the toppled direction. An important observation from these images not stated already is that between images 4 and 5 the raised liquid comes back into contact with the thin layer of solid PEO deposited. If autophobism plays a large role, the liquid would be expected to simply roll off the solid layer. However, it is clear this is not the case, the liquid layer in fact wets the solid substrate, which then offers a new base line for PEO precipitation. This happens once more between images 6 and 7, and the liquid once again clearly wets the substrate. This is the first firm evidence that the liquid is not receding due to repulsion forces from the PEO spherulites.
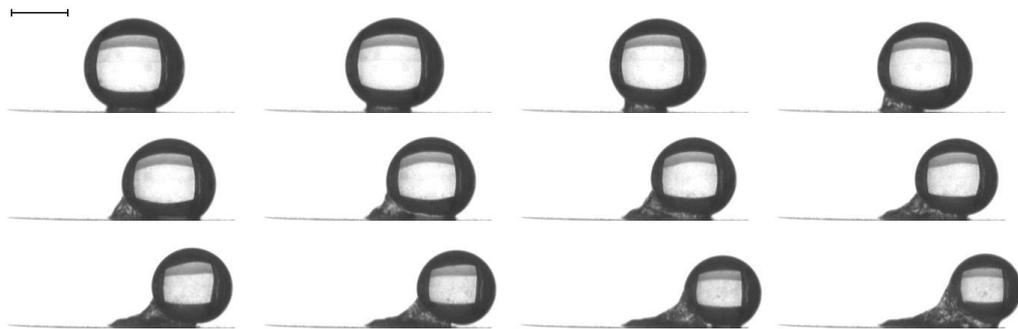
Figure 6.31: Time lapse image sequence of an elevated liquid droplet as it topples over due to structural instability, and wets the solid PEO layer. Total duration 3 minutes 40 seconds. Scale bar represents 1 mm.

Due to the small length scale over which the spherulite collar forms it is difficult to directly observe lateral contraction around the liquid perimeter, particularly in the early stages of precipitation. However, at low pressures, the very early precipitation and tall structures that form as a result give an opportunity to observe this contraction in action. Fig.6.32 is a time-lapse sequence of images of a droplet with initial concentration $c_0 = 5\%$ at reduced pressure $P = 100$ mbar. Similar experiments at ambient conditions show a narrowing of the liquid-solid contact line with time, but thus far it has been difficult to show that the solid structure continues to shrink as the liquid is raised. In Fig.6.32 this shrinking

solid process is obvious. Between images 7 and 12 the structure that supports the remaining liquid clearly reduces in diameter by a factor of around 2, which is in favour of the contracting solid collar hypothesis. It should be noted however
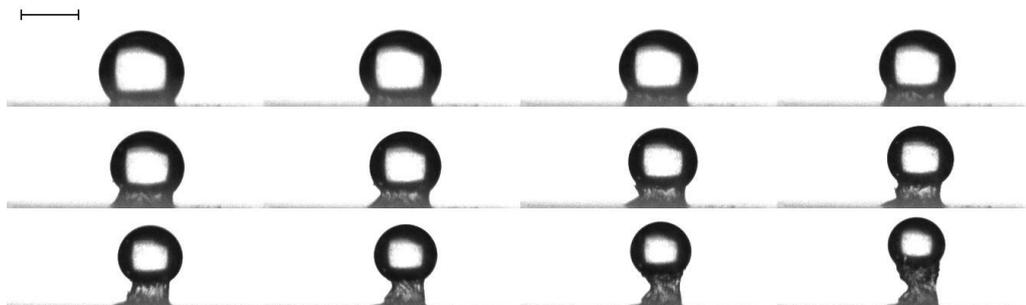
Figure 6.32: Time-lapse sequence of images illustrating the contraction of the thin supporting solid structure leading to height increase of the liquid phase. Total duration 3 minutes 51 seconds. Scale bar represents 1 mm.

that it is possible that because evaporation is now predominantly occurring at the peak of the tall structure that this could induce upward vertical flow, which in turn could induce contraction of the solid polymer skin. This is certainly possible, however it seems unlikely as directional flows of this type are usually only induced by evaporation when a liquid-air interface must be replenished, such as with the coffee-ring effect advective flow induced by the pinned contact line. In the case of the tall PEO structure there is no obvious reason why the liquid-air interface must be replenished, therefore we would not expect liquid to flow vertically out of the solid supporting structure.

Finally, the last piece of evidence offered here in favour of the contracting collar hypothesis is Fig.6.32, a time-lapse sequence of images of a $c_0 = 20\%$ droplet drying under slow drying conditions with $RH \approx 81\%$. Under these conditions, precipitation appears to no longer occur preferentially at the contact line, but uniformly over the air-liquid interface, indicative of a less than unity Péclet number. In the first image, the droplet quickly become entirely encased in a solid layer of PEO spherulites. At this point one may expect the droplet to simply reduce in size as observed in the late stages of other PEO droplets. However, because this spherulite layer is newly formed, it contains a large amount of water still. Over the next 52 minutes, small droplets appear to squirt out from the solid spherulite layer which can only be explained through contraction of the solid layer. If the remaining liquid simply evaporated through the solid skin,

Figure 6.33: Late stages in drying of PEO droplet ($c_0 = 20\%$) in high relative humidity ($RH = 81 \pm 2\%$). Solid layer forms uniformly over droplet surface. As this layer contracts it exerts a downward pressure on the remaining liquid, causing the liquid to extrude from the surface in several locations at once. Total duration 52.5 minutes. Scale bar represents 1 mm.

the volume of the flat structure would simply decrease, possibly inducing skin buckling of the spherulite layer as described by Pauchard 3.7.1. However, if the skin itself contracts (and remains pinned to the glass substrate at the perimeter), this would induce a downward pressure on the remaining liquid encased within. Because the liquid cannot accommodate this downward pressure by either losing volume through evaporation or buckling the substrate, the resulting upward pressure exerted from the liquid is sufficient to pierce the contracting skin and leak out. Effectively, the contraction of the spherulites leaves the remaining liquid nowhere to go but to burst through the polymer skin, as seen by multiple eruption points from image 3 onwards. This is very strong evidence in favour of the contracting spherulites being the major contributor to the structural changes a droplet undergoes after precipitation begins.

6.4   PEO-Water-Ethanol Mixtures

Thus far the drying behaviour of PEO droplets has focused entirely on aqueous solutions. This is partly due to the fact that PEO dissolves very easily into water at ambient conditions up to concentrations of 50%, whereas in other solvents (such as ethanol or methanol), the temperature must be raised before the polymer becomes soluble. In order to explore the effects of different solvents without also increasing the temperature, which as we have seen can disrupt the pillaring process entirely, PEO was dissolved into water-ethanol mixtures of various solvent ratios, while keeping the polymer concentration fixed at $c_0 = 10\%$. This sets an upper limit on the ethanol content at 80% as a 1:1 mass ratio between PEO and water is required for all the polymer to stay in solution.

The reader should keep in mind that altering the solvent has potentially the greatest number of side effects on the pillaring process of any modification to the initial conditions studied so far:

- Péclet number. Due to the increased volatility of ethanol compared with water, the initial evaporation rate would increase with increasing ethanol content, and therefore increase the droplet Péclet number. Accurately measuring the evaporation rate against initial ethanol concentration is difficult as the ratio of water to ethanol will shift in favour of water with time. However, to give an rough idea of the increase in evaporation rate ethanol content will have on a droplet, two separate 40ml containers of water and ethanol were left to dry for ≈ 64 hours at $RH = 59 \pm 1$, $T = 22°$C. Measuring the mass of these containers at the start and end of this period gave the evaporation rates of water and ethanol as $\dot{V} = 5.1$ and 167 nl/s respectively, showing an increase in a factor of ~ 30 from water to ethanol.

- Surface tension. Ethanol also has a lower surface tension than water, which means the contact angle will reduce with increasing ethanol content. In these experiments initial volume is kept constant, which as found in the previous chapter leads to a minimum pillaring contact angle due to the geometric constraints of the droplet at $t = t_{\mathrm{p}}$.

- Solubility. In this chapter it has been shown that the fractional precipitation time t_{p}/t_0 is inversely proportional to the Péclet number. However, the solubility of PEO-water-ethanol ternary mixtures was shown in Chapter 2.4.1 Fig.2.26, which suggests that solubility, and therefore saturation concentration, will be highest at intermediate ethanol volume fractions. Assuming then that the solvent ratio remains constant throughout drying, this would lead to a later precipitation time for mixed solvent solutions than in their respective PEO-solvent binary mixtures.

- Solvent ratio evolution. All solvent mixtures examined in this work lie below the water-ethanol azeotropic point. As discussed in section 3.6.1, this means that the solvent ratio will shift in favour of water as time goes on, leading to a varying evaporation rate, surface tension and saturation concentration with time.

- PEO crystallisation. The presence of ethanol could potentially alter the

crystallisation process of PEO. As the current understanding of pillar formation goes, the precipitation of large spherulites, which then continue to lose solvent and contract, is of fundamental importance for the formation of tall central structures. Quite how spherulites will form in the presence of a solvent mixture is unknown.

- Convection. In section 3.5, emphasis was put on the ongoing debate between whether Marangoni or buoyancy driven convection is dominant in water-ethanol droplets. Convection currents in drying PEO droplets will be studied in depth in the next chapter, but for now we should note that their effects on the pillaring process are unknown.

Fig.6.34 shows the fully dried structures that formed at the differing ethanol concentrations. At low initial ethanol concentrations ($c_e < 50\%$), fully dried structures remain very similar to those from pure water. However at a certain
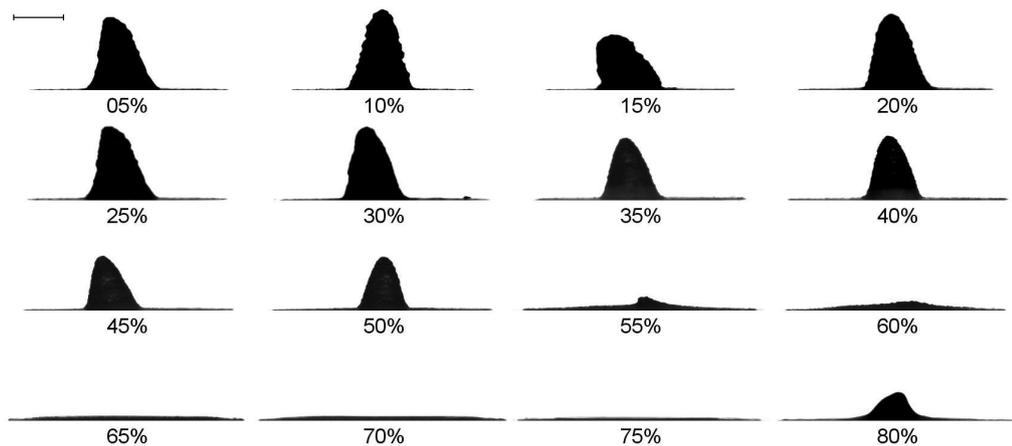
Figure 6.34: Structures formed at $t = t_f$ from droplets of PEO-water-ethanol mixtures at ambient conditions on glass coverslips. Labels indicate initial ethanol concentration by mass. Scale bar represents 1 mm.

initial ethanol concentration between $c_e = 55$ and 60%, pillar formation stops. This can be explained as simply a product of the reduction of initial contact angle of the droplets. Indeed Fig.6.35 is a series of fully dried droplets over the same range of initial ethanol concentration, but deposited on a hydrophobic surface, which shows that the range of c_e in which the ethanol content led to the formation of flat uniform disks now forms pillars. Fig.6.36 is a plot of the initial contact angles of the PEO-water-ethanol droplets as a function of ethanol concentration
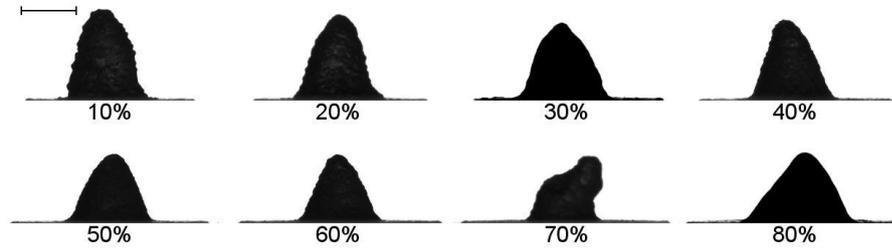
Figure 6.35: Structures formed at $t = t_{\mathrm{f}}$ from droplets of PEO-water-ethanol mixtures at ambient conditions on Granger's solution coated glass coverslips. Labels indicate initial ethanol concentration by mass. Scale bar represents 1 mm.
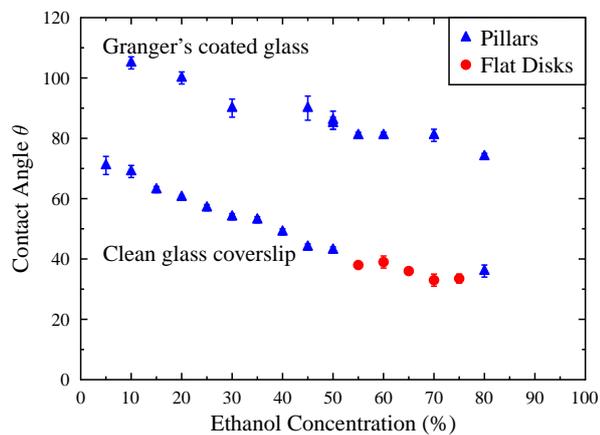
Figure 6.36: Plots of initial contact angle against ethanol concentration on both clean and Granger's solution coated glass coverslips.

on both glass and Granger's coated glass substrates. This is fairly strong evidence that the geometric constraints at $t = t_\mathrm{p}$ are the main limiting factor for pillar formation in PEO-water-ethanol ternary mixtures.

However, one may notice the unexpected pillar in both the bottom right image in Fig.6.34, and the lower right triangle in Fig.6.36, indicative of an initial ethanol concentration of 80%. This finding seems to singlehandedly discount the contact angle argument entirely. To explain this surprising result we must first examine the dependency of evaporation rate over the range of ethanol concentration, and the effect this has on fractional precipitation time t_p/t_0.

Fig.6.37 is a plot of normalised volume versus time for a select few initial ethanol concentrations. Dashed lines show the fractional volume at $t = t_p$. From this it is
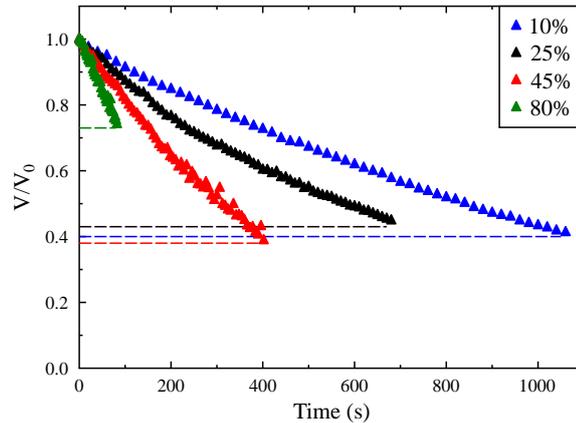
Figure 6.37: Plots of V/V_0 against time for various initial ethanol concentrations on clean glass substrates. Dashed lines mark the fractional volume when precipitation begins and remains fairly constant for $c_\mathrm{e} = 10$, 25 and 45%, but is significantly higher at $c_\mathrm{e} = 80\%$.

clear that as ethanol content is increased from 10 to 45%, while evaporation rate increases, the fractional volume at which precipitation begins is fairly constant. This is interesting as previously we had seen that increasing evaporation rate reduces the fractional precipitation time by increasing the Péclet number. Here however this does not seem to be the case. Initially it was considered that at concentrations less than $\sim 45\%$, all the ethanol has has evaporated away from the droplet well before precipitation begins, meaning that the droplets revert back to behaving as droplets with PEO dissolved in a purely water solvent. To help clarify this, the evaporation rate immediately prior to precipitation was extracted from

the profile images of the droplets and divided by droplet radius for calculations of K, which should then give an indication of the ethanol content. Fig.6.38 is a plot
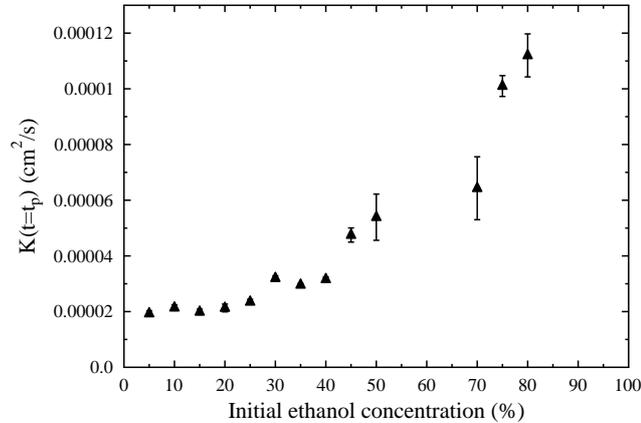
Figure 6.38: Plot of K (the proportionality between evaporation rate $\dot{V}$ and droplet radius R) immediately prior to PEO precipitation against initial droplet ethanol concentration.

of K versus initial ethanol content. The initial flat region ($c_e < 25\%$) suggests that at low initial ethanol concentrations the droplet is most likely a purely PEO-water droplet at $t = t_p$, and therefore we would expect pillar formation to follow the behaviour discussed in this and the previous chapter. However, above this region K increases significantly, which strongly suggests that a high quantity of ethanol is still present as precipitation begins at $t = t_p$. Again,. the increasing quantity of ethanol at $t = t_p$ could go some way to explaining the pillar formation cut-off above $c_e = 55\%$, but can not explain the reemergence of pillars at $c_e = 80\%$.

A large range in c_e between 50 and 70% is missing from this plot due to the difficulty in measuring the droplet volume from the profile images of the droplets at $t = t_p$. This is because late in the first stage of drying, the centre of the droplet dips down to a lower height than that of the liquid perimeter of the droplet, as shown in Fig.6.39. This dipping prior to precipitation is highly unusual, and as yet has not been observed under any conditions in purely PEO-water droplets. The fact that the apex of the droplet can dip in this manner suggests that the perimeter of the droplet is of a much higher viscosity than the center, which can only be explained as due to a large quantity of polymer here. Despite this, precipitation does not occur until $t \approx 400$ s, some 100 seconds before the initial appearance of the central dip. This suggests that the Péclet number was sufficient
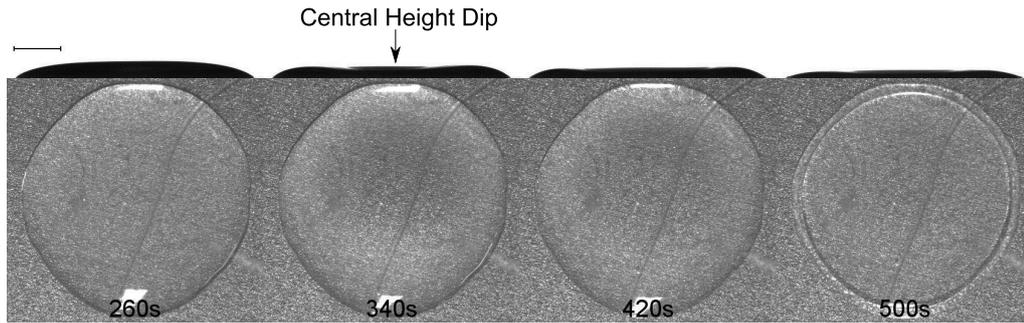
Figure 6.39: Images of a droplet with initial ethanol concentration $c_e = 55\%$ captured from the side and above during an unusual stage in the droplet drying process in which the centre of the droplet dips to a lower height than the perimeter before precipitation begins. Scale bar represents 1 mm.

to sweep the polymer to the droplet perimeter, but for some reason, most likely due to the alteration in the solubility of the polymer, the PEO can not form spherulites until further ethanol is removed.

Fig.6.40 is a plot of the data published by Hammouda [40] (which was already plotted in Fig.2.26), but rescaled for mass fractions, with initial PEO concentration $c_0 = 10\%$. This plot assumes that the solubility is unchanged by increasing
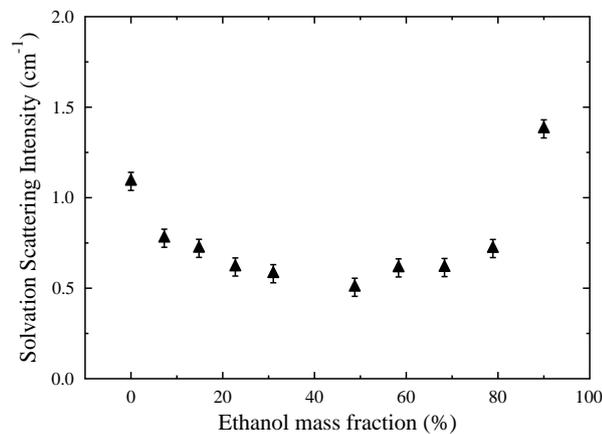
Figure 6.40: Scattering intensity versus ethanol mass fraction with PEO concentration $c_0 = 10\%$. This data was originally published by Hammouda [40] for ethanol-water mixtures at $T = 50°C$ and PEO volume fraction $\phi = 4\%$, which has been rescaled for total ethanol mass fractions of water-ethanol-PEO solutions to match the data in this work.

PEO content from $\phi = 4\%$ to $c_e = 10\%$ and reducing temperature from 50°C to

22°C.

With all these measurements in mind, we can begin to explain the effect initial ethanol content has on the pillaring process:

- $c_e < 30\%$. In this range, the evaporation rate scaled by the initial radius at $t = t_p$ shows that all ethanol has been removed from the droplet prior to precipitation. Initial contact angle is also decreasing, but has not yet reached a significantly low enough value (which was found to be around $\theta_0 \sim 40°$ in the first chapter). Therefore the concentration gradient that develops immediately prior to the precipitation, which is governed by the Péclet number is unaffected, and the geometric constraints are not altered enough to stop pillar formation.

- $30 < c_e < 55\%$. From Fig.6.38 we can see that in this range ethanol content at $t = t_p$ steadily increases. Therefore the solubility, and thus the precipitation time, should also be increasing, which as we have shown in Chapter 5 would lead to a reduced value of V_p, with flat dried deposits as the result. Furthermore contact angle steadily decreases in this range, and at around $c_e = 55\%$ (the apparent transition concentration between pillars and flat disks), the initial contact angle has reduced below $40°$, which from the first chapter appeared to be the minimum pillaring droplet contact angle.

- $55 < c_e < 75\%$. In this ethanol concentration range the contact angle does not vary significantly. Fig.6.39 showed that while polymer had built up at the perimeter to a sufficient amount that a highly viscous ring formed, precipitation did not occur until some time later, suggesting that precipitation is being inhibited by the ethanol content. Predicting the precipitation time in this range is complex as not only does the PEO conentration increase as time goes on, but also the ethanol-water ratio gradually shifts in favour of water with time. Because contact angle is no longer changing in this range, the dominant factors must be the complex interplay between increasing concentration and time dependent precipitation concentration, and the evaporation rate which decreases as the solvent ratio shifts in favour of water.

- $c_e = 80\%$. This is the final surprising result, and could potentially be explained by the decrease in PEO solubility at the high ethanol quantity end

of Fig.6.40. While at intermediate ethanol fractions solubility is high, at either extreme the solubility is reduced. This high ethanol content reduction in c_{sat}, would then lead to earlier precipitation, and therefore pillars. Alternatively, the behaviour at $c_{\text{e}} = 80\%$ could be due to the fact that initial contact angle is no longer reducing, but the evaporation rate is, leading to an increasing Péclet number, and therefore earlier precipitation.

Admittedly, the understanding of the pillar formation behaviour of PEO-water-ethanol ternary mixtures is far from complete. A more rigorous approach to the dynamic ethanol-water ratio in drying droplets is required for a full understanding of this behaviour. Furthermore, this work has not taken into account potential solvent concentration gradients within the droplet, which as discussed in section 3.6, is still a topic of debate. Nor has this taken into account the viscosity of the solution as a function of ethanol concentration, which is plotted in Fig.6.41. Up
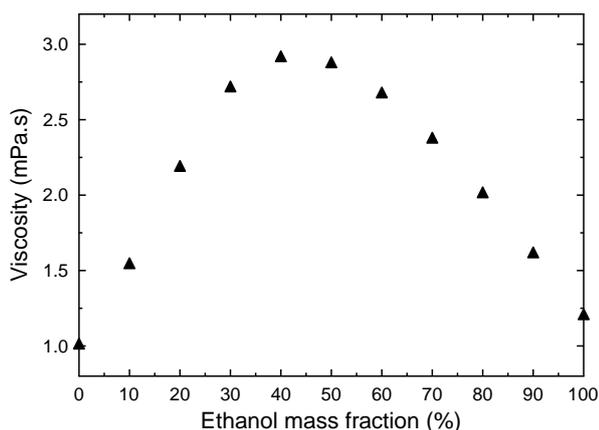
Figure 6.41: Plot of solution viscosity as function of ethanol concentration by mass in water-ethanol binary mixtures. Data taken from book by Charles Simmonds published in 1919 [164].

until now the viscosity has generally been considered to be unimportant to the receding/growth stages, although in the next chapter we will see that this may not be a good assumption to make, particularly when polymer entanglements are taken into account. Despite all this, we have shown that on a hydrophobic surface the PEO forms tall central structures regardless of ethanol content, and the high viscosity region does not tie up in any particular way with the final structures that formed. Therefore, while the understanding of how ethanol content affects the build up of the polymer at the contact line, and the resulting saturation time, is

incomplete, the geometric argument proposed in the previous chapter still holds, and pillar formation is still a result of the droplet having a sufficient volume at $t = t_{\mathrm{p}}$ for the shrinking radius to reach zero before the remaining liquid is lost to evaporation.

While this chapter has developed our understanding of the role of evaporation and diffusion in the pillar forming process of PEO droplets, further work is required to combine the geometric constraints argument and the Péclet model into a unified theory for pillar formation. In the next chapter, we will see that there is a further condition that can play a crucial role in controlling pillar formation in PEO droplets which has not yet been considered - the molecular weight.

Whoever undertakes to set himself up as a judge of Truth and Knowledge is shipwrecked by the laughter of the gods.

ALBERT EINSTEIN

Chapter 7

The Role of Molecular Weight

We have explored the effects of droplet geometry, atmospheric conditions, and to some extent the effect of solvent quality. In this chapter I will present experimental investigations into how pillar formation is affected by polymer molecular weight, or M_W. From the Péclet argument, one would expect high M_W to form pillars preferentially as these longer polymers diffuse more slowly, and Pe varies inversely with Diffusion coefficient. However, the experimental results presented in the following section shows that the Pe argument is not sufficient to explain the behaviour, as there is a limited M_W range over which we observe pillars to form.

By varying concentration and pressure, I fully investigate the range of pillar forming conditions. Then I present three explanations for this behaviour which we developed during the course of the experiments. Even though there are problems with the explanations, there is much to be learned from the dead-ends I explored along the way. Firstly I consider how the viscoelastic properties of the droplet may affect individual polymer motion and build-up at the edge; then I consider the Pe argument in more detail, taking polymer overlap and entanglements into account with regard to single polymer diffusivity; and finally I consider how the viscosity of the liquid may affect the overall motion of the contact line during precipitation.

7.1   Narrow Pillar Region
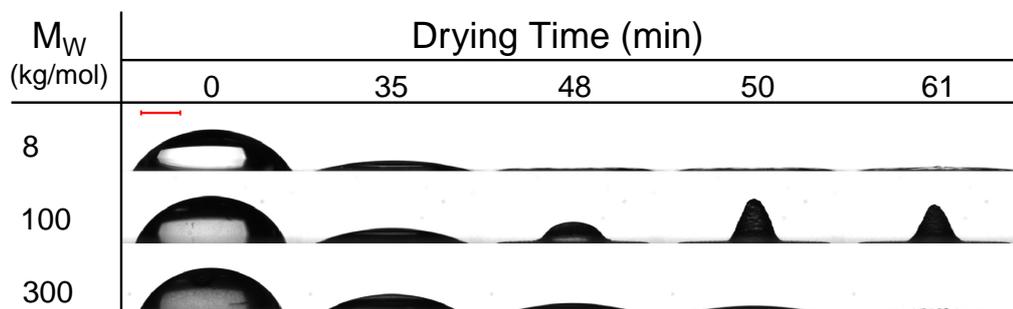
Figure 7.1: Time-lapse profile images of droplets drying at ambient conditions at 0, 35, 48, 50 and 61 minutes. $M_W = 8$, 100 and 300 kg/mol in top middle and bottom rows respectively. Red scale bar represents 1 mm.

Fig.7.1 shows time-lapse images of droplets with initial concentration $c_0 = 10\%$ during drying at ambient conditions ($T = 22 \pm 1°C$, $RH = 50 \pm 5\%$) and PEO molecular weight $M_W = 8$, 100 and 300 kg/mol. The 4 stages of drying (pinned drying, pseudo-dewetting, boot-strap building and late stage contraction) can only be seen with $M_W = 100$ kg/mol, suggesting that at ambient conditions for $c_0 = 10\%$ an intermediate range in chain length is required for pillar formation. Also worth noting is that the initial contact angle θ_0 appears to increase with M_W. While the contact angle at the times at which these images were taken (roughly10 seconds after deposition) decreases with molecular weight, spreading stopped in all droplets at approximately the same equilibrium contact angle of around 70°. The appearance of a molecular weight dependency on contact angle is due to increasing spreading time with molecular weight as droplet viscosity increases. However the reader should note that as discussed in Chapter 3, the surface tension of PEO solutions decreases with concentration, and the concentration dependency varies with M_W (the greatest reduction in γ_L found at $M_W = 80$ kg/mol [83]), so defining the point at which a highly viscous, evaporating (and therefore increasing concentration) droplet reaches an equilibrium contact angle from profile imaging is difficult. Furthermore, attempts to measure the advancing and receding contact angles with respect to M_W has proven difficult at high molecular weights due to the difficulty in pipetting the highly viscous liquids without introducing unwanted cavitation effects. The cloudiness of higher M_W solutions is due to the presence of previously discussed non-dissolving micron sized PEO clusters.

Fig.7.2 is a series of fully dried droplets, initial concentration $c_0 = 10\%$, over the molecular weight range $3.35 \leq M_W \leq 600$ kg/mol as viewed from the side and above. From the profile images it is clear that there is a narrow region in
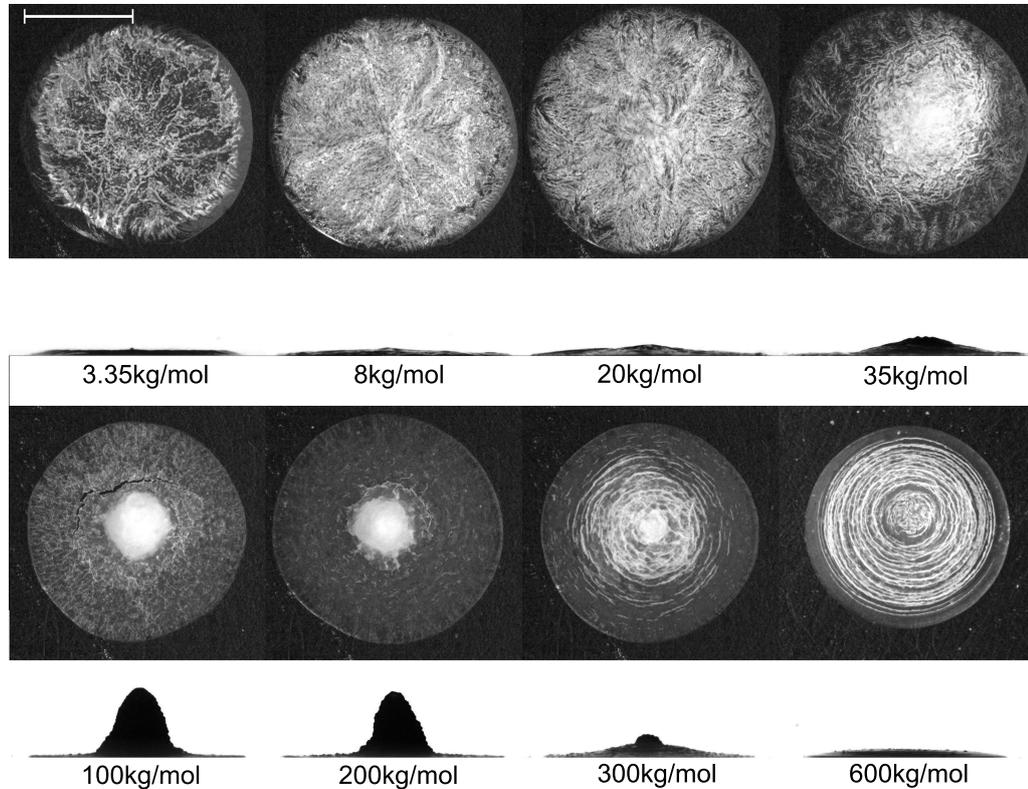
Figure 7.2: Fully dried deposits as viewed from the side and above with varying PEO molecular weight. Concentration fixed at $c_0 = 10\%$. Scale bar represents 1 mm.

molecular weight $(35 \lesssim M_W \lesssim 300$ kg/mol) in which pillars form. Images from above show entirely different structures at either M_W extreme, with a highly crystalline appearance at low M_W, and large concentric rings at high M_W. While 3.35 and 600 kg/mol droplets appear to follow similar behaviour from the profile images, specifically in the formation of uniform flat disks, images from above suggest entirely different drying processes. Initially it was believed that these concentric rings may indicate some form of stick-slip behaviour in which the liquid recedes in distinct phases. However, more careful analysis showed that these rings actually appear much later in the drying process, namely after the surface has entirely solidified, suggesting that these appear due to some form of internal stresses in the solid PEO layer. Indeed the formation of these rings can be seen again much later in this chapter in Fig.7.16. These stress lines may even suggest wrinkling in the solid layer, which adds weight to the idea that

the contraction of the solid layer is crucial to the droplet behaviour during the precipitation stage. While interesting, this research has been and will continue to be focused primarily on the conditions which mark the boundary between pillar and flat deposit formation, so observations will be made primarily from profile images during the early stages of drying.

The reader may also notice when comparing Figures 7.1 and 7.2 that the fully dried 300 kg/mol droplet is a flat uniform deposit in the first, but a small central mound in the second. This is likely to be due to differences in ambient atmospheric conditions and shows that 300kg/mol is close to the boundary between pillars and flat deposits. Over the majority of repeats a flat uniform deposit seems to be the more typical fully dried structure for PEO droplets with $M_W = 300$ kg/mol.

Fig.7.3 is a grid of fully dried droplet profile images with varying M_W and c_0. This was repeated over the course of a single week and showed good reproducibility, with only minor variance in the surface structure of these pillars. However, when repeated again several months later, these dried structures were significantly smaller, which we explain as being a result of the increased relative humidity at that time of year ($\approx 60\%$). The large empty region in the lower right section of
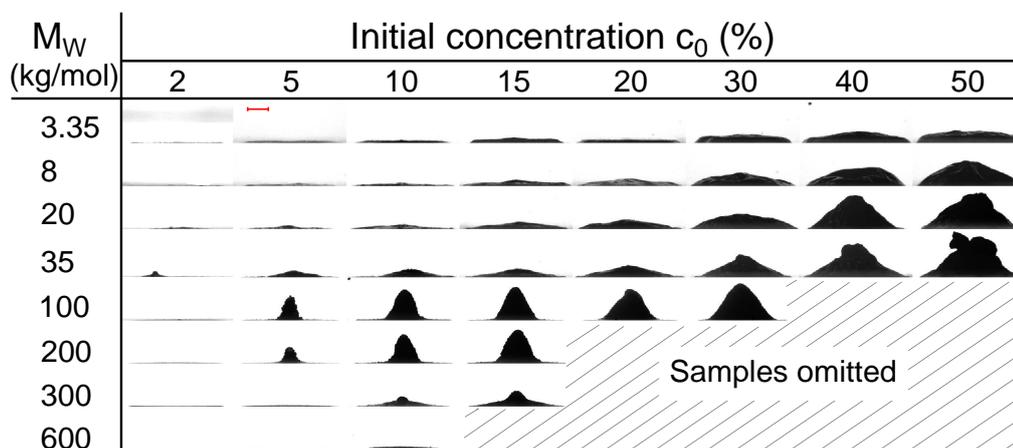
Figure 7.3: Table of fully dried droplet profile images with varying M_W and c_0 in atmospheric conditions $T = 22 \pm 2°C$ and $RH = 35 \pm 5\%$. Samples in the lower right region were omitted due to difficulties of depositing 10 μl droplets of such high viscosity liquids. Red bar represents 1 mm.

the grid represents droplets which were difficult to pipette in small quantities due to their high viscosities, and so were omitted. As discussed in Chapter 4, due to

the difficulty in removing large undissolved clusters from droplets with high M_W, this plot shows droplets in which no post-mixing filtration has taken place. The difference this makes in drying behaviour at 100 kg/mol is only obvious at high concentrations. At $c_0 = 30\%$, previously it had been shown that droplets form highly irregular, structurally unstable deposits, whereas in this figure the deposit resembles a large central conical structure, much more like those at lower concentrations. Very little difference is observed at $c_0 = 10\%$, which is the standard droplet concentration for the majority of experiments. Therefore it is assumed that these clusters make very little difference to droplet behaviour with regards to the boundary between pillar and flat deposit formation, although the effect of filtering is an interesting and unresolved question.

Fig.7.3 seems to show that increasing concentration simply enlarges the structures that form at all molecular weights, similar to the effects discussed in Chapter 5. 200 kg/mol is very similar to 100 kg/mol despite having a smaller observable concentration range. Interestingly, while at 10% the pillaring region includes 300kg/mol, at 5% it does not. Having a lower concentration pillar cutoff is in line with the geometric constraints argument proposed in Chapter 5, but this is at a higher value of c_0 than previously observed.

7.1.1   Predictions From Previous Models

Let us now consider the predictions made from the previous two chapters and how they tie up with these observations.

In the first chapter I detailed a geometric constraint of the droplet once precitation begins which defines the boundary between droplets which form tall central pillars and those which form the more typical coffee-ring type stains. If the volume is above a certain value (V_p) once the droplet starts porecipitating solid spherulites, the contracting collar will push the liquid phase inwards at a significant enough speed that at the time when this liquid base radius reaches zero there will still be a large volume of liquid remaining, leading to tall central deposits. However, if the volume is below this value, the evaporation rate will be sufficient that the volume will reach zero before the radius, and the pseudo-dewetting phase will be cut short, resulting in a coffee-ring type stain with thickness proportional to the duration of the pseudo-dewetting stage. Assuming no molecular weight

dependency on the saturation concentration, as predicted by the water "dress" model of PEO solvation [40], and no molecular weight dependency on spherulite growth, which is supported by the work of Beech et. al. [57] shown in Fig.2.32, we would therefore expect no effect of M_W on the geometric argument. It should also be noted however that very low molecular weights ($M_W < 1$ kg/mol) are viscous liquids [165] that dissolve in water at any concentration (although above 50% this would then be the majority solvent, and it would be said that it is the the water that is dissolving in the PEO), and so this argument clearly breaks down. Such low molecular weight liquid polymers are not investigated in this work.

The second thing to consider is the Péclet number. In the previous chapter the diffusion coefficient of the polymer was assumed to be constant, with the exception of increasing atmospheric temperature, in which the increasing D was proposed as the cause of diminishing the pillar formation. So how would Pe vary with M_W? Well, much like the effect of concentration, no molecular weight dependency on evaporation rate has been observed. Therefore, if we are to stick with the Péclet model we must consider the effect molecular weight has on the diffusion coefficient. In Chapter 2 the relationship between D and M_W was discussed in depth, and shown to be fairly complex depending on the concentration regime (dilute, semidilute or entangled), and on what type of diffusion coefficient is being considered (self, cooperative or gradient). For now let us simply consider self diffusion in very dilute solutions. The Stokes-Einstein equation gives the diffusion coefficient of a polymer as:

$$D_0 = \frac{k_B T}{6\pi\eta_s R_h} \tag{7.1}$$

Fig.7.4 is a plot of the very low concentration self diffusion coefficient as a function of molecular weight, with values of molecular weight used in these experiments marked on the plot. From this we can immediately see that increasing M_W reduces the diffusion coefficient. We saw from the results of increasing temperature that increasing the diffusion coefficient has the result of enabling the polymers to homogenise within the droplet much more easily, which then leads to a lower Péclet number and flat uniform deposits. From this plot we would therefore expect earlier precipitation time with increasing molecular weight, thus increasing pillar formation. This can therefore explain how pillar formation does not occur at low molecular weights due to the high diffusion coefficient, but can not explain the pillar formation cutoff above ≈ 300 kg/mol.
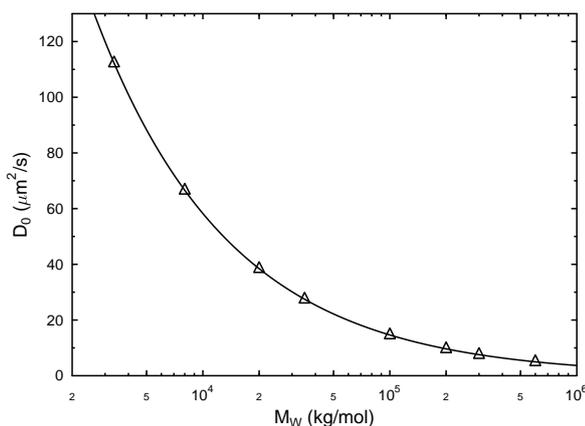
Figure 7.4: Plot of D_0, the self diffusion coefficient at very low concentrations calculated using equation 7.1, against polymer molecular weight. Triangles represent values of M_W used in these experiments.

7.2 Explaining The Narrow Pillaring Region

Through the course of this research I have developed several hypotheses to explain some of this behaviour. Some of which rely heavily on the Péclet argument, some proposing entirely different mechanisms at play. This section will detail the explanations developed chronologically over the course of this research. These will largely consider that the lower molecular weight pillar formation cut-off is due to the reduced Péclet number, and attempt to explain what causes the formation of flat homogeneous disks at high M_W.

7.2.1 The Viscoelasticity Argument

In Chapter 2 it was discussed that one of the main features of polymer solutions which distinguishes them from other liquids are their viscoelastic properties. Not only do polymeric liquids undergo shear thinning, but can display both fluid and solid like properties, with the dominant behaviour being depending on the amplitude and timescale over which shear forces are applied. Indeed, elastic properties are particularly prevalent in highly entangled solutions. It is logical that a highly entangled network will display more spring-like properties than a solution in which the chains are able to move about freely. Furthermore, the Péclet number argument requires purely fluid-like behaviour to lead to polymeric advection

to the droplet perimeter, and does not take into account any resistance to the outward radial flow due to the structural constraints of the polymer network.

With this in mind, it is proposed that the mechanism behind the loss of pillar formation in high molecular weight droplets is the emergence of highly elastic properties. Evaporation is typically considered a process which does not deform a droplet. However, it is also known that the enhanced evaporation at the contact line induces radial outward flow, which could in turn induce shear forces within the droplet, with a timescale associated with the evaporation rate of the droplet. The question is, can the evaporation induce a shear force great enough to cause an elastic response from the entangled polymer network, which would in turn resist the outward radial flow and remain fixed in position?

7.2.2 Convection Currents

During the course of this research in close collaboration with Dr. Haida Liang and Dr. David Fairhurst, I helped develop a technique for tracking fluid flows in a drying droplet using OCT (a light scattering imaging technique discussed in Chapter 4). This technique led to further collaboration with The Technische Universt at Darmstadt , and the coauthoring of a methods paper [166]. With this in mind, let us consider the predictions the viscoelasticity hypothesis would have on the internal fluid flows in the drying PEO droplets. If the introduction of high elasticity is to blame for the high M_W pillar cutoff, then we would expect to see no internal flows in droplets above ≈ 200 kg/mol.

Fig.7.5 is set of OCT images of 5μl PEO droplets ($c_0 = 5\%$) over the molecular weight range 20 to 300 kg/mol at time $t = 0$. The coloured lines represent the paths of the suspended particles over the first 5 minutes of drying, tracked using the ImageJ particle tracker plugin [139] as described in section 4.3.2. Interestingly, particle motion does not appear to be dominated by the outward radial flows as with the coffee-ring effect, but instead we observe two large internal convection currents, which are repeatably upwards in the centre of the droplet and downwards along the surface of the droplet. The observation of convection currents led to the question: are these flows dominated by buoyancy effects or surface tension gradients? A simple test would be to invert the droplet, thus reversing the direction of gravity with respect to the substrate-droplet system.
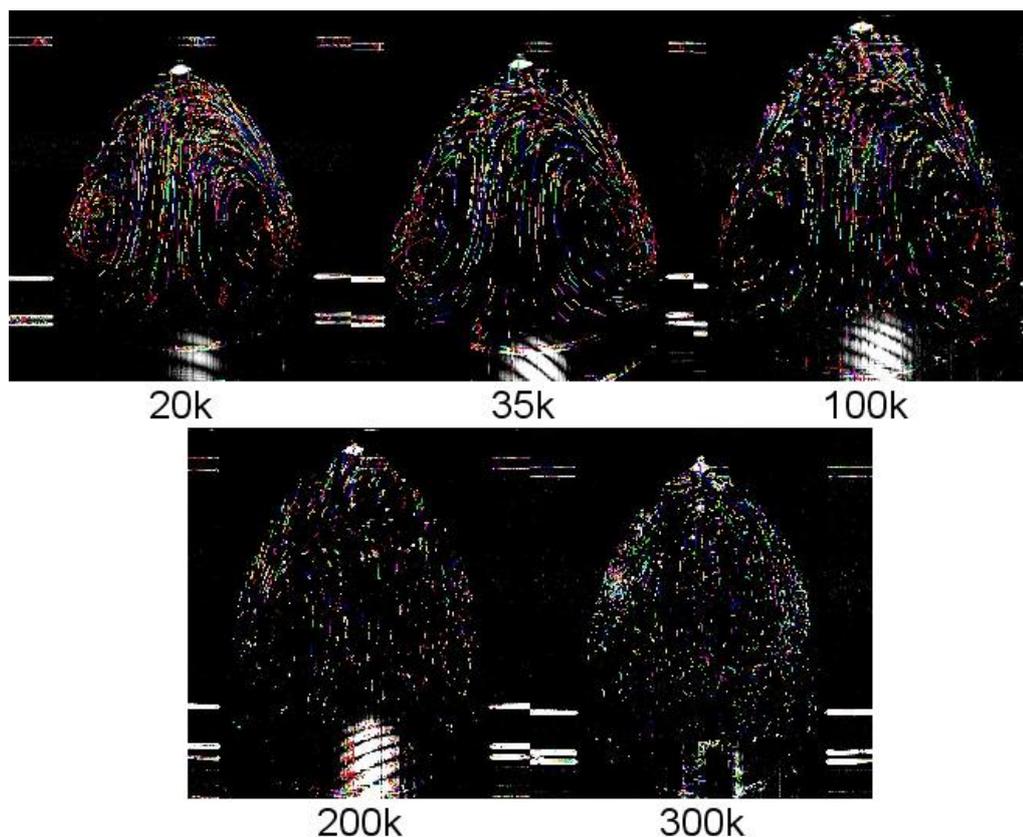
Figure 7.5: OCT Images of a single x-z plane in PEO droplets over the molecular weight range 20 to 300 kg/mol ($V_0 \approx 5$ μl, $c_0 = 5\%$). Coloured lines represent the paths of tracked microspheres over the first 100s of drying. At low molecular weights clear convection currents can be seen, with upward and downward motion in the centre and along the droplet surface respectively. Convection currents slow as molecular weight is increased and seemingly stop entirely at $M_W \approx 300$ kg/mol.

From previous experiments it became clear that inverting the substrate post droplet deposition had absolutely no effect on the fully dried structure as shown by Fig.7.6 Therefore we suspected that OCT imaging would show that the convection currents would flow in the direction given as if someone had simply taken a mirror image of the upright droplet, as shown in the diagram Fig.7.7. If this was observed one would infer that surface tension gradient (Marangoni) effects must be the dominant cause of convection as gravity is not playing a significant role. In fact, in the literature buoyancy effects are often assumed to be of no consequence when the size of the droplet is below the capillary length, which these PEO droplets are (droplet height $\approx 0.94 \pm 0.1$ mm, capillary length of water $\lambda_c \approx 2$ mm). This common assumption is one I have found to be highly ill considered. The capillary length is the length scale at which gravitation effects are significant enough to

Figure 7.6: Time-lapse sequence of images of a 10 μl PEO droplet, $c_0 = 10\%$, $M_W = 100$ kg/mol, suspended upside down. Images show that inverting the droplet has no effect on the pillar formation process. Scale bar represents 1 mm.
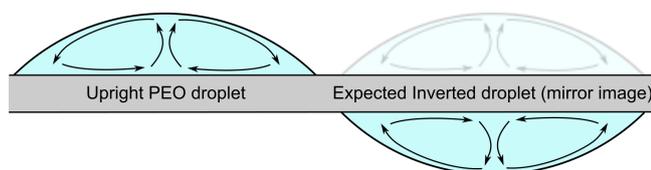
Figure 7.7: Diagram of the expected effect of inverting the droplet on the direction of convection currents.

deform the liquid-air interface. However, for convection to be driven by buoyancy, gravity must be significant enough to overcome viscosity effects, not the surface tension. It seems to me that a different length scale is required for setting the lower limit on buoyancy driven flows in droplets which takes into account the viscosity of the liquid. Indeed, our observations show that when the droplet is inverted, gravity works to reverse the direction of the flow with respect to the droplet-substrate interface, as shown in Fig.7.8. Therefore it is concluded that buoyancy is the dominant factor in driving convection currents in drying PEO droplets.

Interestingly however, inverting the droplet, and thus reversing the direction of the large convection currents has no effect on the fully dried structures. Indeed, the reader may remember that in Chapter 5 it was observed that the spherulites forming over the droplet surface appear to move down toward the substrate during the boot-strap building phase. Three potential explanations for this motion were discussed: gravity; surface flows; and contraction. The first two suggestions can now be dismissed as inverting the droplet both switches the direction of gravity, and redirects flow away from the substrate, but does not stop the motion of spherulites towards the substrate, adding weight to the argument that this motion is not the motion of individual spherulites but the collective motion of a spherulite collar that is undergoing evaporation driven contraction.

While novel, these buoyancy driven convection currents are considered to be unimportant in the pillar forming process, and so the outward radial flow of the
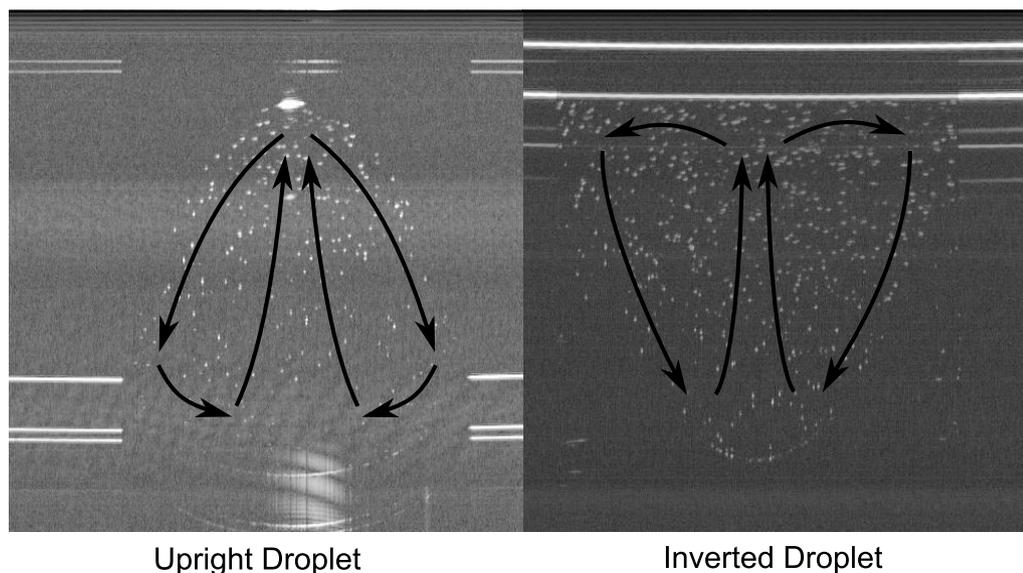
Figure 7.8: Comparison of direction of convection currents observed via OCT in an upright and inverted PEO droplet ($c_0 = 5\%$, $M_W = 20$ kg/mol). Findings show that when the droplet is inverted, the direction of flow remains downward at the droplet-air interface and upward in the centre, suggesting density changes at the surface (or buoyancy) is the driving force behind convection.

dissolved polymers (which *must* occur for the concentration to build up here and for precipitation to begin at the contact line) is expected to occur over a very small scale close to the droplet perimeter well below the sensitivity of OCT imaging. Perhaps more important than the observation of convection currents (for this section at least) is the observation that internal fluid flows appear to stop (or at least slow down to such an extent that convective motion is lower than the sensitivities of OCT within the lifetime of the droplet) at $M_W = 300$ kg/mol, in agreement with the predictions of the viscoelasticity argument.

7.2.3 Rheology

As shown in section 2.4.4 Ebagnini et. al. [56] measured the storage and loss moduli of PEO solutions with M_W and c_0, but found no cross-over between viscous and elastic behaviour in the frequency range 0.01 to 1 Hz at molecular weights below 1000kg/mol. In this work oscillation experiments were first performed on $M_W = 300$ kg/mol as this is the molecular weight at which pillar formation stops at $c_0 = 5\%$. Oscillation experiments were performed over the concentration

range 5% to 20% and then compared with similar experiments at $M_W = 100$ and 200 kg/mol, in which as we have seen pillar formation occurs. If the droplets are responding elastically to evaporation rather than via internal flow then there must be an obvious G'' to G' dominance crossover at 300 kg/mol, which is not present at molecular weights below 300 kg/mol.

Figures 7.9 and 7.10 show that at $M_W = 100$ and 200 kg/mol no such crossover was observed in the frequency and concentration range available[*], whereas Fig.7.11 shows that at $M_W = 300$ kg/mol there is a clear frequency region in which the elastic response is dominant, with a decreasing crossover frequency with increasing concentration, supporting the frequency dependent viscoelastic relaxation hypothesis. These results appear to be in stark contrast with the results of
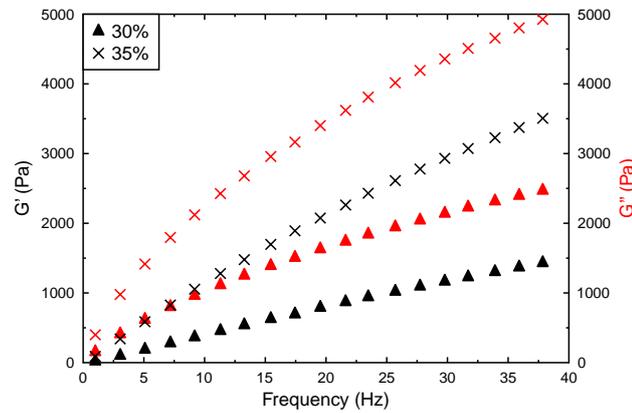
Figure 7.9: Elastic and response moduli (G' and G'' respectively) plotted against frequency for PEO solutions of $c_0 = 30$ and 35%, $M_W = 100$ kg/mol. Results show that the viscous response is dominant in the concentration and frequency range observed.

Ebagninin in which below $M_{\leq}400$ kg/mol the viscous properties remain dominant [56]. However their frequency range was limited to below 1Hz. Indeed at $M_W = 400$ kg/mol, $c_0 = 10\%$ their findings suggested that 1 Hz is approaching the cross-over frequency between viscous and elastic behaviour, and with increasing molecular weight the crossover frequency reduces. Our results show that at $c_0 = 10\%$ and $M_W = 300$ kg/mol, the crossover frequency is found between 11

---

[*]The solutions tested are at the maximum concentrations available. Concentrations far below these values are not measured as elastic response are considered more important in more highly entangled solutions. Put simply, if there is not an elastic response at $x\%$ concentration, it is highly unlikely for there to be an elastic response at concentrations less than $x\%$.
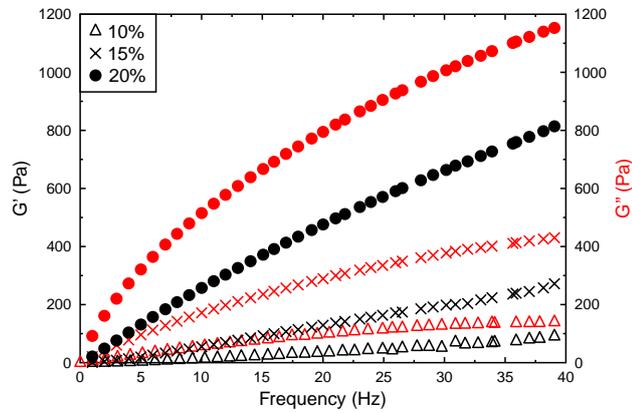
Figure 7.10: Elastic and response moduli (G' and G'' respectively) plotted against frequency for PEO solutions of $c_0 = 10$, 15 and 20%, $M_W = 200$ kg/mol. The viscous response is dominant in the concentration and frequency range observed.
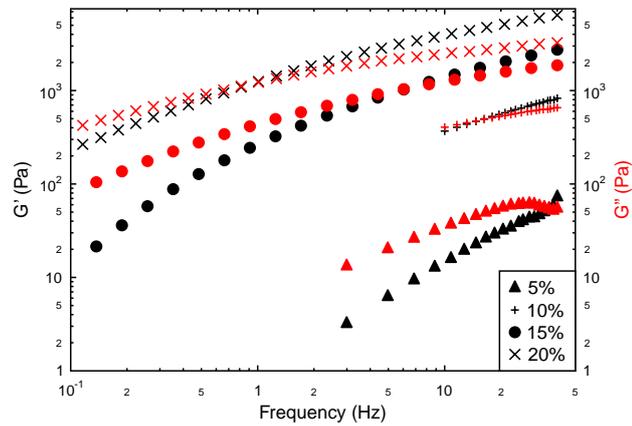

Figure 7.11: Elastic and response moduli (G' and G'' respectively) plotted against frequency for PEO solutions of $c_0 = 5$, 10, 15% and 20%, $M_W = 300$ kg/mol. Results show a crossover between viscous and elastic response at a frequency which decreases with increasing concentration.

and 12 Hz, which is somewhat in agreement with the results we would expect
if we extrapolated from the findings of Ebagninin. However, Ebagninin et. al.
performed these measurements at ambient temperatures $(20.0 \pm 0.1°\text{C})$ whereas
in our measurements temperature was kept constant at $T = 10°\text{C}$ in order to
reduce evaporation (and therefore concentration changes) during measurements.
A better method of reducing evaporation effects without altering the viscosity
of the solution by reducing the temperature would be to surround the cone and
plate geometry with a solvent trap. However, these measurements were taken
from purely preliminary experiments to test the plausibility of the viscoelasticity
hypothesis, and so more careful means of controlling of temperature was not yet
introduced. While these results do support the viscoelasticity argument as there
is an obvious crossover to elastic behaviour at 300 kg/mol solutions, the next
section details results which effectively dismisses this argument entirely, and it is
because of these findings that the oscillation experiments were not repeated more
carefully with use of a solvent trap at ambient conditions.

7.2.4   Molecular Weight Versus Pressure

Figures 7.12 and 7.13 are grids of profile images of fully dried droplets at 5% and
10% respectively, wth varying molecular weight and pressure. The emergence
of elasticity as the reason behind the loss of pillar formation at high M_W would
predict that increasing evaporation rate effectively reduces the timescale of the
applied shear or increases the frequency. The graphs in the previous section
show elastic behaviour at higher frequencies so faster evaporation should lead to
an increased elastic response. At 5% it seems that reducing pressure increases
pillar size between 8 and 200 kg/mol, whereas at 300 and 600 kg/mol pillaring
does not occur at any pressure. This fits with both the Péclet argument for
the low range of M_W and supports the viscoelasticity argument for $M_\text{W} > 300$
kg/mol. At the lowest pressures observed, we can calculate a simple estimate of
the maximum possible extensional force this could induce on a single polymer
coil. Let us assume that a single polymer can be described as two solid balls
connected together by a spring. The ball closest to the droplet centre, ball A,
feels no drag from the solvent, but is fixed in place. Ball B however is closer to
the contact line, and feels a drag force from the outward radial flow of the solvent
directed towards the contact line. The drag force on this end of the polymer

M_W (kg/mol)	Pressure (mbar)					
	20	50	100	200	500	1000
3.35						
8						
20						
35						
100						
200						
300						
600						
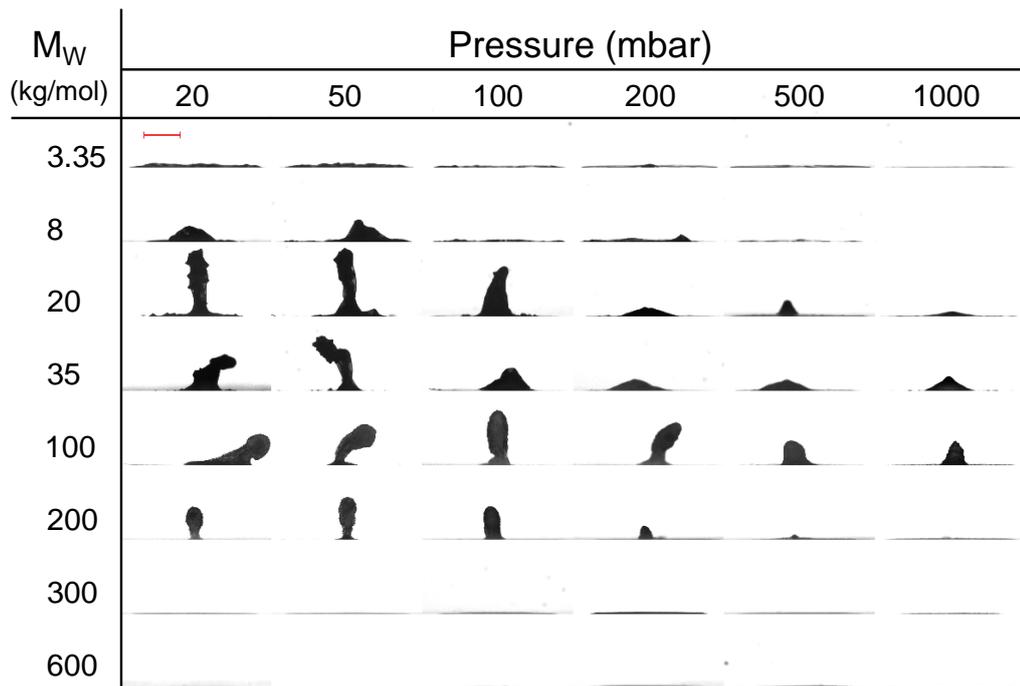
Figure 7.12: Table of fully dried droplet profile images with varying molecular weight and pressure at fixed initial concentration $c_0 = 5\%$. Red bar represents 1 mm.

chain is given by Stoke's law:

$$F = 6\pi\eta_s R_h v_s \qquad (7.2)$$

where v_s is the velocity of the solvent. Let us assume that this velocity is equal to our estimate of the local evaporative flux j, which at 20 mbar is around 20×10^{-7} m/s. Therefore, for a polymer of molecular weight $M_W = 100$ kg/mol (where $R_h \approx 14$ nm), the drag force (which is equal to the extensional force under the present assumption that we are in the extreme case in which one end of the polymer is fixed in place, while the other is being dragged to the contact line) can be estimated to be of the order 10^{-15} N. From the arguments of Dittmore et. al. [30] in which they measured single PEO molecule elasticity under extensional forces, this evaporative induced stretching force would around 3 orders of magnitude lower than that required to stretch the polymer out of the swollen coil configuration. However, it may yet be sufficient to induce an elastic response from a more concentrated polymer solution.

In fact, we only need to repeat the experiments that led to Fig.7.12 but at a higher droplet concentration to disregard this possibility. Fig.7.13 shows that at $c_0 = 10\%$ all molecular weights observed form pillars given a low enough

pressure. This does not tie in with the viscoelasticity explanation as by increasing
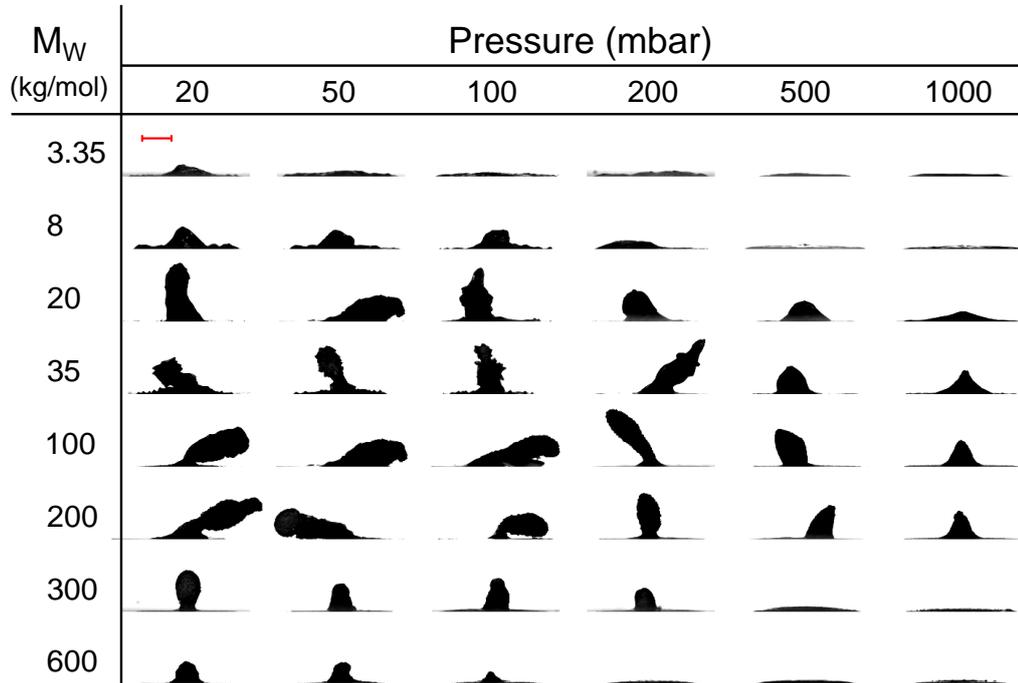
Figure 7.13: Table of fully dried droplet profile images with varying molecular weight and pressure at fixed initial concentration $c_0 = 10\%$. Red bar represents 1 mm.

evaporation rate we would expect to induce a greater shear rate and therefore a more elastic response from the solution, which from our argument would then prevent outward radial flow in the droplet and result in a uniform flat fully dried deposit. This is not what was found, but rather it would seem that all molecular weights will form pillars given the right concentration and atmospheric conditions.

Despite this, perhaps the largest problem with the viscoelastic argument is that it presupposes shear is induced within the droplet due to evaporation. Firstly, we can not measure these potential shear rates as we have no idea of the flow fields experienced across a single polymer. All we can estimate is the local evaporative flux close to the contact line, but this does not necessarily indicate the solvent flow gradient experienced across a single (or network) of polymers. Furthermore, it may be extensional flow rather than shear flow that these polymers experience, which would induce an altogether different type of response. The comparison would be like comparing stretching an elastic band (extensional) with placing an elastic band on a flat plane and rubbing your hand down the length of it (shear). Therefore the assumption of shear forces induced in a drying droplet is flawed.

It is clear that when we consider the experimental evidence and the lack of a sound argument, an alternative hypothesis is now required to explain the narrow region in M_{W} in which tall central pillars form. For this next argument we go back to the Péclet number, but now introduce a more complex molecular weight and concentration dependent definition of the polymer diffusivity.

7.2.5 The Diffusivity Regimes Argument

This argument is centred around the idea that two different methods of diffusivity could be relevant to the D term in the Péclet number. At low molecular weights the polymers are small enough to behave as non-interacting objects that display solo motional behaviour only. As molecular weight is increased, this self diffusion term decreases and the ability for the droplet evaporation rate to drag the polymers to the contact line is increased, resulting in early precipitation and tall central pillars. At some point however, solo diffusive behaviour may not be the important factor. Instead, what we could have is large networks of polymers which display cooperative diffusive effects, which as discussed in the Polymers chapter, are always higher than the self diffusive behaviour. This transition from fast self diffusion at low M_{W}, to slow self diffusion at a higher M_{W}, to fast cooperative diffusion at even higher M_{W}, could result in a narrow molecular weight range in which droplets have a high Péclet number and thus dry to tall central pillars.

Now let us go through this idea in more detail. In a dilute solution, the interchain distance is sufficiently large that the polymers can be assumed to be non-interacting, and so polymer migration follows the Stokes-Einstein equation for self diffusion:

$$D_0 = \frac{k_B T}{6\pi \eta_{\mathrm{s}} R_{\mathrm{h}}} \tag{7.3}$$

However, as the concentration approaches the overlap concentration c^*, polymer interaction becomes common, and the self diffusion coefficient of polymer chains reduces with concentration:

$$D_{\mathrm{s}} = D_0 \left(\frac{c}{c^*}\right)^{-\frac{1}{2}} \tag{7.4}$$

The overlap concentration c^* is calculated from:

$$c^* = \frac{Nb^3}{\frac{4}{3}\rho \pi R_{\mathrm{G}}^3} \tag{7.5}$$

where $\rho = 1.064$ g/cm^3, $b = 1.1$ nm and R_{G} is given by:

$$R_{\mathrm{G}} = bN^{\nu} \tag{7.6}$$

and ν is the Flory exponent (for PEO in water $\nu = 3/5$).

A key point to note here is that in a semi-dilute unentangled solution we are assuming that polymers still predominantly diffuse as solo entities, and therefore the diffusive back-flow down the concentration gradient that builds up at the droplet perimeter is given by the concentration modified self diffusion coefficient only.

When the concentration reaches the entanglement concentration c_{e} however, it is possible that the diffusivity regime transitions from being dominated by the motion of single polymer chains (and therefore self diffusion D_{s}), to the motion of entangled networks (and therefore cooperative diffusion D_{c}) where [17]:

$$D_{\mathrm{c}} = \frac{D_0}{1.6}\left(\frac{c}{c^*}\right)^{3/4} \tag{7.7}$$

$$\propto M_{\mathrm{W}}^{-3/5}\left(\frac{c}{M_{\mathrm{W}}^{-4/5}}\right)^{3/4} \tag{7.8}$$

$$\propto c^{3/4} \tag{7.9}$$

The importance of this assumption is that now, although motion of individual chains is still slow, the connected network can collectively react to concentration gradients much more quickly, more like a solid. The idea is that a concentration gradient, such as a region of highly entangled polymers side by side with a region of purely water, will result in the polymer network very quickly expanding or swelling into the region of low concentration. Therefore entanglements effectively increase the gradient diffusion coefficient of the solution, thus reducing the Péclet number.

Following this argument, we would now expect flat uniform deposits to form from droplets with either a very high self diffusion coefficient, or a high cooperative diffusion coefficient, whereas pillars will form in the intermediate region in which polymers have slow diffusion due to neighbouring polymers hindering their motion, but are not so concentrated (or long) that entanglements form. Fig.7.14 shows values of the theoretical gradient diffusion coefficient against concentration and molecular weight. The dip shows slow diffusion hindered by overlap with neighbours but not enhanced by entanglements.
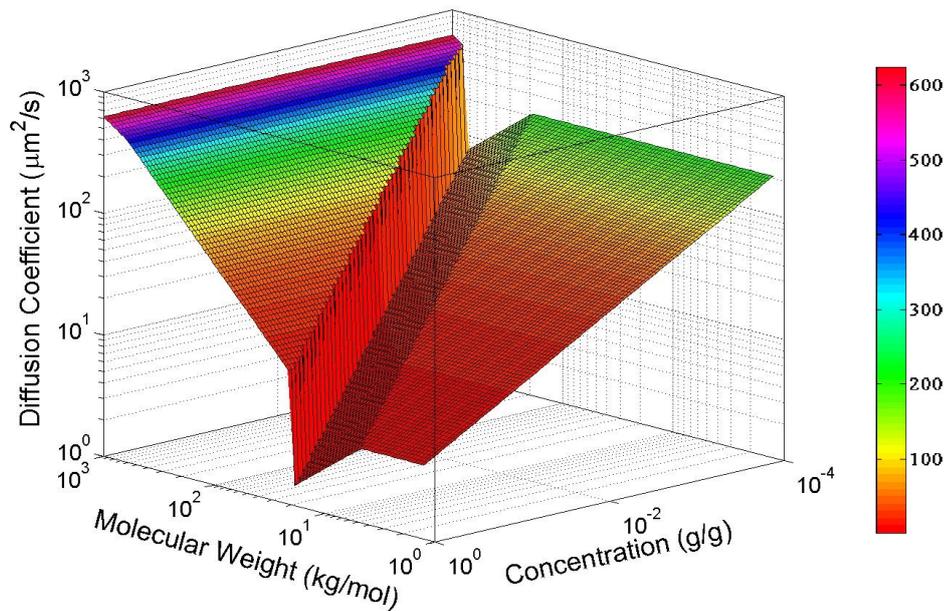
Figure 7.14: Theoretical 3D plot of the diffusion coefficient of PEO in solution with varying concentration and molecular weight. Dip shows predicted high Péclet number region.

By calculating the product DPe for all droplets and distinguishing between which droplets form pillars and puddles, the theoretical gradient diffusion coefficient should plot the approximate boundary between pillar and puddle formation. Figure 5 shows that for droplets with initial concentration $c_0 = 10\%$, with varying pressure and M_W we see reasonable agreement with theory.

Despite the agreement, there are several approximations that must be taken into account. Firstly, this does not consider variations of D in both time and position: it is clear that as precipitation begins, the D curve for $c = 10\%$ in Fig.7.15 is not relevant as the concentration of the droplet has become much higher. Secondly, it must be emphasised that the geometric constraints discussed in Chapter 5 are important. While there is reasonable agreement in this plot at $c_0 = 10\%$, in that the diffusion coefficient marks the boundary between flat disks and pillars quite well, this may be rather fortuitous. At $c_0 = 5\%$, it is clear that polymer networks are less prevalent than at 10%, therefore we would expect a higher initial Péclet initial number. While this may be true, a prediction of a higher value of Pe should not be confused with predictions of taller central pillars as it is still the volume at $t = t_p$, which is the most important factor for pillar formation (assuming no
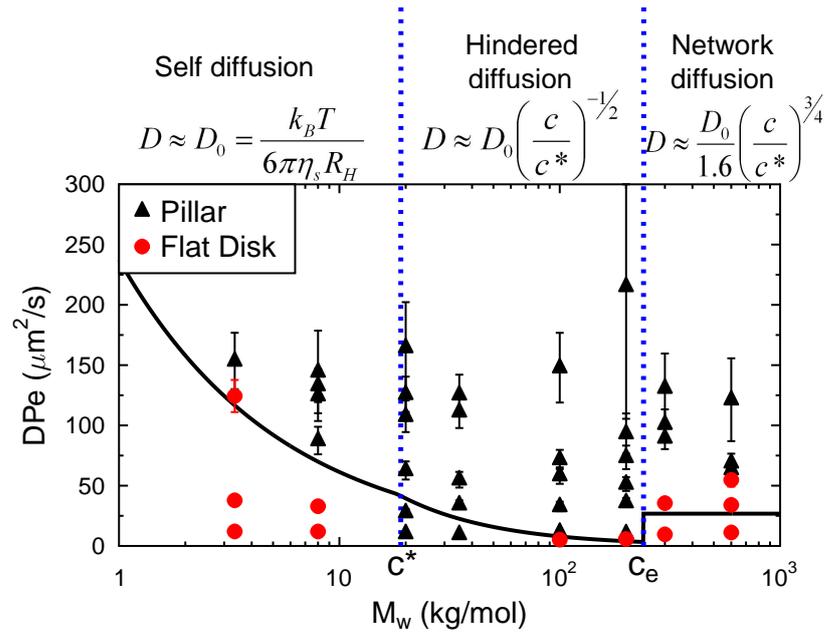
Figure 7.15: Calculated values of the DPe for PEO solution droplets with varying evaporation rate and M_{W}, and initial concentration $c_0 = 10\%$. Differentiation is made between droplets which form pillars (black triangles) and flat deposits (red circles) and plotted against D values from the theoretical model (solid black line). Different diffusive regimes (self diffusion, hindered diffusion and cooperative diffusion) separated by dashed blue lines.

molecular weight dependency on evaporation rate and receding speed). Therefore, because the concentration profiles are assumed to be identical at $t = t_{\mathrm{p}}$ for all values of c_0, initial concentration is considered less important on the diffusivity term than the polymer molecular weight. Thirdly, the simple 1D model of the Péclet number cannot account for any intrinsically 3D effects such as convection currents, surface tension gradients and droplet geometry. Finally, deviations from the theoretical line in figure 5 could be a result of the high polydispersity of PEO, which were listed in Table 4.1.

7.2.6 Precipitation Time

This diffusivity argument is essentially an extension of the Péclet model for the competition between advective flux and diffusive backflow but now taking into account concentration regimes into the diffusive behaviour. However, this presupposes that pillar formation remains a simple product of the volume remaining at t_{p}/t_0. Therefore, at ambient conditions we would expect t_{p}/t_0 to be lowest in

the intermediate region of M_W. Due to the difficulty in measuring t_p accurately from profile images, particularly at low M_W, the perimeter of PEO droplets were observed under a microscope through cross-polarised filters, giving clear images of the exact moment which semi-crystalline regions form at the droplet perimeter to within ± 1s. The downside of this method is that t_0 can now no longer be measured. Volume measurements have shown that the evaporation rate is not strongly dependent on M_W, therefore t_0 is assumed to be constant in this investigation.

Fig.7.16 shows the time-lapse images of each molecular weight, and it is clear that as M_W is increased the precipitation time is reduced. This is in stark contrast with the diffusivity argument which predicts that the central M_W range forms pillars due to slow diffusion and thus earlier precipitation. It was predicted that at high molecular weights the high cooperative diffusion would limit any concentration gradients from building up, suppressing early precipitation at the droplet perimeter. These new images in fact suggest that the Péclet number increases with molecular weight, which is what was originally predicted in the previous chapter from the self diffusion relation with M_W.

So the question remains, if the droplets are not reacting elastically to evaporation induced shear, and the polymer entanglements are not causing fast cooperatjve diffusion limiting early precipitation, what stops pillars from forming at high molecular weight?

7.2.7 Resisting the Contracting Collar

A third hypothesis is the addition of an as yet unconsidered potentially limiting case for the formation of pillars - liquid resistance to the effects of contracting collar described in Chapter 5. Up until now it has been assumed that the contraction of the spherulites around the droplet perimeter induces an immediate receding response from the liquid phase, however clearly if the liquid resists this motion the receding contact line stage will be diminished. With this in mind, it is now argued that with solutions of high molecular weight the contraction of the advancing crystallisation front is insufficiently strong to push the liquid phase during precipitation, either due to the increasing droplet viscosity or to additional effects of contact line friction caused by an increasing adhesion force
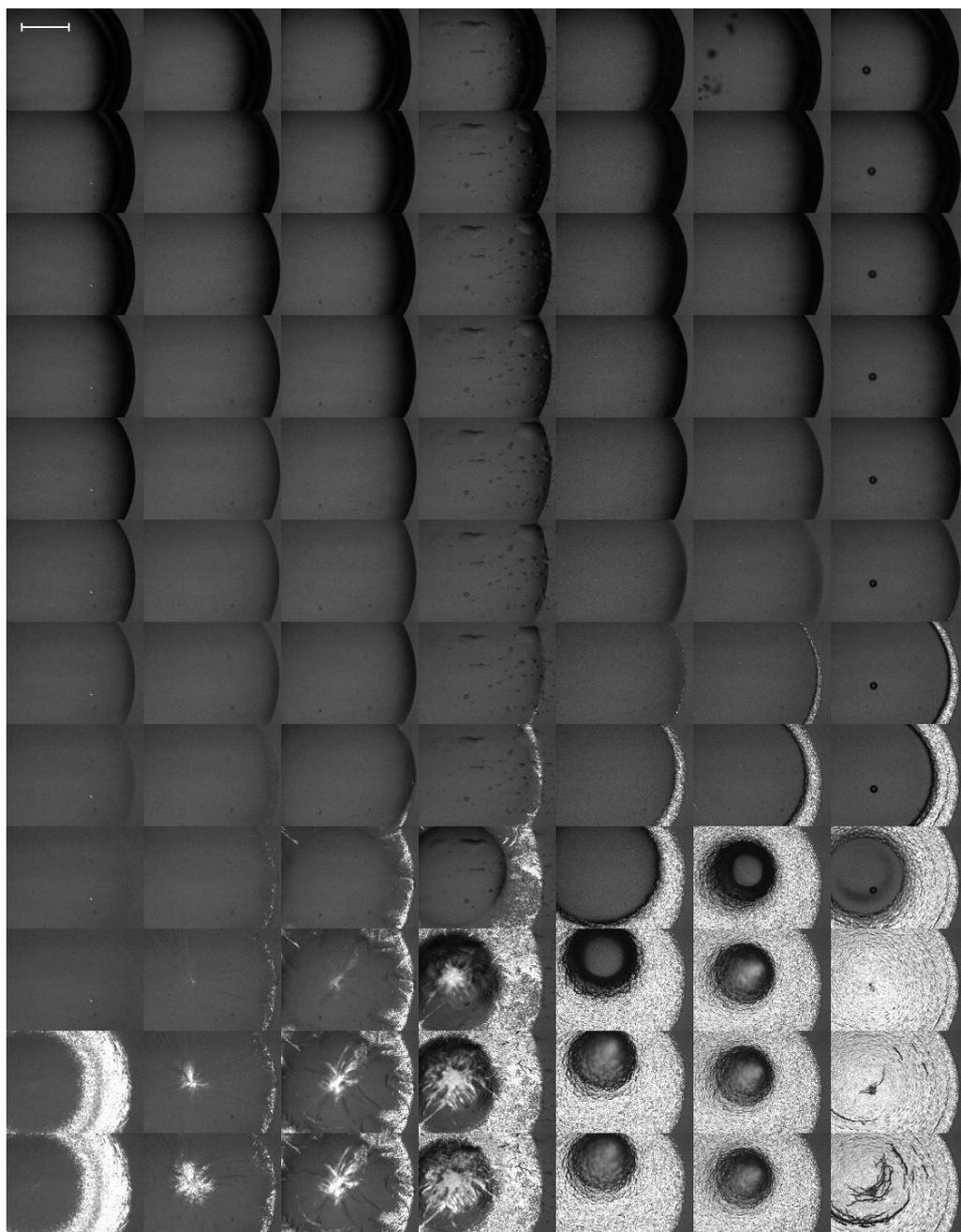
Figure 7.16: Series of vertical time-lapse images of PEO droplets as viewed under $2\times$ magnification through cross-polarised filters. From left to right $M_W = 3.35$, 8, 2, 35, 100, 200 and 300 kg/mol. Total time lapsed 4400 s. Scale bar represents 1 mm.

between polymer and substrate [167].

Careful studying of the images suggests that this may indeed be the case, as
a polymer skin can sometimes be seen to build up on the free surface of high
M_{W} droplets, which eventually covers the droplet preventing pillar formation as
shown in Fig.7.17. Typically, at lower molecular weights, this skin may indeed
be forming in the same manner, but due to the low viscosity, the liquid is able
to retreat away from the solidifying layer, leading to it depositing as a thin flat
layer on the substrate. Here however the remaining liquid finds it more difficult to
retreat and we instead end up with the skin advancing up the surface. Admittedly
it is difficult to prove that a skin forms over the surface of the droplet from these
profile images alone.

Figure 7.17: Time-lapse profile images of high molecular weight ($M_{\mathrm{W}} = 300$ kg/mol)
droplet under reduced pressure ($P = 500$ mbar) showing an apparent growth of
solid skin up the surface of the droplet, rather than the previously observed receding
contact line stage. Scale bar represents 1 mm.

Assuming there is no additional frictional force between the polymer and the
substrate with increased chain length †, this leaves the solution viscosity as the
culprit behind resistance to the contracting semi-crystalline collar. Further ex-
periments to measure the viscosity of very high concentration droplets (which are
difficult to prepare) and to estimate the forces generated at the contact line by
the solid deposit will be needed to quantify this hypothesis. An order or mag-
nitude prediction can be obtained from scaling arguments, which show that the
viscosity of entangled polymer solutions in good solvents varies with [10]:

$$\eta \sim (c/c^*)^{3.75} \sim c^{3.75} M_{\mathrm{W}}^3 \tag{7.10}$$

If we now assume that the Péclet number is given by the ratio of the evapora-
tion rate and the self diffusion coefficient D_{s} (taking into account the effect of

---

†In fact the opposite has been found in the literature for PDMS in which frictional forces
are greatest at low M_{W} [168]

dilute, semi-dilute and concentrated regimes on D_s), we can replot the data from Fig.7.15, but mark the approximate boundaries between pillar and flat deposit formation with the $Pe = 1$ line at low molecular weight, and the an arbitrary scaled viscosity curve (proportional to M_W^3) at high molecular weight, as shown in Fig.7.18.
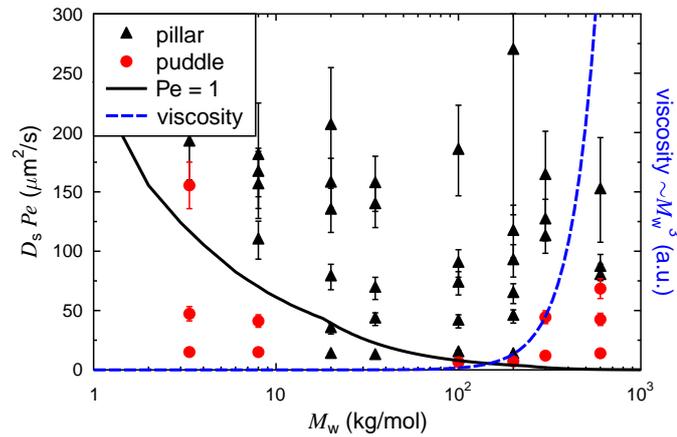
Figure 7.18: Plot of all $c_0 = 10\%$ droplets, with (black) triangles indicating those that formed pillars and (red) circles those that formed flat deposits. The horizontal axis is polymer molecular weight and vertical axis the product PeD_s which increases with evaporation rate. Error bars reflect uncertainties in measuring the evaporative flux accurately. The solid line corresponds to $Pe = 1$ and the dashed (blue) line represents $\eta \sim M_W^3$ indicating how viscosity depends on molecular weight

Despite the arbitrary scale of the viscosity curve, the reader should keep in mind that we are looking for an increasing *resistance* to receding, which would be proportional to but not equal to the viscosity as it is unknown what squeezing force is induced by contracting collar. Furthermore, quite how this resistance would effect the geometric constraints placed on the pillaring formation predictions is unknown. Therefore it is recognised that scaling the viscosity on the plot in this manner has several deficiencies in terms of predicting a pillar/flat-deposit boundary, however it does give fairly good agreement with the results, and provides encouragement that these two effects are critical in controlling pillar formation.

One final observation which may yet add another unforeseen complication to our understanding the lack of pillar formation at high molecular weights is the unusually high compressibility of the tall central structure that forms during the precipitation stage. Fig.7.19 is a time-lapse sequence of profile images of a droplet

droplet with $M_{\mathrm{W}} = 600$ kg/mol at reduced pressure $P = 200$ mbar. Surprisingly,
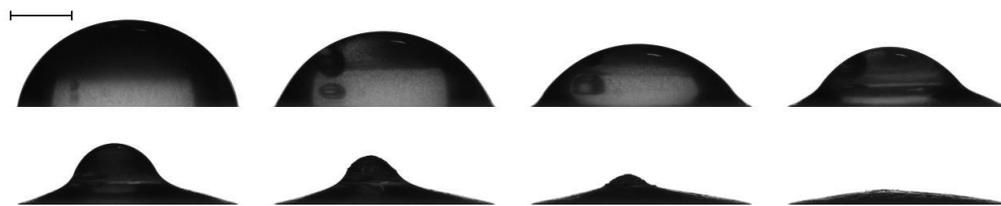
Figure 7.19: Time-lapse profile images of high molecular weight ($M_{\mathrm{W}} = 600$ kg/mol) droplet under reduced pressure ($P = 200$ mbar) showing that the central structure formed after the surface has entirely solidified is sufficiently compressible that late stage drying reduces the structure to a flat deposit. Total time lapsed 1 hour and 10 minutes. Scale bar represents 1 mm.

by the 6th image the structure is entirely covered in a solid layer, which with a careful eye the reader should see from the roughness of the structures surface. Despite this tall central region, late stage contraction continues and leads to a flat deposit. Until now this has not been observed. While late stage contraction does repeatedly show a slow reduction in volume of the tall central structures after surface precipitation stops, this is the first example of one compressing down into a flat layer. This observation could be explained as simply a side effect of the way the solid skin forms up the surface of these high viscosity drops. Because the skin formation does not lead to liquid receding very close to the contact line, there is a large volume of liquid distributed under the solid surface by the 6th image. As further volume is lost, the surfaces collapses inwards significantly, enough that the structure could be lost entirely. This explanation is slightly lacking as it cannot convincingly explain how this central structure can be lost whereas others cannot. However, that is largely due to the rarity of such late stage flattening and thus the small sample of observations of this occurrence.

Our observations of the effects of molecular weight and the various explanations presented in this chapter have led to our 4th paper focusing on the properties of PEO in solution [169]. Further work, particularly measurements of the viscosity of the liquids immediately prior to precipitation, could be highly useful for furthering our understanding of the effects of chain length on the PEO pillar forming process.

Before you try to convince anyone else, be sure you are convinced, and if you cannot convince yourself, drop the subject.

JOHN HENRY PATTERSON

Chapter 8

Conclusions

Well here we are, at the last section of this thesis. Here the results and ideas discussed over the last three chapters will be summarised, with overviews of the respective strengths and weaknesses of the various theories put forward for explaining the unusual behaviour of drying PEO droplets under the myriad of experimental conditions observed.

8.1 Pillar Formation - How Does It Happen?

First let us review the current understanding of the pillar formation process. This can be broken down into four distinct stages:

8.1.1 Pinned Drying

After deposition PEO droplets very quickly spread to a radial size that remains fixed for the droplet lifetime owing to high pinning forces between the polymer and substrate. Evaporation then leads to steadily reducing volume, surface area, height and contact angle, but more importantly, the combined effects of the pinned contact line and enhanced evaporation at the perimeter leads to outward radial flow of the dissolved polymers to the droplet perimeter via the well established coffee-ring effect [1]. Surprisingly, the evaporation rate is seemingly independent of polymer concentration, which is suspected to be due to the am-

phiphilic properties of PEO resulting in a fixed number of CH_2 units at the interface regardless of concentration and because evaporation is vapour diffusion limited rather than ballistic.

When the droplet concentration at the contact line reaches the saturation concentration, $c_{\mathrm{sat}} = 50\%$ [52], solid PEO precipitates as water-rich semi-crystalline spherulites. These spherulites grow outwards from central nucleation points, but due to their large number, their compactness, and the uniformity in which they nucleate around the droplet perimeter, the combined growth and nucleation processes appear as simply a growing crystallisation front up the droplet surface. These spherulites form fixed boundaries with their neighbours, but due to these spherulites being fairly water rich, further evaporation leads to these fixed boundary spherulites shrinking in size*. This leads to both an advancing precipitation front, and contraction of the already well defined spherulites, resulting in a continually contracting solid collar around the liquid droplet perimeter that continually squeezes the remaining liquid phase inwards. This mechanical squeezing results in the appearance of a precipitation driven contact line receding, or pseudo-dewetting.

8.1.2   Pseudo-Dewetting

As the contact line recedes solid crystallites are continually precipitated at the contact line and deposited as a thin solid layer. This squeezing continues leading to different shaped liquid droplets depending on the geometry of the droplet when precipitation begins, and the competition between the evaporation rate (which works to reduce the volume to zero) and the receding speed (which works to reduce the base radius to zero). Depending on whether volume or radius reaches zero first we either are left with the common coffee-ring type stains (volume lost before $R = 0$) or tall central pillars (Liquid radius vanishes before $V = 0$). Of course due to the nature of the droplets the base radius can not actually reach zero, but it is the trajectory of $\dot{R}$ towards a zero radius value that is important. The minimum volume at the precipitation time in terms of the receding speed

---

*Quite what water content remains in the spherulites is unknown as *in situ* density measurements during the spherulite growth stage are difficult, but the various observations of shrinking post-precipitation suggests they are water rich.

and the droplet radius is given by:

$$V_\mathrm{p} > \frac{lR_0^2}{2} \tag{8.1}$$

Where l is a constant of proportionality between $\dot{R}$ and K (which in itself is a constant of proportionality between $\dot{V}$ and R, which encapsulates effects of atmospheric conditions) and has units of length. For a fixed initial radius, evaporation rate, initial volume and receding speed, it is now clear that the formation of either coffee-ring or pillar depends on the time required for precipitation. Early precipitation means large volumes when the contracting collar forms, with tall pillars as the result, whereas late precipitation leads to flat puddles that reduce to nothing before the receding phase is complete.

This precipitation time further depends on two factors: the initial concentration (as a high concentration droplet will reach the saturation concentration earlier than a low concentration droplet); and how quickly polymer chains build up at the contact line. Indeed, varying the ability for the polymer to build up preferentially at the contact line can lead to a third final full dried result - a flat pancake-like deposit.

In order for precipitation to take place preferentially at the contact line (rather than say, the droplet apex), the concentration here must be higher than elsewhere. As discussed, the coffee-ring effect acts to drag polymer's to the contact line, so a higher concentration here should not be a problem. Opposing this motion however is the polymers diffusivity, which works to drive the polymers to homogeneity. Therefore, for precipitation at the contact line to occur, the advective flow induced by the coffee-ring effect must be greater than the diffusive backflow driving the droplet to uniformity. The Péclet number (Pe) encapsulates this competition: a low Péclet number would lead to shallow concentration gradients, no preferential deposition at the edge and a flat uniform final deposit; whereas a high Péclet number would give very early crystallisation at the contact line, followed by a receding contact line and increasing height during stage 2, and a final pillar-shaped deposit. If we assume that the majority of evaporation occurs only in a narrow region close to the contact line, an estimate of the Péclet number in a drying drop is given by:

$$Pe \approx \frac{B}{\pi} \frac{c}{c_\mathrm{sat} - c} \frac{KT(1 - RH/100)}{PD \tan \theta} \tag{8.2}$$

High values of Pe lead to earlier fractional precipitation times, whereas very low

values of Pe lead to non-preferential precipitation at the contact line and uniform "pancake" deposits.

8.1.3   Boot-strap building

During this stage θ continues to increase, but unlike the previous stage h and A now also increase. The increasing surface area observation sets PEO drying apart from the well observed skin-buckling phenomena of drying Dextran droplets [7, 124, 125]. The term boot-strap building was coined due to the height increase giving the droplet the appearance of the droplet pulling up on it its own boot-straps. Around $\theta = 90°$ solid spherulites begin to deposit directly on top of previous deposits, lifting up the edge of the liquid droplet. Due to continuing evaporation, the liquid base radius continues to reduce, resulting in a solid conical structure. As with pseudo-dewetting, this stage is also driven by solid precipitation, but they are differentiated by whether the droplet height is decreasing or not. In cases where c_0 is high ($> 25\%$), stage 1 is short and stage 2 is skipped altogether, resulting in very large and often unstable pillar formations. The boot-strap building stage ends when the structure is completely encased in a solid spherulite layer. However, it does not end here as liquid is often still be present within.

8.1.4   Late Stage Contraction

When the remaining liquid is completely encapsulated by solid PEO the drying rate reduces significantly. Further volume loss leads to the solid structure formed at the end of the boot-strap building stage slowly shrinking until the deposit is completely dry. This can be seen as an increasing pillar opacity and reducing size. Because this process is so slow no definitive duration is measurable. In some rare cases - either due to high compressibility of the spherulite skin or due to the geometry of the structure - the shrinking that occurs during this stage is significant enough to remove entirely any visible central structures, leading to a deposit similar to the uniform "pancake" as seen with very low Péclet numbers.

Now let us round up the observations from the drying droplet system variables and go over the associated explanations once more.

8.2   Summary of Results

Concentration. The results from varying concentration at ambient conditions show a transition in final droplet structure at around $c_0 = 3\%$. Above this value, PEO forms the novel tall central structures, or pillars, whereas below this concentration the droplet dries into coffee-ring like structures. These results show good agreement with the model as the pillar formation cutoff is here being controlled by the time required to precipitate only. The result that $\dot{R}$ remains constant for all concentrations led to a simple calculation of the minimum pillaring volume of $V_p \approx 2.1 \pm 0.5$ μl, which is in good agreement with the observed minimum pillaring volume of 1.8 μl. What is required now is a method of predicting the time required for the contact line to reach c_{sat} from the initial concentration. This however is difficult due to the nature of the outward radial flow of the polymer to the contact line as described by the Péclet model, which includes a concentration dependency. The $c/(c_{sat} - c)$ terms shows that as concentration increases, so too does the Péclet number. A more rigorous approach to predicting the motions of the polymer to the contact line is required in order to predict a value of the precipitation time as a function of initial concentration.

Contact Angle. By reducing contact angle we find a minimum initial value (at fixed V_0) below which pillaring does not occur. This is in tentative agreement with the model as, without taking into account the effect of radius on evaporation rate and receding speed, we expect that by increasing R and reducing h, it will get progressively easier for the evaporation rate to lead to zero volume before the receding speed leads to a zero radius. However solving mathematically for the minimum contact angle gave a value of around 68°, whereas experimentally the minimum was found to be around 40°. This discrepancy could be due to the assumption that the receding speed is independent of radius being false. If the receding speed increases with radius for example, we would then expect this minimum contact angle to reduce (as it would be easier for shallow droplets to now form pillars). The small sample of observations of $\dot{R}$ at different initial radii seemingly agree with this statement, but not a large enough sample was taken to make any real conclusions. Furthermore, the $1/\tan\theta$ term in the Péclet model suggests that the effect of the outward radial solvent flow to the contact line on the motion of polymers should increase as contact angle reduces during evaporation. When both the lack of a geometrical argument that takes into account droplet

radius and the increasing Péclet number with time are taken into account, it is easy to see why understanding of the effects of θ_0 are far from complete. Further work is required to explore the initial radius dependency on $\dot{R}$.

Volume. Provided the droplet has a height below 4/5 of the capillary length the initial volume has no observable effect on the drying process. As initial droplet height approaches the capillary length however, gravity effects become important leading to a high probability of the liquid phase toppling over, or growing sideways, during the boot-strap building stage. The Péclet number predicts no effect of droplet size on the fractional time at which the droplet precipitates, in agreement with the results.

Pressure and Relative Humidity. As predicted, reducing pressure (and thus increasing evaporation rate) leads to earlier fractional precipitation. At the end of the pseudo-dewetting stage, $\theta > 90°$ and R is very small. The solid structures that form during the boot-strap building phase become more slender as pressure is reduced, and often more unstable, toppling over under their own weight and growing in the direction they toppled. Conversely as relative humidity is increased and evaporation rate lowered, there appears to be an upper limit, beyond which pillar formation reverts to flat uniform "pancake" like deposits, in agreement with predictions. Interestingly, in an over-saturated environment (atmospheric water content is above the dew point, $RH = 100\%$) dried deposits absorb moisture and revert to liquid droplets.

Temperature. There appears to be an upper temperature limit (between 40°C and 50°C) above which pillars do not form. Instead the final solid deposit is a smooth flat disk. In a separate experiment the melting temperature of solid PEO was found to be between 65°C and 70°C, and PEO (M_W) in aqueous solution is known to crystallise above $T = 66°C$ [52], therefore the temperature was not increased past 60°C. From the literature [100] it is known that in the temperature range we are working at total evaporative flux of water is linearly proportional to temperature, $\dot{V} \propto T$. When $c_0 > c^*$ (the overlap concentration) the cooperative diffusion coefficient is a function of concentration, temperature and viscosity [19]:

$$D_c \propto (1 - c_0/100)\frac{2k_BT}{6\pi R_\mathrm{h}\eta} \tag{8.3}$$

where η is the solution viscosity, which from previous work was found to follow $\eta \propto T^{-\alpha}$ where α lies between 2 and 3. Combining these various dependencies

on T, at constant concentration, gives:

$$Pe \propto T^{-\alpha} \tag{8.4}$$

Thus an increase in temperature will lead to smaller Péclet number, as the effects of faster evaporation are insignificant compared to the reduction in viscosity and increase in diffusion. This reduced value of Pe is consistent with the observation that pillar formation is reduced with increasing T. However, for completeness it is clear that the temperature variance of the solubility of PEO needs to be taken into account. As we have shown, above $T = 66°$ PEO crystallises out of solution. Therefore we would expect the solubility (and therefore c_{sat}) to reduce as temperature approaches this value, which in turn would be expected to both reduce the fractional precipitation time t_{p}/t_0 and have an increase on the Péclet number due to the $c/c_{\mathrm{sat}} - c$ term. Because the saturation concentration has not been measured as a function of temperature by either myself or in the literature, it is difficult to predict this change in saturation concentration, and thus effect on the droplet behaviour. Further measurements of c_{sat} as a function of temperature are required before a more rigorous approach to predicting pillar formation with temperature can be made.

Substrate Inclination. On an incline, 10 μl PEO droplets display either uphill toppling between 5 and 10%, stable symmetrical growth between 10 and 20%, and downhill toppling above 20%. This is explained as being due to the unique properties of these droplets having a non-uniform contact angle due to the downward bulging of the initial droplet under gravity. Assuming the droplet is large enough that when placed on a slope the effective height of the droplet increases above the capillary length, the top edge will have a lower contact angle than the bottom. Due to the contact angle dependency of the Péclet number we would therefore know that the outward radial flux to this region will be greater than that towards the bottom, and therefore this would precipitate earliest. This is indeed what was observed. The interesting low concentration uphill growth aspect comes in much later when the bottom edge precipitates. Surprisingly, this edge recedes at a faster pace than the top edge, and causes the lower advancing crystallisation front to push the remaining liquid over the top of the upper region of the PEO constricting collar. A possible culprit for the disparity in receding speed could be the differing radius of curvature these respective contact angles are given by. If receding speed increases with droplet volume (which as mentioned is a question that needs further exploration), then the larger radius of curvature

at the upper edge could explain the increased receding speed. It must be stressed however that little progress has been made with understanding slope behaviour. Indeed, explanations thus far can not account for the fact that his uphill toppling over effect only occurs at low concentrations.

Water-Ethanol Ratio. Varying ethanol:water ratios proved to have a puzzling outcome on the results which can be summarised as follows:

- $c_e < 30\%$ - **Pillars**. In this range, all ethanol has been lost due to evaporation well before precipitation begins and droplets behave as standard water PEO droplets with steadily decreasing initial contact angle.

- $30 < c_e < 55\%$ - **Pillars**. In this range, the ethanol content at the precipitation time steadily increases, while initial contact angle continues to reduce (but does not reduce below the already observed minimum contact angle of 40°).

- $55 < c_e < 75\%$ - **Flat Deposits**. At $c_e = 55\%$ initial contact angle lowers below 40° and levels off at a roughly constant value with flat uniform deposits as the result. Additionally it was found that while the polymer builds up at the perimeter to a sufficient quantity that a highly viscous ring forms, precipitation does not occur until some time later, suggesting that precipitation is being inhibited by the ethanol content. Determining whether the contact angle or the complex behaviour of c_{sat} with the non-constant ethanol:water ratio is responsible for the loss of pillar formation is difficult, but both are presumed to play a role.

- $c_e = 80\%$ - **Pillars**. The surprising result that at this high ethanol concentration pillar formation begins once more could either be due to the reduced solubility at high ethanol concentrations, or due to a combination of increase in evaporation rate (and thus increase in Péclet number) with a lack of continued decrease in contact angle.

Furthermore, by repeating experiments on hydrophobic surfaces, pillar formation occurs at all ethanol concentrations, which suggests the geometry plays a large role on drying behaviour. While the understanding of how ethanol content affects the build up of the polymer at the contact line, and the resulting saturation time,

is incomplete, the argument that pillaring is the result of a geometric constraint at the precipitation time still holds.

Molecular Weight.   There appears to be just a narrow region in molecular weight ($35 \leq M_{\mathrm{W}} \leq 200$ kg/mol) in which pillar formation occurs. Below and above this range, flat uniform deposits are the result. From the diffusion coefficient term in the Péclet number (assuming diffusivity is dominated by the very low concentration term for self diffusion), which decreases as $M_{\mathrm{W}}^{-3/5}$, we would expect the precipitation time to decrease as molecular weight is increased. Essentially, small chains diffuse too quickly to be dragged to the droplet perimeter, whereas large chains diffuse more slowly and thus preferential deposition is possible. However, this argument can not explain the high M_{W} pillar formation cutoff. For this, it is hypothesised that the high viscosity of the high M_{W} droplets resist motion driven the contraction of the spherulite collar, and so despite early precipitation and growth of spherulites around the droplet perimeter, the liquid phase is too viscous to easily recede. The formation of a skin on the droplet surface early in the precipitation stage shows some agreement with this final hypothesis. However it has also been observed that in the very high molecular weight range, tall central structures that form at the end of the precipitation stage show significant late stage contraction that the structure can shrink down into a flat uniform deposit. It is unclear if this is a consequence of the slightly different structure of these high M_{W} central pillars or if the spherulite layer at this molecular weight has a significantly higher compressibility.

8.3   Further Suggestions for Future Experiments

From the observations found from varying molecular weight it is clear that it would be useful to have a method of measuring the droplet viscosity *in situ*, particularly immediately prior to precipitation. However standard rheometer methods have proven difficult due to the high likelihood of precipitation during measurement at these high concentrations, and due to the high viscosity of these solutions proving difficult to pipette in reliable quantities.

One potentially novel method for measuring viscosity with time without the need for pipetting or limiting evaporation is through diamagnetic levitation. In pre-

vious work, Hill et. al. from the University of Nottingham showed that if a levitating water droplet is disturbed by a short controlled blast of air, the droplet will vibrate [142]. This vibration can be monitored by shining a collimated laser through the droplet directly at a photodetector. As the droplet wobbles under the influence of the sharp air blast, the amplitude of the laser detected will oscillate with several distinguishing features. In the work by Hill et. al. the eigenfrequency of this oscillation was used to measure the surface tension (assuming zero surface elasticity) of the droplets. For our work the assumption of zero surface elasticity may not be valid, so difficulty could arise here. More importantly however, the decay of this oscillation can also be used to calculate the solution viscosity. This gives a direct *in situ* method of measuring the increase in droplet viscosity during evaporation prior to precipitation (once precipitation begins the droplet surface would be too highly light scattering for this technique to work). Preliminary experiments using pendant droplets have been attempted during the course of my research, however this led to unreliable results due to the small sizes of the pendant droplets (maximum horizontal diameter of around ~ 5 mm) compared with the typical drop size in the work of Hill et. al. ($R \approx 1$ cm).

Other potential research could include altering the polymer structure, namely replacing the linear chain PEO with branched PEO. Dextran, the water soluble polymer that became the focus of the work of Pauchard et. al. [7] is a highly branched polysaccharide, which unlike PEO displays a glassy phase transition and a late stage skin buckling which leads to an array of unusual final structures. If the drying experiments of this work were repeated with increasingly branched PEO, formation of spherulites would become progressively more difficult (as it takes a much longer time to line up a branched polymer than a linear one), and behaviour may mirror those of Dextran skin buckling rather than the novel 4 stages discussed in this work.

Of course the drying droplet behaviour discussed in this thesis places no special emphasis on PEO in particular, this is simply the polymer that this unusual behaviour was noticed. I would in fact expect that this behaviour is fairly universal, given the right conditions. The saturation concentration, the spherulite growth rate, the droplet substrate pinning forces, the precipitate contraction rate, the solute diffusion coefficient and the droplet evaporation rate etc., are all attributes that could potentially be manipulated to fit the droplet geometric constraints of pillar formation discussed in this thesis. It may be worthwhile continuing this

investigation into sessile droplet systems including polymer, colloidal, granular or liquid crystal solutions.

While the work of Deegan explained the outward radial flow that leads to the common coffee-ring stain, this work offers insight into a particular example of some of the unusual behaviours that can occur once a significant quantity of a given solute is swept to the contact line. Much current research is focused entirely on eliminating the coffee-ring effect in order to better control solute deposition. This work on the other hand has had an entirely different approach: find ways to control the final solute deposit structure by altering both the droplet geometry and the phase transitions that occur as a direct result of the coffee-ring effect. Instead of suppressing the coffee-ring effect, let's use it to our advantage. Quite how these constrains would differ depending on the particular material (whether functional or not) that is collected at the contact line could prove intellectually intriguing. Indeed self-assembly is a highly diverse field of current research, which this investigation into self-forming-pillars could offer further insight. The eventual aim of this line of research would be to cheaply print functional solutes that deposit themselves into a position and structure depending on the many controllable variables discussed. This aim may be a long way off, but research such as this into spontaneous pillar formation may (or may not) prove to be an important stepping stone in the advancement of printing technology.

8.4   Concluding Remarks

The reader may have noticed that as this thesis has progressed I have often commented that our understanding is far from complete and that a further more rigorous mathematical approach is required, with particular relevance to the ethanol:water ratio system which I have only tentatively explained. This is not my attempt to simply pass this problem onto someone else, but expressing that I feel I have brought each section as far as I can take it under my own expertise within the time constraints made available. Mathematical modelling is not my strength, but rather coming up with ideas and experimental tests are what I do best. Many a time have I been in the shower and had a mini "Eureka!" moment, only to find that my mathematical abilities are not adequate to explore my own idea! It is moments like this that I am glad to have had the opportunity to

collaborate with as many minds as I have.

Despite the gaps in my understanding of my own findings, I feel that this research has been a success. I have explored an entirely new drying droplet system, and come up with enough experimental variables and subsequent explanations that my experimentalist brain has been continually challenged for the last 3 years. This work has led to the publication of 5 papers [148, 158, 166, 169, 170] with a 6th in the pipeline, and that is not to mention the various times in various continents that I have given presentations on this work, and the exciting conversations with the leaders in several fields that these presentations have resulted in. I can not think of many times in my life that I have felt more successful than when hearing a professor say the two simple words "great talk".

On that note I would like to conclude. It is my genuine hope that the reader found this thesis and the subject matter therein to be just the right balance of engaging, fascinating, and above all, inspiring.

Bibliography

[1] R. D. Deegan, O. Bakajin, and T. F. Dupont. Capillary flow as the cause of ring stains from dried liquid drops. *Nature*, 389(6653):827–829, 1997.

[2] Á. G. Marín, H. Gelderblom, D. Lohse, and J. H. Snoeijer. Order-to-disorder transition in ring-shaped colloidal stains. *Physical Review Letters*, 107(8):85502, 2011.

[3] P. J. Yunker, T. Still, M. A. Lohr, and AG Yodh. Suppression of the coffee-ring effect by shape-dependent capillary interactions. *Nature*, 476(7360):308–311, 2011.

[4] A. Stannard. Dewetting-mediated pattern formation in nanoparticle assemblies. *Journal of Physics: Condensed Matter*, 23:083001, 2011.

[5] S. M. Rowan, M. I. Newton, F. W. Driewer, and G. McHale. Evaporation of microdroplets of azeotropic liquids. *The Journal of Physical Chemistry B*, 104(34):8217–8220, 2000.

[6] G. Li and K. Graf. Microstructures formation by deposition of toluene drops on polystyrene surface. *Phys.Chem.Chem.Phys.*, 11(33):7137–7144, 2009.

[7] L. Pauchard and C. Allain. Buckling instability induced by polymer solution drying. *Europhysics Letters*, 62(6):897–903, JUN 2003.

[8] F. Parisse and C. Allain. Drying of colloidal suspension droplets: experimental study and profile renormalization. *Langmuir*, 13(14):3598–3602, 1997.

[9] H. Hu and R. G. Larson. Marangoni effect reverses coffee-ring depositions. *The Journal of Physical Chemistry B*, 110(14):7090–7094, 2006.

[10] M. Rubinstein and R. H. Colby. *Polymer physics*, volume 105. Oxford University Press New York, 2003.

[11] J. A. Riddick, E. E. Toops Jr, R. L. Wieman, and R. H. Cundiff. Physicochemical characterization of clinical dextran. *Analytical Chemistry*, 26(7):1149–1155, 1954.

[12] P. J. Flory. *Principles of polymer chemistry*. Cornell Univ Pr, 1953.

[13] R. A. L. Jones. *Soft condensed matter*, volume 23. IOP Publishing, 2002.

[14] H. Tao, C. Huang, and T. P. Lodge. Correlation length and entanglement spacing in concentrated hydrogenated polybutadiene solutions. *Macromolecules*, 32(4):1212–1217, 1999.

[15] W. Brown and T. Nicolai. Static and dynamic behavior of semidilute polymer solutions. *Colloid & Polymer Science*, 268(11):977–990, 1990.

[16] P. S. Doyle and M. Gupta. *Polymer and sphere diffusion in confinement*, 2004.

[17] M. Doi and S. F. Edwards. *The theory of polymer dynamics*, volume 73. Oxford University Press, USA, 1988.

[18] U. Zettl, S. T. Hoffmann, F. Koberling, G. Krausch, J. Enderlein, L. Harnau, and M. Ballauff. Self-diffusion and cooperative diffusion in semidilute polymer solutions as measured by fluorescence correlation spectroscopy. *Macromolecules*, 42(24):9537–9547, 2009.

[19] T. Nicolai and W. Brown. Cooperative diffusion of concentrated polymer solutions: A static and dynamic light scattering study of polystyrene in dop. *Macromolecules*, 29(5):1698–1704, 1996.

[20] M. Doi and S. F. Edwards. *The theory of polymer dynamics*, volume 73. Oxford University Press, USA, 1988.

[21] W. Brown. Slow-mode diffusion in semidulute solutions examined by dynamic light scattering. *Macromolecules*, 17(1):66–72, 1984.

[22] W. Brown. Diffusion of poly (ethylene oxide) in semidilute aqueous solution: dynamic light scattering and gradient diffusion. *Polymer*, 26(11):1647–1650, 1985.

[23] D. K. Bick and T. C. B. McLeish. Topological contributions to nonlinear
elasticity in branched polymers. *Physical Review Letters*, 76(14):2587–2590,
1996.

[24] J. Qin and S. T. Milner. Counting polymer knots to find the entanglement
length. *Soft Matter*, 7(22):10676–10693, 2011.

[25] M. Rubinstein, R. H. Colby, and A. V. Dobrynin. Dynamics of semidilute
polyelectrolyte solutions. *Physical Review Letters*, 73(20):2776–2779, 1994.

[26] A. V. Dobrynin, R. H. Colby, and M. Rubinstein. Scaling theory of poly-
electrolyte solutions. *Macromolecules*, 28(6):1859–1871, 1995.

[27] T. A. Kavassalis and J. Noolandi. New view of entanglements in dense
polymer systems. *Physical Review Letters*, 59(23):2674–2677, 1987.

[28] Y. H. Lin. Number of entanglement strands per cubed tube diameter, a
fundamental aspect of topological universality in polymer viscoelasticity.
Macromolecules, 20(12):3080–3083, 1987.

[29] R. P. Wool. Polymer entanglements. *Macromolecules*, 26(7):1564–1569,
1993.

[30] A. Dittmore, D. B. McIntosh, S. Halliday, and O. A. Saleh. Single-molecule
elasticity measurements of the onset of excluded volume in poly (ethylene
glycol). *Physical Review Letters*, 107(14):148301, 2011.

[31] W. M. Kulicke, M. Kötter, and H. Gräger. Drag reduction phenomenon
with special emphasis on homogeneous polymer solutions. *Polymer Char-
acterization/Polymer Solutions*, pages 1–68, 1989.

[32] D. H. Fisher and F. Rodriguez. Degradation of drag-reducing polymers.
Journal of Applied Polymer Science, 15(12):2975–2985, 1971.

[33] H. J. Choi, C. A. Kim, J. I. Sohn, and M. S. Jhon. An exponential decay
function for polymer degradation in turbulent drag reduction. *Polymer
Degradation and Stability*, 69(3):341–346, 2000.

[34] H. Thissen, T. Gengenbach, R. du Toit, D. F. Sweeney, P. Kingshott, H. J.
Griesser, and L. Meagher. Clinical observations of biofouling on PEO coated
silicone hydrogel contact lenses. *Biomaterials*, 31(21):5510–5519, 2010.

[35] L. Wallstrm and K. A. H. Lindberg. Wood surface stabilization with polyethyleneglycol, PEG. *Wood Science and Technology*, 29(2):109–119, 1995.

[36] S. Guilbert, N. Gontard, and L. G. M. Gorris. Prolonging the shelf-life of perishable food products using biodegradable lms and coatings. lebensm. *Wiss u.-Technol*, 29:10–17, 1996.

[37] V. V. Namboodiri and R. S. Varma. Microwave-accelerated suzuki cross-coupling reaction in polyethylene glycol (PEG). *Green Chemistry*, 3(3):146–148, 2001.

[38] S. E. Matter, P. S. Rice, and D. R. Campbell. Colonic lavage solutions: plain versus flavored. *The American Journal of Gastroenterology*, 88(1):49, 1993.

[39] A. C. Dumetz, R. A. Lewus, A. M. Lenhoff, and E. W. Kaler. Effects of ammonium sulfate and sodium chloride concentration on PEG/protein liquid liquid phase separation. *Langmuir*, 24(18):10345–10351, 2008.

[40] B. Hammouda. Solvation characteristics of a model water-soluble polymer. *Journal of Polymer Science Part B: Polymer Physics*, 44(22):3195–3199, 2006.

[41] F. E. Bailey Jr and R. W. Callard. Some properties of poly(ethylene oxide) in aqueous solution. *Journal of Applied Polymer Science*, 1(1):56–62, 1959.

[42] R. Kjellander and E. Florin. Water structure and changes in thermal stability of the system poly (ethylene oxide)-water. *J.Chem.Soc., Faraday Trans.1*, 77(9):2053–2077, 1981.

[43] S. Sasić, V. H. Segtnan, and Y. Ozaki. Self-modeling curve resolution study of temperature-dependent near-infrared spectra of water and the investigation of water structure. *The Journal of Physical Chemistry A*, 106(5):760–766, 2002.

[44] T. Shikata, R. Takahashi, and A. Sakamoto. Hydration of poly (ethylene oxide) s in aqueous solution as studied by dielectric relaxation measurements. *The Journal of Physical Chemistry B*, 110(18):8941–8945, 2006.

[45] E. E. Dormidontova. Role of competitive PEO-water and water-water hydrogen bonding in aqueous solution PEO behavior. *Macromolecules*, 35(3):987–1001, 2002.

[46] R. L. Cook, H. E. King Jr, and D. G. Peiffer. Pressure-induced crossover from good to poor solvent behavior for polyethylene oxide in water. *Physical Review Letters*, 69(21):3072–3075, 1992.

[47] R. L. Cook, H. E. King Jr, and D. G. Peiffer. High-pressure viscosity of dilute polymer solutions in good solvents. *Macromolecules*, 25(11):2928–2934, 1992.

[48] K. Devanand and J. C. Selser. Polyethylene oxide does not necessarily aggregate in water. *Nature*, 343(6260):739–741, 1990.

[49] M. Polverari and T. G. M. van de Ven. Dilute aqueous poly (ethylene oxide) solutions: clusters and single molecules in thermodynamic equilibrium. *The Journal of physical chemistry*, 100(32):13687–13695, 1996.

[50] W. F. Polik and W. Burchard. Static light scattering from aqueous poly (ethylene oxide) solutions in the temperature range 20-90°C. *Macromolecules*, 16(6):978–982, 1983.

[51] S. Bekiranov, R. Bruinsma, and P. Pincus. Solution behavior of polyethylene oxide in water as a function of temperature and pressure. *Physical Review E*, 55(1):577, 1997.

[52] B. Hammouda, D. L. Ho, and S. Kline. Insight into clustering in poly (ethylene oxide) solutions. *Macromolecules*, 37(18):6932–6937, 2004.

[53] P. G. De Gennes. A second type of phase separation in polymer solutions. *Comptes rendus de l'Académie des sciences. Série 2, Mécanique, Physique, Chimie, Sciences de l'univers, Sciences de la Terre*, 313(10):1117–1122, 1991.

[54] S. Kinugasa, H. Nakahara, N. Fudagawa, and Y. Koga. Aggregative behavior of poly (ethylene oxide) in water and methanol. *Macromolecules*, 27(23):6889–6892, 1994.

[55] B. Hammouda. The mystery of clustering in macromolecular media. *Polymer*, 50(22):5293–5297, 2009.

[56] K. W. Ebagninin, A. Benchabane, and K. Bekkour. Rheological charac-
terization of poly (ethylene oxide) solutions of different molecular weights.
Journal of colloid and interface science, 336(1):360–367, 2009.

[57] D. R. Beech, C. Booth, I. H. Hillier, and C. J. Pickles. The crystallization
of poly (ethylene oxide) fractions: temperature dependence of growth rate.
European Polymer Journal, 8(6):799–807, 1972.

[58] C. Devoy and L. Mandelkern. Effect of molecular weight on the radial
growth rates of polymer spherulites. *Journal of Polymer Science Part A2:
Polymer Physics*, 7(11):1883–1894, 1969.

[59] P. G. De Gennes, F. Brochard-Wyart, and D. Quéré. *Capillarity and wetting
phenomena: drops, bubbles, pearls, waves*, chapter 1. Springer Verlag, 2004.

[60] G. N. Lewis and K. S. Pitzer. *Valence and the Structure of Atoms and
Molecules*, page 83. The Chemical Catalog Company, Incorporated, 1923.

[61] S. R. Palit. Thermodynamic interpretation of the Eötvös constant. 1956.

[62] J. V. Ward and P. Ward. *Biology and habitat*, volume 1, pages 74, 96, 172,
180. John Wiley & Sons, 1992.

[63] W. A. Zisman. Relation of the equilibrium contact angle to liquid and solid
constitution. *Advances in Chemistry Series*, 43(1):51, 1964.

[64] G. H. Findenegg and S. Herminghaus. Wetting: statics and dynamics.
Current opinion in colloid & interface science, 2(3):301–307, 1997.

[65] T. Young. An essay on the cohesion of fluids. *Philo. Trans. Soc. London*,
95(65), 1805.

[66] M. K. Chaudhury and G. M. Whitesides. Direct measurement of
interfacial interactions between semispherical lenses and flat sheets
of poly(dimethylsiloxane) and their chemical derivatives. *Langmuir*,
7(5):1013–1025, 1991.

[67] K. L. Johnson, K. Kendall, and A.D. Roberts. Surface energy and
the contact of elastic solids. *Proceedings of the Royal Society of Lon-
don.A.Mathematical and Physical Sciences*, 324(1558):301–313, 1971.

[68] Krüss: Advancing surface science. `http://www.kruss.de/en/theory/measurements/contact-angle/measurement-contact-angle.html`. Accessed: 28/05/2012.

[69] C. Allain, D. Ausserre, and F. Rondelez. A new method for contact-angle measurements of sessile drops. *Journal of colloid and interface science*, 107(1):5–13, 1985.

[70] Accu dyne test: Surface energy for PTFE. `http://www.accudynetest.com/polymer_surface_data/ptfe.pdf`. Accessed: 28/05/2012.

[71] T. Main and D. Lim. The human external auditory canal secretory system - an ultrastructural study. *The Laryngoscope*, 86(8):1164–1176, 1976.

[72] N. J. Shirtcliffe, G. McHale, M. I. Newton, G. Chabrol, and C. C. Perry. Dual-scale roughness produces unusually water-repellent surfaces. *Advanced Materials*, 16(21):1929–1932, 2004.

[73] W. Barthlott and C. Neinhuis. Purity of the sacred lotus, or escape from contamination in biological surfaces. *Planta*, 202(1):1–8, 1997.

[74] D. Quere. Rough ideas on wetting. *Physica A: Statistical Mechanics and its Applications*, 313(1):32–46, 2002.

[75] S. Shibuichi, T. Onda, N. Satoh, and K. Tsujii. Super water-repellent surfaces resulting from fractal structure. *The Journal of physical chemistry*, 100(50):19512–19517, 1996.

[76] C. W. Extrand. Criteria for ultralyophobic surfaces. *Langmuir*, 20(12):5013–5018, 2004.

[77] K. K. S. Lau, J. Bico, K. B. K. Teo, M. Chhowalla, G. A. J. Amaratunga, W. I. Milne, G. H. McKinley, and K. K. Gleason. Superhydrophobic carbon nanotube forests. *Nano Letters*, 3(12):1701–1705, 2003.

[78] J. R. Moffat, K. Sefiane, and M. E. R. Shanahan. Effect of TiO_2 nanoparticles on contact line stick-slip behavior of volatile drops. *The Journal of Physical Chemistry B*, 113(26):8860–8866, 2009.

[79] R. D. Deegan. Pattern formation in drying drops. *Physical Review E*, 61(1):475, 2000.

[80] D. Myers and J. Wiley. *Surfactant science and technology*. Wiley Online Library, 1988.

[81] M. W. Kim. Surface activity and property of polyethyleneoxide (PEO) in water. *Colloids and Surfaces A: Physicochemical and Engineering Aspects*, 128(1-3):145–154, 1997.

[82] B. A. Noskov, A. V. Akentiev, G. Loglio, and R. Miller. Dynamic surface properties of solutions of poly(ethylene oxide) and polyethylene glycols. *The Journal of Physical Chemistry B*, 104(33):7923–7931, 2000.

[83] B. H. Cao and M. W. Kim. Molecular weight dependence of the surface tension of aqueous poly (ethylene oxide) solutions. *Faraday Discuss.*, 98(0):245–252, 1994.

[84] P. G. De Gennes, F. Brochard-Wyart, and D. Quéré. *Capillarity and wetting phenomena: drops, bubbles, pearls, waves*, chapter 2. Springer Verlag, 2004.

[85] A. M. Cazabat and G. Guna. Evaporation of macroscopic sessile droplets. *Soft Matter*, 6(12):2591–2612, 2010.

[86] A. Fick. *Phil. Mag. S. 4*, 10:30–39, 1855.

[87] R. D. Deegan, O. Bakajin, T. F. Dupont, G. Huber, S. R. Nagel, and T. A. Witten. Contact line deposits in an evaporating drop. *Physical Review E*, 62(1):756, 2000.

[88] C. E. Klots. Evaporative cooling. *The Journal of chemical physics*, 83:5854, 1985.

[89] J. C. Maxwell and W. D. Niven. *The Scientific Papers of James Clerk Maxwell*, volume 2. Dover Pubns, 2003.

[90] D. H. Shin, S. H. Lee, J. Y. Jung, and J. Y. Yoo. Evaporating characteristics of sessile droplet on hydrophobic and hydrophilic surfaces. *Microelectronic Engineering*, 86(4-6):1350–1353, 2009.

[91] M. E. R. Shanahan, K. Sefiane, and J. R. Moffat. Dependence of volatile droplet lifetime on the hydrophobicity of the substrate. *Langmuir*, 2011.

[92] B. Rieger, H. R. C. Dietrich, L. R. Doel, and L. J. V. Vliet. Diffusion of microspheres in sealed and open microarrays. *Microscopy research and technique*, 65(45):218–225, 2004.

[93] G. D. Nadkarni and S. Garoff. An investigation of microscopic aspects of contact angle hysteresis: Pinning of the contact line on a single defect. *EPL (Europhysics Letters)*, 20:523, 1992.

[94] R. D. Deegan. *Deposition at pinned and depinned contact lines: Pattern formation and applications.* PhD thesis.

[95] CP Royall, R. van Roij, and A. Van Blaaderen. Extended sedimentation profiles in charged colloids: the gravitational length, entropy, and electrostatics. *Journal of Physics: Condensed Matter*, 17:2315, 2005.

[96] A. L. Kholodenko and J. F. Douglas. Generalized Stokes-Einstein equation for spherical particle suspensions. *Physical Review E*, 51(2):1081, 1995.

[97] A. Askounis, D. Orejon, V. Koutsos, K. Sefiane, and M. E. R. Shanahan. Nanoparticle deposits near the contact line of pinned volatile droplets: size and shape revealed by atomic force microscopy. *Soft Matter*, 7(9):4152–4155, 2011.

[98] X. Shen, C. M. Ho, and T. S. Wong. Minimal size of coffee ring structure. *The Journal of Physical Chemistry B*, 114(16):5269–5274, 2010.

[99] D. Kaya, VA Belyi, and M. Muthukumar. Pattern formation in drying droplets of polyelectrolyte and salt. *The Journal of chemical physics*, 133:114905, 2010.

[100] W. P. Lee and A. F. Routh. Temperature dependence of crack spacing in drying latex films. *Industrial & Engineering Chemistry Research*, 45(21):6996–7001, 2006.

[101] N. D. Vassileva, D. van den Ende, F. Mugele, and J. Mellema. Capillary forces between spherical particles floating at a liquid-liquid interface. *Langmuir*, 21(24):11190–11200, 2005.

[102] J. C. Loudet, A. G. Yodh, and B. Pouligny. Wetting and contact lines of micrometer-sized ellipsoids. *Physical Review Letters*, 97(1):18304, 2006.

[103] B. J. Park and E. M. Furst. Attractive interactions between colloids at the oil-water interface. *Soft Matter*, 7(17):7676–7682, 2011.

[104] J. C. Loudet, A. M. Alsayed, J. Zhang, and A. G. Yodh. Capillary interactions between anisotropic colloidal particles. *Physical Review Letters*, 94(1):18301, 2005.

[105] K. Uno, K. Hayashi, T. Hayashi, K. Ito, and H. Kitano. Particle adsorption in evaporating droplets of polymer latex dispersions on hydrophilic and hydrophobic surfaces. *Colloid & Polymer Science*, 276(9):810–815, 1998.

[106] H. B. Eral, D. M. Augustine, MHG Duits, and F. Mugele. Suppressing the coffee stain effect: how to control colloidal self-assembly in evaporating drops using electrowetting. *Soft Matter*, 7(10):4954–4958, 2011.

[107] A. V. Getling. *Rayleigh-Bénard convection: structures and dynamics*, volume 11. World Scientific Pub Co Inc, 1998.

[108] J. Thomson. On certain curious motions observable on the surfaces of wine and other alcoholic liquors. *Philosophical Magazine*, 10(330), 1855.

[109] M. F. Schatz, S. J. VanHook, W. D. McCormick, J. B. Swift, and H. L. Swinney. Onset of surface-tension-driven Bénard convection. *Physical Review Letters*, 75(10):1938–1941, 1995.

[110] J. G. Speight. *Lange's handbook of chemistry*, volume 1. McGraw-Hill New York, 2005.

[111] G. Vazquez, E. Alvarez, and J. M. Navaza. Surface tension of alcohol + water from 20 to 50°C. *Journal of Chemical and Engineering Data*, 40(3):611–614, 1995.

[112] H. Hu and R. G. Larson. Analysis of the effects of Marangoni stresses on the microflow in an evaporating sessile droplet. *Langmuir*, 21(9):3972–3980, 2005.

[113] V. X. Nguyen and K. J. Stebe. Patterning of small particles by a surfactant-enhanced marangoni-bnard instability. *Physical Review Letters*, 88(16):164501, 2002.

[114] R. Savino, D. Paterna, and N. Favaloro. Buoyancy and marangoni effects in an evaporating drop. *Journal of Thermophysics and Heat Transfer*, 16(4):562–574, 2002.

[115] F. Girard, M. Antoni, and K. Sefiane. On the effect of Marangoni flow on evaporation rates of heated water drops. *Langmuir*, 24(17):9207–9210, 2008.

[116] F. Girard, M. Antoni, S. Faure, and A. Steinchen. Evaporation and Marangoni driven convection in small heated water droplets. *Langmuir*, 22(26):11085–11091, 2006.

[117] J. Clark. Nonideal mixtures of liquids. `http://chemguide.co.uk`. Accessed: 28/05/2012.

[118] K. Sefiane, L. Tadrist, and M. Douglas. Experimental study of evaporating water-ethanol mixture sessile drop: influence of concentration. *International Journal of Heat and Mass Transfer*, 46(23):4527–4534, 2003.

[119] K. Sefiane, S. David, and M. E. R. Shanahan. Wetting and evaporation of binary mixture drops. *The Journal of Physical Chemistry B*, 112(36):11317–11323, 2008.

[120] J. R. E. Christy, Y. Hamamoto, and K. Sefiane. Flow transition within an evaporating binary mixture sessile drop. *Physical Review Letters*, 106(20):205701, 2011.

[121] K. H. Kang, S. J. Lee, C. M. Lee, and I. S. Kang. Quantitative visualization of flow inside an evaporating droplet using the ray tracing method. *Measurement Science and Technology*, 15:1104, 2004.

[122] K. H. Kang, S. J. Lee, and C. M. Lee. Visualization of flow inside a small evaporating droplet. In *5th International Symposium on Particle Image Velocimetry, Busan, Korea*, volume 22, 2003.

[123] G. W. C. Kaye, T. H. Laby, and National Physical Laboratory (Great Britain). *Kaye & Laby Tables of Physical & Chemical Constants*. National Physical Laboratory, 1995.

[124] L. Pauchard and C. Allain. Stable and unstable surface evolution during the drying of a polymer solution drop. *Physical Review E*, 68(5):052801, 2003.

[125] L. Pauchard, J. P. Hulin, and C. Allain. Drops that buckle. *Europhysics News*, 36(1):9–11, 2005.

[126] T. Kajiya, D. Kaneko, and M. Doi. Dynamical visualization of "coffee stain phenomenon" in droplets of polymer solution via fluorescent microscopy. *Langmuir*, 24(21):12369–12374, 2008.

[127] T. Okuzono, K. Ozawa, and M. Doi. Simple model of skin formation caused by solvent evaporation in polymer solutions. *Physical Review Letters*, 97(13):136103, 2006.

[128] Y. Minoura, T. Kasuya, S. Kawamura, and A. Nakano. Degradation of poly (ethylene oxide) by high-speed stirring. *Journal of Polymer Science Part A-2: Polymer Physics*, 5(1):125–142, 1967.

[129] A. Nakano and Y. Minoura. Degradation of polymers by high-speed stirring. *Journal of Applied Polymer Science*, 15(4):927–936, 1971.

[130] J. A. Odell, A. J. Muller, K. A. Narh, and A. Keller. Degradation of polymer solutions in extensional flows. *Macromolecules*, 23(12):3092–3103, 1990.

[131] E. M. d'Autry. *Positive-displacement pipette*, 1982.

[132] Dew point calculator. `http://www.lenntech.com/calculators/humidity/relative-humidity.htm`. Accessed: 12/07/2012.

[133] A.F. Stalder, G. Kulik, D. Sage, L. Barbieri, and P. Hoffmann. A snake-based approach to accurate determination of both contact points and contact angles. *Colloids And Surfaces A: Physicochemical And Engineering Aspects*, 286(1-3):92–103, 2006.

[134] L. B. Rockland. Saturated salt solutions for static control of relative humidity between 5° and 40°C. *Anal. Chem.*, 32(10):1375–1376, 1960.

[135] F. E. M. O'brien. The control of humidity by saturated salt solutions. *Journal of scientific instruments*, 25:73, 1948.

[136] A. F. Fercher, W. Drexler, C. K. Hitzenberger, and T. Lasser. Optical coherence tomography-principles and applications. *Reports on progress in physics*, 66:239, 2003.

[137] E. Roth and A. F. Fercher. Ophthalmic laser interferometry. *Proc. SPIE*, 658:48–51, 1986.

[138] S. Lawman and H. Liang. Fourier domain optical coherence tomography for high-precision profilometry. In *Proc. SPIE*, volume 7391, page 73910H, 2009.

[139] I. F. Sbalzarini and P. Koumoutsakos. Feature point tracking and trajectory analysis for video imaging in cell biology. *J. Struct. Biol.*, 152(2):182–195, 2005.

[140] J. P. Robinson. Principles of confocal microscopy. *Methods in cell biology*, 63:89–106, 2001.

[141] G. Cox and C. J. R. Sheppard. Practical limits of resolution in confocal and nonlinear microscopy. *Microscopy research and technique*, 63(1):18–22, 2004.

[142] R. J. A. Hill and L. Eaves. Vibrations of a diamagnetically levitated water droplet. *Physical Review E*, 81(5):056312, 2010.

[143] M. V. Berry and A. K. Geim. Of flying frogs and levitrons. *European Journal of Physics*, 18:307, 1997.

[144] V. P. Privalko, V. B. Sobolev, N. A. Rekhteta, and V. N. Sichko. Structure-dependent magnetic susceptibility of sharp poly (ethylene oxide) fractions. *Journal of Macromolecular Science, Part B: Physics*, 37(6):765–771, 1998.

[145] Poly(ethylene oxide) [MW 100,000]. `http://www.polysciences.com/Core/Display.aspx?pageId=98\&categoryId=298\&PageIndex=4\&productId=422`. Accessed: 12/07/2012.

[146] R. Souda. On sub-t_g dewetting of nanoconfined liquids and autophobic dewetting of crystallites. *Phys.Chem.Chem.Phys.*, 14(12):4118–4124, 2012.

[147] Wolfram MathWorld: Spherical cap. `http://mathworld.wolfram.com/SphericalCap.html`. Accessed: 12/09/2012.

[148] D. Willmer, K. A. Baldwin, C. Kwartnik, and D. J. Fairhurst. Growth of solid conical structures during multistage drying of sessile poly (ethylene oxide) droplets. *Phys.Chem.Chem.Phys.*, 12(16):3998–4004, 2010.

[149] S. Das, A. Marchand, B. Andreotti, and J. H. Snoeijer. Elastic deformation due to tangential capillary forces. *Physics of Fluids*, 23:072006, 2011.

[150] G. G. Stokes. On the effect of the internal friction of fluids on the motion of pendulums. 1851.

[151] M. Reiner. The Deborah number. *Physics Today*, 17:62, 1964.

[152] N. E. Hurlburt, P. C. Matthews, and A. M. Rucklidge. Solar magnetoconvection(invited review). *Solar Physics*, 192(1):109–118, 2000.

[153] B. I. Shraiman. Diffusive transport in a Rayleigh-Bénard convection cell. *Physical Review A*, 36(1):261, 1987.

[154] J. C. Maxwell. *Theory of heat.* Dover Publications, 2001.

[155] B. G. Thompson and A. F. Kuckes. *IBM-PC in the Laboratory.* Cambridge University Press, 1992.

[156] Hyperphysics: Mean free path. `http://hyperphysics.phy-astr.gsu.edu/hbase/kinetic/menfre.html`. Accessed: 09/09/2012.

[157] S. G. Jennings. The mean free path in air. *Journal of Aerosol Science*, 19(2):159–166, 1988.

[158] K. A. Baldwin, S. Roest, D. J. Fairhurst, K. Sefiane, and M. E. R. Shanahan. Monolith formation and ring-stain suppression in low-pressure evaporation of poly(ethylene oxide) droplets. *Journal of Fluid Mechanics*, In press.

[159] M. Mohsen-Nia, H. Modarress, and H. Rasa. Measurement and modeling of density, kinematic viscosity, and refractive index for poly (ethylene glycol) aqueous solution at different temperatures. *Journal of Chemical & Engineering Data*, 50(5):1662–1666, 2005.

[160] W. B. Russel, D. A. Saville, and W. R. Schowalter. *Colloidal dispersions.* Cambridge Univ Pr, 1992.

[161] E. H. Trinh. Compact acoustic levitation device for studies in fluid dynamics and material science in the laboratory and microgravity. *Review of scientific instruments*, 56(11):2059–2065, 1985.

[162] G. P. Arrighini, M. Maestro, and R. Moccia. Magnetic properties of poly-atomic molecules. I. magnetic susceptibility of H$_2$O, NH$_3$, CH$_4$, H$_2$O$_2$. *The Journal of chemical physics*, 49:882, 1968.

[163] D. Fairhurst. Droplet contact angle on a slope. private communication, 2011.

[164] C. Simmonds. *Alcohol, Its Production, Properties, Chemistry, And Industrial Applications*. Macmillan And Co., 1919.

[165] Poly(ethylene glycol) and poly(ethylene oxide). `http://www.sigmaaldrich.com/materials-science/material-science-products.html?TablePage=20204110`. Accessed: 09/09/2012.

[166] S. Manukyan, I. Roisman, J. Venzmer, C. Tropea, H. M. Sauer, K. A. Baldwin, D. J. Fairhurst, and H. Liang. Imaging internal flows in a drying sessile polymer dispersion drop using spectral radar optical coherence tomography (SR-OCT). accepted, July 2012.

[167] M. J. de Ruijter, T. D. Blake, and J. De Coninck. Dynamic wetting studied by molecular modeling simulations of droplet spreading. *Langmuir*, 15(22):7836–7847, 1999.

[168] A. Galliano, S. Bistac, and J. Schultz. Adhesion and friction of PDMS networks: molecular weight effects. *Journal of colloid and interface science*, 265(2):372–379, 2003.

[169] K. A. Baldwin and D. J. Fairhurst. The effects of molecular weight, evaporation rate and polymer concentration on pillar formation in drying poly(ethylene oxide) droplets. accepted, October 2012.

[170] K. A. Baldwin, M. Granjard, D. I. Willmer, K. Sefiane, and D. J. Fairhurst. Drying and deposition of poly (ethylene oxide) droplets determined by Péclet number. *Soft Matter*, 2011.